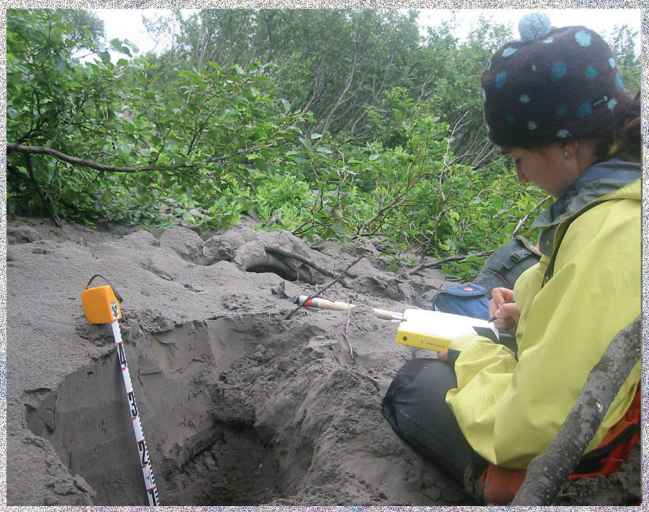
Geology of the 2006 Eruption













High-angle oblique aerial view, from the southeast, of Augustine Volcano's 2006 summit lava dome. Smooth collar around the south half of the dome is 2006 fall deposits that fill the 40-m-tall scarp formed during the 1976 eruption. Alaska Volcano Observatory photo taken May 13, 2006, by Cyrus Read.

The 2006 Eruption of Augustine Volcano, Alaska
Power, J.A., Coombs, M.L., and Freymueller, J.T., editors
U.S. Geological Survey Professional Paper 1769

Chapter 8

Timing, Distribution, and Volume of Proximal Products of the 2006 Eruption of Augustine Volcano

By Michelle L. Coombs[1], Katharine F. Bull[2], James W. Vallance[3], David J. Schneider[1], Evan E. Thoms[1], Rick L. Wessels[1], and Robert G. McGimsey[1]

Abstract

During and after the 2006 eruption of Augustine Volcano, we compiled a geologic map and chronology of new lava and flowage deposits using observational flights, oblique and aerial photography, infrared imaging, satellite data, and field investigations. After approximately 6 months of precursory activity, the explosive phase of the eruption commenced with two explosions on January 11, 2006 (events 1 and 2) that produced snow-rich avalanches; little or no juvenile magma was erupted. Seismicity suggests that a small lava dome may have extruded on January 12, but, if so, it was subsequently destroyed. A series of six explosions on January 13–14 (events 3–8) produced widespread but thin (0–30 cm) pyroclastic-current deposits on the upper flanks above 300 m altitude and lobate, 0.5- to 2-m-thick pyroclastic flows that traveled down most flanks of the volcano. Between January 14 and 17, a smooth lava lobe formed in the east half of the roughly 400-m-wide summit crater and was only partially covered by later deposits. An explosion on January 17 (event 9) opened a crater in the new lava dome and produced a ballistic fall deposit and pyroclastic flow on the southwest flank. During the interval from January 17 to 27, a rubbly lava dome effused. On January 27, explosive event 10 generated a pyroclastic current that left a deposit, rich in dense clasts, on the north-northwest flank. Immediately following the pyroclastic current, a voluminous 4.7-km-long pyroclastic flow swept down the north flank. Three more explosive blasts on January 27 and 28 produced unknown but likely minor on-island deposits. The cumulative volume of erupted material from the explosive phase, including domes, flows, and fall deposits (Wallace and others, this volume), was 30×10^6 m^3 dense-rock equivalent (DRE).

The continuous phase of the eruption (January 28 through February 10) began with a 4-day period of nearly continuous block-and-ash flows, which deposited small individual flow lobes that cumulatively formed fans to the north and northeast of the summit. A single larger pyroclastic flow on January 30 formed a braided deposit on the northwest flank. Roughly 9×10^6 m^3 (DRE) of magma erupted during this period. Around February 2, the magma flux rate waned and a northward lava flow effused and reached a length of approximately 900 m by February 10. Approximately 11×10^6 m^3 (DRE) of magma erupted during the second half of the continuous phase.

After a 23-day hiatus, lava effusion recommenced in early March (the effusive phase) and was accompanied by frequent (but volumetrically minor) block-and-ash flows. From March 7 to 14, extrusion increased markedly; two blocky lava-flow lobes, each tens of meters thick, moved down the north and northeast flank of the volcano; and a new summit lava dome grew to be ~70 m taller than the pre-2006 summit. This phase produced 26×10^6 m^3 (DRE) of lava. Active effusion had ceased about March 16, but, in April and May, three gravitational collapses from the west margin of the north lava flow produced additional block-and-ash flows. The basic sequence of the 2006 eruption closely matches that of eruptions in 1976 and 1986.

Introduction

The 2006 eruption of Augustine Volcano was monitored at an unprecedented level of detail for an Alaskan volcano. Precursory activity was detected by a network of seismic and GPS instruments, airborne gas measurements, and thermal and satellite data. As the eruption commenced in January of 2006, these tools were augmented by on-island remote cameras, helicopter-based thermal imaging, pressure sensors, and more. Despite the

[1]Alaska Volcano Observatory, U.S. Geological Survey, 4200 University Drive, Anchorage, AK 99508.

[2]Alaska Volcano Observatory, Alaska Division of Geological and Geophysical Surveys, 3354 College Road, Fairbanks, AK 99709.

[3]U.S. Geological Survey, Cascades Volcano Observatory, 1300 SE Cardinal Court, Vancouver, WA 98683.

volcano's remote location on Augustine Island, 115 km from Homer, Alaska, the Alaska Volcano Observatory (AVO) was able to follow closely the course of the eruption and correlate visual and thermal changes, geophysical signals, and eruptive deposits to gain a better understanding of the eruptive processes at work at this most active of Cook Inlet volcanoes.

The 2006 eruption unfolded in a series of three distinct phases (Power and others, 2006): an explosive phase of 17 days duration (January 11 to 28); a continuous phase of 13 days duration (January 28 to February 10); and an effusive phase of 13 days duration (March 3 to 16). The phases were distinguished by variations in eruptive style and magma composition (Larsen and others, this volume; Power and Lalla, this volume; Vallance and others, this volume; Wallace and others, this volume) and by corresponding deformation of the edifice (Cervelli and others, this volume). The overall sequence was similar to other historical eruptions of Augustine Volcano: beginning with an explosive onset, followed by lessening intensity, and finally concluding with an effusive phase (Power and others, 2006).

In this paper, we present a detailed chronology of the geologic events during the 2006 eruption, describing how and when on-island deposits (lava flows and domes and pyroclastic-flow, lahar, and avalanche deposits) were produced. The 2006 sequence was mostly determined as the eruption progressed, primarily from seismicity and numerous observational overflights, combined with aerial photographs, remotely operated on-island cameras, and satellite imagery. Continued analysis of the data generated during the eruption, as well as study of the stratigraphy of erupted deposits, has allowed us to further refine the timeline of events and their resulting deposits, sometimes deposit by deposit.

In addition to the chronology, we present a geologic map of the on-island deposits from the 2006 eruption (plate 1). The map was initially generated during the eruption but was greatly refined during a field campaign in the summer of 2006. Initiating the mapping as the eruption progressed allowed us to map the new deposits in a level of spatial and temporal detail not previously possible for the eruption of an Alaskan volcano. In some cases, we are able to distinguish deposits erupted during individual, minutes-long explosive events. Map units are introduced in the text in the order in which they were emplaced, and the Description of Map Units is found on the accompanying plate. Vallance and others (this volume) and Larsen and others (this volume) provide descriptions of the sedimentology and petrology, respectively, of the erupted products. The 2006 deposit map depicts sometimes ephemeral deposits and is meant to augment the more comprehensive geologic map of the island (Waitt and Béget, 2009).

Finally, we present volume estimates for individual deposits and combine these with our temporal framework to infer the time-eruptive volume progression of the eruption. In addition, component studies of the deposits reveal shifts in the composition of magmas feeding the eruption (Vallance and others, this volume) and, by combining component and volume data, we quantify the fluxes of two magmatic compositional end members. We show that the explosive phase produced pyroclastic flows initially rich in a low-silica andesite (57 weight percent SiO_2) that become progressively more silica rich and voluminous. The continuous-phase deposits, rich in high-silica andesite (62.5 weight percent SiO_2), are consistent with nearly continual spalling, degradation, and collapse of a rapidly growing summit lava dome. The effusive phase marked a change back to the low-silica andesite. These observations provide a framework within which we evaluate underlying magmatic processes that drove the eruption and show how eruptive style relates to magma flux.

Geologic Background

Augustine Volcano is an island volcano, located in upper Cook Inlet in south-central Alaska, that is part of the eastern Aleutian volcanic arc. Located 275 km southwest of Anchorage and 115 km west-southwest of Homer, Augustine Island is roughly circular, 9 km by 11 km in diameter, and Augustine Volcano reached an altitude of 1,260 m prior to the 2006 eruption. The volcano comprises a summit dome complex surrounded by an apron of pyroclastic and debris-avalanche deposits. On the south shoulder of the volcano, sedimentary rocks of the Jurassic Naknek Formation crop out from sea level to 400 m above sea level (asl) (Waitt and Béget, 2009).

The oldest known products of Augustine Volcano are late Pleistocene in age and comprise bedded hyaloclastite of olivine basalt and dense juvenile rhyolite (Johnston, 1978). Records of early to middle Holocene Augustine eruptions are scarce and limited to a few small tephra exposures on the south flank and some distal ashes with Augustine compositional affinities (Waitt and Béget, 2009). The late Holocene, prehistoric eruptive record is more complete and shows that Augustine often erupted explosively, producing sometimes thick tephra falls, an apron of flowage deposits, and an edifice consisting of overlapping lava domes and short lava flows (Waitt and Béget, 2009). In addition, the late Holocene has been marked by repeated edifice failures and debris avalanches, as recent as 1883 (Béget and Kienle, 1992). Augustine has erupted historically in 1883, 1935, 1964, 1976, and 1986, each time producing andesitic through dacitic fall deposits, pyroclastic flows, and lava domes.

The last several eruptions of Augustine Volcano have been remarkably similar in eruptive style and compositions of erupted material, and the 2006 eruption was no exception. In particular, the 2006 eruption followed a pattern similar to the 1976 eruption. After roughly 9 months of precursory seismicity, the 1976 eruption commenced on January 22 with 3 days of 13 explosive events, the first of which excavated a large crater at the summit that was 550 m by 350 m across and 200 m deep (Johnston, 1979; Swanson and Kienle, 1988; Power and Lalla, this volume). After a quiescent period of 12 days, the volcano then entered another, slightly less explosive phase from February 6 through 15, when it produced northward-directed, lithic-rich pyroclastic flows and, during the second half of this

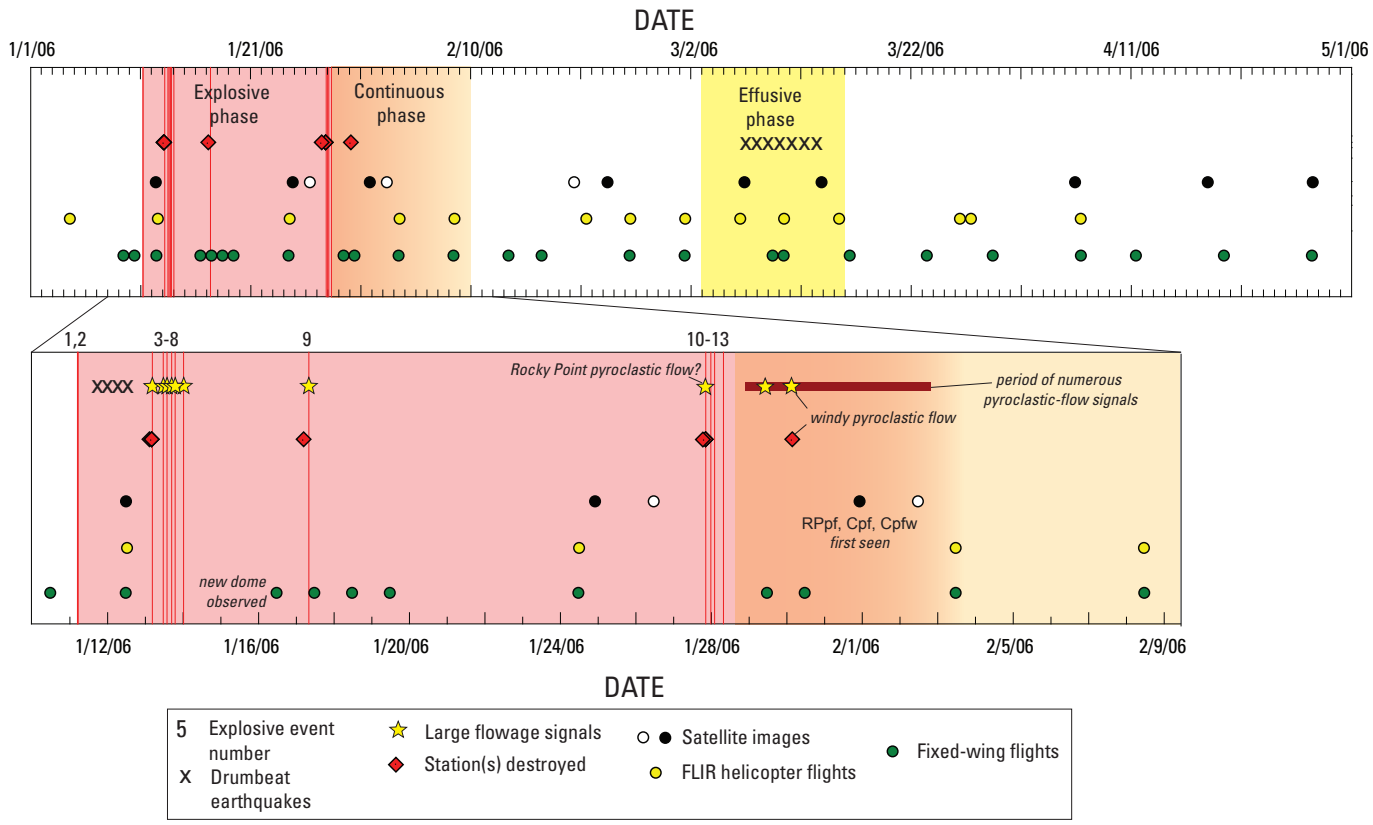


Figure 1. Timeline of eruptive events and observations during the 2006 eruption. Vertical red lines indicate timing of explosive-phase events 1–13. Timing of drumbeat earthquakes from Power and Lalla (this volume). For satellite images, open circles are Hyperion data, black circles are ASTER data (see Wessels and others, this volume, for details). Colored fields indicate the three eruptive phases defined in the text; transition from dark to light orange within continuous phase marks transition from pyroclastic-flow to lava-flow activity.

interval, a summit lava dome (Stith and others, 1977; Kamata and others, 1991). This phase resembled the 2006 continuous phase in the duration, progression, and character of the resulting deposits. After tapering effusive activity through February 1976, the final stage of the eruption occurred April 13 through 18 with expansion of the lava dome and shedding of accompanying block-and-ash flows (Johnston, 1978). The Kamata and others (1991, figs. 2, 3) map of the 1976 deposits mimics the distribution of the 2006 deposits.

The 1986 eruption sequence resembles the 1976 and 2006 sequences but with some distinct differences. The 1986 eruption also began with approximately 9 months of precursory, shallow seismicity, followed by a 12-day-long explosive phase marked by a series of discrete explosions (Power, 1988). After a 13-day lull, the first dome-building phase began and was marked by the effusion of a lava dome and short, steep northward lava flow and numerous small pyroclastic flows (Yount and others, 1987; Power, 1988). This period was followed by 3 months of quiet and then a final dome-building phase in August of 1986. This final phase was accompanied by the growth of a lava spine atop the new dome and emplacement of multiple pyroclastic flows.

Methods

Because of eruptive activity, field work on Augustine Island was limited throughout January and February 2006. Preliminary deposit maps were made using vertical and oblique aerial photos taken during observation flights, satellite imagery, and images acquired by remote on-island cameras (table 1; fig. 1). Because much of the eruption occurred in the winter, some deposits became covered by snow and were obscured in all images except those acquired immediately after emplacement. Those syn- and post-event images greatly aided the mapping process.

Photographs were taken with numerous digital cameras during field work, and observational and gas-measurement flights to and around Augustine Island that took place during the 2006 eruption. New deposits were often first observed and documented during such flights. At times, when vertical imagery was not also available, deposits would be roughly mapped using these oblique photos, and the exact locations would be refined when georeferenced imagery (orthophotos, for example) became available.

Table 1. List of observations and data used to compile deposit chronology.

[Main events shown in bold. For a complete list of flights, see Neal and others (this volume). For a complete list of satellite data and FLIR observations, see Wessels and others (this volume). For a complete list of low-light camera observations, see Sentman and others (this volume). Overflights and field work typically spanned over an hour or more and occurred around midday. Unit abbreviations are included in Observation column; for complete unit descriptions see plate 1]

Date	Time (AKST unless noted)	Image type or eruptive event	Observation	Comments
12/2/05		Overflight photographs		
12/12/05		Overflight photographs	Ash on surface; no flowage deposits	
12/20/05	12:37:00	ASTER daytime visual and thermal images	Two northeast-striking 250°C thermal features at summit	Thin clouds, but can see island
12/20/05		Overflight and fieldwork photographs	Snow-covered summit; ash seen on 12/12/2005 photos still visible below snow line; no flowage deposits	
12/22/05		Overflight and fieldwork photographs, FLIR	Snow-covered summit and flanks; no flowage deposits; some increased heat flow and fumarolic activity at summit with maximum temp. of at least 210°C	
1/4/06		Airphotos and orthophoto	Snow-covered flanks; no flowage deposits	
1/4/06		Overflight and fieldwork photos, FLIR	Snow-covered flanks; no flowage deposits; maximum summit fumarole temperature at least 390°C; overall heating of summit region	
1/10/06		Overflight photographs	Confirm that no flowage events are present	
1/11/06	**0444**	**Explosive event 1; beginning of explosive phase**		
1/11/06	**0512**	**Explosive event 2**		
1/11/06		Overflight photographs	First appearance of Exma on upper flanks	Lower flanks obscured by clouds
1/12/06	12:42:44	ASTER daytime VIS and thermal	Plume moving south	Mostly cloudy
1/12/06		Overflight and fieldwork photos, FLIR	Full extent of Exma from events 1 and 2 visible; ash from events 1 and 2 on north flank; low-level fluctuating ash emissions ongoing throughout day; new vent visible through 1986 dome, just south of 1986 spine	Better visibility than 1/11/2006
1/12/06		Burr Point camera photographs	Good views of north flank Exma	
1/13/06	**0424**	**Explosive event 3**		
1/13/06	**0847**	**Explosive event 4**		
1/13/06	0900	Burr Point camera photographs	Pyroclastic-flow-generated ash cloud on northeast and east flank; no active flows to north or northwest	Still rather dark. Cloud related to event 4
1/13/06	0915	Burr Point camera photographs	Coignimbrite cloud still present above northeast and east flanks; steaming, dark flow deposits are visible down north and northwest flanks	Significantly lighter than previous photo; flow deposits likely from event 3
1/13/06	0930 to 1115	Burr Point camera photographs	Ash cloud dissipates; steam rising from east flank is visible and it looks like most of the flows from event 4 flowed east	
1/13/06	0946	Mound camera photographs	Ash cloud mostly fills field of view; some sky visible in upper right (to the north)	
1/13/06	1032, 1039, 1106	Mound camera photographs	Ash plume rising straight up from vent; steam/ash rises from east flanks; some point-source steaming visible from surface of new flow(s)	
1/13/06	**1122**	**Explosive event 5**		

Table 1. List of observations and data used to compile deposit chronology.—Continued

Date	Time (AKST unless noted)	Image type or eruptive event	Observation	Comments
1/13/06	1130	Burr Point camera photographs	Plentiful ash billowing up from east flank, but also some ash/steam in foreground of photo on lower north flank; small Expf flow is seen making its way down the upper northwest flank	Five minutes after the end of event 5
1/13/06	1135	Mound camera photographs	Bushes visible in foreground, but rest of view is dark with gray airborne ash	
1/13/06	1145	Burr Point camera photographs	Dark ash cloud rising from summit and east flank; north flank has cleared and new dark Expf flows visible on upper north flank—one is still steaming, being emplaced? Newly steaming deposits low on north-northwest flank (lower right of photo)	
1/13/06	1206	Mound camera photographs	Ash rising from middle ground of image, plume above	
1/13/06	1428	Mound camera photographs	Nice views of new steaming flow deposits	
1/13/06	1630	Burr Point camera photographs	Plume, white in the last few images, appears to have become more ash rich and vigorous	
1/13/06	1638, 1640	Mound camera photographs	Image is darker, plume looks more ash rich	
1/13/06	**1640**	**Explosive event 6**		
1/13/06	1640 to 1714	Mound camera photographs	Series of dark images shows pyroclastic flow or surge coming toward camera	
1/13/06	1645	Burr Point camera photographs	Dark, billowing cloud rises from summit and east flank and covers east half of image; discrete pyroclastic flow descends just east of north lava flow; no flows on northwest flank	
1/13/06	1700 to 1715	Burr Point camera photographs	Ash from event 6 dissipates relatively quickly, only small plume from summit remains by 5:15	
1/13/06	**1858**	**Explosive event 7**		
1/13/06	unknown	Numerous satellite data sources	New vent visible in location of 1986 dome	
1/14/06	**0014**	**Explosive event 8**		
1/16/06		Overflight photographs	Summit has fresh snow; new lava dome visible (Exd1); many flank photos	Ash-covered unvegetated areas look deceptively like new flows
1/16/06	daytime	Mound camera photographs	New east flows visible underneath summit cloudcap	Camera view is now tilted
1/16/06		Numerous satellite data sources	Dome (Exd1) dimensions of 200 m by 160 m	
1/17/06	**0758**	**Explosive event 9**		
1/18/06		Overflight photographs	Entire island ash covered; ballistic blocks visible on upper south flank	Good lighting
1/21/06		Numerous satellite data sources	January 16 lava dome (Exd1) elongated; crater visible	
1/24/06		Aeromap airphotos	Good views of new Expf and Expct deposits on flank	Summit obscured by clouds
1/24/06		Overflight and fieldwork photographs, FLIR	Fresh snow on summit and flanks; light ash on southeast flank; dark, hot, steaming, levied flows on east, northeast, and north flanks; Exd1 visible on east part of summit, maximum temp of 140°C	Summit partially obscured by clouds/steaming
1/24/06	22:44:16	ASTER nighttime thermal	Thermal features at summit; weaker thermal features on flanks	Clear

Table 1. List of observations and data used to compile deposit chronology.—Continued

Date	Time (AKST unless noted)	Image type or eruptive event	Observation	Comments
1/26/06	12:03:15	Hyperion and ALI	Hot flowage deposits on northeast flank	Clear
1/27/06	**2024**	**Explosive event 10**		
1/27/06	**2337**	**Explosive event 11**		
1/28/06	**0204**	**Explosive event 12**		
1/28/06	**0742**	**Explosive event 13**		
1/28/06	1420	Mound camera photographs	Dark, billowing, ash-rich plume with white steam collar around its base above vent	
1/28/06	1429	Mound camera photographs	Plume looks slightly more energetic; ash raining to the south-southwest	
1/28/06	**1431**	**Explosive event 14; beginning of continuous phase**		
1/28/06	1418	Mound camera photographs	First sight of dark-gray ash in plume	
1/28/06	1431	Mound camera photographs	More ash falling; plume has bifurcated with second smaller arm rising more straight up; no flows are visible	
1/28/06	1436 to 1707	Mound camera photographs	Dark-gray plume present all afternoon until darkness falls; ash appears to rain to the south in all images	
1/29/06	1007 to 1015	Mound camera photographs	Thick billowing plume rises from summit and moves south; another ash cloud rises from north half of summit and moves down north flank	
1/29/06	1117	Strong (unnumbered) event		
1/29/06	1127	Homer camera photographs	Tall, wide plume visible above low clouds at top of image	
1/29/06	~1230	Overflight photographs	Island is ash covered and flows are steaming on west and north flanks	Photos from afar
1/29/06	1547 to 1642	Mound camera photographs	Images are starting to clear after being dark for most of the day; dark cloud seen moving south; blue sky in upper right (north); later in sequence cloud rises from north flank, then darkness sets in	
1/30/06	**0621**	**Strong (unnumbered) event**		
1/30/06		Overflight photographs	Views of plume from afar	No good island shots
1/30/06		Numerous satellite data sources	Two new lava lobes visible at summit (Exd2)	
1/31/06	22:50:44	ASTER nighttime thermal	RPpf and Cpfw visible; surface to east of RPpf obscured by plume	
2/2/06	11:53:18	Hyperion and ALI	Strong thermal features from dome at summit and block-and-ash flow down northeast flank	
2/3/06		Overflight and fieldwork photographs	White plume to 1,800 m asl; ash-rich plume rising from north flank	Volcano shrouded in clouds
2/3/06	**roughly 1200**	**Continuous-phase activity lessens**		
2/7/06		Numerous satellite data sources	900-m-long lava flow to north	
2/7/08	Night	Low-light camera in Homer	North flank pyroclastic-flow and lava activity	
2/8/06	0800 to 0830	Views from Homer	With binoculars, incandescent flows visible on north flank	

Table 1. List of observations and data used to compile deposit chronology.—Continued

Date	Time (AKST unless noted)	Image type or eruptive event	Observation	Comments
2/8/06	Morning	Mound camera photographs	Steaming (new dome?) at summit; grey (coignimbrite?) cloud on north flank	
2/8/06	midday	Overflight and fieldwork photographs, FLIR	Dark Cpf and RPpf flows on north flank in high contrast to fresh white snow; deposits range from 10 to 25°C with some bigger, hotter blocks	Summit obscured by lenticular cloud; first rock samples collected (from RPpf)
2/10/06		**Continuous phase ends; hiatus begins**		
2/16/06		Overflight photographs		Most of flanks obscured, but great summit views including dome
2/19/06	11:52:42	Hyperion satellite image	Smaller thermal feature at summit as compared to 2/2/06 image	
2/20/06		Overflight and fieldwork photographs; FLIR	Good views of Cpf, RPpf; visited deposits; Eflf dome and north flow visible especially in FLIR images	Rock samples collected from Exlh, Expf, Cpf; summit obscured somewhat by steaming and clouds
2/21/06		Airphotos and orthophoto	Good coverage of north-flank flow deposits	Summit is obscured by steam
2/22/06	12:37:03	ASTER daytime visual and thermal	Good views of flows	
2/24/06		Numerous satellite data sources	1,000-m-long lava flow to north	
2/24/06		Overflight and fieldwork photographs; FLIR	Excellent views of summit, including north lava flow	
3/1/06		Overflight and fieldwork photographs	No apparent changes since 2/24/06	
3/3/06		**Effusive phase begins**		
3/4/06		Mound camera photographs	Ash emissions	
3/5/06	nighttime	Low-light camera in Homer	Incandescence traveling down northeast slope	Probably associated with avalanching from lava dome
3/6/06	0517 to 0702	Burr Point camera photographs	Incandescence near the summit; no flows travel down flanks	
3/6/06	0621	Low-light camera in Homer	Incandescence traveling down northeast slope	
3/6/06		Fieldwork photographs	Active pyroclastic flow down northeast chute; north lava flow visible; northeast lava flow has not yet formed	Clear weather; excellent views
3/6/06	1417	Mound camera photograph	Pyroclastic flow moving down north flank	Coincident with 3-minute-long seismic signal
3/6/06	1616	Burr Point camera photographs	Small pyroclastic flow moving down northeast chute	
3/6/06	1947 to 2347	Burr Point camera photographs	Incandescence at summit and north and northeast flanks	Flows travel farther down flanks than during the morning of 3/6/06
3/6/06	22:39:02	ASTER nighttime thermal	Strong thermal anomalies at summit and north and northeast flanks	Light clouds
3/7/06	daylight hours	Mound camera photographs	All visible flanks covered in fresh ash	
3/7/06	daylight hours	Burr Point camera photographs	Ash emissions; north lava flow steaming; still no lava flow down northeast chute	Clear weather
3/8/06	1932 to 2002	Burr Point camera photographs	Incandescence at summit and north and northeast flanks	Clouds partially obscure lower flanks

Table 1. List of observations and data used to compile deposit chronology.—Continued

Date	Time (AKST unless noted)	Image type or eruptive event	Observation	Comments
3/9/06		Overflight photographs	Active block-and-ash flows from summit and northeast lava-flow front; northeast lava flow more active than north lava flow; entire northeast sector blanketed by light ash (coignimbrite)	Strong backlight on new deposits, unable to see how far northeast lava flow has progressed down chute
3/9/06	Evening/night	Burr Point camera photographs	Clear views of incandescent areas, including margins of northeast lava flow	
3/10/06		**Strongest effusive pulse begins**		
3/10/06	0828, 0830, 0859	Mound camera photographs	Block-and-ash flows moving down north and northeast flanks	
3/10/06		Overflight and fieldwork photographs; FLIR	Clear views of both north and northeast lava flows; active block-and-ash flows down east chute and from front of northeast lava flow	Excellent photos and FLIR shot of growing lava flows
3/13/06	Daytime	Burr Point camera photographs	Northeast flow has reached its final length	
3/13/06	22:45:18	ASTER nighttime thermal	Thermal data show extents of the north and northeast lava flows and delineate the hottest areas within them; match up well with low-light camera images from the same night	Clear
3/14/06	Early morning	Low-light camera in Homer	Incandescence, block-and-ash flows	
3/15/06		Fieldwork photographs; FLIR	Both north and northeast lava flows thickened and lengthened compared to 3/10/06; rockfall activity and ash emission diminished	Clear views
3/15/06		Mound camera photographs	Comparison between these and March 10 photos shows advance of northeast lava flow	
3/15/06		Strongest effusive pulse ends		
3/16/06		Overflight photographs	No major changes from last observation	Poor viewing conditions
3/22/06		Overflight photographs	No major changes from last observation	Clear views but images are mostly backlit
3/26/06		Overflight and fieldwork photographs; FLIR	No major changes from last observation; lava-flow fronts still hot, no significant temperature changes	
4/5/06	22:51:30	ASTER nighttime thermal	Summit and deposits still warm	Clear view
4/6/06		Overflight and fieldwork photographs; FLIR	Lava-flow fronts cooler; flow tops similar when compared to previous surveys; lava-flow dimensions unchanged; fumarole/vent atop dome very hot (650°C)	Fresh snow has covered many deposits
4/8/06	**1635 to 1708 AKDT**	**Two rockfall signals seen in seismic data**		
4/11/06		Overflight photographs	Small debris field on west side of north lava flow and narrow spokelike ash-fall deposit on northwest flank, both likely result of 4/8/06 rockfall(s)	
4/17/06	**1656 to 1732 AKDT**	**Rockfall signals seen in seismic data**		
4/18/06	~1430 AKDT	High-magnification photos from Homer	Intense steaming at summit and upper north flank	Photographs taken through binoculars by Dennis Anderson
4/19/06		Overflight photographs	Dark, sinuous debris deposit along west side of north lava flow (Pba) and spokelike ash-fall deposit on west flank	Both likely from April 17 rockfalls
4/27/06	12:37:30 AKDT	ASTER daytime visual and thermal		Partly cloudy with high cirrus clouds over east part of island

Table 1. List of observations and data used to compile deposit chronology.—Continued

Date	Time (AKST unless noted)	Image type or eruptive event	Observation	Comments
5/12/06		Airphotos	No changes	Good views of summit and flanks; no orthophoto made
5/13/06		Fieldwork photographs; FLIR	North-south linear trend of fumaroles and mineralization at summit; scarp along west side of north lava flow that fed April rock avalanches; images of all flowage deposits; summit vent cooled to 428°C	Clear summit views; rock sampling
5/16/06	22:45:16 AKDT	ASTER nighttime thermal	Summit and deposits still warm	Clear view
5/23/06		Overflight photographs	Good views of summit that show individual lava lobes	
5/26/06	**0106 to 0748 AKDT**	**Rockfall signals seen in seismic data**		
5/26/06		Mike Byerly photographs	Sequence of six photographs shows rock avalanche	Taken from boat north of island
5/26/06	0638, 0653, 0708 AKDT	Burr Point camera photographs	Two images: first just shows start of avalanche, second shows large ash cloud	
5/29/06	12:37:25 AKDT	ASTER daytime visual and thermal		Clear image
6/2/06		Overflight photographs	Dark debris deposits along west side of north lava flow	Likely from May 26 rock avalanches
7/12/06		Airphotos and orthophoto		Orthophoto used as base for 2006 geologic map (plate 1)
9/30/06	1630 AKDT	Citizen photographs from Homer	Strange, possibly meteoric cloud observed halfway down north flank	
10/1/06	**0750 to 0915 and 2116 to 2145 AKDT**	**Lahar(?) signals seen in seismic data**		
10/12/06		Overflight photographs	Pink, braided flow deposits atop lower parts of 2006 deposits on north flank	
10/15/06		Overflight photographs	Pink, braided flow deposits atop lower parts of 2006 deposits on north flank	

Commercial vertical aerial photography was obtained on several occasions throughout the eruption (table 1). Photographs from January 4, February 21, and July 12 were processed commercially to create orthophotos (fig. 2). Photos of the whole island were acquired at 1:36,000 scale, and during each flight a single flight line over the summit yielded photos at 1:12,000 scale. The digital orthophotos were produced at a resolution of 0.5 m/pixel. For features observed only on nonorthorectified photos, the vertical airphotos were digitally scanned at a high resolution, georeferenced to the January 4 base map, and optimized for the area of interest. Orthophoto base maps were supplemented by a 10-m-resolution digital elevation model (DEM) of the island generated in 1990.

Remote automated cameras provided time-stamped images of the volcano during the eruption (Paskievitch and others, this volume). Images from the cameras at the informally named "Mound" on the volcano's east flank and at Burr Point at the northernmost coastline (fig. 3) often provided important information about event timing when no other data were available (figs. 4, 5).

Thermal imagery was obtained weekly or biweekly during the main phases of the eruption using Forward-Looking Infrared Radiometer (FLIR) cameras (Wessels and others, this volume). The primary FLIR unit is a gimbal-mounted camera that mounts to the underside of a helicopter. FLIR images were often useful in determining the outline of new features in low light or partially steamy conditions and also in making preliminary determinations of the character of deposits based on temperature. In addition, Advanced Spaceborne Thermal Emission and Reflection Radiometer (ASTER) and Hyperion satellite imagery provided emplacement timing and temperature information for certain deposits (Wessels and others, this volume).

We undertook a 3-week-long field campaign in August 2006, after the cessation of eruptive activity. During this time, we field checked deposits that had previously been mapped only from imagery; determined stratigraphic relations; collected samples for petrology, component studies, and grain-size analysis; and measured deposit thicknesses, where possible.

Before and during the eruption, numerous geophysical instruments were installed on the island by AVO, as well as by

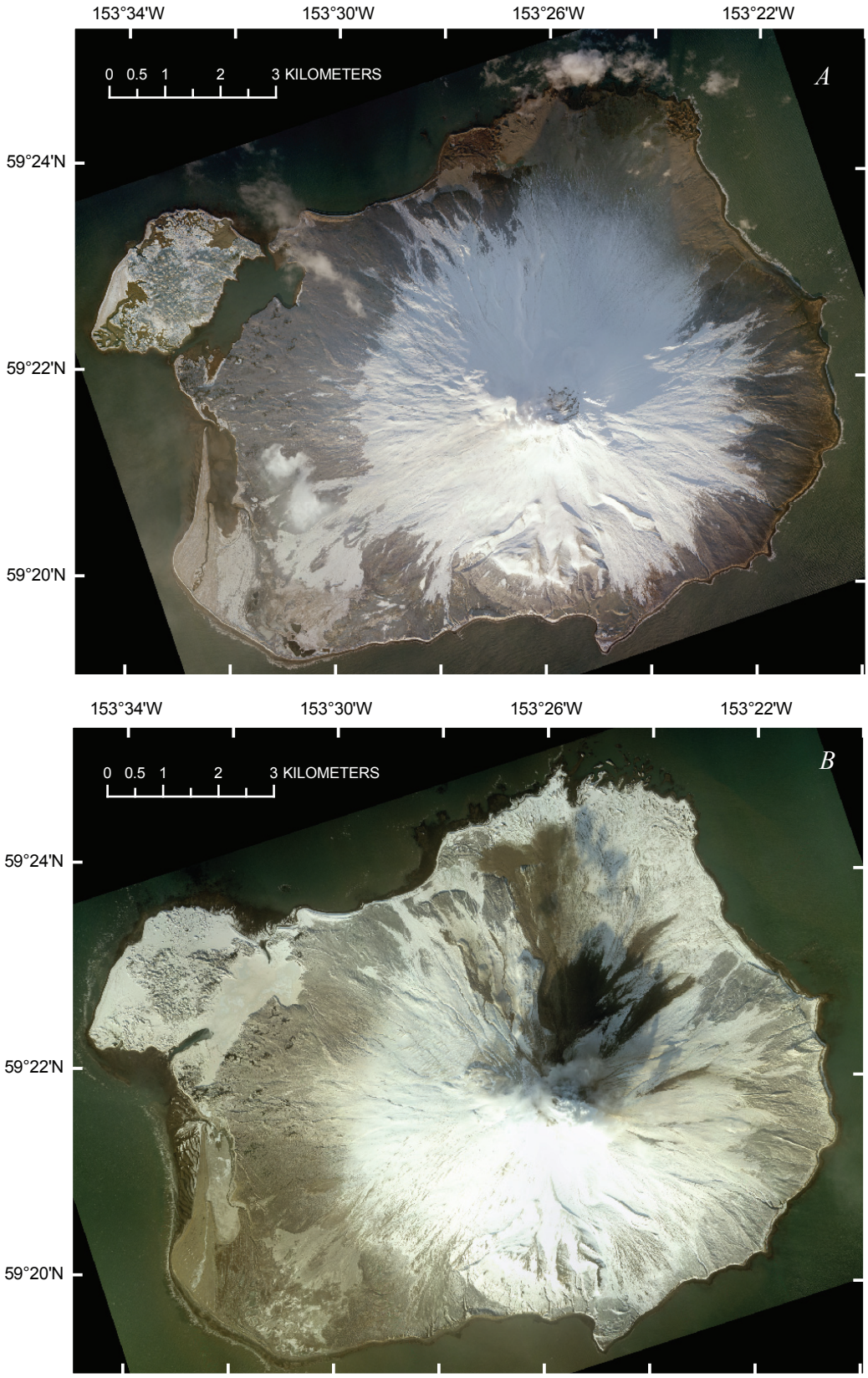


Figure 2. Orthophotographs of Augustine Island from *A*, January 4, 2006; *B*, February 22, 2006; and *C*, July 12, 2006. The projection is UTM Zone 5 and the datum is WGS 84.

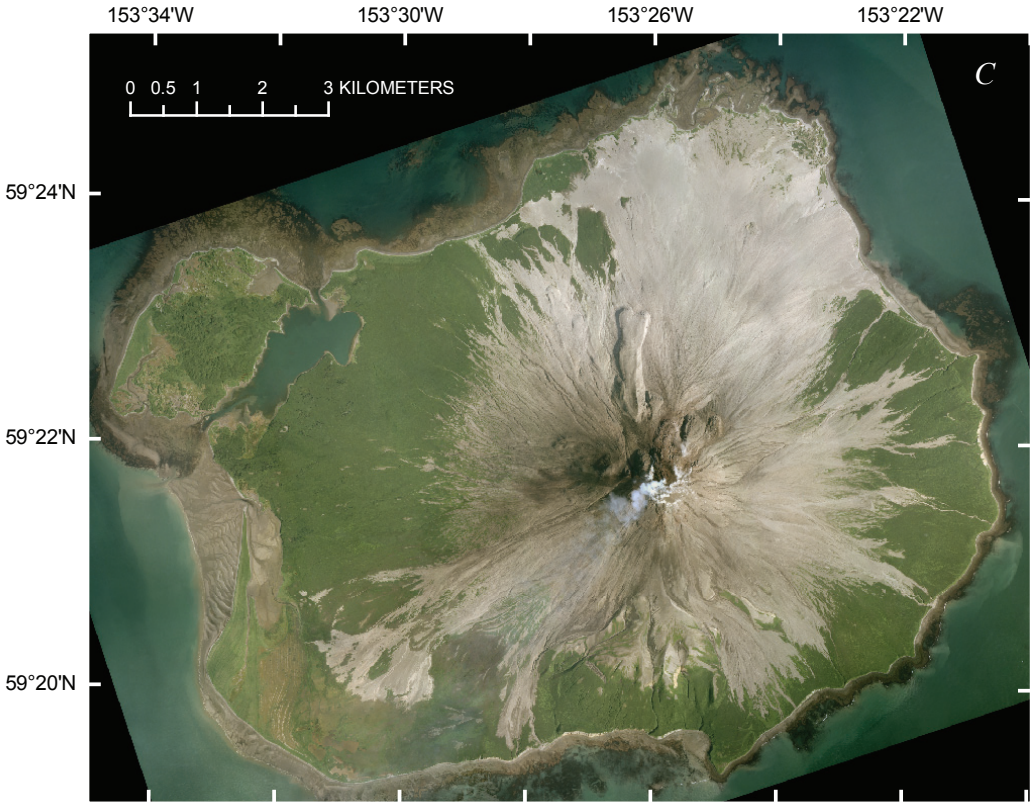


Figure 2.—Continued.

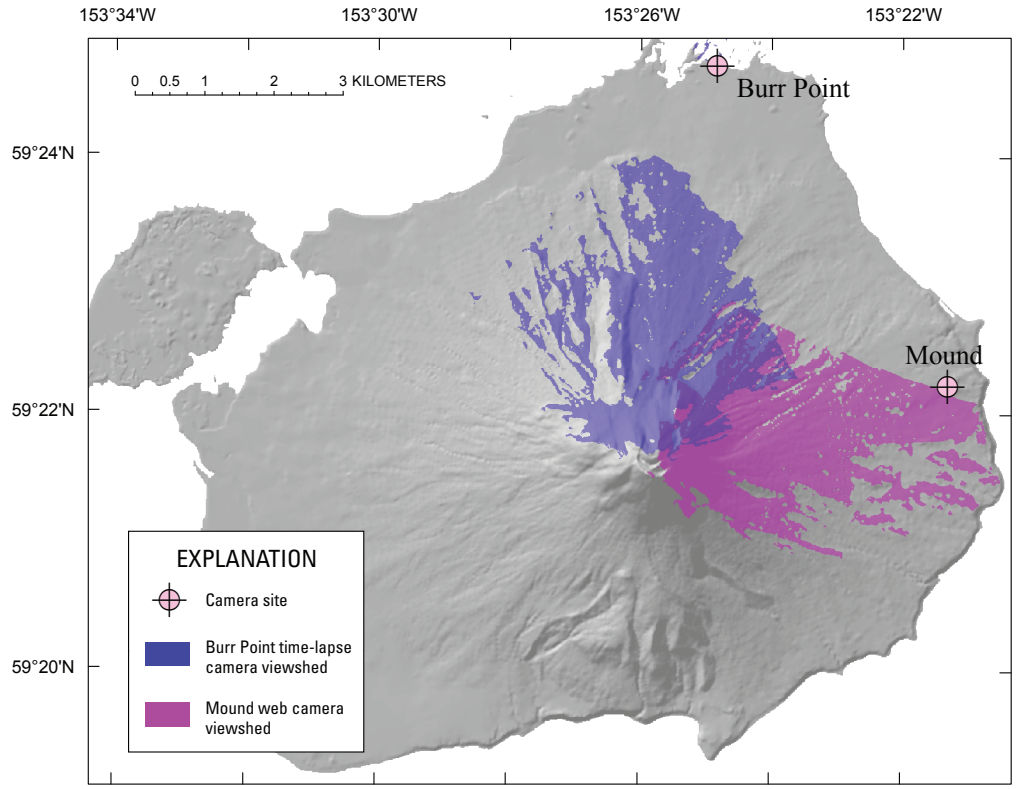


Figure 3. Shaded relief map showing location of on-island cameras and their viewsheds. Digital elevation model from 1990.

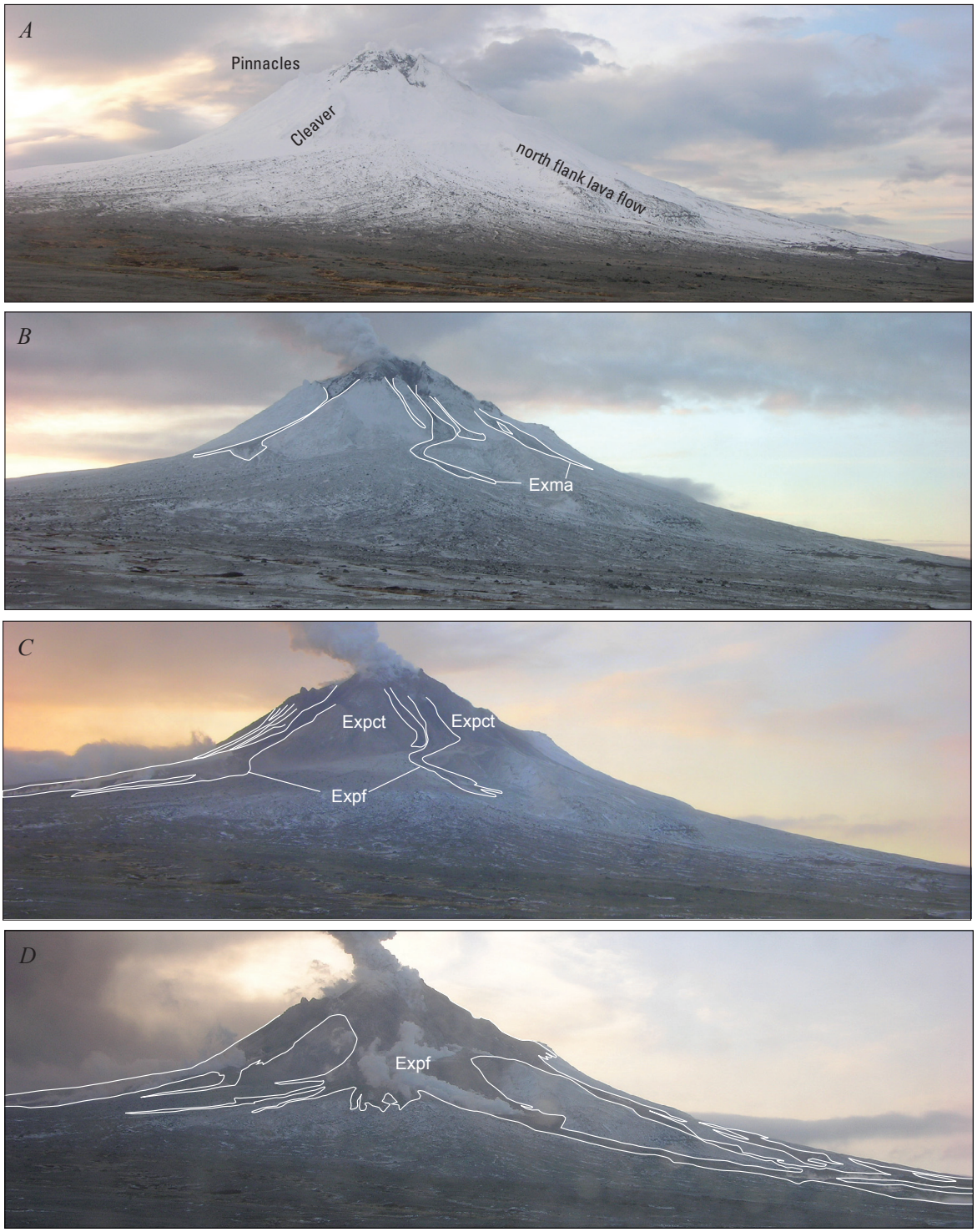


Figure 4. Views of the north flank of Augustine Volcano from the Burr Point time-lapse camera. All times are in AKST. *A,* 1100 January 5. *B,* 1030 January 12, 2006. Mixed-avalanche deposits formed during events 1 and 2 are outlined. *C,* 1045 January 13, 2006. Pyroclastic flow and current deposits (units Expf and Expct) emplaced during event 4 are outlined. *D,* 1200 January 13, 2006. Pyroclastic-flow deposits emplaced during event 5 are outlined. *E,* 1645 January 13, 2006. Ash cloud from event 6 pyroclastic flow is visible. *F,* January 14, 2006. Pyroclastic-flow deposits newly emplaced during events 7 and 8 are outlined. Other flows from these events may have followed drainages recently filled by previous flow events and, therefore, were not recognized. *G,* February 28, 2006. The Rocky Point pyroclastic-flow deposit (RPpf), pyroclastic-flow deposits (Cpf) from the continuous phase (January 28–31), and the north lava flow (Eflf), which began growing at the end of the continuous phase, are outlined. *H,* May 23, 2006. Lava flows (Eflf) and block-and-ash-flow deposits (Efba) are outlined.



Figure 4.—Continued.

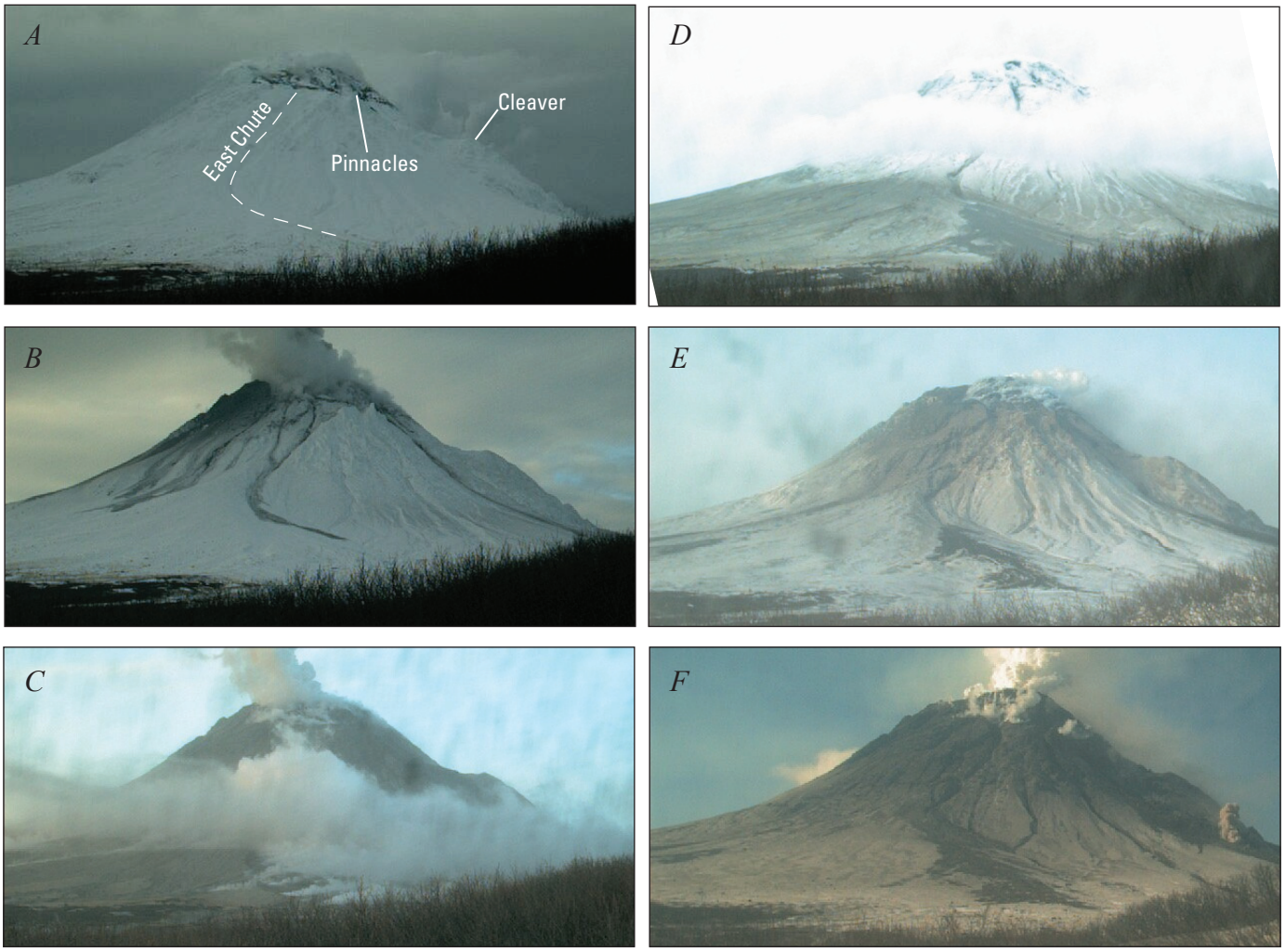


Figure 5. Views of the east flank of Augustine Volcano from the Mound web camera. *A,* January 9, 2006. *B,* January 12, 2006. Mixed-avalanche deposits from events 1 and 2 are visible. *C,* 1106 AKST January 13, 2006. Pyroclastic-flow deposits from events 3 and 4 are still steaming. *D,* January 16, 2006. Pyroclastic-flow and ash-fall deposits from events 3–8 blanket the lower flanks; the upper edifice is coated in new snow. *E,* February 8, 2006. The new steaming dome is visible at the summit. Thickest deposits from events 3 through 8 are still warm and snow-free in the east chute (left center) and on the southeast flank (bottom center). *F,* March 15, 2006. Summit dome has enlarged, and northeast lava flow has reached its final length; note small rockfall/block-and-ash flow at its toe.

the National Science Foundation Earthscope/Plate Boundary Observatory. These include a permanent network of short-period seismometers, a temporary network of broadband seismometers in place from December 20, 2006, to August 2006 (Power and Lalla, this volume), and a network of continuous GPS (CGPS) stations installed in 2004 (Pauk and others, this volume). CGPS provided information about edifice inflation and deflation (Cervelli and others, this volume), and the seismic network detected volcano-tectonic and long-period earthquakes, explosion signals, and emergent, cigar-shaped seismic signals associated with the movement of material over the ground surface (McNutt and others, this volume; Power and Lalla, this volume). The latter were particularly useful in the context of this study to help determine the emplacement locations of several flowage deposits. In addition to the invaluable data they provided while operational, the destruction of several stations recorded the timing of flow emplacement, making them almost as valuable in their demise.

While geophysical data are almost always recorded in UTC (Universal Time, Coordinated), we use Alaska Standard Time (AKST) throughout this paper unless noted, because it better correlates with the more common visual observations described herein. To convert AKST to UTC, add 9 hours. Alaska Daylight Time (AKDT), which is in effect annually after March 21, is 1 hour later than AKST. To convert AKDT to UTC, add eight hours.

Table 2. Explosive-phase events and associated flow behavior.

[Locations of seismic stations are shown on fig. 8]

Event No.	Date (2006)	Onset time (AKST)	Duration (mm:ss)[1]	Long coda[2]	Broadband delayed pulse[3]	Seismic station destroyed	Flow direction	Pyroclastic flow	Lahar	Mixed avalanche
1	1/11	0444	1:18	AUW			W			Upper flanks
2	1/11	0512	3:18	AUE	AU12, AU14		NW–E			Upper flanks
3	1/13	0424	11:00	AUE	AU14	AUP	ENE	Likely	Likely, to coast	Likely
4	1/13	0847	4:17	AUE	AU14		ENE	Confirmed, camera	Likely	Possible
5	1/13	1122	3:24	AUW	AU12		NNW	Confirmed, Burr Point camera	Likely, to coast	
				AUL			N	Confirmed, Burr Point camera	Likely, to coast	
				AUE	AU14		E	Confirmed, Mound camera	Likely, to coast	
6	1/13	1640	4:00	AUE	AU14		E,NE	Confirmed, Mound camera		
							N	Confirmed(small), Burr Point camera		
7	1/13	1858	3:00	AUW	AU12		NNW	Likely	Likely	
				AU14			NE	Likely	Likely	Probable
					AU13		SSW,SSE?	Likely	Likely	Likely
8	1/14	0014	3:00	AUW	AU12		NW	Likely	Likely	
				AUE	AU14		ENE	Likely	Likely	Probable, moderate
					AU13		SSW, SSE?	Likely	Likely, to coast	Likely, to coast
9	1/17	0758	4:11	AUE			ENE	Possible		
				AUW			WNW	Likely		
					AU12		NW	Likely		
					AU15		SW	Confirmed, over-flight photos		
10	1/27	2024	9:00		AU12		WNW	Likely		
					AU14		E	Possible		
						AUL, AUH	N	Confirmed, large		
11	1/27	2337	1:02	AUE			E	Possible, small		
12	1/28	0204	2:06	AUW	AU12		N, WNW	Likely		
				AUE	AU14		E	Likely		
13	1/28	0742	3:00	AUW			N, WNW	Likely		

[1]Reported durations were measured at seismic station Oil Point, 30 km northeast of Augustine Volcano.
[2]Long coda indicates explosion/flow signals with extended durations that were detected at seismic station(s). Modified from McNutt and others (this volume).
[3]Broadband delayed pulse indicates that secondary, high frequency signals were detected on broadband seismometers after the initial signal.

Volcanic Activity And Resulting Deposits

Similar to recent eruptions of Augustine Volcano, the 2006 activity began with a series of short, discrete explosions, followed by an interval of nearly continuous but less energetic explosive activity that tapered to lava effusion. After a 3-week-long hiatus, effusive activity resumed in March to produce two lava flows. This sequence and the naming of three phases (explosive, continuous, and effusive) was generally established during the eruption and described in Power and others (2006) and only slightly refined here (fig. 1; table 1).

The Explosive Phase—January 11–28

Discrete explosive events, each several minutes long, occurred during a 17-day period from January 11 to January 28.

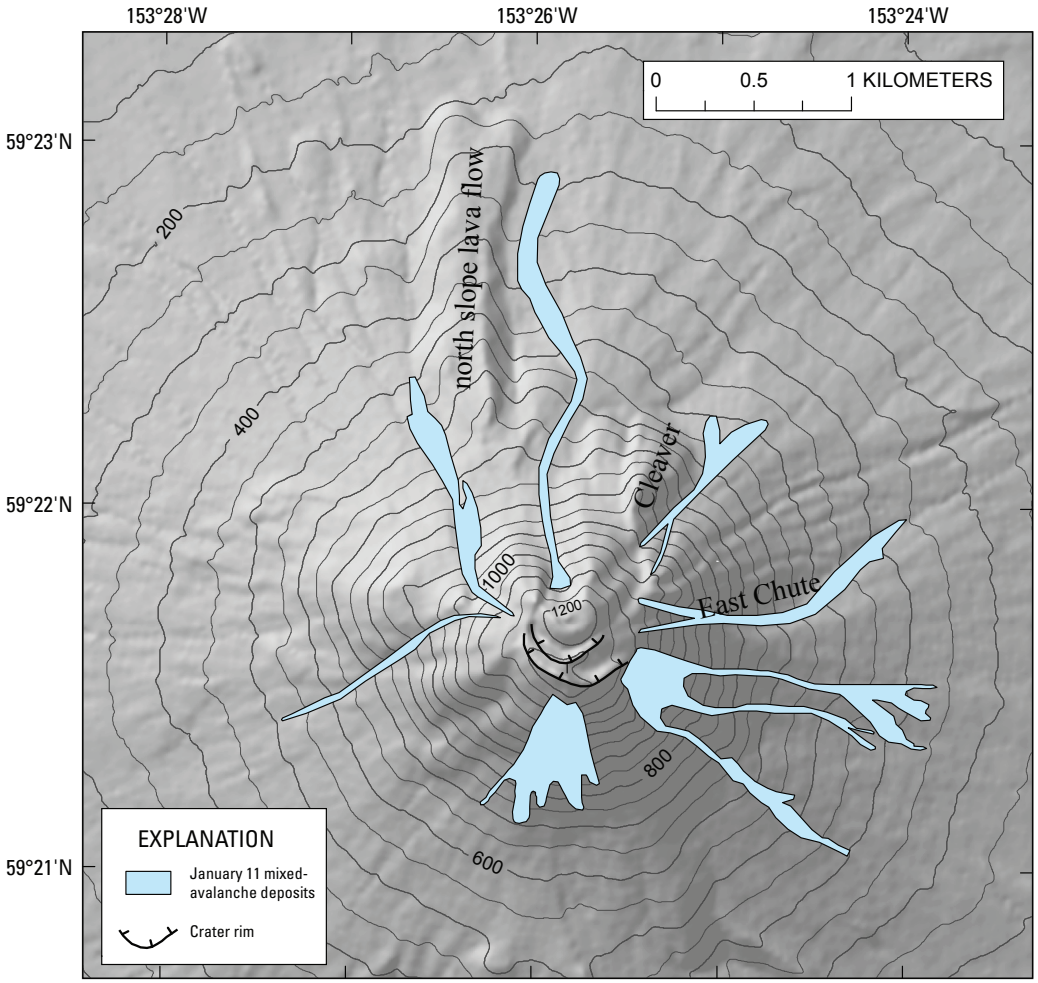


Figure 6. Map showing distribution of mixed-avalanche deposits that formed during explosive events 1 and 2 on January 11, 2006. These deposits were covered by later events; their locations are approximate. Contours show pre-2006 topography; contour interval is 50 m.

This time period is termed the "explosive phase" and individual events have been numbered 1 through 13 (Petersen and others, 2006; Power and others, 2006; table 1). Each event is best characterized by its seismic signal, which for many events records energy released during the initial ejection of material from the vent followed by ground shaking caused by movement of pyroclastic and other flows over the ground surface (McNutt and others, this volume). Aerial surveillance on January 12, 16, and 18; time-lapse photography; and seismicity constrain emplacement of pyroclastic flows during the sequence of explosive events. Seismic signals from stations downslope of flows or beside flow paths include 10–30-minute-long, high frequency, cigar-shaped codas and increase in amplitude on temporary broadband stations 10–20 minutes after explosions (table 2). Broadband stations downstream of flows show increased seismicity as much as 20 minutes after initial explosion signals. Such distinctive signals on instruments below or next to flows and their absence in other quadrants indicate pyroclastic-flow directions (McNutt and others, this volume). Between the explosive events, seismicity and visual observations show that lava effusion formed at least three small lava domes at the summit. In this section we describe the individual explosive events and their resulting deposits, as well as the lava domes effused during more quiescent intervals.

January 11: Explosive Events 1 and 2

At approximately 1530 AKST on January 10, a strong swarm of volcano-tectonic (VT) earthquakes began, culminating in two explosions at 0444 and 0512 AKST early in the morning of January 11 (table 1). These explosions, events 1 and 2, were 1 and 3 minutes long, respectively, as recorded seismically (table 2). They produced ash plumes that reached heights greater than 9 km asl and moved to the north and northeast of the volcano (Bailey and others, this volume; Schneider and others, 2006). Ash fragments sampled during on-island field work on January 12 are primarily dense or weathered, suggesting that these explosions did not release juvenile magma (Wallace and others, this volume).

An overflight of the volcano on the afternoon of January 11 revealed dark flowage deposits on the snow-covered upper south flank, but much of the rest of the volcano was hidden by clouds. An airplane volcanic gas flight, FLIR helicopter flight, and Burr Point time-lapse photographs on January 12 provided much clearer observations of the new deposits (table 1). Presumably all new deposits viewed on January 12 formed during the January 11 explosions.

The new deposits were present on most flanks of the volcano, extending as far as 2.5 km from the summit and reaching down to 300 m asl (figs. 4*B*, 5*B*, 6). Most were narrow and elongate, followed topographic lows, and ended in multiple lobate flow fronts (fig. 7). They were medium gray, and closer photographs reveal that they consisted of mixed snow, ice, and dark-colored debris; no steaming was observed (fig. 7*B*). Several had dark rills that suggest liquid water may have flowed down the central part of the deposits after the mixed snow and debris had come to rest. The flow deposits on the upper south flank appeared more snow rich than the others and formed a broad sheet rather than individual elongate lobes. None of the deposits appeared to have involved running water that flowed beyond the termini of the snow lobes. None of these deposits were sampled and essentially all were covered by subsequent flows on January 13, 14, and 17. Though not included on the deposit map, they appeared similar to later mixed-avalanche deposits of unit Exma (plate 1).

Seismic data provide some clues regarding flow emplacement during explosive events 1 and 2 (table 2). Each explosion registered as a seismic signal on all island seismometers, but some seismometers also recorded prolonged, broader spectrum waveforms after the actual explosions. These are interpreted to reflect the ground shaking caused by flow of rock and ice over the ground surface in the area near the particular seismometer. For event 1, a somewhat extended signal, or long coda, is evident at seismic station AUW on the west flank. For event 2, a long coda was recorded on seismic station AUE on the east flank. In addition, broadband seismometers AU12 and AU14 (on the northwest and northeast flanks, respectively) recorded delayed broad spectrum pulses after event 2, which likely record the passage of avalanches. These results suggest that most of the flows were emplaced during event 2.

January 11–12: Dome Growth?

In the 36 hours following events 1 and 2, several sequences of small, regularly spaced VT earthquakes, many with identical waveforms, were recorded at rates as high as 3 to 4 per minute and lasted for several hours (Power and Lalla, this volume). Similar earthquakes, often referred to as clones or drumbeats, have been associated with the emplacement of lava domes at other volcanoes, such as Mount St. Helens (Dzurisin and others, 2005). These earthquakes at Augustine suggest that the effusion of new lava may have begun late on January 11. In addition, subdaily CGPS solutions show that steady summit inflation ceased at roughly 1800 AKST on January 11; this is interpreted as the result of magma arriving at the surface and relieving pressure within the conduit (Cervelli and others, this volume, fig. 8).

Thermal and visual images acquired during a FLIR flight on January 12 revealed a new vent atop the 1986 dome at the volcano's summit, but no unambiguous new lava was observed (Wessels and others, this volume, fig. 6*D*). Later in the eruption, however, juvenile lava was observed without a distinctly strong thermal signature. There may, then, have been new lava at the surface on January 12, but it was not recognized thermally or it was visually hidden by ash and steam. If a dome did form, it was ephemeral and subsequently destroyed by blasts and/or partially covered by younger deposits. Abundant, dense, angular clasts in deposits from ensuing explosions may have been fragments of this ephemeral dome (Vallance and others, this volume).

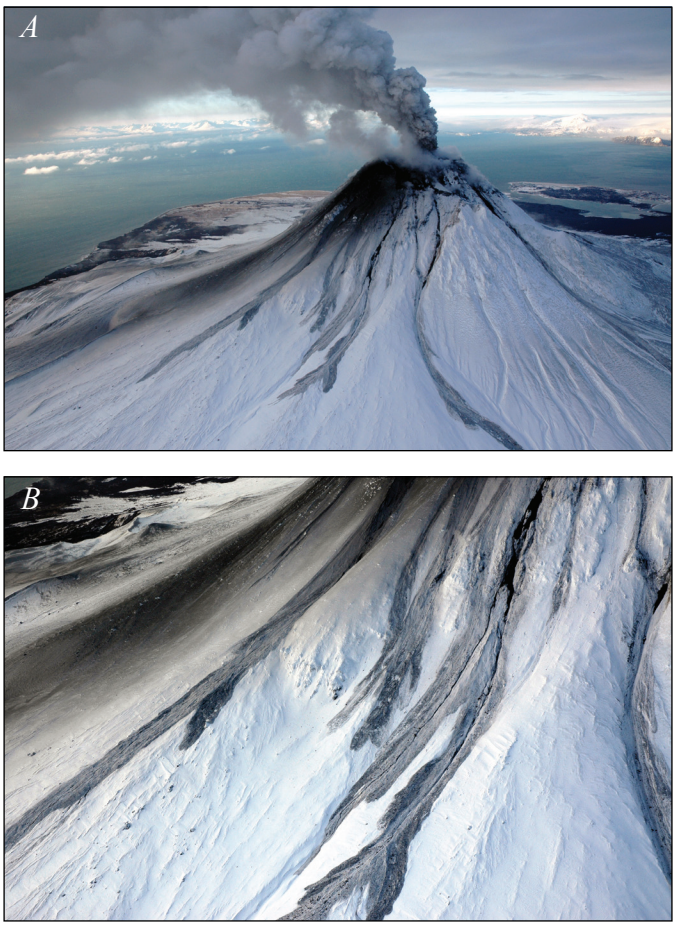


Figure 7. Oblique views of January 11, 2006, mixed-avalanche deposits. *A,* Mixed-avalanche deposits on the southeast and east flanks. View to the west. *B,* Detailed view of same deposits. Note streak of discolored snow at upper left that marks ash deposition. Photos by M.L. Coombs, January 12, 2006.

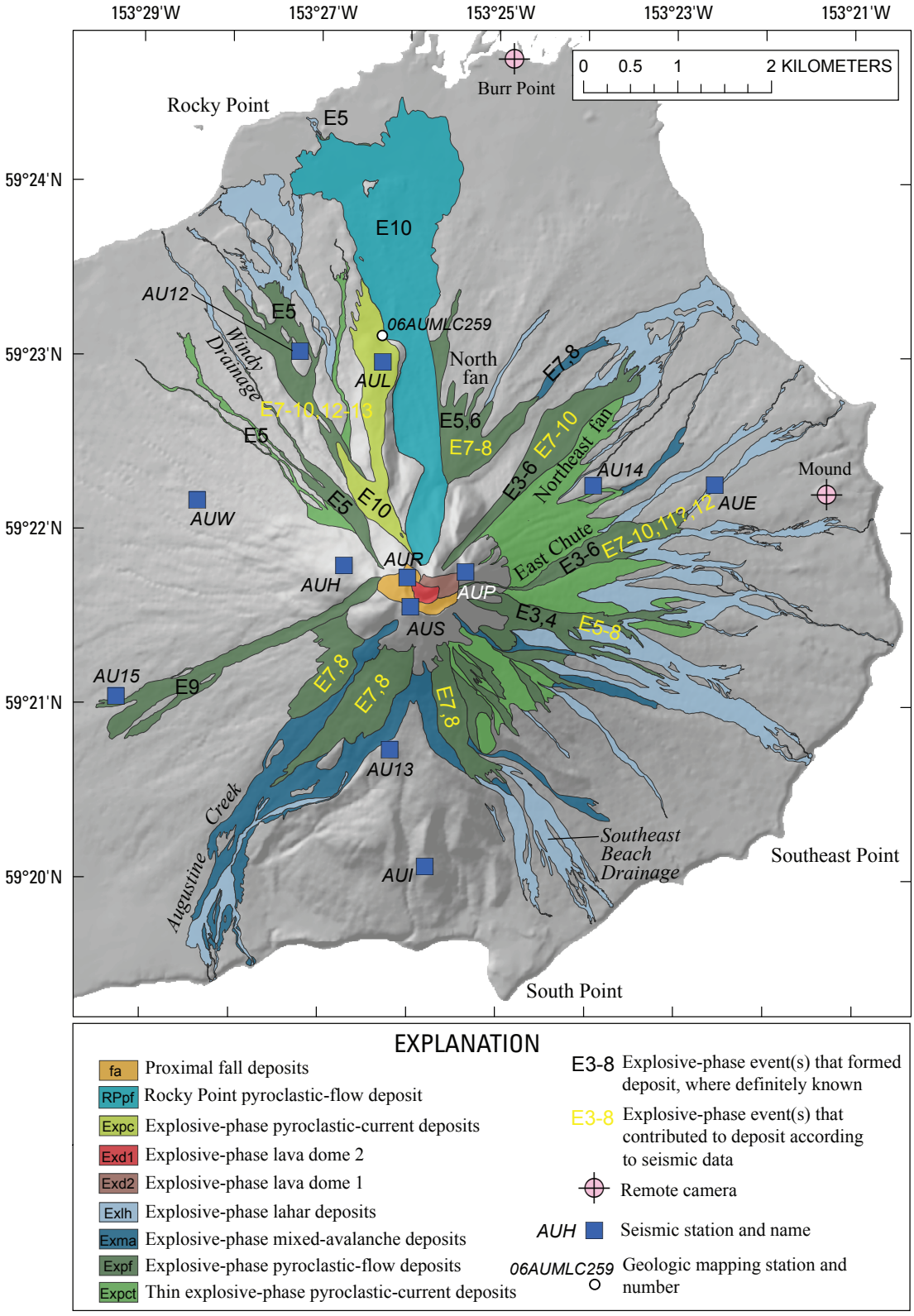


Figure 8. Map showing distribution of deposits from the explosive phase. Summit geophysical stations were destroyed during event 3. Station AUE recorded particularly strong seismic signals during events 3 and 4, thought to indicate that these events produced larger flows to the east (McNutt and others, this volume). Station AUL was destroyed during event 10, and debris from the station was found within a pyroclastic-flow deposit at station 06AUMLC259.

January 13 and 14: Explosive Events 3–8

A second series of six powerful explosions (events 3 through 8), ranging in duration from 3 to 11 minutes, occurred in a roughly 20-hour period between 0424 AKST January 13 and 0014 AKST January 14, as recorded by seismometers and an on-island pressure sensor (Petersen and others, 2006; Power and others, 2006; McNutt and others, this volume; Power and Lalla, this volume). The explosions produced ash plumes that reached altitudes of 14 km asl (Bailey and others, this volume) and deposited trace amounts of ash on the Kenai Peninsula communities of Homer and Port Graham (Wallace and others, this volume).

Explosive events 3 through 8 all resulted in the emplacement of hot pyroclastic deposits on most flanks of the volcano, which take two forms: thin (0–30 cm), laterally extensive (200–600 m wide by as much as 1.5 km long) sheets on the upper flanks, topped by farther-traveled coarse lobate flows (100 to 600 m wide by as much as 3 km long) (Vallance and others, this volume). These deposits have been mapped as two separate units: thin explosive-phase pyroclastic-current deposits (unit Expct) and explosive-phase pyroclastic-flow deposits (unit Expf), respectively (plate 1; fig. 8). Pyroclastic surges likely accompanied the explosions as well but the deposits were poorly preserved. In addition, the emplacement of pyroclastic flows on snow generated areally extensive mixed-avalanche deposits (unit Exma), lahars, and hyperconcentrated flows (unit Exlh; plate 1). These secondary deposits are described in detail in Vallance and others (this volume).

Some of the explosions that occurred on January 13 and 14 were photographed or bracketed by images from the Burr Point and Mound cameras (table 1), allowing us to link emplacement of some flows on the east and north flanks to individual events. The first overflight to the island after events 3–8 was on January 16 (fig. 9). Observers saw that the vegetation-free slopes of the volcano had been uniformly coated in brown ash-fall deposits; this coating somewhat obscured new flowage deposits. Closer inspection revealed that new flows had traveled down many slopes of the volcano and reached the coastline in several places (figs. 8, 9). Most followed tracks of earlier historic flows, but some, such as in the informally named Augustine Creek area (fig. 9*A*), destroyed vegetation. Later visits to the deposits revealed that pyroclastic flows had been limited to the upper two thirds of the edifice and that the flows that reached the coast were exclusively lahars and hyperconcentrated flows (fig. 8; Vallance and others, this volume).

Events 3 and 4

Events 3 and 4 occurred before sunrise on January 13 (0424 and 0847 AKST; table 1) and, thus, were not captured by the on-island cameras. The seismic signals for the two events lasted 11 and 4 minutes, respectively. Event 3 destroyed seismic station AUP and continuous GPS AV05 (collocated with AUP), located about 300 m from the volcano's summit (fig. 8). Both events produced the longest signal durations at short-period seismic station AUE, and the waveforms recorded there have codas indicative of pyroclastic flows (McNutt and others, this volume). Broadband station AU14 shows delayed seismic pulses during both events. These observations suggest that pyroclastic flows from the two events traveled predominantly to the east (fig. 8; table 2).

The event 3 seismic signal at station AUE was particularly long (>30 minutes) and was likely caused, in part, by lahars passing nearby, as well as by pyroclastic flows upslope (McNutt and others, this volume).

Due to darkness, no imagery is available to discriminate between flows emplaced during event 3 or event 4. The first image available after sunrise on the morning of January 13 from the Burr Point camera, at 0900 AKST, shows gray-brown ash clouds on the northeast and east flanks. Those ash clouds were the result of event 4, which began 13 minutes prior (table 1). A series of images from the Burr Point camera from 0915 to 1115 AKST show the ash clouds dissipating and new, fragmental steaming deposits on the northeast and east flanks (fig. 4*C*). No new discrete deposits were visible on the northwest flank, but the entire snow-covered upper northwest flank had been dirtied by either ash-fall deposits or thin surge or flow deposits. This blanket likely correlated to widespread pyroclastic-current deposits, recognized during August 2006 field work, that compose unit Expct (plate 1; fig. 8; Vallance and others, this volume). The results of events 3 and 4 on the south and west quadrants of the volcano are unknown but likely minor because of the absence of seismicity there.

Event 5

After a two-and-half-hour lull, event 5 began at 1122 AKST on January 13 and lasted for 3 minutes, 24 seconds. The first Burr Point image after this event, at 1130 AKST, showed an ash cloud rising from the summit and the east flank, while ash and steam shrouded the upper north flank (table 1). Steam and ash were visible rising from discrete tracks on the upper north and northwest flanks and along a single track on the lower north-northwest flank. By 1145 AKST, much of the ash and steam had cleared from the summit area, but a dark-gray cloud remained above the summit and east and southeast flanks. New discrete flow lobes were visible on the upper north and northwest flanks, as well as much farther down towards informally named Rocky Point (fig. 4*D*). A single flow was captured moving down the upper north flank. By 1200 AKST, the upper flanks were clear of steam and ash, though the lower east-southeast flank was still obscured in ash. Discrete flowage deposits were steaming on the upper north flank.

Seismicity during event 5 corroborates visual evidence. North and northwest of the volcano, stations AUL and AU12 both responded to flows during event 5 but not during earlier events. Because these were the first widespread pyroclastic flows of the sequence to flow north, they probably generated the lahars that moved downstream of the north fan and

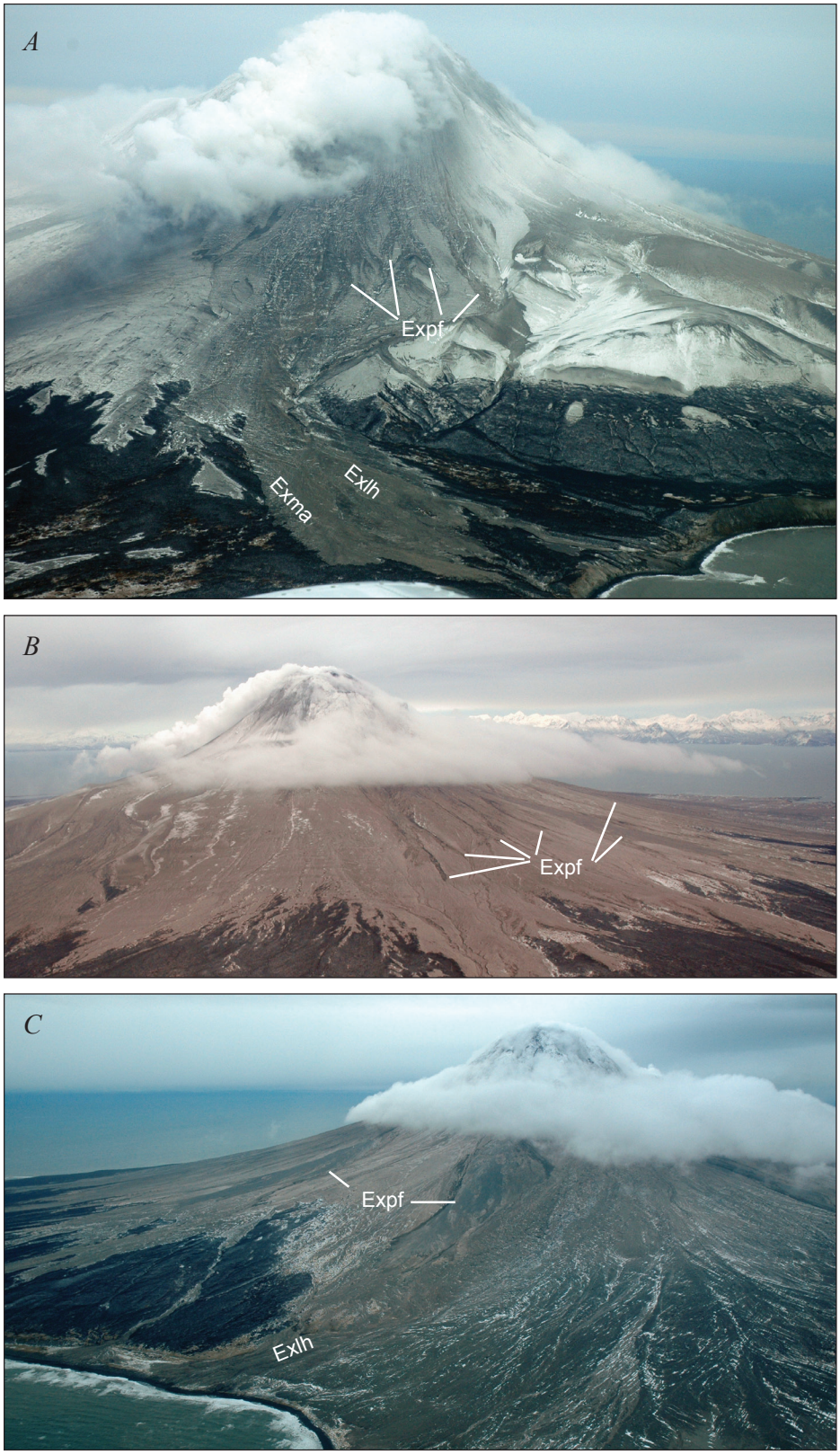


Figure 9. Explosive-phase deposits on the flanks of Augustine Volcano. *A,* Augustine Creek drainage, looking northeast. Lobate Expf, Exma, and Exlh deposits visible. *B,* View to the northwest. Vegetation-free slopes are covered in snow topped with ash fall. *C,* View to the southwest. Photos by R.G. McGimsey, January 16, 2006.

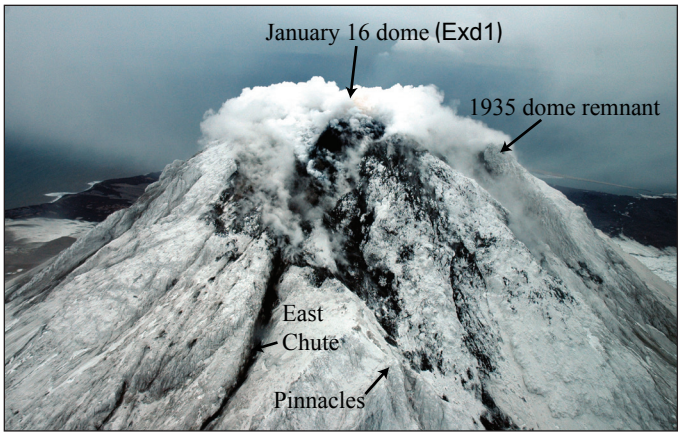


Figure 10. Oblique view of Augustine Volcano's summit showing the new lava dome (Exd1), January 16, 2006. View is to the southwest. This dome was later destroyed and/or buried by subsequent eruptive activity. Photo by R.G. McGimsey.

within informally named Windy Creek to the coast (fig. 8). The signal during event 5, in particular, could plausibly include lahars.

Event 6

A five-hour lull ensued, followed by event 6 that lasted from 1640 to 1644 AKST on January 13. An image taken from Burr Point at 1645 AKST shows a dark, billowing cloud rising from the east flank and a single pyroclastic flow traveling down the north flank just east of the north flank lava flow (fig. 4*E*). Photographs from Burr Point taken at 1715 and 1730 AKST show that flows on the north flank from event 6 all followed previous flow tracks; no new mappable areas are covered. A series of images from the Mound camera show a pyroclastic flow or surge descending the east flank toward the camera (table 1; fig. 5 of Paskievitch and others, this volume). As with previous events, we cannot visually determine the extent of flows from this event on the south or west flanks, but seismicity suggests that little material moved in those directions (table 2).

Events 7 and 8

Event 7 followed event 6 by 2 hours and lasted from 1858 to 1901 AKST on January 13, and event 8 started 5 hours later and lasted from 0014 to 0017 AKST on January 14. Neither of these events was captured by camera due to darkness. Dawn on January 14 brought overcast skies and clouds that obscured the mountain above approximately 500 m altitude. On the north flank, the Burr Point camera revealed only a couple of new flow deposits that must have formed during events 7 and 8 (fig. 4*F*).

Based on protracted seismic signals from instruments AU15, AU13, and AUI to the southwest and south of the volcano, pyroclastic flows and the mixed avalanches and lahars that they generated in Augustine Creek and informally named Southeast Beach Creek (fig. 8) most probably occurred during event 8.

January 16: Lava Lobe (unit Exd1)

Following event 8, the volcano entered a 3-day period of relative quiescence. Observers on a January 16 overflight discovered a dark lava lobe at the summit (fig. 10). Satellite images from the same day show that the lobe was roughly 200 m by 160 m and covered ~27,500 m^2; its thickness was unknown but can have been no more than a few tens of meters. It filled the crater that was likely formed during the explosions on January 13 and covered much of the 1986 dome. A satellite image from January 21 shows the same lobe, elongated to the east, but with a crater at the top. Dense, glassy ejecta, prominent in pyroclastic-flow deposits from event 9 on January 17, may be fragments of this dome (Vallance and others, this volume). The lobe likely reached its final size of roughly 275 m by 225 m by event 9 on January 17. Unlike the previous dome of January 11 and 12, no distinctive seismic signals accompanied its effusion (J. Power, oral commun., 2006).

This feature, explosive-phase dome 1 (unit Exd1; plate 1; fig. 8), was only partially covered by later effusion; a portion of it directly above the informally named East Chute remains exposed (fig. 11). It has a smooth surface, morphologically distinct from subsequent lava lobes. A single sample of the dome is low-silica andesite (57.5 weight percent SiO_2; Larsen and others, this volume).

January 17: Explosive Event 9

Approximately 80 hours after event 8, an 8-minute-long explosion, event 9, commenced in darkness at 0758 AKST on January 17 and sent an ash plume to 13 km asl that drifted to the west over the Alaska Peninsula (Power and others, 2006; Bailey and others, this volume).

Images from the Burr Point and Mound cameras from January 18 show that, if any fragmental flows from event 9 traveled down the north or east flanks, they followed the tracks of previous flows from events 3–8. An overflight on January 18, however, revealed a new flow deposit on the southwest flank (fig. 8). This flow traveled approximately 3.5 km from the summit, following a track previously developed by flows from the 1976 and 1964 eruptions (Waitt and Béget, 2009). Satellite images show that event 9 left a large crater in the new lava dome, and observers on the January 18 overflight noted a new field of ballistic blocks on the west and southwest side of the volcano extending to altitudes as low as 760 m (fig. 8). Data transmission from GPS station AV04 on the west flank stopped coincident with this explosion (fig. 8). The pyroclastic-flow deposit from event 9 is rich in dense, glassy clasts (Vallance and others, this volume) that are likely fragments of the new lava dome that had grown since January 14.

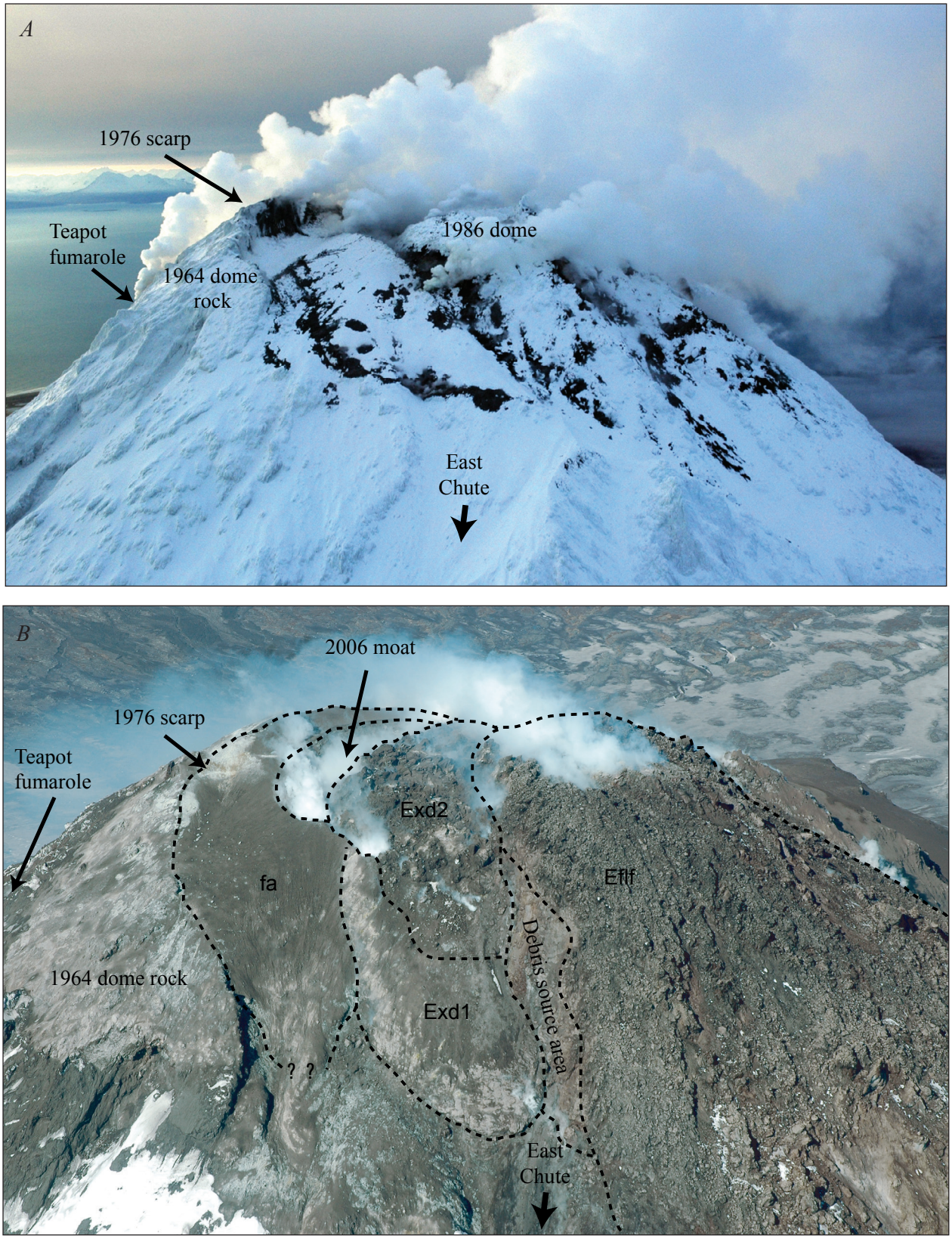


Figure 11. Oblique views of Augustine's summit before and after 2006 eruption. Views are to the west. *A,* Photo by K. Wallace, December 22, 2005. *B,* Photo by M.L. Coombs, May 13, 2006. The 2006 deposits are labeled as follows: Exd1, explosive-phase dome 1; Exd2, explosive-phase dome 2; Eflf, effusive-phase lava flows; fa, fall deposits.

Late January: Lava Effusion (unit Exd2)

Following event 9, Augustine Volcano remained seismically quiet for several days and an overflight on January 24 showed no new deposits on the flanks or changes at the summit. Satellite images from late January show that, at some time, most likely between events 9 and 10 (January 17 to 27), a new lava dome effused at the summit, partially covering explosive-phase lava dome 1 (fig. 8). The lobe is distinct from the earlier lava dome because it is lighter in color and its surface is much more rugged (fig. 11). Samples from this dome are high-silica andesite (62.3 to 63.1 weight percent SiO_2; Larsen and others, this volume). Explosive-phase lava dome 2 (unit Exd2) was likely partially destroyed during events 10–13 and was also later partially covered by effusive-phase lava. Therefore, its original extent is unknown. The portion of the dome that is still exposed lies within a moat formed by proximal 2006 fall deposits and is to the south of the new main summit dome that reached its final height during the effusive phase.

January 27 and 28: Explosive Events 10–13

After 10 days of relative quiescence, four explosions ensued in rapid succession: two on January 27 at 2024 and 2337 AKST (events 10 and 11) and two more on the morning of January 28 at 0204 and 0742 AKST (events 12 and 13). These all occurred at night and were initially detected seismically (Power and Lalla, this volume), and the resulting ash clouds were quickly detected by satellite images and radar (Bailey and others, this volume; Schneider and others, 2006). Event 10, the longest of the four at 9 minutes, sent an ash cloud to 10.5 km asl that drifted southeast. The other three ranged from 1 to 3 minutes in duration and sent ash clouds as high as 7.2 km (Schneider and others, 2006).

Because events 10 through 13 were at night, there were no visual or camera observations. The Burr Point camera was not in operation from January 23 to February 24, probably due to extreme weather conditions (Paskievitch and others, this volume). Observation overflights on January 29 and 30 found the island shrouded in ash during continuous-phase activity.

In the absence of visual observations of these events, seismicity and the destruction of geophysical stations provided clues about the accompanying activity. Event 10 destroyed station AUH, high on the volcano's west flank, 7 minutes after the beginning of the event and coincident with the strongest phase of the seismic signal recorded at broadband stations around the island. Event 10 also destroyed station AUL/AV03 near the toe of the prehistoric north flank lava flow (fig. 8). Unfortunately, the precise time of station AUL/AV03 destruction is unknown: the broadband seismometer at AUL had stopped sending data before the beginning of event 10, for unrelated reasons. The last data packet from GPS site AV03 was sent at 0459 AKST, however, 25 minutes before the start of the event (GPS data were transmitted on an hourly basis). Tellingly, pieces of the station were found within a new deposit below the north flank lava flow at locality 06AUMLC259 (fig. 8). This deposit is map unit Expc (explosive-phase pyroclastic-current deposits) and is mapped separately from other explosive-phase units due to its increased proportion of dense clasts and fines-deficient matrix (fig. 8; plate 1; Vallance and others, this volume). In addition to the different grain-size distribution, the deposit has a lithologic make-up that is transitional between earlier explosive-phase and later continuous-phase deposits—it contains low- and high-silica andesite in approximately equal proportions (Vallance and others, this volume).

In addition to the explosive-phase pyroclastic-current deposit mentioned above, there is evidence that event 10 also generated a second, larger pyroclastic flow. At the Oil Point reference seismic station, 30 km northeast of Augustine Volcano, the event seismic signal lasted 9 minutes (table 2), but its duration was minutes longer at several on-island stations and appears to record multiple flowage events (McNutt and others, this volume, fig. 4). The most plausible candidate to have also formed during event 10 is a 4.8-km-long pyroclastic-flow deposit on the north flank, first observed in an ASTER image from January 31 (Wessels and others, this volume) (fig. 4*G*; fig. 8). Named here the Rocky Point pyroclastic flow (unit RPpf; plate 1), it appears to have descended the north flank just east of the north flank lava flow before spreading out and filling in a small pond near the toe of the lava flow (Vallance and others, this volume). The deposit immediately overlies the explosive-phase pyroclastic-current deposits mentioned previously and immediately underlies the continuous-phase pyroclastic fan on the north flank. It is lithologically similar to continuous-phase deposits because it contains a high fraction of high-silica andesite clasts (Vallance and others, this volume).

While assigning the Rocky Point pyroclastic flow to event 10 is consistent with stratigraphy, the size of the deposit, the duration of the event 10 seismic signal, the airborne ash record from radar, and the lightning record all provide further evidence that link the two:

5. The Rocky Point pyroclastic flow is the single largest deposit of the eruption, with a volume of roughly 17×10^6 m^3 and a length of 4.8 km, thus we expect that the associated seismicity would be the longest flowage-derived signal during the time period when we know the flow was emplaced. Flow velocities of 5–10 m/s would require the emplacement of the flow over 8–16 minutes. For example, the smaller-volume, 3.7-km-long windy pyroclastic flow from the continuous phase (mapped as unit Cpfw) took roughly 7 minutes to come to rest. Between January 24, when observations show the Rocky Point flow to not be present, and the January 31 ASTER image, the longest flow/explosion signal recorded was during event 10.

6. During the continuous phase, the strongest ash signal detected by radar was from the windy pyroclastic flow, suggesting that

the much larger Rocky Point flow was not emplaced during the continuous phase (Schneider and others, 2006).

7. Event 10 produced the greatest number of lightning strikes between January 27 and the end of the eruption, the interval when a lightning-detection unit was operational (Thomas and others, this volume). The high number of lightning strikes can be the result of higher concentrations of airborne ash and/or the presence of additional steam, perhaps created as the Rocky Point pyroclastic flow entered the small pond (S. McNutt, written commun., 2007).

We have little information on the nature of flowage deposits produced during events 11–13 late on January 27 and early on January 28. Event 11 was very brief and it likely produced only minor deposits. The most energetic phases of events 12 and 13 lasted from 1 to 3 minutes, but the seismic signal had a long coda for event 12 at stations AUW and AUE and for event 13 at AUW, suggesting flows may have traveled east and northeast (McNutt and others, this volume). It seems likely that any pyroclastic-flow deposits from these two events are lithologically similar to the Rocky Point flow and to flows of the subsequent continuous phase.

The Continuous Phase—January 28–February 10

On the afternoon of January 28 at about 1430 AKST, 7 hours after event 13, Augustine Volcano entered a period of more continuous eruptive activity that lasted for 13 days. This period was characterized by (1) essentially continuous ash emission to heights of commonly less than 3,600 m asl, generating a variably ash rich plume, as recorded by satellite images and radar (Bailey and others, this volume; Schneider and others, 2006), (2) emplacement of pyroclastic flows on the north flanks of the volcano, as recorded by cigar-shaped seismic signals (Power and Lalla, this volume) and viewed in overflights, and (3) occasional larger seismic signals, thought to represent more explosive events, associated with ash clouds as high as 4,500–7,600 m asl. Ash fall was reported in Homer and Seldovia during this period (Wallace and others, this volume), 115 and 100 km east of the volcano, respectively. Activity waxed and waned during the continuous phase, as evidenced by variations in the number and duration of flow-related seismic events. The most vigorous activity ended on February 3 and was followed by steady effusion of a new lava dome and flow that lasted until approximately February 10. This entire interval from January 28 to February 10 is termed the "continuous phase" to distinguish it from the punctuated nature of the explosive phase.

January 28–February 3: Pyroclastic-Flow Emplacement

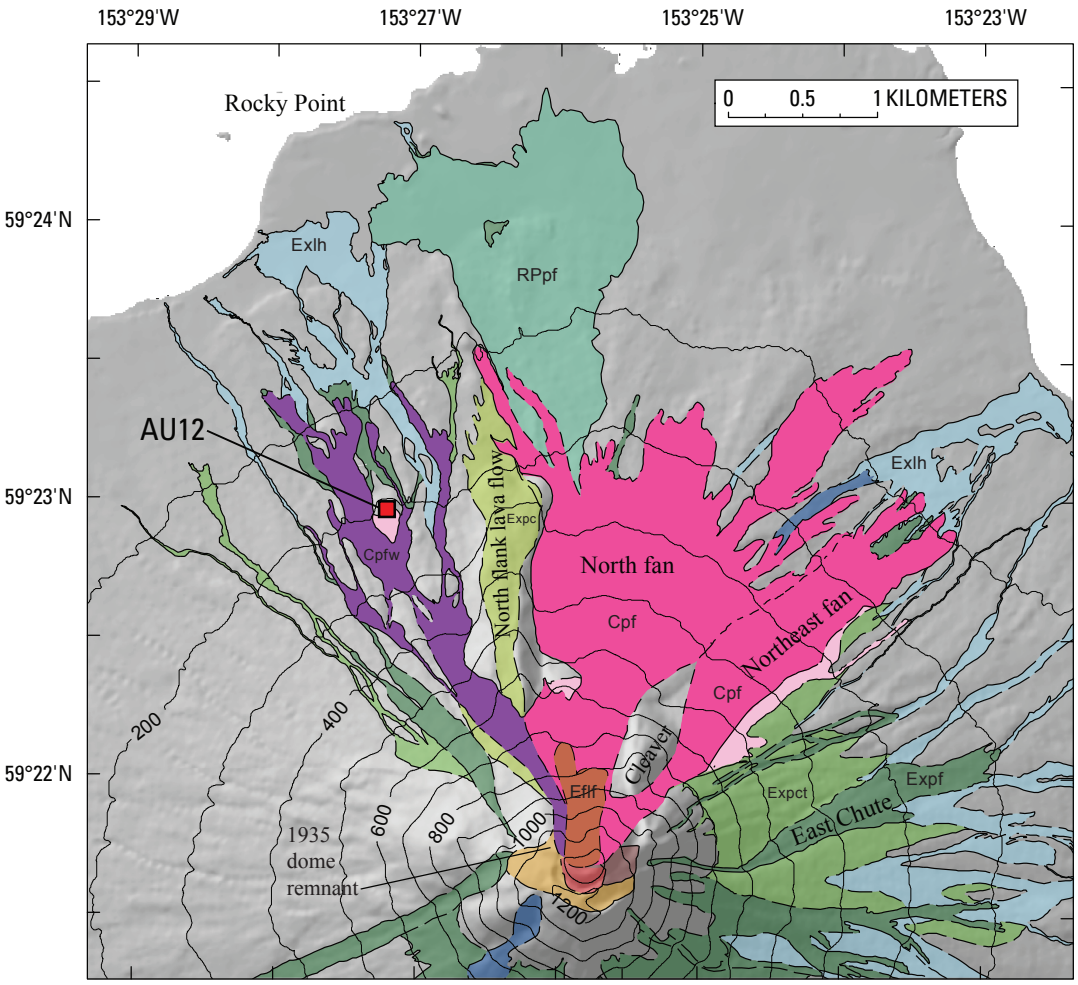
The early continuous phase resulted in a series of pyroclastic-flow deposits (units Cpf, Cpc, and Cpfw) on the north quadrant of the volcano (fig. 12; plate 1). These deposits cover an area of 4.9 km^2 and extend as far as 3.8 km from the summit. Several observation flights during the January 28 to February 3 interval provided information about the style of eruption (table 1), though observations of the volcano were hampered by airborne ash and poor weather. Additional evidence for timing of flow emplacement from this period is from seismicity, satellite images, and flow stratigraphy. The Burr Point time-lapse camera was not operational during the continuous phase, but the Mound camera provided several images of the activity during clear weather.

Seven hours after the four discrete explosive events on January 27 and 28 (events 10–13), seismometers recorded a roughly 2-hour period of volcanic tremor beginning at 1431 AKST on January 28. Starting at about 1418 AKST on January 28, coincident with (or slightly preceding) the increasing seismic tremor, Mound camera images revealed an ash-laden, vertically convecting plume that increased in vigor over the afternoon. Images show that no pyroclastic or debris flows or ash were deposited on the volcano's north flank on January 28.

Beginning at 2200 AKST on January 28, seismic signals, at the rate of 5–10 per hour, first recorded the movement of pyroclastic flows down the flanks. The first visual evidence of flows on the north flank is from 1007 to 1015 AKST on January 29, when the Mound camera showed a thick billowing plume that rose from the summit and moved south and another ash cloud that rose from the north half of the summit and moved down the north flank (fig. 13).

A particularly strong seismic signal was recorded by the network starting at 1118 AKST on January 29. This emergent, broad-spectrum signal lasted for roughly 5 minutes and had the longest duration of any signal during the 13 hours since continuous activity began. Several lines of evidence suggest that it was caused by a large pyroclastic flow on the north flank. In web-camera images from Homer, the top of a wide ash cloud was visible above meteoric cloud tops from 1127 to 1137 AKST. Images from the Mound camera went dark starting at 1126 AKST, suggesting significant ash in the air. An observation flight on January 29 arrived in the vicinity of the island around 1230 AKST. Views of the volcano were hindered by broken clouds below and dense clouds above 2,100 or 2,400 m asl, but observers saw a plume from the summit vent that rose vertically and then turned southward, with ash visible to the south of the island. Observers also noted a prominent ash-and-steam cloud that rose from the upper north flank of the island (fig. 14*A*); the lower north flank was mostly obscured by clouds and ash. During the viewing period, this ash cloud dissipated, revealing discrete but widespread areas of steaming. A more diffuse, brown-gray cloud that drifted low above the coastline was plausibly a coignimbrite cloud. We cannot identify the exact deposit emplaced during this event, but it is likely one of the longer flow lobes on the north fan that extend down to 50–100 m asl (fig. 12).

For most of the rest of January 29, images from the Mound camera were dark, but by 1547 AKST the view cleared



EXPLANATION

Eflf	Late continuous-phase lava flow (later enlarged to effusive-phase lava flow)
Cpf	Continuous-phase pyroclastic-flow deposits
Cpc	Continuous-phase pyroclastic-current deposits
Cpfw	Windy pyroclastic-flow deposit
RPpf	Rocky Point pyroclastic-flow deposit
Expc	Explosive-phase pyroclastic-current deposits
Exd2	Explosive-phase dome 2
Exd1	Explosive-phase dome 1
Exlh	Explosive-phase lahar deposits
Exma	Explosive-phase mixed avalanche deposits
Expf	Explosive-phase pyroclastic-flow deposits
Expct	Thin explosive-phase pyroclastic-current deposits
fa	Fall deposits

Figure 12. Map showing distribution of deposits at the end of the continuous phase (February 10, 2006). The location of broadband seismic station AU12, which was destroyed on January 30, 2006, is shown as a red square. Contours show pre-2006 topography; contour interval is 100 m.

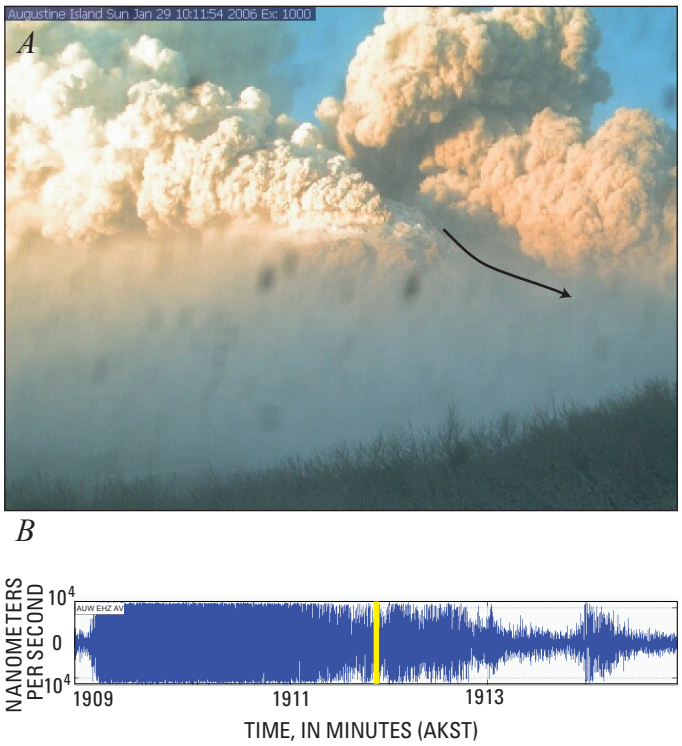


Figure 13. *A,* Mound web camera image from 10:11:54 AKST on January 29, 2006, showing intense steaming and likely ash emission from the summit and a small pyroclastic flow on the north flank (path shown by arrow). *B,* Seismic signal from station AUW showing small pyroclastic flow. Time that image was taken is shown by yellow line.

to show a dark cloud moving south and, in a single image, an ash cloud was visible rising from the north flank.

The destruction of a geophysical station recorded the passage of the single largest pyroclastic flow during the continuous phase. Campaign broadband seismic station AU12, on the northwest flank, was destroyed on January 30 at 0329 AKST (figs. 12, 15). We found the destroyed station at the edge of a pyroclastic-flow deposit in the summer of 2006. This braided deposit is named the windy pyroclastic flow deposit (unit Cpfw; plate 1) and is lithologically identical to other continuous-phase deposits (Vallance and others, this volume). Interestingly, AU12, which was 2.6 km from the summit, was destroyed approximately 4.5 minutes after the start of the flowage seismic signal, yielding an average flow rate of 9.6 m/s. During the 1976 eruption of Augustine Volcano, a series of time-stamped photographs recorded a pyroclastic flow that traveled at 50 m/s on the steep upper slopes and slowed to ~6 m/s as it reached the north coastline (Stith and others, 1977). The flowage seismic signal, which was no longer recorded by AU12 after its destruction, continues for approximately another 3 minutes on nearby broadband station AU11. If we assume that the flow traveled at the slower rate of 6 m/s for the rest of its course on the lower slopes of the volcano, it would have covered roughly 1.1 km in that time, for a total of 3.7 km. This is the exact length of the windy pyroclastic-flow deposit, suggesting that the entire flow was emplaced during this single flowage event. Radar data for this time interval shows the greatest ash signal seen during the continuous phase (Schneider and others, 2006), which is consistent with the idea that the windy pyroclastic flow was emplaced during a single, large event.

Smaller flowage signals continued to be recorded by the seismic network at a relatively high rate through February 3, though none were as large as the two on January 29 and 30. An overflight midday on January 30 revealed a dense vertical column rising from the summit vent to 4,900 m asl before drifting off as an ash cloud to the northeast for roughly 145 km (fig. 14*B*). The northern portion of the vertical eruption column and the tephra cloud moving to the northeast were brown gray and appeared more ash rich; the central, billowing part of the plume immediately above the vent was lighter colored. No fresh flowage deposits were identified in the southwest and southeast quadrants. An ashy haze that surrounded the slopes of the volcano, especially thick on the north flank, prevented views of the ground surface. During an observation flight on

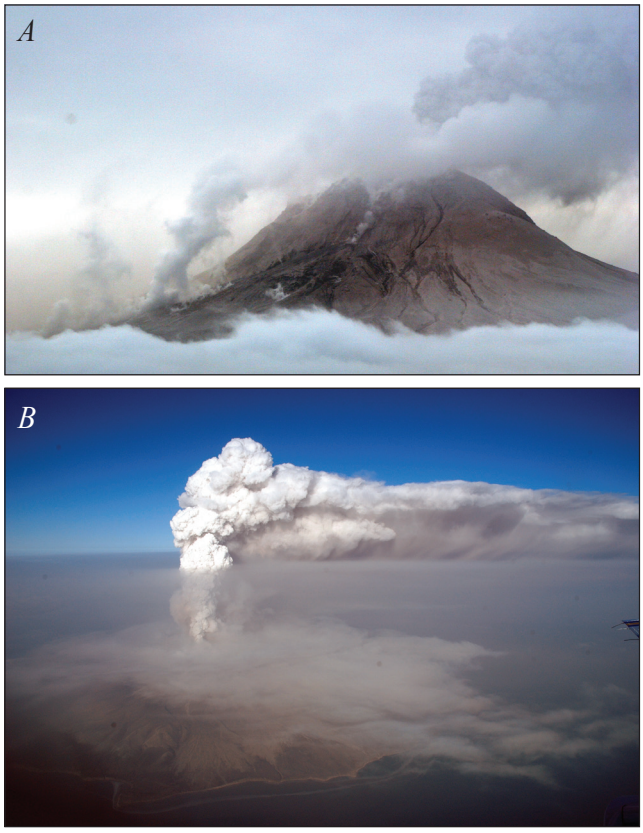


Figure 14. *A,* Photograph of the upper north flank of Augustine Volcano, taken by K. Wallace during January 29, 2006, overflight. Steaming flows are visible. *B,* Photograph of Augustine Island, looking north, taken by R.G. McGimsey during January 30, 2006, overflight.

February 3, the volcano was completely obscured by clouds, but observers saw an ash cloud above the volcano that reached to approximately 1,800 m asl. A brown plume was rising from high on the north flank.

Satellite images provided the first direct view of deposits of explosive events 10–13 and the early continuous phase (table 1). An ASTER image from January 31 showed the windy pyroclastic flow, the Rocky Point pyroclastic flow, and the north continuous-phase pyroclastic fan; much of the northeast flank was obscured in the image by a SO_2-rich plume (Wessels and others, this volume). A Hyperion satellite image from February 2 showed a strong thermal signature from the summit and a thin streak down the northeast chute; these were presumably a summit lava dome and a thin block-and-ash flow deposit (Wessels and others, this volume).

Observers first saw continuous-phase pyroclastic-flow deposits during a FLIR flight on February 8 (fig. 16). The deposits were dark and steaming, contrasting sharply with the surrounding snow-covered flanks. Numerous small pyroclastic flows constructed fans of fragmental debris on the north and northeast flanks. The fans resemble those from 1976 and 1986 eruptions in similar locations. On the northwest flank, the thickest portions of the windy pyroclastic-flow deposit (unit Cpfw) were visible as braided fingers; thinner and presumably cooler portions were obscured by new snow. Field work during August 2006 revealed that all continuous-phase deposits are light gray and poorly sorted and contain abundant, dense, large, high-silica-andesite blocks that resemble rocks of the second explosive-phase dome (Vallance and others, this volume).

February 3–10: Beginning of Lava Flow Effusion

The number of flow-related seismic signals tapered off over a period of 24 hours from roughly February 3 to February 4. Seismicity increased again over a 24-hour period on February 5. Beginning around February 3, the ash emission of the early continuous phase gave way to lava effusion that persisted through February 10, as evidenced by continued rockfall seismic signals, continued deflation as recorded in CGPS (Cervelli and others, this volume), persistent thermal anomalies in satellite data (Bailey and others, this volume), and incandescence at the summit and upper north flank viewed from Homer in early February (Sentman and others, this volume). Lava slowly or intermittently extruded from the summit area became unstable

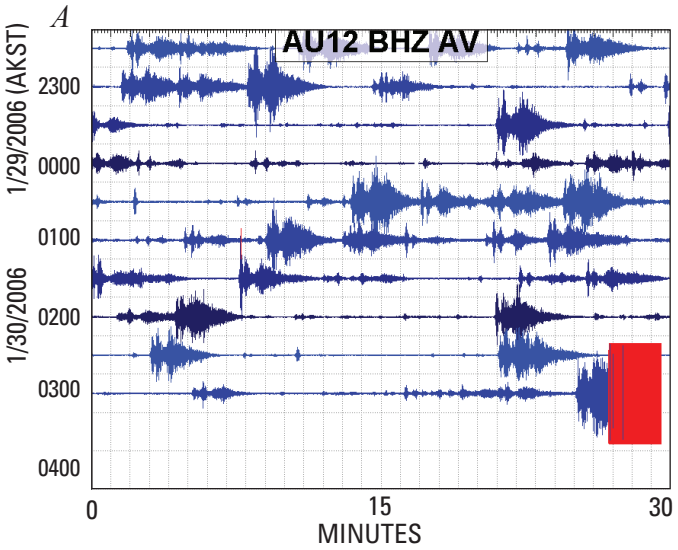




Figure 15. *A,* Seismic record showing a series of pyroclastic-flow signals recorded by campaign broadband seismometer AU12 on Augustine Volcano's northwest flank (see fig. 12 for location). The final flow signal ceased at 0329 AKST on January 30, 2006, when the station was overrun by the windy pyroclastic flow. Red rectangle indicates time period when signal strength exceeded the range of the instrument. *B,* Photograph of destroyed seismic station AU12. The data card was still intact and recorded that the station ceased operation on January 30 at 0329 AKST, presumably coincident with the emplacement of the windy pyroclastic flow. Larger boulders predate the 2006 eruption. The flow left only a thin deposit in this area but melted the station casing and much of the equipment. Flow direction was from top to bottom in the image. Adze is approximately 1 m long. Photo by M.L. Coombs, August 10, 2006.

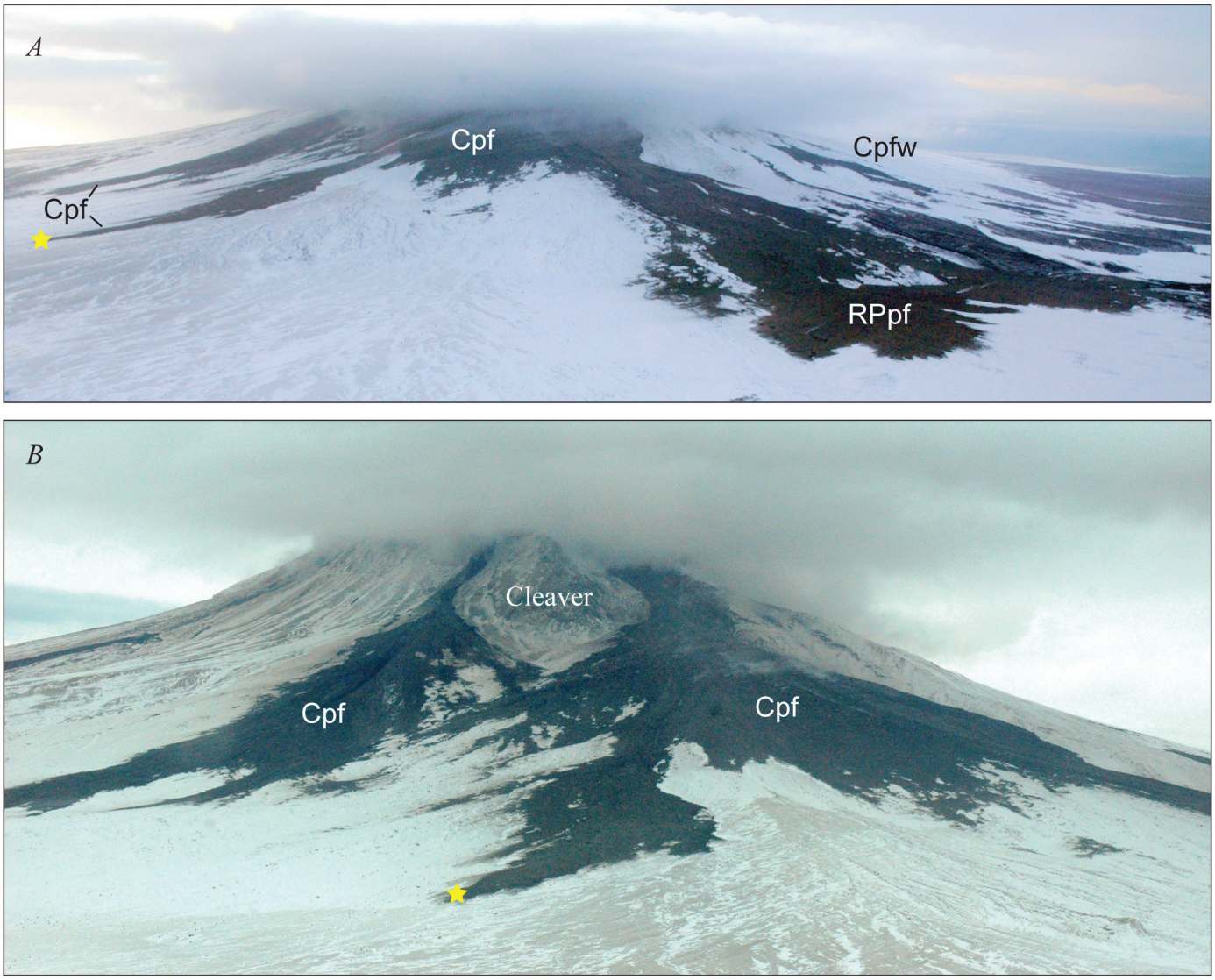


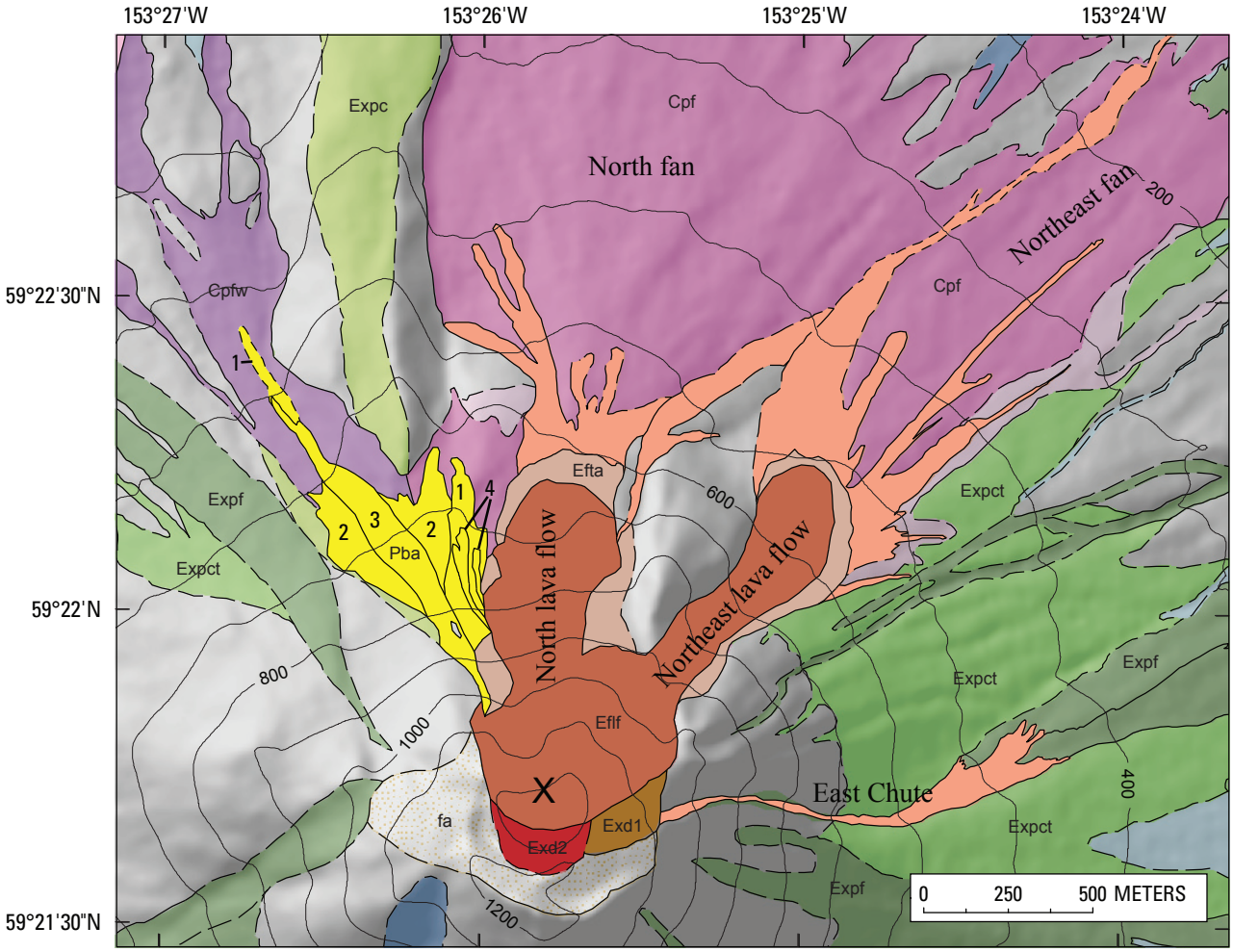
Figure 16 Photographs of continuous-phase pyroclastic-flow deposits, taken Feb 8, 2006. *A,* View towards south. *B,* View towards southwest. Star shows toe of the same flow deposit in both photos. Photos by M.L. Coombs.

and occasionally tumbled down the flanks as block-and-ash flows and rock falls. These events sometimes generated low-level ash clouds to altitudes of less than 3,000 m asl.

By February 7, satellite images showed that a multi-lobe lava flow had made its way down the north flank. It covered 215,000 m^2 and was roughly 900 m long by 300 m across. The lava progressed down a chute between the 1935 dome remnant and the informally named Cleaver (fig. 12). FLIR and visual observations on February 20 and 24 (Wessels and others, this volume) reveal that, by that time, the north lava flow was approximately 1,000 m long and that it extended from a new, dark, rubbly lava dome that covered the north half of Augustine's summit (fig. 4*F*). Given the lack of seismicity after February 10, we interpret that most of this growth occurred before then.

Eruptive Hiatus—February 10–March 3

During the period from February 10 to March 3, seismicity was low and no visual evidence exists to suggest that measurable volumes of magma were being erupted. FLIR flights on February 20 and 24 showed few changes had occurred at the summit (Wessels and others, this volume). However, several small explosions were recorded by seismic instruments and by the on-island pressure sensor (McNutt and others, this volume), and scattered rockfalls were recorded seismically. Periods of incandescence seen with the Homer low-light camera (Sentman and others, this volume) and with the Burr Point camera between February 15 and March 1 likely recorded the fracturing and spalling off of the lava-flow front.



EXPLANATION

- Pba — Block-and-ash flow deposits from April-May 2006
- Efta — Lava-flow talus aprons
- Efba — Effusive phase block-and-ash-flow deposits
- Eflf — Effusive phase lava flows
- Cpf — Continuous phase pyroclastic-flow deposits
- Cpc — Continuous phase pyroclastic-current deposits
- Cpfw — Windy pyroclastic-flow deposit
- Expc — Explosive phase pyroclastic-current deposits
- Exd2 — Explosive phase dome 2
- Exd1 — Explosive phase dome 1
- Expf — Explosive phase pyroclastic-flow deposits
- Expct — Thin explosive-phase pyroclastic-current deposits
- fa — Fall deposits
- 1-4 — Relative order of emplacement of deposits from April and May failure events
- X — Location of intense steaming and small spine

Figure 17. Map showing Augustine Volcano's summit region, highlighting deposits from the effusive phase (March 3–16, 2006) and after (April-May 2006). Contours show pre-2006 topography; contour interval is 100 m.

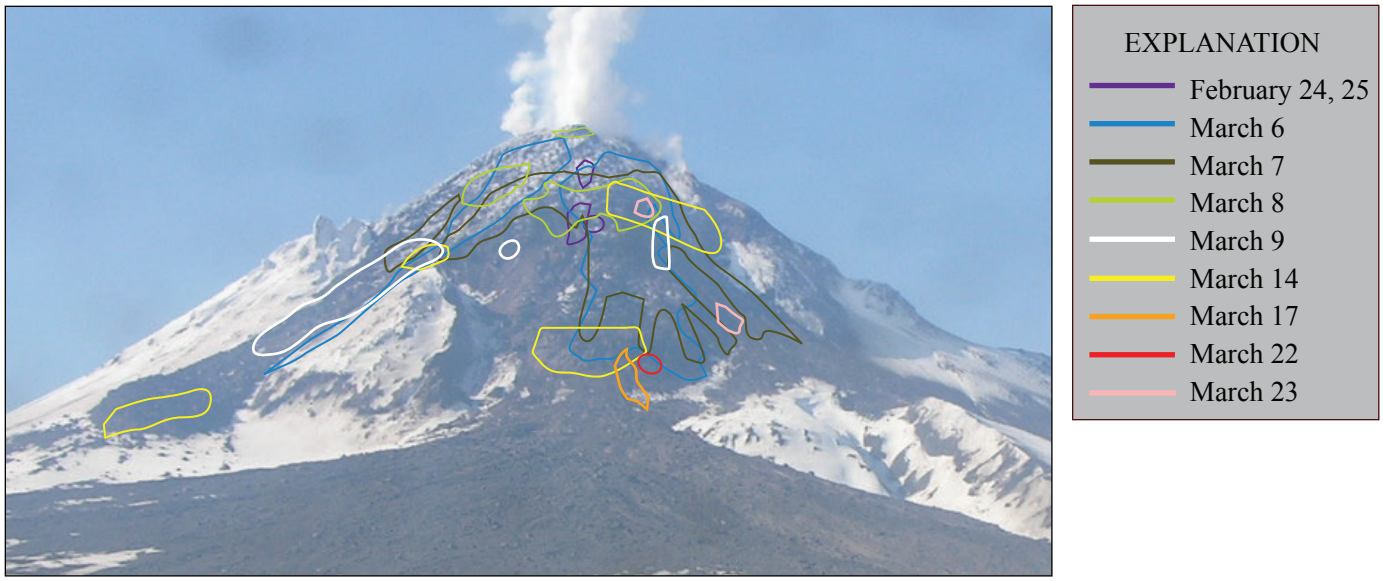


Figure 18. Photograph of the north flank of Augustine Volcano, taken from Burr Point time-lapse camera on May 13, 2006. Areas of incandescence, color-coded by day, are shown.

The Effusive Phase—March 3–16

After an apparent pause in eruptive activity throughout the latter half of February, Augustine Volcano resumed activity in March with the effusion of a larger summit dome, renewed growth of the north lava flow, and formation of a new lava flow down the northeast chute, all accompanied by vigorous block-and-ash flows (fig. 17; plate 1). In contrast to the continuous phase, clear weather and lesser amounts of airborne ash allowed thermal, visual, and satellite observations during this phase, which augmented seismic data. During this time, incandescent areas were observed at the summit and extending down the north flank; motion of incandescent blocks and/or flows was also observed. This activity was seen in nighttime images from the Homer camera, the low-light camera (also located in Homer; Sentman and others, this volume), and the Burr Point time-lapse camera (the Mound camera was not turned on at night due to power considerations; Paskievitch and others, this volume).

An increased number of rockfall seismic signals late in the evening of March 3 heralded the beginning of the effusive phase (Power and Lalla, this volume). On March 4, a series of small, localized ash emissions from the summit were captured with the Mound camera (table 1; fig. 5).

Observations of incandescence, though sometimes hampered by cloudy conditions, commenced during the night of March 5 and provided clues about the style of activity and growth of the lava flows and dome (fig. 18). Two types of incandescence were observed by Burr Point and Homer cameras. First, relatively stationary points and regions of incandescence represented exposed, hot parts of the growing lava dome or flows. Second, glowing streaks that moved downslope in subsequent, closely timed images (Sentman and others, this volume) represented block-and-ash flows shed from the summit dome and from the toes and flanks of the lava flows. These pyroclastic flows descended the north, northeast, and east chutes from the summit and were synchronous with seismic signals (DeRoin and others, 2007). Smaller streaks likely recorded incandescent rockfall or talus; such activity graded into larger block-and-ash flows.

On March 6, seismic vigor increased and clear daytime views revealed steaming and low-level ash emission that extended several hundred meters above the summit. Most of the steaming was on the north flank, and it appeared that the north lava flow that had effused during the end of the continuous phase was once again growing. No lava flow was visible in the northeast chute, although fresh, dark pyroclastic-flow deposits were visible, and a small pyroclastic flow was captured in motion at 1616 AKST by the Burr Point camera (table 1). Nighttime images showed that maximum incandescence occurred on March 6 and 7, when large swaths of the summit and upper north flank were glowing (fig. 18).

Seismicity quieted again for roughly 24 hours starting at 0600 AKST on March 7. Daytime views found no lava flow in the northeast chute on March 7 or 8. Starting at 0600 AKST on March 8, persistent, near-identical (drumbeat) earthquakes began to dominate the seismic signal (fig. 1; Power and Lalla, this volume). For 21 hours from 1730 AKST on March 8 to 1430 AKST on March 13, most on-island seismic stations received such strong signals that they were off the scale. By 1430 AKST on March 14, seismicity returned to pre-March 6 levels.

A lava flow was first observed within the northeast chute during an overflight on March 9. Observers also noted that pyroclastic-flow activity on March 9 was more prevalent to the northeast than to the north, suggesting active growth of the northeast lava flow during this time. That evening, nighttime cameras showed that the margin of the northeast lava flow was

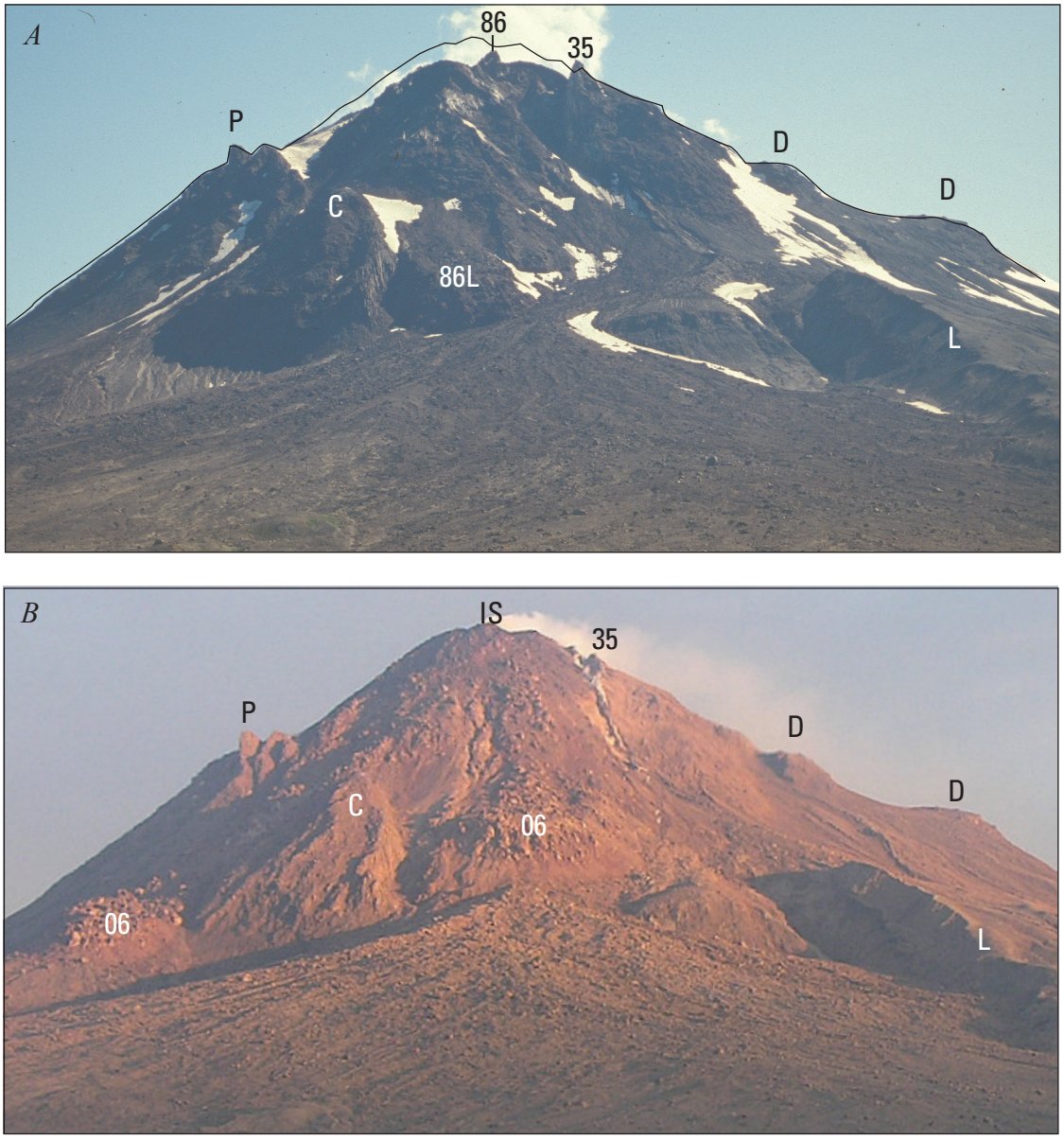


Figure 19. *A,* Augustine Volcano's edifice photographed from Burr Point to the north. Black line indicates edifice profile following the 2006 eruption. Photo by R.G. McGimsey, July 28, 1994. *B,* Augustine's edifice photographed from Burr Point time-lapse camera, July 24, 2006. P, Pinnacles (an old vent breccia; Swanson and Kienle, 1988); C, Cleaver; 86, 1986 lava spine; 35, 1935 dome remnant; D, prehistoric lava domes; 86L, lava flow from 1986 eruption; L, prehistoric north-flank lava flow; 06, lava flows from 2006 eruption; IS, incipient spine atop 2006 dome.

glowing. By March 14, areas of incandescence had moved down the slopes and marked the toes of the north and northeast lava flows (fig. 18).

Field crews flew to the island to acquire FLIR measurements twice during the effusive phase: on March 10 and March 15 (Wessels and others, this volume). Thermal images acquired on these dates delineate the new lava flows, whereas visual images were often partially obscured by steam, ash, and/or backlit conditions. On March 10, the new northeast lava flow was visible in thermal imagery and reached from the top of the new summit dome to the base of the Cleaver, for a total length of roughly 1,000 m. The north lava flow had also advanced from its position at the end of the continuous phase—it measured about 900 m from the summit to the toe. By March 15, the northeast flow had lengthened to about 1,300 m, while the north lava flow had advanced only slightly, if at all. Both flows, however, appeared to have thickened considerably at their toes between March 10 and 15; the toe of the northeast flow was 80 m high, and that of the north lava flow was 85 m.

After March 15, the summit dome and the two lava flows underwent few or no morphological changes, indicating that effusion had largely ceased by that date. Incandescence also decreased and was limited to the west margin of the north lava flow (fig. 18).

The lava flows (unit Eflf; fig. 17; plate 1) from the 2006 eruption are typical of andesitic block lava flows and have prominent lateral levees, blocky surfaces, and steep flow fronts. The north flow is roughly 700 m long from the base of the new dome, as much as 340 m wide, and 85 m thick at the toe. The northeast lava flow extends 900 m from the base of the new dome, is as much as 250 m across, and is 80 m thick at the toe. They are the most voluminous of any lava flows from recent eruptions of Augustine Volcano. The 1986 eruption resulted in a steep blocky flow that appeared to issue from the base of the dome (Swanson and Kienle, 1988); it descended the north summit region to an altitude of approximately 580 m asl (fig. 19*A*). The 2006 north lava flow covered essentially all of that flow and is about as long, but it is about 200 m wider (fig. 19*B*). The 2006 northeast lava flow filled the northeast gully to an altitude of 500 m asl. The two lava flows are essentially continuous with the new summit dome, which covered the north halves of the flow lobes emplaced in January, and filled the north half of the summit crater from the 1935 dome remnant on the west to the informally named Pinnacles to the east (fig. 11; fig. 19*B*). The new dome now forms the volcano's summit, approximately 70 m higher than it was before 2006.

Lava effusion was accompanied by numerous rockfalls and small block-and-ash flows that were detected seismically (DeRoin and others, 2007), observed during overflights, and photographed by cameras. The block-and-ash flows formed prominent, dark deposits (unit Efba) that sit atop the upper reaches of the continuous-phase pyroclastic flows of the north and northeast fans (fig. 17; plate 1). Unit Efba flows also traveled down the east chute. These poorly sorted deposits consist of clasts of mostly dense andesite in a fine-grained matrix (Vallance and others, this volume).

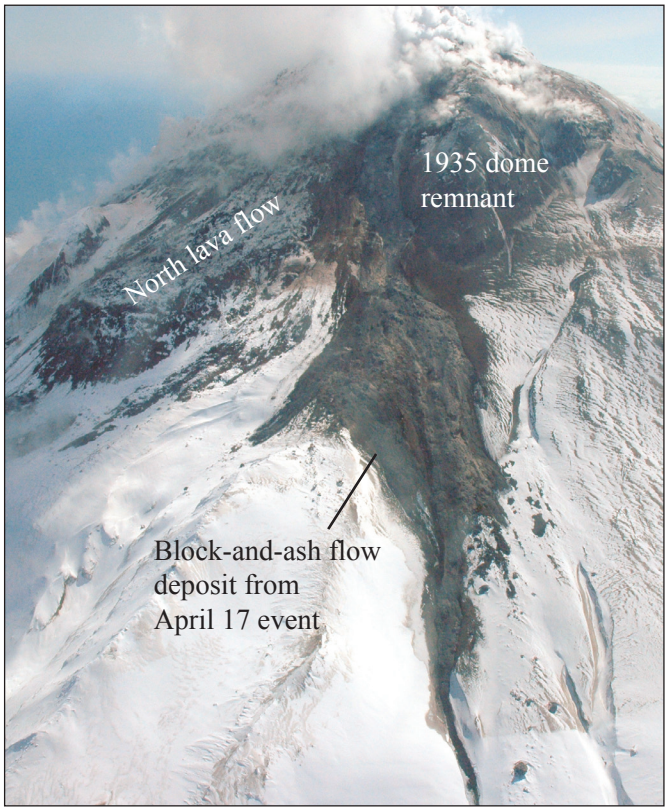


Figure 20. Photograph of Augustine Volcano's upper northwest flank, showing deposit from April 17 block-and-ash/rockfall event. Photo by R.G. McGimsey, April 19, 2006.



Figure 21. Photograph of Augustine Volcano's lower north flank, showing pink lahar deposits atop the 2006 Rocky Point pyroclastic-flow deposit. The lahars are thought to have occurred on October 1 and consist of remobilized fine-grained material from the 2006 eruptive deposits. Dark brown area at right of photo is pre-2006 surface. Field of view is approximately 500 m across. Photo by K.F. Bull, October 15, 2006.

Post-Eruption Activity—Rock Avalanches and Lahars

While eruption of juvenile magma apparently ceased by March 16, secondary activity involving the remobilization of 2006 eruptive deposits continued through October 2006.

Spring 2006 Rock Avalanches

On March 17 through 23, small, point-source incandescent areas were visible along the edges of the new lava flows. Rockfalls were recorded by seismic signals as often as a few times each day. Most signals recorded the downhill path of single, large boulders, as discovered in April when overflight observers saw a single boulder bounce down the west flank, marked the time, and found later that this activity correlated with a minute-long signal at nearby seismometer

AUW. Several longer, stronger seismic signals were found to correlate with larger rock-avalanche events.

The first rock-avalanche signals were detected on April 8. Between 1635 and 1708 AKDT, two bursts, 9 and 17 minutes long, were recorded seismically. Unfortunately, cloudy conditions at the time completely obscured the view from the Burr Point and Mound cameras. During a gas-monitoring flight on April 11, observers saw debris from the events (not present on an April 6 overflight) adjacent to the west margin of the north lava flow (table 1). The debris deposit extended almost as far downslope as the lava flow and had a total length of roughly 750 m. Large blocks—some steaming and some obviously cold—littered the area. A small lahar-like deposit extended downslope beyond the main debris field. Ash produced by this rock avalanche was carried by high winds across the northwest flank, leaving a radial, spoke-shaped deposit. Severely backlit conditions made it difficult to see the source area of the avalanche(s), but the axis of the deposit projected to a point below the summit dome. The deposit from this event was completely covered during subsequent activity, so it is not represented on the map (plate 1).

On April 17, a series of large flowage seismic signals, from 1656 to 1732 AKDT, were recorded by stations AUW, AUE, AUSE, and AUI. Elevated rockfall activity, recorded seismically, continued at a lesser rate until 0240 AKDT on the morning of April 18. Mound and Burr Point camera images from April 17 are obscured by clouds. During a gas-monitoring flight on April 19, observers saw a large amount of rock-avalanche debris on the volcano's northwest flank that had overrun the smaller debris field from April 8 (fig. 20). The main debris was not steaming, and they saw only a few hot blocks, mostly along the margin of the deposit. The distal end of the avalanche debris was incised and showed evidence of minor water flow. Backlit conditions once again prevented observations of the avalanche source area. The deposit was later partially covered by smaller rockfall events, but remnants of it are exposed and are shown on the deposit map as unit Pba (fig. 17; plate 1).

Rockfall activity increased again the night of May 25, leading to two particularly large flowage events on May 26 at 0106 and 0748 AKDT. The second event was the larger of the two and lasted approximately 5 minutes as recorded seismically. Unlike the previous avalanche events, the 0748 AKDT avalanche was photographed by both on-island cameras. Fortuitously, it was also photographed by M. Byerly aboard a boat approximately 5 km northeast of Augustine Island (table 1). Images from the three sources show that the rock avalanche was accompanied by an ash cloud that likely rose to 1 to 2 km above the summit and drifted to the south. An initial small ash puff was recorded along the flank of the lava flow at 0738 AKDT, then a light-gray cloud moved downslope along the west side of the north lava flow, growing in height as it flowed almost to the end of the north-slope lava flow. By ~0800 AKDT, the flowage event had ended but the cloud had diffused, increased in diameter, and drifted around to the south and west side of the summit.

Observers on a June 2 overflight saw the deposits and located the source area of the May 26 events as the upper west side of the northwest lava flow, where a line of fumaroles down the chute marked the breakaway surface. The debris overtopped the upper portion of the north flank lava flow before bifurcating down either side; somewhat more debris was directed along the west side of the lava flow. The debris overlies deposits from previous slides.

October 2006 Lahars

Several months after the cessation of eruptive activity, several small flowage events occurred, though these were different in nature than the spring rockfalls. On October 1, two pulses of seismicity were recorded from 0750 to 0915 (85 minutes) and 2116 to 2145 (29 minutes) AKDT. The signals were strongest on stations located on the east, north, and west flanks, and both were pulsatory with pulses from 2 to 10 minutes in duration (T. Petersen, written commun., 2006). These seismic signals had characteristics of surface clastic flows but persisted much longer than rockfall signals recorded previously.

On October 12 and 15, observers photographed new deposits on the lower north flank of the volcano (table 1). The new deposits were thin, braided, and obviously involved significant water in their emplacement (fig. 21). They were strikingly pinkish and light gray-colored, similar to pink ash-fall deposits associated with continuous-phase pyroclastic flow emplacement (Wallace and others, this volume). The largest of these October flow deposits was just south of the northeastern continuous-phase pyroclastic fan and reached the coastline. Others flowed atop Rocky Point and continuous-phase pyroclastic-flow deposits on the northwest flank, as well as on the west, south, and east sides. Where photographed on the north flank, new flows were most visible below a distinct break in slope at approximately 20 m asl. We believe that the observed lahar deposits correlate with the seismically detected events of October 1 and that they mostly involved remobilization of 2006 ash-fall deposits or matrix from continuous-phase pyroclastic-flow deposits. Deposits from these small-volume lahars are not shown on the 2006 geologic map (plate 1).

Volume Calculations

Methods

Using the geologic map, we have estimated the volumes of on-island erupted material from the eruptive phases of the 2006 Augustine Volcano activity (table 3; fig. 22). Most volumes were determined using the mapped areal extents of units and either estimating or measuring their thickness. Areas were measured from the time-slice maps (figs. 6, 8, 12, 17) to include buried deposits. The proximal, buried extents were either approximated or, where possible, mapped from imagery acquired during the eruption (for example, figs. 4

Table 3. Volume estimates for 2006 deposits.

[DRE, dense-rock equivalent; HSA, high-silica andesite; LSA, low-silica andesite]

Date (2006)	Deposit type (unit)	Deposit area (m^2)[1]	Deposit thickness (m)	Inflated eruptive volume (10^6 m^3)	Cumulative inflated erupted volume (10^6 m^3)[2]	Erupted volume (DRE; 10^6 m^3)	Cumulative erupted volume (DRE; 10^6 m^3)	Cumulative erupted HSA (DRE; 10^6 m^3)	Cumulative erupted LSA (DRE; 10^6 m^3)	Duration (hr:min:sec)	Magma flux (m^3/s)
					Explosive phase						
January 11	Mixed avalanches (Exma)	980,000	n/a	n/a	n/a	n/a	n/a	n/a	n/a		
January 12	Early, ephemeral lava dome	n/a	n/a	n/a	n/a	n/a	n/a	n/a	n/a		
January 13–14	Events 3–8, flows (Expf, Expct, Exma, Exlh)	16,570,000	various	7.39	7.4 (1.9)	4.4	4.4	1.3	3.2		
January 13–14	Events 3–8, fall[3]	n/a	n/a	20.30	27.7	7.7	12.1	3.5	8.6	00:28:41	7,050
January 14–16	Lava dome (Exd1)	30,000	30	0.82	28.5 (2.0)	0.7	12.9	3.7	9.1	59:43:00	3
January 16–17	Continued growth of Exd1	70,000	30	2.06	30.5 (2.1)	1.8	14.7	4.3	10.4	19:58:00	25
January 17	Event 9, flow (Expf)	610,000	0.3	0.18	30.7 (2.1)	0.1	14.8	4.3	10.5	00:04:11	
January 17	Event 9, fall[3]	n/a	n/a	1.73	32.5	0.7	15.5	4.5	11.0	100:00:00	3,100
January 17–27	Lava dome (Exd2)	60,000	0.15	1.89	34.3 (2.2)	1.7	17.2	5.9	11.3	150:00:00	3
January 27–28	Events 10–13, flows (RPpf, Expc)	3,870,000	various	16.90	51.2 (3.7)	10.1	27.3	14.1	13.2		
January 27–28	Events 10–13, fall[3]	n/a	n/a	6.26	57.5	2.4	29.7	15.0	14.7	00:15:08	13,800
					Continuous phase						
January 28–February 2	Flows (Cpf, Cpc, and Cpfw)	4,900,000	various	14.40	71.9 (5.2)	8.7	38.4	21.4	16.9	110:00:00	22
February 2–7	Lava flow (Eflf)	220,000	50	10.80	82.7 (6.1)	9.6	47.9	22.5	25.4		
February 7–10	Continued lava growth (Eflf)	30,000	50	1.50	84.2 (6.1)	1.3	49.3	22.6	26.6	192:00:00	16
					Effusive phase						
February 10–March 3	Hiatus	0	0	0.00	84.2 (6.1)	0.0	49.3	22.6	26.6		
March 3–16	Lava flow and dome (Eflf)	430,000	60	25.90	110.0 (8.9)	23.0	72.3	25.2	47.1		
March 6–16	Block and ash flows (Efba)	510,000	1	0.51	110.5 (8.9)	0.5	72.7	25.2	47.5	240:00:00	27

[1]Where referring to growing feature, like lava dome, deposit area refers to area of new growth only.
[2]Uncertainty estimate given in parentheses.
[3]Data from Wallace and others (this volume).

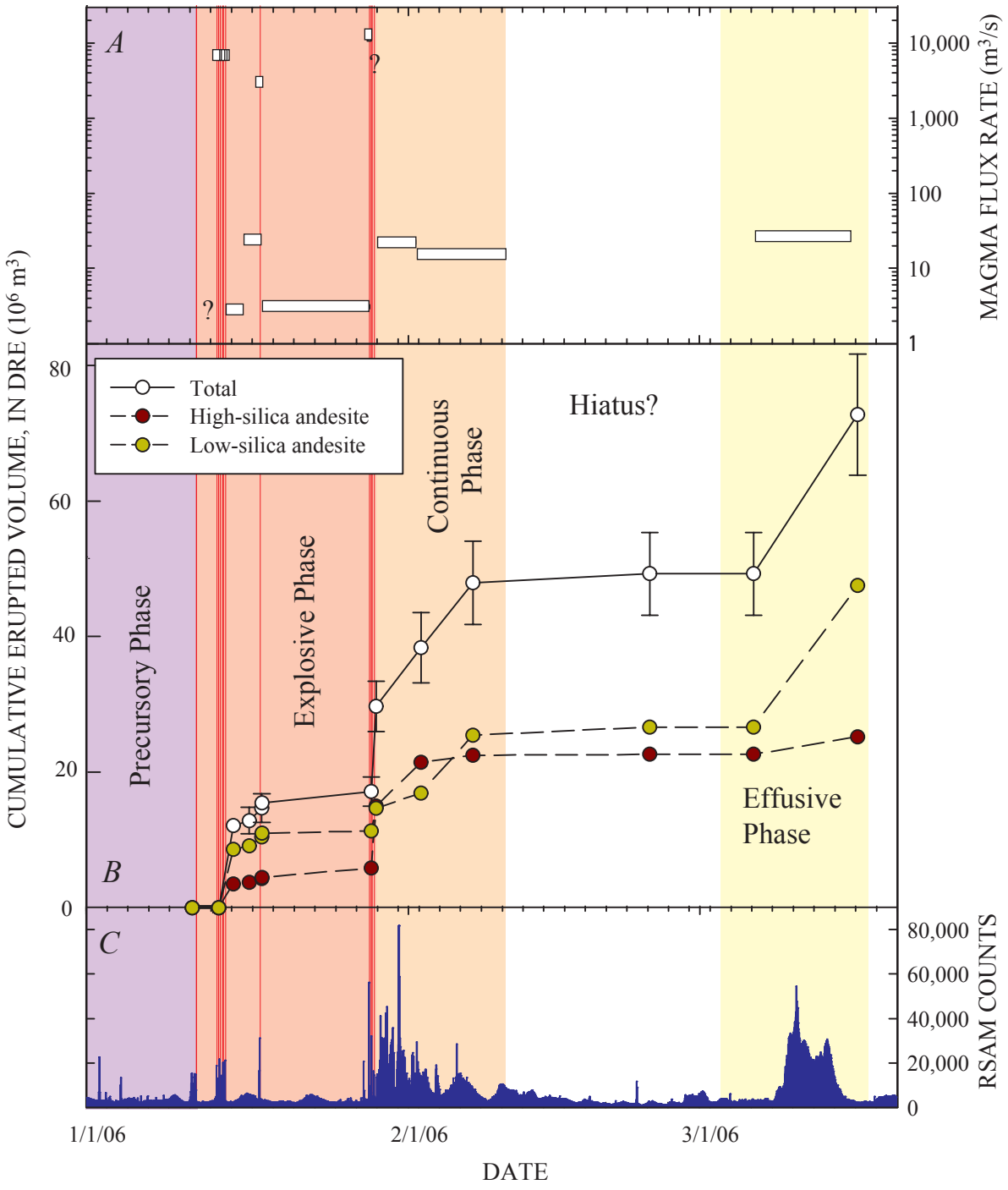


Figure 22. *A,* Magma flux rates (in dense-rock equivalent, or DRE) for intervals through the 2006 Augustine Volcano eruption. Flux rates plotted over red lines are for explosive events and have been calculated using the duration of the explosions; symbols have been enlarged for clarity. Flux rates that have been calculated for longer time periods are represented by bars. Note logarithmic scale. *B,* Cumulative erupted volume, in DRE, for the eruption. *C,* RSAM, or real-time seismic amplitude measurement, counts per day for Augustine station AU15. Explosive events 1–13 are shown as vertical red lines throughout *A*, *B*, and *C*.

and 5). Thicknesses of thinner pyroclastic-flow deposits were measured in the field (Vallance and others, this volume) and then averaged. The thicknesses of lava flows and domes were estimated or, where possible, measured from photographs and FLIR images (Wessels and others, this volume). For the continuous-phase and Rocky Point pyroclastic-flow deposits, volumes were calculated using digital terrain models (DTMs) generated by Aerometrics during the production of the orthophotos from January 4 and February 21, 2006. While these DTMs have unverified vertical accuracy, finding the difference of the two resulted in consistent volume gains over the mapped extents of the most voluminous pyroclastic flow deposits from late January and early February. Because field measurements of these deposits, many of which are several meters thick, were not possible in 2006, the values from the DTM differencing are presented here. Ash-fall volumes were calculated by Wallace and others (this volume) using the root-area method (Fierstein and Nathenson, 1992).

The main source of uncertainty in the calculations resides in the thickness measurements and/or estimates. These have propagated to the volumes and yield uncertainties of 25 to 50 percent. Inflated (erupted) volumes have been converted to dense-rock equivalent (DRE) using the following deposit/DRE ratios: 0.6 for fragmental flows, 0.9 for lava, and 0.4 for tephra-fall deposits.

Component analysis shows that each eruptive phase produced varying proportions of lithologic components (Vallance and others, this volume). Five dominant lithologies are low-silica andesite scoria; dense low-silica andesite; banded andesite; dense intermediate andesite; and high-silica andesite. We lump dense and scoriaceous low-silica andesite into a single compositional category and banded andesite and intermediate and high-silica andesite into another category to calculate volumetric estimates of two general compositional end members for each deposit (table 3). For lava flows, we assume they have the same proportions as block-and-ash flows shed from them; for domes, we assign composition based on the few of whole-rock analyses and surface appearance. Compositional ranges for the low- and high-silica andesite categories are 56 to 59 weight percent SiO_2 and 59 to 63 weight percent SiO_2, respectively (Larsen and others, this volume).

Results

The explosive phase produced about 14.7×10^6 m^3 as pyroclastic flows and 10.8 x10^6 m^3 as tephra fall (these and all subsequent values given as dense rock equivalent, or DRE; table 3). The first explosive-phase lava dome, effused from January 14–17, had a volume of roughly 2.5×10^6 m^3. The second dome, which effused between January 17 and 27, had a volume of roughly 1.7×10^6 m^3. The total volume produced during the explosive phase was 29.7×10^6 m^3. The largest single deposit of the eruption, the Rocky Point pyroclastic flow, erupted during event 10. During the explosive phase, low-silica and high-silica andesites were produced in nearly equal amounts, though during the first half of this phase, low-silica andesite dominated (fig. 22).

Combining volume estimates with eruption intervals allows us to calculate magma flux rates, which show three brief periods of rapid magma release that coincide with explosive events, as well as much lower flux rates during times of dome growth and lava effusion. Using a cumulative duration of events 3–8 of 28 minutes, 41 seconds yields a magma flux of 7,050 m^3/s (table 3; fig. 22). Event 9 lasted for 4 minutes, 11 seconds and yields a flux of 3,100 m^3/s (table 3). During events 10–13 on January 27 and 28, which cumulatively lasted 15 minutes, the calculated flux rate is roughly 14,000 m^3/s; this high rate corresponds with the eruption of the voluminous Rocky Point pyroclastic-flow deposit during event 10. The flux rates for the dome-building interval of January 14–17 and January 17–27 are much lower: 3–25 m^3/s and 3 m^3/s, respectively. If, however, explosive-phase lava dome 2 began growing later than January 17, the rate at which it effused could be much higher.

During the early continuous phase (January 28 through February 2), the volcano erupted 8.7×10^6 m^3 of magma in the form of pyroclastic-flow deposits. The volume of fallout tephra produced during this time is uncertain but was likely volumetrically minor (Wallace and others, this volume). As the vigor of the continuous phase waned, 9.6×10^6 m^3 of lava effused. Assuming continuous eruption during this period, the flux rate during the early continuous phase was 22 m^3/s and dropped to 16 m^3/s during its less vigorous second half. As shown by component studies (Vallance and others, this volume), the high-silica-andesite compositional end member dominated the first half of this phase, producing about three quarters, or 6.4×10^6 m^3, of the magma that fed the pyroclastic flows. The compositions of the lava flow and dome that effused during the second half of the continuous phase are less well known but, on the basis of appearance, are interpreted to be similar to that of the final lava flows—rich in low-silica andesite.

After an apparent hiatus from roughly February 10 through March 3, when no new magma was erupted, the effusive phase produced approximately 23.5×10^6 m^3 of lava and block-and-ash flows. Ash-fallout volumes were again likely minor during this interval (Wallace and others, this volume). This phase of the eruption was dominated by the low-silica-andesite end member, which accounted for roughly 20×10^6 m^3 of lava effused. The magma flux rate during the effusive phase was approximately 27 m^3/s, assuming constant effusion over this interval.

Eruptive Mechanisms During The 2006 Eruption

The 2006 and other recent eruptions of Augustine Volcano share similarities with other intermediate-composition, dome-building volcanoes worldwide. In general, however,

Augustine seems to have briefer, more intense eruptive cycles compared to other dome-forming volcanoes, such as Mount St. Helens in Washington, Unzen volcano in Japan, Soufriere Hills volcano on Montserrat, or Santiaguito volcano in Guatemala, where eruption cycles typically last years (Rose, 1987; Swanson and Holcomb, 1990; Nakada and others, 1999; Kokelaar, 2002). We discuss the eruptive mechanisms responsible for the varying styles of the three eruptive phases of Augustine Volcano in 2006 and the corresponding activity in previous eruptions.

The Explosive Phase—Cyclic Vulcanian Explosions

The explosive phase of the 2006 eruption consisted of a series of discrete explosions, each minutes long, separated by periods of hours to days. Events 1 and 2 on January 11 produced cold mixed avalanches of snow, rock, and ice and fine-grained tephra-fall deposits that appear to contain little or no juvenile material (Wallace and others, this volume). We conclude that little or no magma had reached the shallow edifice and that the explosions were driven by ascending gases that had accumulated beneath the summit.

In contrast, events 3–13 produced ash-rich plumes, pyroclastic flows, and surges and resulting lahars and mixed avalanches that traveled far down all slopes of the volcano. Thus, the main magmatic eruption commenced on January 13. Pyroclastic-flow deposits from these events were not topographically confined and were likely formed during partial collapse of an eruptive column.

We were not able to calculate volumes for each individual event, but for those that we could, the volume varied dramatically. During event 9, the total volume erupted as both fall and flow deposits was ~0.8×10^6 m^3, whereas the volume of flow deposits from event 10 was 10×10^6 m^3 (both in DRE; table 3). For events 3 through 8, the total erupted volume was 12.1×10^6 m^3, which yields an average volume per event of roughly 2×10^6 m^3. For these events we calculate magma flux rates of 103 to 104 m^3/s. Because explosive events 11 through 13 were closely followed by the beginning of the continuous phase, volumes of deposits from these explosions are less well known.

Many of these characteristics are shared by other vulcanian explosions during previous eruptions of Augustine Volcano (Kienle and Shaw, 1979) and other andesitic volcanoes worldwide, including Soufriere Hills, Montserrat (Druitt and others, 2002); Mount Ngauruhoe, New Zealand (Nairn and Self, 1978); Lascar Volcano, Chile (Matthews and others, 1997); Mount Pinatubo, Philippines (Hoblitt and others, 1996); and Galeras Volcano, Columbia (Stix and others, 1997). Vulcanian explosions are attributed to two main mechanisms: either the interaction of magma with external water, or, as in the cases cited here, the sudden release of pressurized magma beneath a cooled or degassed lava cap (Self and others, 1979; Sparks, 1997; Stix and others, 1997; Morrissey and Mastin, 2000).

A consistent model that accounts for vulcanian explosions at other andesitic, dome-building volcanoes (Druitt and others, 2002) involves a shallow conduit filled with pressurized, vesicular magma, capped by degassed magma in the form of a lava dome or plug. As magma rises into the conduit from below and/or shallow crystallization causes vapor exsolution, increased conduit overpressure exceeds the strength of the cap (Sparks, 1997). At this point the cap is destroyed and a fragmentation wave descends into the conduit creating rapidly escalating conduit escape velocities and the formation of an ash-rich plume. The onset of the explosion is thought to be accompanied by a shock wave (Morrissey and Mastin, 2000). This phase is highly unstable and lasts seconds to minutes. Once the fragmentation wave reaches a level in the conduit where pressure is not great enough to drive fragmentation, the explosion greatly lessens in intensity or stops. Then the conduit refills, eventually leading to another degassed solid cap at the top, and the cycle repeats.

Only about half of the explosive events during the 2006 Augustine Volcano explosive phase had the impulsive acoustic waveforms that would result from the initial shock wave typical of vulcanian blasts (Petersen and others, 2006). The acoustic signal from event 1 was large and impulsive, consistent with this event acting as a vent clearing. The next impulsive event was event 5, which produced significant flows down the north flank. Events 8 through 12 were either impulsive or both emergent plus impulsive (Petersen and others, 2006). One explanation for the mix in waveforms is that some recorded partial failures of lava domes or plugs in addition to impulsive gas release.

By estimating the conduit dimension and erupted volume of each event, we can estimate the depth to which each explosion might have evacuated the conduit. We estimate the vent for the 2006 eruption to be roughly 30 by 45 m, elongate in the north-northwest–south-southeast direction, based on the location of an incipient spine atop the final dome (figs. 17, 19*B*); we assume the conduit will retain these dimensions. Events 3–8 each discharged approximately 2×10^6 m^3 of magma, which yields an average evacuation of the conduit to 1.9 km below the summit. If we have underestimated the dimension of the conduit and instead use a diameter of 50 m (similar to that of the 1986 spine), we calculate an average evacuation depth to 1 km. Such depths are consistent with those calculated for vulcanian explosions that occurred in 1997 at Soufriere Hills volcano, Montserrat (Druitt and others, 2002).

Event 10 was the largest of the explosive blasts, producing roughly 12.5×10^6 m^3 (DRE) of magma. Some of the material in the event 10 flow deposits is likely the destroyed portion of the explosive-phase dome 2. This dome had a volume of 1.7 $x10^6$ m^3 prior to event 10, and slightly less than half was destroyed during this event. Using a conservative estimate of 0.8 $x10^6$ m^3 as contributing to the volume of the event 10 flow deposits, juvenile magma erupted during this event would have been roughly 11.7 $x10^6$ m^3 (DRE). A distinct compositional shift, from predominantly low-silica andesite to predominantly high-silica andesite, occurred

during event 10 between emplacement of the explosive-phase pyroclastic-current and Rocky Point pyroclastic-flow deposits (Vallance and others, this volume). Assuming that all of the juvenile magma was evacuated from a conduit with the dimensions above would result in a conduit length of over 11 km! Petrologic and geodetic evidence suggest, however, that the magma storage region that held the erupted high-silica andesite is located at a depth of roughly 5 km below the summit (Larsen and others, this volume; Cervelli and others, this volume), consistent with post-eruption earthquake hypocenters located at this depth (Power and Lalla, this volume). If this is accurate, event 10 likely evacuated the entire conduit and partially evacuated the magma storage region, whether the latter was a chamber, dike, sill, or crystal-mush zone. This is particularly intriguing given the compositional shift that occurred during this event and suggests that the low-silica andesite erupted during the first half of event 10 came from the conduit and that the high-silica andesite erupted during the second half of the event came predominantly from the magma storage region. This also suggests that this event may have cleared the way for the subsequent eruption of large volumes of high-silica andesite during the continuous phase.

An additional constraint on magma movement and withdrawal prior to and during the vulcanian blasts comes from GPS data that show a shallow inflationary source at sea level that was present from June through November of 2005 (Cervelli and others, 2006). Cervelli and others model this as the result of a point source near sea level that pressurized at a rate corresponding to 4×10^5 m^3/yr, or a volume change of 2×10^5 m^3 (Cervelli and others, 2006). This volume is an order of magnitude lower than material erupted during any one of the explosions, thus we suggest that this sea-level inflationary signal was caused by pressurization by magmatic gas, not magma. This pressurization may have been facilitated by the presence of the relatively impermeable zeolitized Naknek Formation near sea level beneath Augustine Volcano (Detterman and Reed, 1980). On November 17, following the 6-month-long signal, a much stronger inflationary signal began at the summit stations and lasted until January 12. The stronger signal has been modeled as the ascent of a north-south-trending dike from near sea level to the summit (Cervelli and others, 2006). Upward earthquake migration was detected in this depth range during the same time interval (DeShon and others, this volume; Power and Lalla, this volume). We suggest that this dike possessed a gas-filled tip that preceded new magma to the surface, culminating in the gas-rich but juvenile-magma-poor January 11 explosions. Magma then reached the surface on January 12 in the form of a lava dome; growing overpressure in the conduit caused vulcanian magmatic blasts to begin on January 13.

The Continuous Phase—Dome Growth and Collapse

The onset of the continuous phase heralded a distinct shift in eruptive style from the explosive phase. This phase was mainly characterized by pyroclastic-flow emplacement that tapered to lava effusion, but activity began the afternoon of January 28 with a two-hour-long period of volcanic tremor and accompanying ash emission. It was not until 2200 AKST the night of January 28 that the first flowage-type seismic signals were detected. Later observations, and discovery of a seismic station destroyed during this interval, revealed that each signal represented a pyroclastic flow of varying size. This activity continued until February 3, when slower effusion apparently led to the formation of a small lava flow.

By evaluating the volumes of erupted pyroclastic flows from this period, we can evaluate whether pyroclastic flows formed primarily as the result of a collapsing, preexisting dome or whether the dome was actively growing during this interval. The first half of the continuous phase produced more than 14×10^6 m^3 of erupted material (not DRE). A circular dome of this volume, if 40 m tall, would have a radius of ~340 m, which would more than cover the entire summit area. This indicates that pyroclastic flows during this period were not just the result of collapse of an existing lava dome but were instead occurring during active effusion and rapid collapse of a growing dome. Satellite imagery from the middle of this period shows that a roughly circular dome was present at the summit and that flows were initiating from its margins.

Similar activity has been recorded at other dome-forming volcanoes, notably Mount Merapi in Indonesia, Soufriere Hills in Montserrat, and Unzen in Japan. Often, periods of block-and-ash flow activity of this intensity are shorter, however, and thought to be due to collapse of a static dome. For example, on November 22, 1994, roughly 3×10^6 m^3 of block-and-ash flows formed over a 7-hour interval at Merapi when a portion of the summit lava dome collapsed (Abdurachman and others, 2000).

The continuous-phase activity is consistent with relatively high initial magma-flux rates that resulted in rapid effusion and almost continual collapse of a growing lava dome. The composition of this dome was predominantly high-silica andesite, unlike the low-silica-andesite-dominated explosive phase. As the dome grew, its margins became unstable and collapsed, forming classic, Merapi-style block-and-ash flows. Most of these traveled to the north and northeast of the summit, forming composite pyroclastic fans much like those formed during the 1976 and 1986 eruptions of the volcano. At least two larger pyroclastic flows, however, were emplaced early in the continuous phase, including the windy pyroclastic flow that erupted on January 30. These flows occurred when larger portions of the lava dome collapsed, or they reflect fluctuations in magma flux.

As magma flux at the conduit waned, lava that reached the surface remained intact to form a new dome and a short steep lava flow to the north. We did not sample the lava flow at this stage, but images from February show that debris from this lava tongue is much darker than underlying flowage deposits from earlier in the continuous phase, suggesting that the composition had perhaps transitioned to the low-silica andesite that erupted later in the effusive phase.

The Effusive Phase—Rapid Effusion of Lava and Block-and-Ash Flows

The flux rate calculated during the effusive-phase rate of ~27 m^3/s is quite high compared to other rates of lava effusion measured elsewhere. During periods of exogenous dome growth between 1980 and 1986, extrusion rates at Mount St. Helens varied from 1.4 to 40.3 m^3/s (Anderson and Fink, 1990), similar to or higher than the rates at Augustine Volcano. However, at Santiaguito in Guatemala, dome growth varied between periods of slow (0.16 m^3/s) and relatively fast (0.6–1.9 m^3/s) extrusion (Rose, 1987). At Mount Merapi in Indonesia, from 1984–1995, lava-dome effusion rates varied from 0.05 to 0.32 m^3/s, with an average long-term rate of 0.039 m^3/s (Siswowidjoyo and others, 1995). Thus, while effusion occurred over a short time period in March of 2006, the resulting volume was equivalent to that seen for domes/flows elsewhere erupted over much longer periods.

The block-and-ash flows during the effusive phase are much smaller in volume than flows from the continuous phase. They are similar to other classic deposits of this type seen at Unzen Volcano in Japan and elsewhere. At Unzen, Ui and others (1999) describe block-and-ash flows that occur when lava is actively flowing downslope, and the tensile strength of the deforming lava is exceeded by the pore pressure in the lava and the downslope tensional force. This causes a local explosion, often around a growing crack, and fragmentation is triggered at the lobe front—a likely explanation for the effusive-phase pyroclastic flows at Augustine Volcano.

The rock-avalanche events that occurred at Augustine Volcano in April and May, well after effusion had ceased, still resulted in observed ash clouds and block-and-ash-flow-type deposits. We suggest that these events resemble rockfall-induced block-and-ash flows that also occurred at Unzen (Ui and others, 1999). The steep slopes near Augustine's summit led to rock falls off the western edge of the still-hot north lava flow. As blocks of hot lava that retained high pore pressures hit the ground, they fragmented upon impact causing small block-and-ash flows. The rockfalls off the north lava flow occurred repeatedly from the same location, exposing fresh parts of the flow interior that had not been fully degassed. This may explain why each block-and-ash flow was somewhat bigger than the last.

Acknowledgments

We thank the entire staff of the Alaska Volcano Observatory (AVO) for their efforts during the 2006 Augustine eruption—without the detailed observations made by many, this paper would not have been possible. In particular, we are grateful for conversations with Peter Cervelli, Pavel Izbekov, Steve McNutt, Tina Neal, Chris Nye, John Power, Stephanie Prejean, and Kristi Wallace that helped us to refine our chronology of events and our ideas about eruptive mechanisms. Comments by Wes Hildreth, John Power, and in particular Tom Sisson improved the manuscript. We also thank the skilled helicopter and fixed-wing pilots who took us to the volcano despite often-challenging conditions. A special thanks to Cheryl Cameron and Seth Snedigar, who have made the AVO image database and other web-based tools that are so useful.

References Cited

Abdurachman, E.K., Bourdier, J.-L., and Voight, B., 2000, Nuées ardentés of 22 November 1994 at Merapi volcano, Java, Indonesia: Journal of Volcanology and Geothermal Research, v. 100, p. 345–361.

Anderson, S., and Fink, J.H., 1990, The development and distribution of lava textures at the Mount St. Helens dome, *in* Fink, J.H., ed., Lava flows and domes; emplacement mechanisms and hazard implications: Berlin, Springer-Verlag, International Association of Volcanology and Chemistry of the Earth's Interior, p. 25–46.

Bailey, J.E., Dean, K.G., Dehn, J., and Webley, P.W., 2010, Integrated satellite observations of the 2006 eruption of Augustine Volcano, *in* Power, J.A., Coombs, M.L., and Freymueller, J.T., eds., The 2006 eruption of Augustine Volcano, Alaska: U.S. Geological Survey Professional Paper 1769 (this volume).

Begét, J.E., and Kienle, J., 1992, Cyclic formation of debris avalanches at Mount St. Augustine volcano: Nature, v. 356, no. 6371, p. 701–704.

Cervelli, P.F., Fournier, T., Freymueller, J.T., and Power, J.A., 2006, Ground deformation associated with the precursory unrest and early phases of the January 2006 eruption of Augustine Volcano, Alaska: Geophysical Research Letters, v. 33, L18304, doi:10.1027/2006GL027219.

Cervelli, P.F., Fournier, T.J., Freymueller, J.T., Power, J.A., Lisowski, M., and Pauk, B.A., 2010, Geodetic constraints on magma movement and withdrawal during the 2006 eruption of Augustine Volcano, *in* Power, J.A., Coombs, M.L., and Freymueller, J.T., eds., The 2006 eruption of Augustine Volcano, Alaska: U.S. Geological Survey Professional Paper 1769 (this volume).

DeRoin, N., McNutt, S.R., Reyes, C., and Sentman, D.D., 2007, Rockfalls at Augustine Volcano, Alaska; 2003–2006: Eos Transactions of the American Geophysical Union, v. 88, S43–1038.

DeShon, H.R., Thurber, C.H., and Power, J.A., 2010, Earthquake waveform similarity and evolution at Augustine Volcano from 1993 to 2006, *in* Power, J.A., Coombs, M.L., and Freymueller, J.T., eds., The 2006 eruption of Augustine Volcano, Alaska: U.S. Geological Survey Professional Paper 1769 (this volume).

Detterman, R.L., and Reed, B.L., 1980, Stratigraphy, structure, and economic geology of the Iliamna quadrangle, Alaska: U.S. Geological Survey Bulletin 1368-B, 86 p, 1 sheet.

Druitt, T.H., Young, S.R., Baptie, B., Bonadonna, C., Calder, E.S., Clarke, A.B., Cole, P.D., Harford, C.L., Herd, R.A., Luckett, R., Ryan, G., and Voight, B., 2002, Episodes of cyclic Vulcanian explosive activity with fountain collapse at Soufriere Hills Volcano, Montserrat, *in* Druitt, T.H., and Kokelaar, B.P., eds., The Eruption of Soufriere Hills Volcano, Montserrat, from 1995 to 1999: London, The Geological Society, p. 281–306.

Dzurisin, D.J., Vallance, J.W., Gerlach, T.M., Moran, S.C., and Malone, S.D., 2005, Mount St. Helens reawakens: Eos (American Geophysical Union Transactions), v. 86, no. 3, p. 25, 29.

Fierstein, J., and Nathenson, M., 1992, Another look at the calculation of fallout tephra volumes: Bulletin of Volcanology, v. 54, p. 156–167.

Hoblitt, R.P., Wolfe, E.W., Scott, W.E., Couchman, M.R., Pallister, J.S., and Javier, D., 1996, The pre-climactic eruptions of Mount Pinatubo, June 1991, *in* Newhall, C.G., and Punongbayan, R.S., eds., Fire and Mud; eruptions and Lahars of Mount Pinatubo, Philippines: Seattle, University of Washington Press, p. 457–511.

Johnston, D.A., 1978, Volatiles, magma mixing, and the mechanism of eruption at Augustine Volcano, Alaska: University of Washington Ph.D. dissertation, 187 p.

Johnston, D.A., 1979, Onset of volcanism at Augustine Volcano, lower Cook Inlet, *in* Johnson, K.M. and Williams, J.R., Jr., eds., The United States Geological Survey in Alaska; accomplishments during 1978: U.S. Geological Survey Circular 0804-B, p. B78–B80.

Kamata, H., Johnston, D.A., and Waitt, R.B., 1991, Stratigraphy, chronology, and character of the 1976 pyroclastic eruption of Augustine Volcano, Alaska: Bulletin of Volcanology, v. 53, p. 407–409.

Kienle, J., and Shaw, G.E., 1979, Plume dynamics, thermal energy, and long-distance transport of vulcanian eruption clouds from Augustine Volcano, Alaska: Journal of Volcanology and Geothermal Research, v. 6, p. 139–164.

Kokelaar, B.P., 2002, Setting, chronology, and consequences of the eruption of Soufriere Hills Volcano, Montserrat (1995–1999), *in* Druitt, T.H., and Kokelaar, B.P., eds., The Eruption of Soufriere Hills Volcano, Montserrat, from 1995–1999: London, The Geological Society, p. 1–44.

Larsen, J.F., Nye, C.J., Coombs, M.L., Tilman, M., Izbekov, P., and Cameron, C., 2010, Petrology and geochemistry of the 2006 eruption of Augustine Volcano, *in* Power, J.A., Coombs, M.L., and Freymueller, J.T., eds., The 2006 eruption of Augustine Volcano, Alaska: U.S. Geological Survey Professional Paper 1769 (this volume).

Matthews, S.J., Gardeweg, M.C., and Sparks, R.S.J., 1997, The 1984–1996 cyclic activity of Lascar Volcano, northern Chile; cycles of dome growth, dome subsidence, degassing and explosive eruptions: Bulletin of Volcanology, v. 59, p. 72–82.

McNutt, S.R., Tytgat, G., Estes, S.A., and Stihler, S.D., 2010, A parametric study of the January 2006 explosive eruptions of Augustine Volcano, using seismic, infrasonic, and lightning data *in* Power, J.A., Coombs, M.L., and Freymueller, J.T., eds., The 2006 eruption of Augustine Volcano, Alaska: U.S. Geological Survey Professional Paper 1769 (this volume).

Morrissey, M.M., and Mastin, L.G., 2000, Vulcanian eruptions, *in* Sigurdsson, H., Houghton, B.F., McNutt, S.R., Rymer, H., and Stix, J., eds., Encyclopedia of volcanoes: San Diego, Academic Press, p. 463–475.

Nairn, I.A., and Self, S., 1978, Explosive avalanches and pyroclastic flows from Ngauruhoe 1975: Journal of Volcanology and Geothermal Research, v. 3, p. 39–60.

Nakada, S., Shimizu, H., and Ohta, K., 1999, Overview of the 1990–1995 eruption at Unzen Volcano: Journal of Volcanology and Geothermal Research, v. 89, p. 1–22.

Neal, C.A., Murray, T.L., Power, J.A., Adleman, J.N., Whitmore, P.M., and Osiensky, J.M., 2010, Hazard information management, interagency coordination and impacts of the 2005–2006 eruption of Augustine Volcano, *in* Power, J.A., Coombs, M.L., and Freymueller, J.T., eds., The 2006 eruption of Augustine Volcano, Alaska: U.S. Geological Survey Professional Paper 1769 (this volume).

Paskievitch, J., Read, C., and Parker, T., 2010, Remote telemetered and time-lapse cameras at Augustine Volcano, *in* Power, J.A., Coombs, M.L., and Freymueller, J.T., eds., The 2006 eruption of Augustine Volcano, Alaska: U.S. Geological Survey Professional Paper 1769 (this volume).

Pauk, B.A., Jackson, M., Feaux, K., Mencin, D., and Bohnenstiehl, K., 2010, The Plate Boundary Observatory permanent global positioning system network on Augustine Volcano before and after the 2006 eruption, *in* Power, J.A., Coombs, M.L., and Freymueller, J.T., eds., The 2006 eruption of Augustine Volcano, Alaska: U.S. Geological Survey Professional Paper 1769 (this volume).

Petersen, T., De Angelis, S., Tytgat, G., and McNutt, S.R., 2006, Local infrasound observations of large ash explosions at Augustine Volcano, Alaska, during January 11–28, 2006: Geophysical Research Letters, v. 33, L12303, doi:10.1029/2006GL026491.

Power, J., 1988, Seismicity associated with the 1986 eruption of Augustine Volcano, Alaska: Fairbanks, University of Alaska, unpub. M.S. thesis, 142 p.

Power, J.A., and Lalla, D.J., 2010, Seismic observations of Augustine Volcano, 1970–2007, *in* Power, J.A., Coombs, M.L., and Freymueller, J.T., eds., The 2006 eruption of Augustine Volcano, Alaska: U.S. Geological Survey Professional Paper 1769 (this volume).

Power, J.A., Nye, C.J., Coombs, M.L., Wessels, R.L., Cervelli, P.F., Dehn, J., Wallace, K.L., Freymueller, J.T., and Doukas, M.P., 2006, The reawakening of Alaska's Augustine Volcano: Eos (American Geophysical Union Transactions), v. 87, no. 37, p. 373, 377.

Rose, W.I., 1987, Volcanic activity at Santiaguito volcano, 1976–1984, *in* Fink, J.H., ed., The emplacement of silicic domes and lava flows: Boulder, Colo.,The Geological Society of America, p. 17–28.

Schneider, D.J., Scott, C., Wood J., and Hall T., 2006, NEXRAD weather radar observations of the 2006 Augustine volcanic eruption clouds: Eos (American Geophysical Union Transactions), v. 87, Abstract V51C–1686.

Self, S., Wilson, L., and Nairn, I.A., 1979, Vulcanian eruption mechanisms: Nature, v. 277, p. 440–443.

Sentman, D.D., McNutt, S.R., Stenbaek-Nielsen, H.C., Tytgat, G., and DeRoin, N., 2010, Imaging observations of thermal emissions from Augustine Volcano using a small astronomical camera, *in* Power, J.A., Coombs, M.L., and Freymueller, J.T., eds., The 2006 eruption of Augustine Volcano, Alaska: U.S. Geological Survey Professional Paper 1769 (this volume).

Siswowidjoyo, S., Suryo, I., and Yokoyama, I., 1995, Magma eruption rates of Merapi volcano, central Java, Indonesia during one century (1890–1992): Bulletin of Volcanology, v. 57, p. 111–116.

Sparks, R.S.J., 1997, Causes and consequences of pressurisation in lava dome eruptions: Earth and Planetary Science Letters, v. 150, p. 177–189.

Stith, J.L., Hobbs, P.V., and Radke, L.F., 1977, Observations of a nuee ardente from the St. Augustine Volcano: Geophysical Research Letters, v. 4, p. 259–262.

Stix, J., Torres, R.C., Narvaez, M.L., Cortes, G.P., Raigosa, J.A., Gomez, D.M., and Castonguay, R., 1997, A model of Vulcanian eruptions at Galeras Volcano, Columbia: Journal of Volcanology and Geothermal Research, v. 77, p. 285–304.

Swanson, D.A., and Holcomb, R.T., 1990, Regularities in growth of the Mount St. Helens dacite dome, 1980–1986, *in* Fink, J.H., ed., Lava flows and domes; emplacement mechanisms and hazard implications: Berlin, Springer-Verlag, International Association of Volcanology and Chemistry of the Earth's Interior, p. 3–24.

Swanson, S.E., and Kienle, J., 1988, The 1986 eruption of Mount St. Augustine; field test of a hazard evaluation: Journal of Geophysical Research, v. 93, p. 4500–4520.

Thomas, R.J., McNutt, S.R., Krehbiel, P.R., Rison, W., Aulich, G., Edens, H.E., Tytgat, G, and Clark, E., 2010, Lightning and electrical activity during the 2006 eruption of Augustine Volcano, *in* Power, J.A., Coombs, M.L., and Freymueller, J.T., eds., The 2006 eruption of Augustine Volcano, Alaska: U.S. Geological Survey Professional Paper 1769 (this volume).

Ui, T., Matsuwo, N., Sumita, M., and Fujinawa, A., 1999, Generation of block and ash flows during the 1990–1995 eruption of Unzen Volcano, Japan: Journal of Volcanology and Geothermal Research, v. 89, p. 123–138.

Vallance, J.W., Bull, K.F., and Coombs, M.L., 2010, Pyroclastic flows, lahars, and mixed avalanches generated during the 2006 eruption of Augustine Volcano, *in* Power, J.A., Coombs, M.L., and Freymueller, J.T., eds., The 2006 eruption of Augustine Volcano, Alaska: U.S. Geological Survey Professional Paper 1769 (this volume).

Waitt, R.B., and Begét, J.E., 2009, Volcanic processes and geology of Augustine Volcano, Alaska: U.S. Geological Survey Professional Paper 1762, 78 p., 2 map plates [http://pubs.usgs.gov/pp/1762/].

Wallace, K.L., Neal, C.A., and McGimsey, R.G., 2010, Timing, distribution, and character of tephra fall from the 2005–2006 eruption of Augustine Volcano, *in* Power, J.A., Coombs, M.L., and Freymueller, J.T., eds., The 2006 eruption of Augustine Volcano, Alaska: U.S. Geological Survey Professional Paper 1769 (this volume).

Wessels, R.L., Coombs, M.L., Schneider, D.J., Dehn, J., and Ramsey, M.S., 2010, High-resolution satellite and airborne thermal infrared imaging of the 2006 eruption of Augustine Volcano, *in* Power, J.A., Coombs, M.L., and Freymueller, J.T., eds., The 2006 eruption of Augustine Volcano, Alaska: U.S. Geological Survey Professional Paper 1769 (this volume).

Yount, E.M., Miller, T.P., and Gamble, B.M., 1987, The 1986 eruptions of Augustine Volcano, Alaska, hazards and effects, *in* Hamilton, T.D., and Galloway, J.P., eds., The United States Geological Survey in Alaska; accomplishments during 1986: U.S. Geological Survey Circular 0998, p. 4–13.

This page intentionally left blank

The 2006 Eruption of Augustine Volcano, Alaska
Power, J.A., Coombs, M.L., and Freymueller, J.T., editors
U.S. Geological Survey Professional Paper 1769

Chapter 9

Timing, Distribution, and Character of Tephra Fall from the 2005–2006 Eruption of Augustine Volcano

By Kristi L. Wallace[1], Christina A. Neal[1], and Robert G. McGimsey[1]

Abstract

The 2005–6 eruption of Augustine Volcano produced tephra-fall deposits during each of four eruptive phases. Late in the precursory phase (December 2005), small phreatic explosions produced small-volume, localized, mostly nonjuvenile tephra. The greatest volume of tephra was produced during the explosive phase (January 11–28, 2006) when 13 discrete Vulcanian explosions generated ash plumes between 4 and 14 km above mean sea level (asl). A succession of juvenile tephra with compositions from low-silica to high-silica andesite is consistent with the eruption of two distinct magmas, represented also by a low-silica andesite lava dome (January 13–16) followed by a high-silica andesite lave dome (January 17–27). On-island deposits of lapilli to coarse ash originated from discrete vent explosions, whereas fine-grained, massive deposits were elutriated from pyroclastic flows and rock falls. During the continuous phase (January 28–February 10, 2006), steady growth and subsequent collapses of a high-silica andesite lava dome caused continuous low-level ash emissions and resulting fine elutriate ash deposits. The emplacement of a summit lava dome and lava flows of low-silica andesite during the effusive phase (March 3–16, 2006) resulted in localized, fine-grained elutriated ash deposits from small block-and-ash flows off the steep-sided lava flows.

Mixing of two end-member magmas (low-silica and high-silica andesite) is evidenced by the overall similarities between tephra-fall and contemporaneous lava-dome and flow lithologies and by the chemical heterogeneity of matrix glass compositions of coarse lapilli and glass shards in the ash-size fraction throughout the 2005–6 eruption. A total mass of 2.2×10^{10} kg of tephra fell (bulk volume of 2.2×10^{7} m^3 and DRE volume of 8.5×10^{6} m^3) during the explosive phase, as calculated by extrapolation of mass data from a single Vulcanian blast on January 17. Total tephra-fall volume for the 2005–6 eruption is about an order of magnitude smaller than other historical eruptions from Augustine Volcano. Ash plumes of short duration and small volume caused no more than minor amounts (≤1 mm) of ash to fall on villages and towns in the lower Cook Inlet region, and thus little hazard was posed to local communities. The bulk of the ash fell into Cook Inlet. Monitoring by the Alaska Volcano Observatory during the eruption helped to prevent hazardous encounters of ash and aircraft.

Introduction

Augustine Volcano, in the eastern Aleutian arc, has erupted seven times since 1812 and is the most historically active volcano in south-central Alaska's Cook Inlet region (Miller and others, 1998; fig. 1). The most recent eruption in 2005–6 produced ash clouds and fall, pyroclastic flows, and lava domes and flows, similarly to recent eruptions in 1986 and 1976. Four distinct eruptive phases, defined on the basis of the various processes that occurred during the eruption, each generated some form of tephra-fall deposit during this most recent eruption. The four phases include the (1) precursory (April–December 2005), (2) explosive (January 11–28, 2006), (3) continuous (January 28–February 10, 2006), and (4) effusive (March 3–16, 2006) phases (Power and others, 2006). Documentation of tephra fall was challenging because the volcano is on a remote island and most of the tephra fell on water. The eruption occurred during the winter, so tephra deposits on land were subject to high winds and fallout on ephemeral snow. Because tephra volumes were small, tephra that fell onto nearby land surfaces (25–185 km away) comprised fine ash dustings that were mostly less than 1 mm thick and posed little hazard to local populations. Proximal deposits are complex and varied because of near-vent processes, including elutriation from pyroclastic flows and rockfalls and

[1]Alaska Volcano Observatory, U.S. Geological Survey, 4200 University Drive, Anchorage, AK 99508.

modification by reworking. Calculations of tephra-fall volume are based on mass data for an ash-fall deposit from a discrete plume on January 17, 2006. This was the only opportunity to accurately determine tephra-fall volume for a single event, because it was deposited on land and was quickly buried by snowfall, and thus we formulate total mass and volume for all fall deposits erupted during the explosive phase by extrapolation of these data.

This report describes the timing, distribution, character, mass, and origin of tephra-fall deposits from the 2005–6 eruption of Augustine and concludes with a discussion of their significance and hazards. Because most of the explosive events were not observed directly, we infer their origins from time-lapse photography, geophysical data, and deposit characteristics. Magmatic or hydrovolcanic explosions at the vent initiated some tephra falls, and dome collapses that formed pyroclastic flows or rockfalls, and generated fine-grained elutriate ash clouds initiated others. Regardless of origin, tephra plumes resulted from these events and at times extended hundreds of kilometers downwind.

Methods

We describe tephra-fall deposits in terms of (1) time of eruption, (2) distribution, (3) character, including thickness, particle size, composition (componentry and glass geochemistry), and preservation, (4) origin, and (5) mass, when known. Samples collected for this study are archived at the U.S. Geological Survey (USGS) Alaska Tephra Laboratory and Data Center at the Alaska Volcano Observatory (AVO) in Anchorage, Alaska.

Timing of Tephra Production

We adopt the sequence and naming of eruption phases of Power and others (2006) to describe the timing of the 2005–6 eruption. We use event numbers to reference individual explosions of the explosive phase (Vallance and others, this volume; Power and others, 2006; table1).

Tephra Distribution

Explosions that generated discrete plumes had distinct seismic signals (Power and Lalla, this volume; McNutt and others, this volume) that alerted AVO to collect plume data and tephra samples. Data collected include (1) estimation of plume height (from radar and/or pilot reports; Schneider and others, 2006), (2) seismic duration of explosive event (Power and Lalla, this volume), (3) direction of prevailing winds, (4) movement direction of plume in satellite and radar data (Bailey and others, this volume; Schneider and others, 2006), (5) ash-fall reports from nearby towns and villages, and (6) overflight photography. Timely access to these data facilitated tracking of individual plumes. During the continuous phase, secondary plumes of elutriated fine ash from pyroclastic flows and rockfalls were more complicated to track because their onset times and plume heights were difficult to constrain. Tephra fall into Cook Inlet could not be documented, so deposits too small to reach adjacent landmasses 25 km away are not reported here. Herein, the term "proximal" implies Augustine Island and "distal" implies any landmass off the island (that is, Alaska mainland, Kenai Peninsula, Kodiak Island).

Available satellite images and radar data allow reconstruction of plume trajectories (fig. 1) at the time of plume generation and transport, and they closely match the wind forecast data from the National Weather Service (NWS) and the National Atmospheric and Oceanic Administration (NOAA) (fig. 2). Our telephone network allowed people in towns and villages along the path of drifting plumes to report observations of ash clouds and tephra fall, although much of the tephra fall occurred in sparsely settled or uninhabited areas. Other papers in this volume present more detailed data on plume trajectories and distribution using various satellite data (Bailey and others, this volume; Webley and others, this volume). With one exception, we did not reconstruct deposit isopachs, because tephra fell over water or in remote, uninhabited areas and because some tephra lobes overlapped to form a single undifferentiated layer. Plume heights in text are all from radar data (Schneider and other, 2006, and data taken from poster by D.J. Schneider and others, 2006) for consistency and differ from pilot-reported heights, although both are shown in table 1.

Tephra Character

We characterize tephra-fall deposits in terms of thicknesses when known, particle size, composition (componentry and glass geochemistry), and preservation. We collected proximal tephra samples at 65 field stations in July–August 2006 and during brief visits to the island and affected regions while the eruption was in progress (fig. 3 and appendix 1). We deployed ash-collection buckets on Augustine in late December 2005 in an attempt to collect temporally constrained samples during times when it was unsafe to be on the island. The buckets were colocated with geophysical instruments to facilitate recovery during brief visits to the island throughout the eruption. Distal samples were collected during the eruption either during helicopter-based fieldwork or by local citizens upon request.

We use standard volcanic terminology to characterize particle size (Fisher, 1961; Schmid, 1981; Chough and Sohn, 1990). We did not perform quantitative particle-size analyses because distal sample quantities were insufficient and, in proximal samples, deposits were reworked owing to wind or melting of underlying snow. We constructed generalized stratigraphic sections to represent proximal fall deposits on all four quadrants of the island to show the relations between deposits eruption (fig. 4). Sections are derived from best preserved

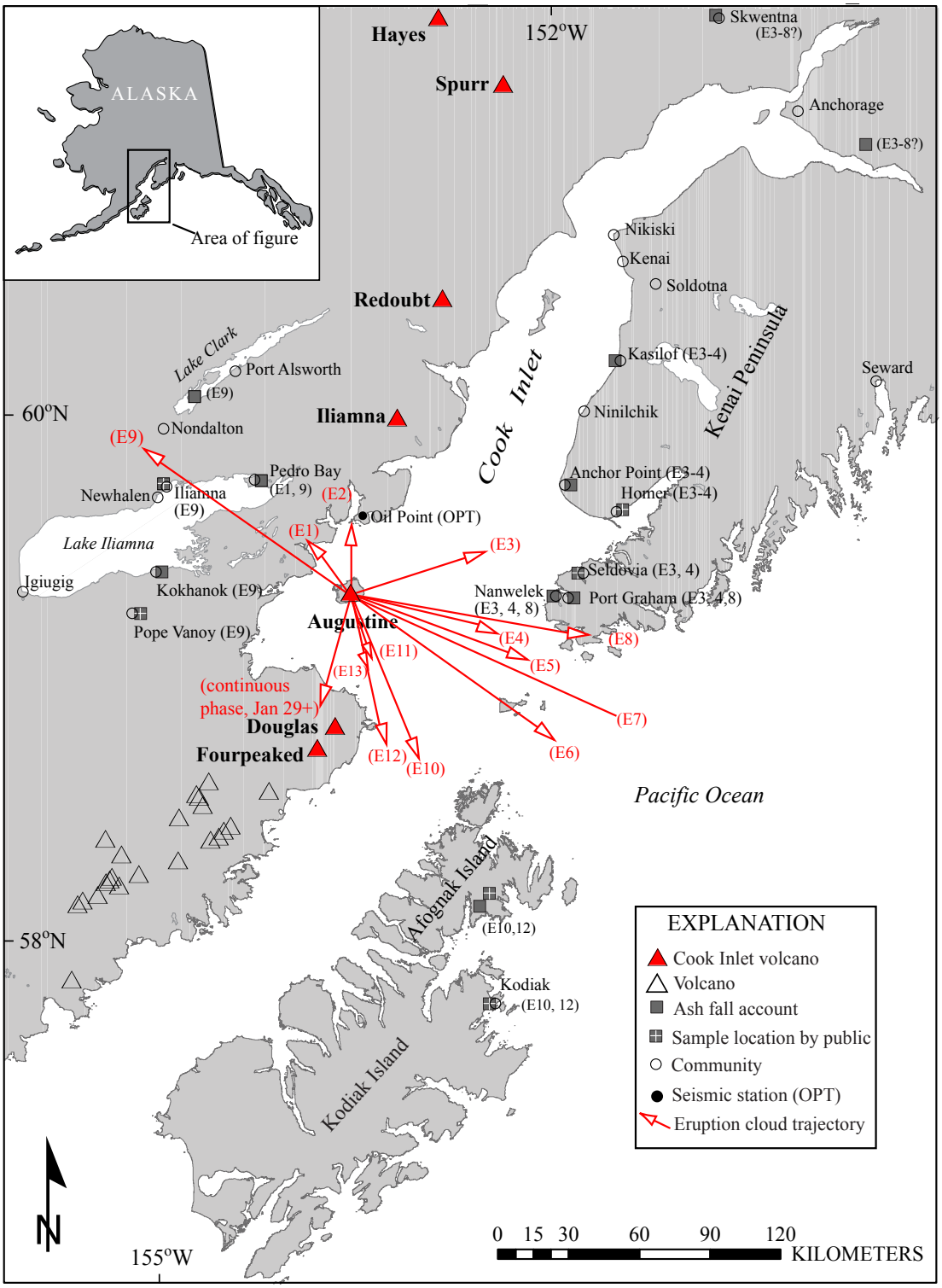


Figure 1. Map of south-central Alaska showing location of Augustine and other volcanoes, surrounding communities, ash-fall accounts, and ash-plume trajectories during the explosive and continuous phases of the 2005–6 eruption of Augustine. Plume trajectories are based on Nexrad radar data (data taken from poster of D.J. Schneider and others, 2006); E indicates explosive event number. Ash-fall accounts are eyewitness reports of ash fall. Such accounts are associated with event numbers but may fall off the path of the radar-derived plume trajectory, which indicates that shifting winds at different altitudes carried ash in those directions.

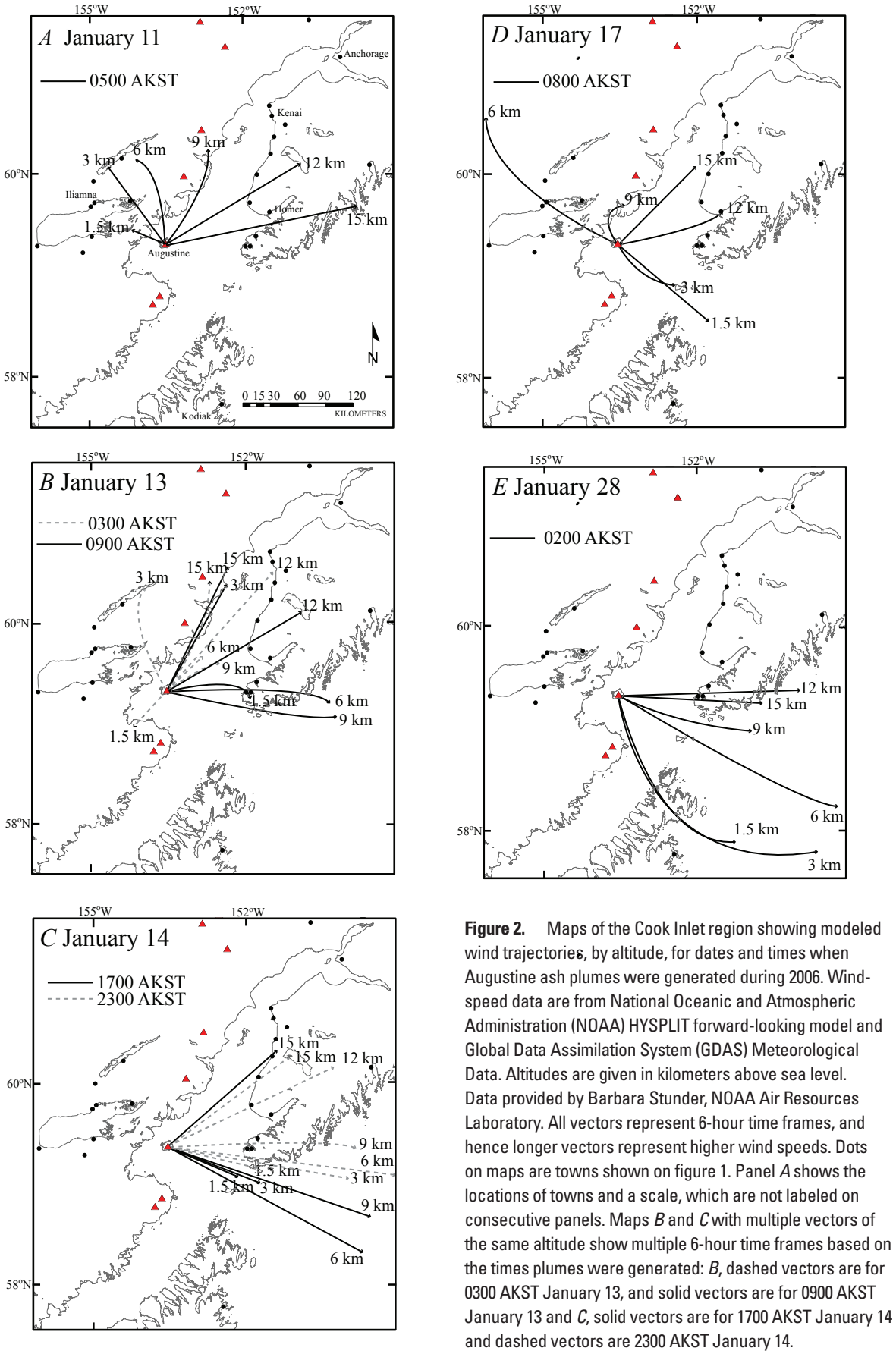


Figure 2. Maps of the Cook Inlet region showing modeled wind trajectories, by altitude, for dates and times when Augustine ash plumes were generated during 2006. Wind-speed data are from National Oceanic and Atmospheric Administration (NOAA) HYSPLIT forward-looking model and Global Data Assimilation System (GDAS) Meteorological Data. Altitudes are given in kilometers above sea level. Data provided by Barbara Stunder, NOAA Air Resources Laboratory. All vectors represent 6-hour time frames, and hence longer vectors represent higher wind speeds. Dots on maps are towns shown on figure 1. Panel *A* shows the locations of towns and a scale, which are not labeled on consecutive panels. Maps *B* and *C* with multiple vectors of the same altitude show multiple 6-hour time frames based on the times plumes were generated: *B*, dashed vectors are for 0300 AKST January 13, and solid vectors are for 0900 AKST January 13 and *C*, solid vectors are for 1700 AKST January 14 and dashed vectors are 2300 AKST January 14.

deposits protected by vegetation cover on the mid to lower flanks of the island.

Previous studies show that tephra from historical eruptions of Augustine have a range of glass compositions (for example, Kienle and Swanson, 1987; Johnston, 1978; Daley, 1986; and Roman and others, 2005). Therefore where possible, we use grain-discrete analysis of the glass fraction to help characterize the geochemistry of tephra deposits. Glass analyses were determined using a Cameca SX-50 electron microprobe at the University of Alaska Fairbanks Advanced Instrumentation Lab (table 2 and appendix 2). Analyses are of distal glass shards and of matrix glass of proximal lapilli. Brown, clear, and hybrid glass (mixture of brown and clear glass) identified throughout the eruption (fig. 5) posed some analytical challenges. Brown glass contains abundant microlites, while clear glass is mostly microlite free. Identifying pure glass pools in brown "glass" was challenging, and these data show significant scatter as a result. All glass analyses were filtered to eliminate the inclusion of mineral data (appendix 2), although the distinction between truly heterogeneous glass and scatter resulting from partial analysis of glass plus microlites is sometimes difficult to make. Larsen and others (this volume, their table 4) show glass analyses from tephra-fall deposits where they made a concerted effort to identify pure glass pools using backscatter imaging on the electron microprobe. For brevity, we pared down the hundreds of glass analyses that we performed to a summary of ranges of compositions listed by eruptive phase, event number, and lithology (table 2). Raw, filtered glass compositions are given in appendix 2.

We did component analyses using proximal, coarse-grained deposits and sorted clasts > 5mm into lithologies based on macroscopic appearance (table 3, fig. 5). The resulting lithologic types are the same as those used by researchers studying other proximal products from the eruption (Coombs and others, this volume; Vallance and others, this volume; Larsen and others, this volume). Component analyses are reported in percent of n clasts per sample.

Preservation of both distal and proximal tephra-fall deposits is discussed, because we think it is an important consideration for the future interpretation of these deposits as well as for the understanding of prehistoric tephra records, at least in this region. Eruption histories deciphered using Holocene tephrostratigraphic studies often show only minimum numbers of eruptions, because tephra-fall deposits are not always faithfully recorded in the geologic record (for example, Riehle, 1985; de Fontaine and others, 2007; Schiff and others, 2008). Thus, a discussion of preservation (or lack of) here is relevant to interpreting prehistoric tephra-fall records when direct observations were not made.

Tephra Origin

Multiple volcanic processes can generate ash clouds and ash fall—short-lived blasts, either magmatic or phreatic; sustained magmatic eruption; and elutriation of ash from pyroclastic flows. Integration of field observations and laboratory analyses of tephra-fall and other deposits of the 2005–6 eruption of Augustine is critical to interpreting the origins of the fall deposits. Close coordination with researchers who studied other aspects of the eruption (Coombs and others, this volume; Vallance and others, this volume; Larsen and others, this volume) allowed for consistent identification and characterization of all eruptive products. Evidence used to interpret deposit origin includes (1) duration of plume generation and plume height, (2) volume of fall deposits, (3) componentry of fragmental deposits, (4) contemporaneous volcanic activity, (5) seismicity, (6) acoustic signals, and (7) gas and steam emissions.

Tephra Mass

We used mass-per-unit-area sampling to calculate mass and volume of tephra fall. The mass per unit area (g/m^2) of a sample is the mass (g) of dried sample divided by the area (m^2) from which the sample was collected. These values were plotted on a base map, and contours of equal mass (isomass contours) were constructed. On the basis of our coarse sampling, we were able to draw four isomass contours: 10, 50, 100, and 10,000 g/m^2. Total mass of the tephra deposit was then calculated using the root-area method developed by Pyle (1989) and modified by Fierstein and Nathenson (1992) (table 4). This method accounts for the mass of tephra that fell beyond the most distal isomass contour (that is, 0 g/m^2). We calculate bulk and dense-rock-equivalent (DRE) deposit volume by assuming a bulk density of 1,000 kg/m^3 and a rock density of 2,600 kg/m^3, then dividing the total mass by these densities (Sarna-Wojcicki and others, 1981) (table 4). When calculating eruption rates (erupted mass/eruption duration), we use seismic duration at a distant station (32 km from Augustine; Power and Lalla, this volume) as a proxy for the length of time that a plume was generated (fig. 1).

We used mass per unit area, rather than deposit thickness, to calculate tephra-fall mass and volume, because individual deposits fell in place along with snow and subsequently were buried by snowfall. Modification by compaction does not alter results using this method (Scott and McGimsey, 1994). Tephra was collected from 10 sites of areas 0.04 to 0.25 m^2 (20×20 cm to 50×50 cm), depending on the amount of ash present. The tephra was preserved as a layer in the snowpack, which facilitated sampling the thin and sometimes diffuse deposit (fig. 6). Several snow pits were excavated at each sample site to expose the deposit and to select a representative sample location. Snow overlying the tephra deposit was shoveled away, a plastic measured-area template was placed on the deposit, and a trowel was used to trace out the measured area. The tephra deposit and some underlying snow were collected into large plastic, sealable bags using a trowel. In addition to tephra from the snowpack, one sample was collected on January 17 by a resident of the village of Iliamna, 90 km northwest of Augustine, who collected falling ash on a measured piece of aluminum foil.

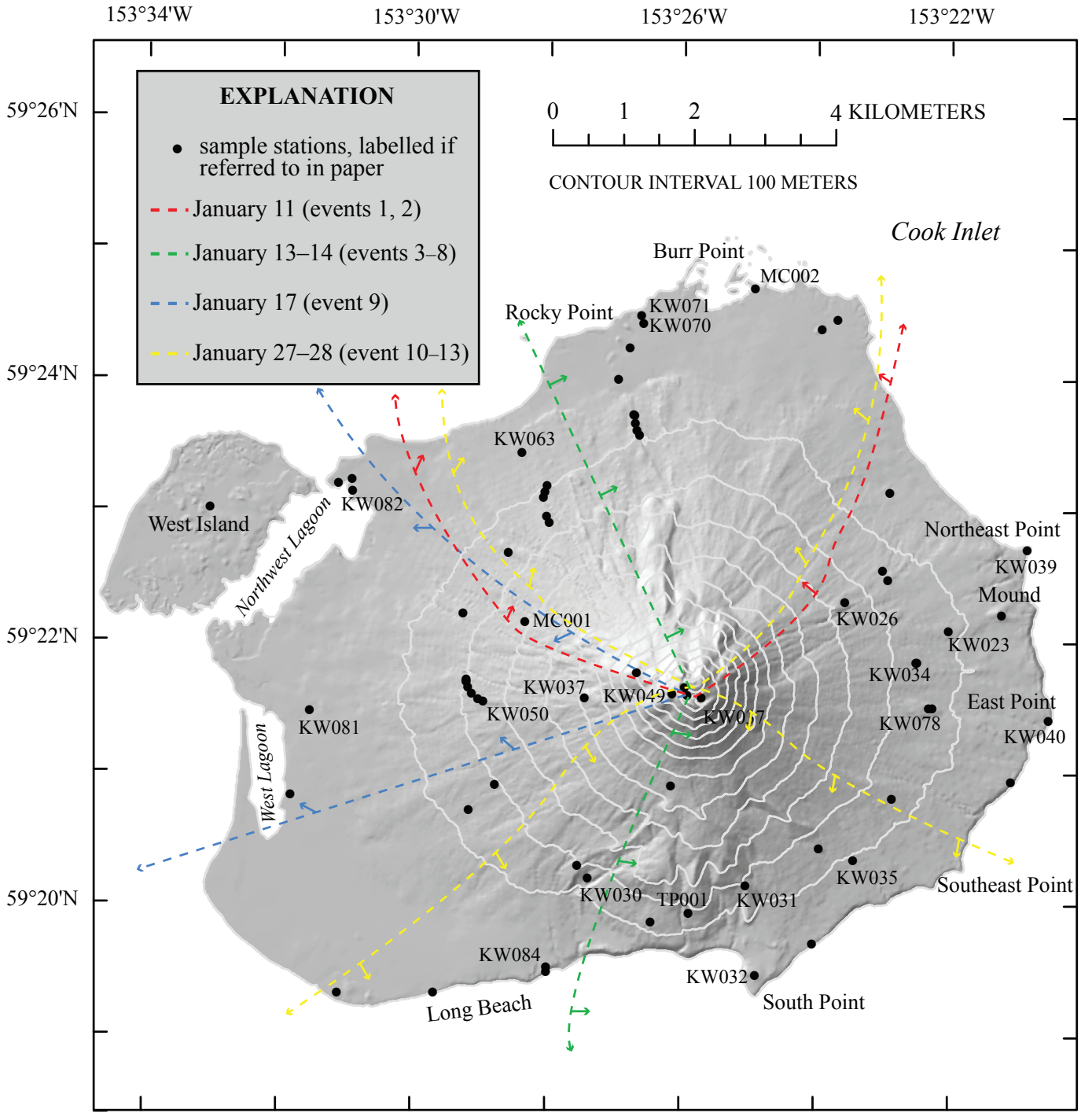


Figure 3. Shaded relief map of Augustine Island showing sample locations (black dots) for this study and dashed lines indicating the boundaries of ash-fall deposits from explosive events that occurred during the explosive phase of the 2005–6 eruption (January 11–28, 2006). Station names are shown for all samples referred to in the paper. Common geographic place names are shown though all except Burr Point are informal. Digital elevation model from 1990.

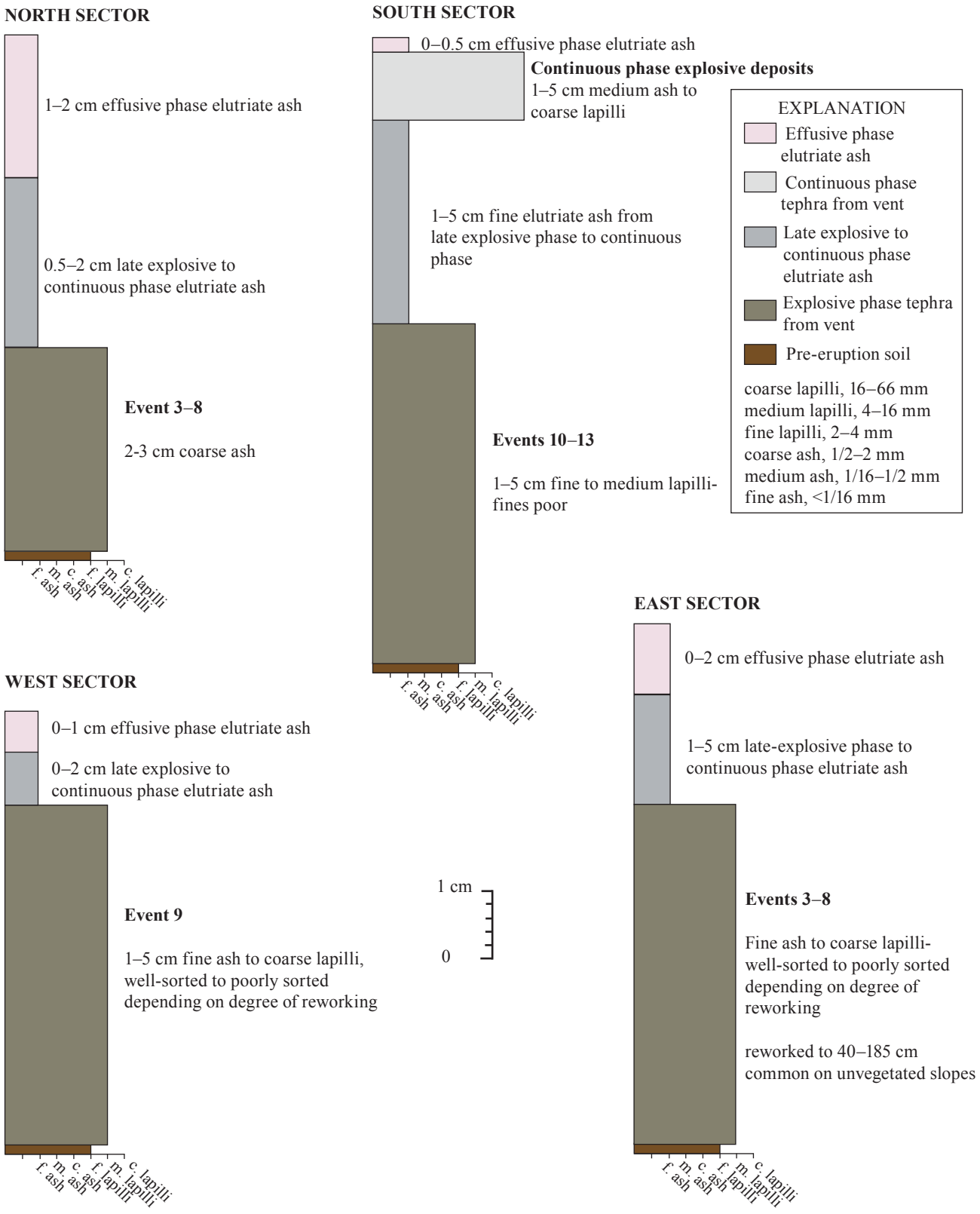


Figure 4. Generalized stratigraphic sections by volcano sectors, showing relations between and characteristics of proximal tephra-fall deposits from the explosive, continuous, and effusive phases of the 2005–6 eruption. Sections are derived from best preserved deposits in vegetated areas on the mid to lower slopes of the island.

Distribution, Character, and Origin of Tephra Deposits

In the following section, we describe in chronological order the tephra-fall deposits that formed during the four discrete phases of the 2005–6 eruption. For each phase, we describe the main eruptive phenomena, describe the resulting tephra deposits, and discuss the origin of tephra generated.

Precursory Phase Tephra Deposits (December 2005)

Distribution and Character of Precursory Phase Tephra

Following more than 7 months of increasing volcanic unrest in the form of seismicity and edifice inflation (Cervelli and others, this volume), several seismic signals suggested a series of small volcanic explosions at Augustine in mid-December. The three largest occurred on December 10, 12, and 15 (Power and others, 2006; Power and Lalla, this volume). Visual observations, radar, and satellite imagery failed to detect the ash plumes from these explosions because they were small or contained very little ash. Nonetheless, we were able to document resulting deposits during observation overflights and landings on the island within days of their occurrence.

A discontinuous, dark-colored dusting of fine to medium ash was observed on the island on December 12. This minor tephra-fall deposit was restricted to the southern sector of Augustine Island and nearby Cook Inlet. A sample collected on December 20 comprises both altered and fresh-looking, possibly juvenile, glass shards (fig. 3, sample TP001). The bulk of the deposit is fragments of altered rock and crystal fragments that are likely reworked older volcanic material.

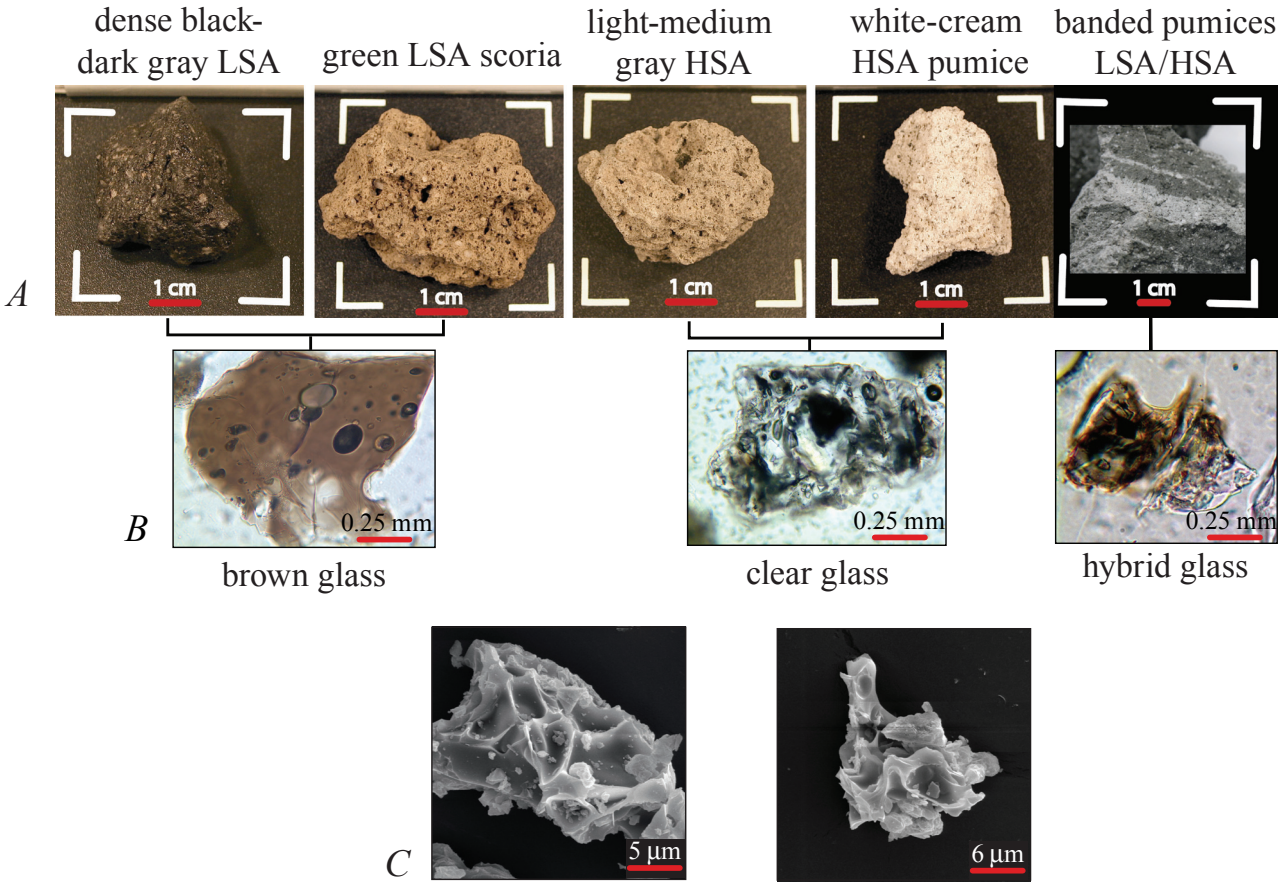


Figure 5. Photographs, photomicrographs, and SEM image of Augustine tephra. *A*, Photographs illustrating clast types erupted during the explosive phase, January 11–28, 2006. LSA, low silica andesite; HSA, high silica andesite. *B*, Transmitted-light photomicrographs illustrating glass phases, including brown, clear, and hybrid varieties. Typically, clear glass is associated with HSA magma and brown glass is associated with LSA magma, although most clasts contain a mixture of both magma compositions. *C*, Scanning electron microscope (SEM) image of vesicular ash particles erupted by Augustine Volcano on January 13, 2006. SEM photographs courtesy of Pavel Izbekov, University of Alaska Fairbanks.

Unaltered glass shards and pumice composed of both clear and brown glass show a range of SiO_2 between 73 and 77.5 wt. percent (table 2 and fig. 7). Reworking by high winds, deposition on snow cover and subsequent burial by younger tephra-fall deposits have now obliterated this deposit as a distinct entity from the geologic record.

Origin of Precursory Phase Tephra

Plumes that are not radar-reflective, the very small volume of deposits, and a lack of clear evidence of juvenile material, coupled with the presence of altered and clearly older lithic fragments, lead us to interpret these tephra deposits as being the result of phreatic explosions. Further evidence, such as impulsive, shallow seismicity suggestive of hydrothermal activity and a marked increase in gas and steam emissions above background levels at the volcano support this interpretation (Power and Lalla, this volume; Buurman and West, this volume; McGee and others, this volume).

Explosive Phase Tephra Deposits (January 11–28, 2006)

Distribution and Character of Explosive Phase Tephra

From January 11–28, a total of 13 discrete explosions sent ash plumes between 4 and 14 km asl and produced tephra fall downwind along several azimuths from the volcano (table 1, fig. 1). Strong seismicity associated with these events lasted 1–11 minutes (averaging 4 minutes; Power and Lalla, this volume) and closely matched the duration of plume generation. Plumes quickly detached from the vent and were distributed downwind (Bailey and others, this volume). The discrete and brief character of these explosions allowed us to discriminate individual ash clouds and to track their distribution using Nexrad radar (Schneider and others, 2006), satellite-image analysis (Bailey and others, this volume), and eyewitness reports. On January 11, 13, and 14, several plumes were generated within hours of one another (table 1) and subsequently coalesced. In such cases, individual ash clouds are poorly differentiated (Bailey and others, this volume). Minor amounts of tephra (1–3 mm) commonly fell between 25 and 185 km downwind from the volcano, and trace amounts (<0.5 mm) of fine ash were reported on one occasion as far as Castella, California, nearly 3,000 km southeast of Augustine.



Figure 6. Photograph showing measured-area sampling of an Augustine ash deposit (from January 17, 2006) preserved in the snow pack west of the volcano near Lake Iliamna. Photo by Christina Neal, March 10, 2006.

January 11, 2006 (Explosive Events 1 and 2)

Two explosions within 30 minutes, events 1 and 2, generated ash plumes to maximum heights of 6.5 and 10.2 km asl, respectively (Schneider and others, 2006). Radar data and satellite images show that the first of the two plumes traveled northwest, and ash fall was reported from villages surrounding Lake Iliamna, 25–80 km west and northwest of Augustine (fig. 1). Satellite images showed that the second ash plume traveled northeast over Cook Inlet, and no deposits were preserved.

On January 12, a field crew visited Augustine Island, and oblique aerial photographs taken that day show a dark-colored, distinct tephra deposit on the south flank and a less obvious dusting of ash on the snow-covered west and north flanks. Low-level ash emissions observed that day probably formed the dark spokelike fall deposit on the south, but we infer the ash on the west and north to have formed during events 1 and 2 (fig. 3). Observations suggested that the preexisting dome complex was partially destroyed during this explosion (Coombs and others, this volume). No tephra-deposit thicknesses were recorded. Samples collected from the west and north flanks of the volcano consist of coarse ash to lapilli with coatings of fine ash (table 3 and fig. 3, samples MC001 and MC002). The coarse fraction includes mainly gray, angular-to-subrounded, dense glassy-to-crystalline fragments and free crystal fragments. Orange, yellow, and red altered clasts of dense lava fragments are common. Vesicular particles are rare. We cannot determine whether the fresh-looking dense fragments are juvenile or recycled tephra or lava from previous eruptions.

A distal tephra-fall deposit, presumably from event 1, was sampled on March 10, 2006, 30 km northwest of Augustine. The deposit was dark colored and present as either a discrete 1–3 mm thick layer or distributed over a depth of 5 mm in the snow pack and underlying a fall deposit from event 9 (January 17) in this region (fig. 8). The event 1 deposit ranges from fine to coarse ash and contains a mixture of old-looking crystallized particles and fresh-looking unaltered clear, brown, and

Table 1. Summary of significant tephra-producing events of the 2005–2006 eruption of Augustine Volcano.

[Duration of seismic signal at station OPT is used as a proxy for duration of plume generation (Power and Lalla, this volume). Plume heights determined from Nexrad radar (data from poster of D.J. Schneider and others, 2006) and have error of ± 1.5 km (D.J. Schneider, oral commun., 2006); plume heights from pilot reports (PIREPs) are from the National Weather Service or Federal Aviation Administration. Plume direction based on satellite data (Bailey and others, this volume), National Oceanic and Atmospheric Administration HYSPLIT model forward trajectories, GDAS meteorological data, and eyewitness accounts. Maximum distance of tephra fall was from confirmed eyewitness reports or from Moderate Resolution Imaging Spectroradiometer (MODIS) satellite imagery. Observation of event: PIREP, pilot report; ph, overflight and fieldwork photograph; st, satellite images; web, web camera; tl, time-lapse camera; dep, photographs of deposits. Origin of tephra plume: vp, ash plume originating from vent; pf, ash cloud from elutriation of pyroclastic flow; rf, ash cloud from a rockfall event. Date of observation overflight for ease of identifying images in the Alaska Volcano Observatory image database (*http://www.avo.alaska.edu/images/*). nd, no data. All dates from 2006 unless noted.]

Event date, AKST (UTC)	Event no.	Event time, AKST	Seismic duration at OPT, min:sec	Plume height, in km asl	Plume height source	Plume direction	Maximum distance, in km	Observation of event	Origin of plume	Eye-witness account	Date of observation flight
					Precursory Phase						
12/15/05	nd	nd	nd	nd	nd	nd	nd	dep	vp	F	12/20/05
					Explosive phase						
1/11	1	4:44:00	01:18	6.5	radar	N, NE, NW	80	dep, st	vp	T	1/11, 1/12
1/11	2	5:12:00	03:18	10.2	radar	N, NW	80	dep, st	vp	T	1/11, 1/12
1/13	3	4:24:00	11:00	10.2	radar	E-SE	120	ph, st, dep	vp	T	1/16
1/13	4	8:47:00	04:17	10.2	Radar	E-SE	120	ph, st, dep, PIREP, web, tl	vp	T	1/16
				14-15	PIREP						
				16.0	PIREP						
1/13	5	11:22:00	03:24	10.5	radar	SE	120	ph, st, dep, PIREP, web, tl	vp	T	1/16
				16.0	PIREP						
1/13 *(01/14)*	6	16:40:00	04:00	10.5	radar	SE	120	ph, st, dep, PIREP, web, tl	vp	T	1/16
				9-11	PIREP						
1/13 *(01/14)*	7	18:58:00	03:00	13.5	radar	E SE	120	ph, st, dep	vp	T	1/16
1/14	8	0:14:00	03:00	10.2	radar	E SE	120	ph, st, dep	vp		1/16
1/17	9	7:58:00	04:11	13.5	Radar, PIREP	NW	140	ph, st, dep, PIREP	vp	T	1/18, 1/24
1/27 *(01/28)*	10	20:24:00	09:00	10.5	radar	SE	185	dep, st	vp	T	1/29, 1/30
1/27	11	23:37:21	01:02	3.8	radar	S SE	185	dep, st	vp	T	1/29, 1/30
1/28	12	2:04:13	02:06	7.2	radar	S SE	185	dep, st	vp	T	1/29, 1/30

1/28	13	7:42:00	03:00	7.2	radar	S SE	185	ph, st, dep, PIREP, web	vp	T	1/29, 1/30
Continuous phase											
1/28	14	14:31:00	nd	3.8	radar		185	ph, st, dep, PIREP, web	vp, pf	T	1/29, 1/30
				8.0	PIREP						
				9.0	PIREP						
1/29	nd	11:17:00	05:30	7.2	radar	S SW	185	ph, st, dep, PIREP, tl	vp, pf	T	1/29, 1/30
				9.0	PIREP						
				15.0	PIREPs						
1/30	nd	3:25:00	02:04	7.2	radar	NE	160	ph, st, dep, PIREP	vp, pf	T	1/30, 2/3, 2/8
				4.0	radar						
1/30	nd	6:21:00	nd	7.2	radar	E NE	160	ph, st, dep	vp, pf		1/30, 2/3, 2/8
2/8/07			nd	nd	nd	N - local	nd	ph, web	pf	F	2/8
Effusive phase											
3/4, 3/6, 3/7, 3/9, 3/10	nd	nd	nd	nd	nd	nd	85	ph, dep, web	rf, pf	T	3/6, 3/9, 3/10, 3/15

Table 2. Summary of groundmass glass average compositions for 2005–6 tephra from Augustine Volcano.

[All glass compositions determined using a Cameca SX-50 electron microprobe equipped with four wavelength-dispersive spectrometers and one energy-dispersive spectrometer at the University of Alaska Advanced Instrumentation Laboratory, Fairbanks, Alaska. Glasses analyzed using 15KeV, 10nA, and 10 micron-wide defocused beam. Oxide values given in weight percent and normalized to 100 percent anhydrous. Stdev, standard deviation; n, number of shards analyzed; GS, glass shard; MG, matrix glass from lapilli clast.]

Sample No.	SiO_2	TiO_2	Al_2O_3	FeO	MgO	CaO	Na_2O	K_2O	MnO	Cl	Total	Sample type
Precursory phase—December 2005												
clear glass-sample AT-703A.												GS
mean	76.96	0.26	13.30	1.46	0.28	2.07	3.85	1.71	nd	0.12	98.09	
stdev	0.62	0.33	0.90	0.76	0.22	0.68	1.23	0.85	nd	0.16		
n	7											
brown glass-sample AT-703B.												GS
mean	73.93	1.10	13.13	2.06	0.49	2.18	4.00	2.81	nd	0.27	97.69	
stdev	0.98	0.83	0.53	0.50	0.40	0.60	1.08	1.78	nd	0.09		
n	4											
Explosive phase—January 11, 2006, explosive events 1–2												
brown glass-samples AT-746, AT-769, AT-753, and AT-761.												GS
mean	65.56	0.96	16.44	4.22	1.68	4.78	4.68	1.54	nd	0.13	98.71	
stdev	0.89	0.32	0.48	0.52	0.61	0.70	0.33	0.23	nd	0.10		
n	5											
clear glass-samples AT-746, AT-769, and AT-761.												GS
Mean	77.09	0.23	12.38	1.57	0.22	1.84	4.51	2.01	nd	0.13	99.51	
stdev	0.88	0.17	0.38	0.37	0.10	0.67	0.32	1.18	nd	0.11		
n	9											
Explosive phase—January 13–14, 2006, explosive events 3–8												
dense low-silica andesite (DLSA)-samples AT-957B, AT-920A, and AT-967D.												MG
mean	68.16	0.84	15.27	3.55	0.80	4.10	5.01	2.00	0.05	0.23	99.81	
stdev	1.48	0.23	0.79	0.66	0.24	0.44	0.25	0.14	0.05	0.09		
n	11											
low-silica andesite scoria (LSAS)-samples AT-960A, AT920B, and AT-967A.												MG
mean	66.56	1.17	14.50	4.93	1.58	4.39	4.67	1.68	0.13	0.40	98.48	
stdev	1.02	0.16	0.57	1.04	0.27	0.36	0.39	0.10	0.05	0.13		
n	5											
high-silica andesite pumice (HSA)-sample AT-912D.												MG
mean	75.00	0.25	12.51	2.25	0.45	2.10	4.93	2.08	0.09	0.34	98.59	
stdev	0.53	0.13	0.45	0.71	0.04	0.11	0.32	0.06	0.03	0.13		
n	7											
Explosive phase —January 17, 2006, explosive event 9												
low-silica andesite scoria (LSAS)-samples AT-924A, AT-934A, AT905B, AT-943A, AT-949A.												MG
Mean	66.99	0.98	14.74	4.51	1.38	4.19	4.89	1.83	0.13	0.35	98.12	
stdev	1.59	0.20	1.10	0.63	0.22	1.13	0.39	0.49	0.10	0.12		
n	8											

Table 2. Summary of groundmass glass average compositions for 2005–2006 tephra from Augustine Volcano.—Continued

[All glass compositions determined using a Cameca SX-50 electron microprobe equipped with four wavelength-dispersive spectrometers and one energy-dispersive spectrometer at the University of Alaska Advanced Instrumentation Laboratory, Fairbanks, Alaska. Glasses analyzed using 15KeV, 10nA, and 10 micron-wide defocused beam. Oxide values given in weight percent and normalized to 100 percent anhydrous. Stdev, standard deviation; n, number of shards analyzed; GS, glass shard; MG, matrix glass from lapilli clasts.]

Sample No.	SiO_2	TiO_2	Al_2O_3	FeO	MgO	CaO	Na_2O	K_2O	MnO	Cl	Total	Sample type
Explosive phase—January 17, 2006, explosive event 9												
dense low-silica andesite (DLSA)-samples AT-940B , AT-923A, and AT-961B.												MG
mean	66.36	0.92	15.45	4.78	1.05	4.90	4.65	1.55	0.18	0.16	100.15	
stdev	1.21	0.16	1.01	0.71	0.23	0.55	0.24	0.20	0.09	0.06		
n	5											
high-silica andesite pumice (HSA)-samples AT-934B, AT-925C, AT-924C, and AT-961C.												MG
mean	74.42	0.47	12.34	2.36	0.41	2.10	5.23	2.25	0.07	0.34	100.38	
stdev	0.69	0.17	0.93	0.70	0.12	0.14	0.38	0.30	0.07	0.21		
n	6											
clear glass-samples AT-757, AT-759, AT-751, AT-744, AT-748, AT-767, AT-764, and AT-762.												GS
mean	76.25	0.47	12.36	1.89	0.33	1.45	4.03	3.07	nd	0.15	99.71	
stdev	0.91	0.38	0.71	0.34	0.20	0.75	0.62	1.48	nd	0.12		
n	13											
brown glass-samples AT-757, AT-759, AT-751, AT-744, AT-748, AT-767, and AT-762.												GS
mean	71.72	0.57	15.36	1.93	0.34	3.13	4.78	2.03	nd	0.15	99.12	
stdev	0.80	0.70	1.67	0.84	0.23	0.82	0.34	0.50	nd	0.15		
n	13											
Explosive phase —January 27–28, 2006, explosive events 10–13												
dense low-silica andesite (DLSA)-samples AT-932A, and AT-917A.												MG
mean	68.88	1.01	14.34	3.58	0.83	4.09	5.10	1.83	0.10	0.24	98.96	
stdev	4.00	0.66	0.81	2.61	0.89	0.58	0.06	0.18	0.14	0.17		
n	2											
high-silica andesite pumice (HSA)-sample AT-928A.												MG
mean	76.10	0.30	12.61	0.98	0.15	2.06	5.12	2.41	0.14	0.13	99.14	
stdev	0.20	0.02	0.66	0.42	0.01	0.09	0.35	0.19	0.10	0.11		
n	2											
clear glass-samples AT-733, AT-719, and AT-916.												GS
mean	75.30	0.26	13.29	1.11	0.31	1.93	4.98	2.61	0.06	0.18	100.04	
stdev	0.52	0.30	0.96	0.62	0.11	0.37	0.15	0.70	0.08	0.17		
n	3											
brown glass-sample AT-733.												GS
mean	69.28	0.60	15.88	2.79	0.85	4.09	4.52	1.72	0.03	0.24	98.80	
n	1											
Continuous phase—January 28–February 10												
clear glass-samples AT-770, AT-913, AT-909, and AT-953.												
Mean	76.04	0.50	12.52	1.63	0.32	1.76	4.60	2.35	0.12	0.21	99.68	GS

Table 2. Summary of groundmass glass average compositions for 2005–2006 tephra from Augustine Volcano.—Continued

[All glass compositions determined using a Cameca SX-50 electron microprobe equipped with four wavelength-dispersive spectrometers and one energy-dispersive spectrometer at the University of Alaska Advanced Instrumentation Laboratory, Fairbanks, Alaska. Glasses analyzed using 15KeV, 10nA, and 10 micron-wide defocused beam. Oxide values given in weight percent and normalized to 100 percent anhydrous. Stdev, standard deviation; n, number of shards analyzed; GS, glass shard; MG, matrix glass from lapilli clasts.]

Sample No.	SiO_2	TiO_2	Al_2O_3	FeO	MgO	CaO	Na_2O	K_2O	MnO	Cl	Total	Sample type
Continuous phase—January 28–February 10												
clear glass-samples AT-770, AT-913, AT-909, and AT-953.												
stdev	0.82	0.29	0.43	0.32	0.11	0.34	0.33	0.29	0.08	0.06		
n	21											
brown glass-samples AT-770, AT-909, and AT-953.												
mean	67.74	0.39	17.02	2.46	0.92	5.02	4.38	1.83	0.14	0.14	98.34	GS
stdev	1.72	0.36	1.51	0.95	0.41	1.19	0.82	0.81	0.02	0.17		
n	5											
Effusive phase—March 3–16												
clear glass-samples AT-915 and AT-919.												GS
mean	74.67	0.38	12.62	2.08	0.40	2.10	5.19	2.16	0.12	0.30	100.75	
stdev	0.36	0.07	0.09	0.19	0.07	0.13	0.21	0.10	0.05	0.08		
n	4											
brown glass-samples AT-915 and AT-919.												GS
mean	65.26	0.66	15.87	4.01	1.57	5.17	5.35	1.55	0.26	0.32	100.19	
stdev	0.94	0.04	0.08	0.50	0.82	0.47	0.53	0.19	0.10	0.16		
n	3											

hybrid glassy particles. Glass compositions range between 65–67 and 76–78 wt. percent silica (SiO_2) for brown and clear glass, respectively (table 2 and fig. 7).

Because of reworking by high winds, deposition onto snow, and subsequent burial by younger tephra-fall deposits, we recognized no primary exposures on the island following the eruption. Distal deposits are also not likely to be preserved in the geologic record owing to their small volume, deposition onto snowpack, and reworking by surface runoff.

January 13–14, 2006 (Explosive Events 3–8)

On January 13 and 14, six discrete explosions (events 3–8) produced ash plumes that reached between 10 and 13.5 km asl and that dispersed to the east-southeast (Schneider and others, 2006; fig. 1).

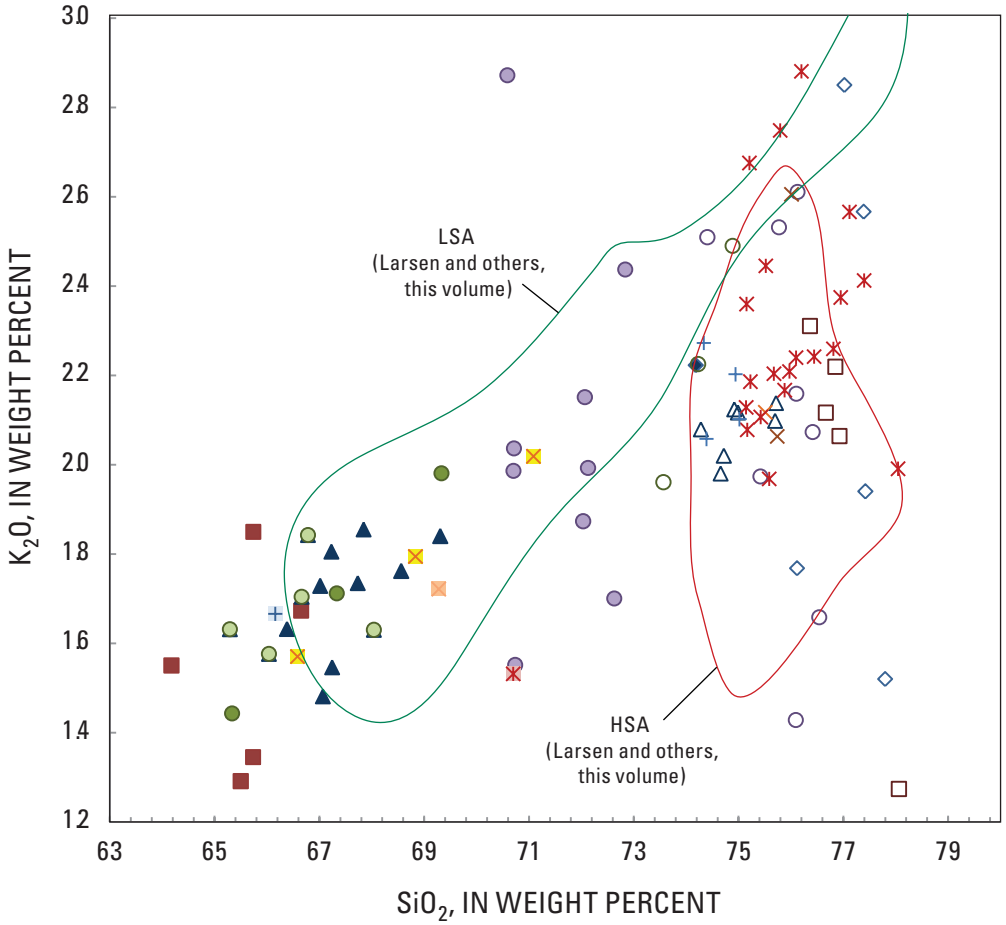
The Kenai Peninsula communities of Homer, Seldovia, Nanwelek, and Port Graham, 90–120 km downwind of Augustine, reported ash fall. In many cases ash fell with snow and snowflakes were particularly large and intricate, probably because of nucleation around ash particles (Adam Duran, oral commun., 2006). Ash from three or perhaps four of the six clouds fell entirely into Cook Inlet (events 5–7 and possibly event 3). In addition to ash fall on surrounding communities soon after these explosions, airborne ash clouds from the events took circuitous routes following high-level wind patterns. Back trajectories of the NOAA HYSPLIT wind-forecast model suggest that ash fell in northern California (January 16), communities on the southern Kenai Peninsula (January 17 and 19), Anchorage (January 19), and Palmer (January 31) because of recirculating plumes containing residual ash generated by explosive events of January 13–14.

We could not differentiate individual distal deposits from events 3–8 because they overlap and form a composite layer (table 1). The cumulative distal deposit was as much as 1 mm thick, gray-brown in color, and composed of fine to medium ash (table 3, fig. 9). Distal ash contains clear, brown, and hybrid glass shards.

Oblique aerial photographs of the island taken during a January 16 overflight show a continuous, distinctive dark-brown tephra deposit covering fresh snow on the north, east, and south flanks (fig. 3). In contrast, clean white snow on the west flank suggested little to no tephra deposition on that quadrant of the island. During August 2006, proximal ash-fall

deposits from these events were chiefly preserved on the volcano's north, northeast, east, and southeast flanks but were most voluminous on the eastern sector of Augustine Island.

Except in a few locations where primary stratigraphy is preserved (fig. 3, station KW026), we are unable to differentiate proximal deposits from the six discrete explosions. Total deposit thicknesses range from 5 to 185 cm. Thicker accumulations (on the eastern flank, fig. 10*B,* and fig. 3, stations KW034, KW078) are clearly wind and water reworked, and 5 cm is a representative thickness value for proximal, primary deposits (table 3; fig 3, station KW023; fig. 10*A*). Proximal tephra consists of light-gray, fine ash to medium lapilli (table 3). Light-gray, well-sorted, fine-ash deposits were documented on the north flank, in addition to coarse-grained deposits. Together, these deposits contain the first clear evidence of juvenile material since the start of the eruption. Such evidence includes abundant fresh-looking, angular clasts, vesicular ash and lapilli, and unaltered glass



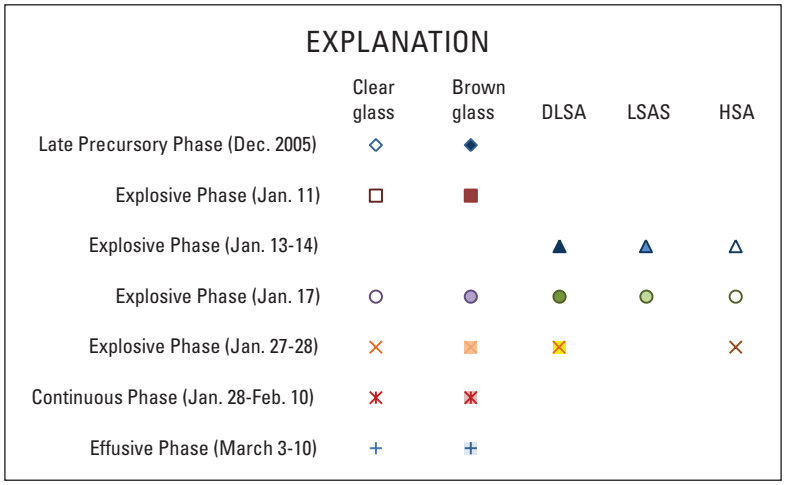


Figure 7. Plot of weight percent SiO_2 versus K_2O from microprobe analysis of groundmass (matrix) glass and glass shards for 2005–6 Augustine tephra-fall deposits. Data are separated by phase of eruption and by lithology. DLSA, dense low-silica andesite; LSAS, low-silica andesite scoria; HSA, high-silica andesite. Note that clear glass shards and HSA matrix glasses have more evolved and restricted compositions (74-78 wt. percent SiO_2), whereas brown glass shards and low-silica andesite matrix glasses have a wider range of compositions (64-74 wt. percent SiO_2). Low-silica andesite (LSA) and high-silica andesite (HSA) fields show matrix glass compositions of 2006 pyroclasts from Larsen and others (this volume).

Table 3. Summary of basic tephra-deposit characteristics for the 2005–6 eruption of Augustine Volcano.

[Maximum recorded thickness on Augustine Island (proximal thickness) was determined in July–August 2006, 6 months after the eruption ended. Maximum recorded thickness of tephra deposits on land surfaces off Augustine Island (distal thickness) was determined near the time of deposition. Bulk particle size for proximal tephra deposits uses volcanic terminology (Fisher, 1961; Schmid, 1981; Chough and Sohn, 1990): c, coarse; m, medium; f, fine. All distal deposits contain f. ash - m. ash. Componentry, in percent of clasts >5mm: HSA, high-silica andesite, gray–white pumices; DLSA, dense low-silica andesite, black–dark gray clasts; LSAS, low-silica andesite scoria; greenish-gray; banded clasts are typically pumiceous and contain gray and white/cream bands; LF, lithic fragments are nonjuvenile accidental clasts. n, number of clasts used to average componentry data; nd, no data. Componentry is from coarse-grained proximal deposits; no data from deposits with only fine-grained tephra.]

Eruption phase and date	Event no.	Max. proximal thickness, in cm	Max. distal thickness, in mm	Particle size range	HSA	DLSA	LSAS	Banded	LF	n
					Componentry					
Precursory Phase										
December 2005		0.2	0		nd	nd	nd	nd	nd	nd
Explosive Phase										
January 11, 2006	1–2	nd	3	f.ash–m. lapilli	nd	nd	nd	nd	nd	nd
January 13-14	3–8	180	1	f.ash–c. lapilli	26	22	41	2	9	475
January 17	9	1	3	f.ash–c. lapilli	35	32	20	2	11	977
January 27-28	10–13	5	1	f.ash–m. lapilli	52	18	8	8	14	215
Continuous Phase										
January 28-Feburary 10		5	1	f.ash–m. ash	60	13	6	13	8	195
Effusive Phase										
March 3-March 16		2	<1	f.ash	nd	nd	nd	nd	nd	nd

as determined by scanning electron microscopy (fig. 5). We identify four juvenile lithologies in the coarse-grained deposits (1) porphyritic, dense (black to dark gray), low-silica andesite (herein called dense low-silica andesite), (2) scoriaceous (greenish-gray), low-silica andesite (herein called low-silica andesite scoria), (3) porphyritic, pumiceous, high-silica andesite (light gray to white) (herein called high-silica andesite), and (4) banded clasts of varying textures and colors but predominantly pumiceous (fig. 5).

Componentry of undifferentiated fall deposits is 41 percent dense low-silica andesite, 22 percent low-silica andesite scoria, 26 percent high-silica andesite, 2 percent banded clasts, and 9 percent nonjuvenile lithic fragments (table 3). Glass compositions range from 66 to 69 wt. percent SiO_2 for low-silica andesite lapilli clasts and from 74 to 76 wt. percent SiO_2 for high-silica andesite (table 2 and fig. 7).

Deposits on exposed, nonvegetated slopes are most prone to reworking by wind and water (fig. 3, stations KW034, KW078, and fig. 10*B*). Deposits found in alder stands are largely unaffected by high winds and surface runoff, and outcrops of fine ash draped on branches were preserved some six months after deposition (fig. 3, station KW082, and fig. 10*C*). Figures 10*C*, *D* and *G* show only modest postdepositional modification resulting from slow melting of snow under and overlying the deposits. Distal tephra-fall deposits are not likely to be preserved in the geologic record, and certainly not as an identifiable discrete layer, because ash fall emplaced directly onto snow is remobilized during subsequent melting.

January 17, 2006 (Explosive Event 9)

Explosive event 9 on January 17 produced a plume as high as 13.5 km asl (Schneider and others, 2006) that dispersed to the west-northwest. Ash fall was first observed the same day by residents in villages surrounding Lake Iliamna, 50–120 km from Augustine (fig. 1). Observers described the deposit as a very thin dusting (<1 mm) of dark-colored ash. During field work in March 2006, the event 9 deposit formed a prominent and fairly continuous layer in the snowpack that ranged from a dark-colored discrete layer, 1–3 mm thick, to a disseminated layer over a depth of 0.5–3 cm within snow (fig. 8). Distal ash fall contains brown, fine to medium ash



with clear, brown, and hybrid glass shards. Glass compositions are in the range of 71–73 and 75–77 wt. percent SiO_2 for brown and clear glass, respectively (table 2, and fig. 7).

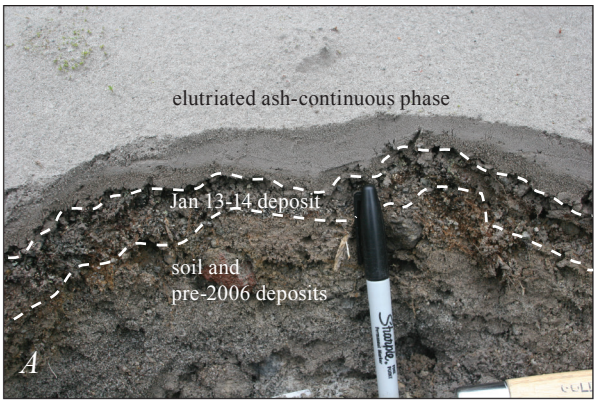
Proximal tephra deposits from event 9 crop out on the western sector of the island (figs. 3, 4). Oblique aerial photographs of the island during an overflight of the volcano on January 17 show a distinct dark brown deposit on the western flank and in the area within 3 km of the summit. A new lava dome, first identified during an overflight on January 16, was partially destroyed by the January 17 explosion, leaving a large crater in the new dome (Coombs and others, this volume). Observers on an overflight on January 18 identified

Figure 8. Photograph showing two distal ash layers preserved in the snow pack, 40 km west-northwest of Augustine. The lower layer is from event 1 on January 11, 2006. Event 1 tephra was deposited onto snow cover and subsequently buried by more snow. The deposit is 1–3 mm thick in this region and either discrete (shown here) or disseminated over a zone 5 mm thick. The upper layer is from event 9 on January 17, 2006, and is 1–3 mm thick in this region and either discrete (shown here) or disseminated over a zone 0.5–3 cm thick. Black cap on marker is 5 cm. Photo by Kristi Wallace, March 10, 2009.





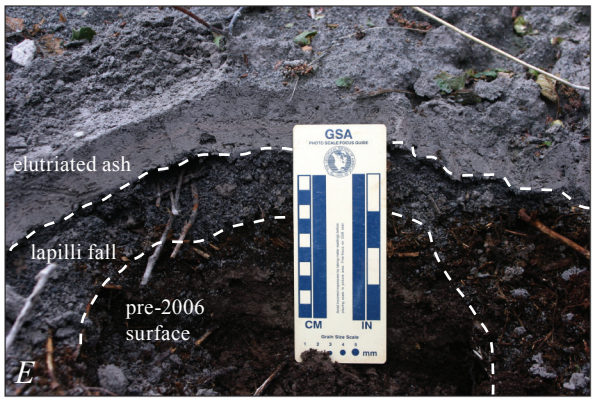
Figure 9. Photographs showing a dusting of ash on snow and a vehicle in Homer, Alaska on January 13, 2006. Photos courtesy of Michael Fairbanks.

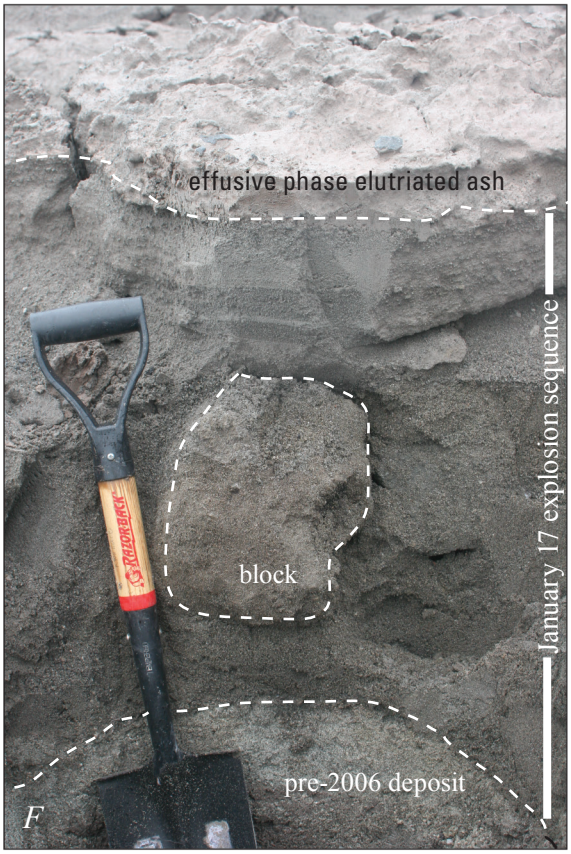

elutriated ash-continuous phase
Jan 13-14 deposit
soil and
pre-2006 deposits
A


B


C


D


elutriated ash
lapilli fall
pre-2006
surface
GSA
CM
IN
mm
E


effusive phase elutriated ash
block
pre-2006 deposit
January 17 explosion sequence
F


G

a ballistic field on the upper west flank, extending 760 m from the vent (fig. 3, station KW049, and fig. 11).

Proximal deposits observed in August 2006 range from 1 to 65 cm thick (4 and 1 km from the vent respectively) and include fine ash to coarse lapilli (fig. 3, stations KW082 and KW037, fig. 10*C*, *F*). Proximal deposits contain the same lithologies seen in deposits from events 3–8: (1) 32 percent dense low-silica andesite, (2) 20 percent low-silica andesite scoria, (3) 35 percent high-silica andesite, (4) 2 percent banded clasts, and (5) 11 percent nonjuvenile lithic fragments (table 3). Glass compositions range from 65 to 69 and from 74 to 75 wt. percent SiO_2 for low-silica andesite and high-silica andesite, respectively (table 2 and fig. 7).

The tephra deposit from this event is well preserved in alder stands low on the west flank of the island and in one primary, near-vent (1 km) deposit on a bench on the upper west flank (fig. 3, stations KW082 and KW037, fig. 10*C, F*). All other exposures on nonvegetated slopes are wind and water reworked.

January 27–28, 2006 (Explosive Events 10–13)

On January 27–28, four explosions produced ash plumes between 3 and 10.5 km asl (Schneider and others, 2006) and caused ash fall on Afognak and Kodiak Islands, as far as 185 km to the southeast and south-southwest of Augustine (fig. 1). Distal ash fall was reportedly minor, with less than 1 mm of accumulation on snow. Distal deposits contain brown, fine ash with clear, brown, and hybrid glass shards, and glass compositions range from 69 to 76 wt. percent SiO_2 (table 2 and fig. 7).

Direct observations of proximal tephra deposits from this time period were not possible immediately following their emplacement because of persistent airborne ash around the island during the continuous eruptive phase that began immediately after event 13. However, proximal deposits on the south flank are attributed to events 10–13, because those plumes were the only ones during the eruption that traveled in that direction. Proximal tephra deposits on the southern sector of the island are 1–5 cm thick and contain fine ash to medium lapilli (table 3; fig. 3, station KW032; fig. 4, and fig. 10*E*).

Componentry of these undifferentiated fall deposits is 18 percent dense low-silica andesite, 8 percent low-silica andesite scoria, 52 percent high-silica andesite, 8 percent banded clasts, and 14 percent lithic fragments (table 3). Glass compositions range from 66.5 to 72 wt. percent SiO_2 for low-silica andesite and from 76 to 77 wt. percent SiO_2 for high-silica andesite (table 2 and fig. 7). Proximal fall deposits on the north sector of the island are 1–5 cm thick, contain well-sorted, gray fine ash, and are considered to be elutriate from pyroclastic flows emplaced to the north on January 27 (fig. 3, station KW070, and fig. 4) (Coombs and others, this volume). Elutriate deposits from January 27–28 are indistinguishable from elutriate deposits from the continuous eruptive phase that immediately followed the emplacement of these deposits.

Origin of Explosive Phase Tephra

The explosive phase was characterized by discrete, short-duration (1–11 minutes) explosions that produced ash plumes with tops from 4 to 14 km asl (Schneider and others, 2006) and small-volume tephra deposits (table 1). Strong seismic (McNutt and others, this volume) and infrasonic (Peterson and others, 2006) signals accompanied individual explosions; the first explosive event was preceded by a series of volcano-tectonic earthquakes on January 10 and 11 (Buurman and West, this volume; Power and Lalla, this volume; Power and others, 2006). These observations suggest a Vulcanian-style eruption mechanism (Morressey and Mastin, 2000).

Despite the general similarity among the 13 events of the explosive phase, there are some important differences. Events 1 and 2 were relatively short (1:18 and 3:18 minutes) with impulsive seismic and infrasonic signals. Unlike later events, these generated only small-volume, mixed-rock-and-snow avalanches but no pyroclastic flows (Coombs and others,

Figure 10. Photographs showing the condition and preservation of proximal tephra-fall deposits on Augustine Island from the 2005–6 eruption. *A*, Primary tephra deposit on the east flank with coarse ash to fine lapilli base from January 13–14 explosions capped by fine gray ash from the elutriation of pyroclastic flows and rockfalls, black cap on marker is 5 cm (fig. 3, KW023). *B,* Thick accumulation of wind and water reworked tephra from the January 13–14 explosions on the east flank; shovel is 60 cm long (fig. 3, KW034). *C*, Tephra preserved in an alder stand on the west flank, showing only minimal reworking; the deposit remains draped on tree branches after melting out from snow cover. Silver and orange markings on trowel handle are 1.5 cm each (fig.3, KW082). *D*, Fall deposit on the south flank, attributed to explosive events 10–13. Coarse lapilli clasts projecting out of fine-ash deposit (white arrows) indicate that fine ash deposits are thinner than maximum lapilli axes. Black cap on marker is 5 cm (fig 3, KW084). *E*, Lithic lapilli fall of low-silica andesite deposit (January 27–28 explosions) on the south coast of Augustine capped by fine elutriated ash from the continuous and effusive phases (fig. 3, KW032). *F*, Near vent exposure of January 17 tephra-fall deposit on the upper west flank, including a ballistic block; shovel is 60 cm long (fig. 3, KW037). *G,* Typical exposure of a tephra deposit overlying leaf litter and a well-defined organic layer in alder stands on Augustine Island. Pre-2006 tephra deposits underlie the organic horizon (fig. 3, KW063). All photos by Kristi Wallace, August 7, 2006.

this volume). Plumes from events 1 and 2 appear to have contained low concentrations of ash and only deposited very thin, localized tephra. Proximal deposits from these events are dominated by dense and altered material. Distal tephra deposits do contain glass with intermediate to silicic glass compositions. Because of the similar compositions of matrix glasses between juvenile 2006 tephra and that from the 1976 and 1986 eruptions, however, it is impossible to know if the analyzed shards are new 2006 material or recycled from previous eruptions. On the basis of other lines of evidence, we think that the glass in the distal January 11 ash may be recycled. This was also the case for ash from the 2004–5 eruption of Mount St. Helens, where clean glass in distal ash was determined to have derived from nonjuvenile sources (Rowe and others, 2008). Because events 1 and 2 contained little or no juvenile material, they were likely caused when gases at the top of the ascending magma body reached the surface (Larsen and others, this volume). Interestingly, event 11 on January 27 had a similar seismic signal (McNutt and others, this volume), a low ash signal in radar (Schneider and others, 2006), and may have formed by a similar process, although its deposits were not uniquely identified.

Vulcanian explosions of January 13–14 (events 3–8) generated plumes 10–16 km asl and column-collapse pyroclastic flows that spread radially on all sides of the volcano, as well as secondary lahars and mixed snow and rock avalanches (Vallance and others, this volume). Tephras from these events are dominated by low-silica andesite (63 percent), with lesser amounts of high-silica andesite, lithics, and banded clasts (table 3). The succession of six discrete explosive plumes within less than 24 hours suggests rapid ascent of magma to the surface. Following event 8, a low-silica andesite lava lobe effused at the summit (Coombs and others, this volume; Larsen and others, this volume).

On January 17, after a 3-day pause in explosive activity, a Vulcanian explosion (event 9) produced one of the highest



Figure 11. Photograph illustrating ballistic field near the summit of Augustine, upper west flank (fig.3, KW049). Fine ash generated from pyroclastic flows and rockfalls during the effusive phase drape ballistic blocks on the surface. New dome steaming in the background. Note circled figure for scale. Photo by Kristi Wallace, August 2006.

plumes of the eruption sequence (table 1). Like tephra from the January 13–14 events, event 9 tephra was predominantly low-silica andesite (52 percent), but deposits have slightly higher proportions of high-silica andesite compared to January 13–14 events (table 3). Low-silica andesite lapilli closely resemble the low-silica andesite of the new lava lobe in texture and composition (Coombs and others this volume; Larsen and others, this volume). The new lava dome probably sealed the vent and allowed pressure to build until it ruptured, and explosive decompression of gas-rich magma generated a vigorous plume.

Vulcanian explosions of January 27 and 28 (events 10–14) occurred after a 10-day hiatus in explosive events. Between January 17 and 27, a new high-silica lava-dome lobe grew at the summit (Coombs and others, this volume; Larsen and others, this volume). In coarse-grained fall deposits from events 10–13, high-silica andesite lithologies predominate (52 percent) and closely match the composition of the January 17–27 dome. Subordinate low-silica andesite is more commonly dense and black to dark gray rather than scoriacious (table 3). In addition to vent explosions that resulted in relatively coarse fall deposits, fine elutriated ash from large pyroclastic flows of January 27 (Coombs and others, this volume) fell on the north flank of the volcano. These fine-ash deposits are indistinguishable from continuous phase deposits (see below) in terms of predominance of high-silica andesite shards.

The succession of magma compositions throughout the explosive phase from low-silica to high-silica andesite, as shown in tephra-deposit componentry, is also seen in componentry of pyroclastic-flow deposits (Vallance and others, this volume). Petrological studies (Larsen and others, this volume; Webster and others, this volume) suggest that mixing between an old shallow (4–6 km below the surface) high-silica andesite magma and a deep, young mafic end member (basalt) produced the low-silica andesite that was predominantly erupted during the early explosive phase (January 13, 14, and 17). The high-silica andesite that predominated in the late explosive phase (January 27 and 28) was likely remobilized by the injection of the mafic magma, allowing it to rise to the surface (Larsen and others, this volume).

Continuous Phase Tephra Deposits (January 28–February 10, 2006)

Distribution and Character of Continuous Phase Tephra

The continuous phase of the eruption lasted from January 28 through February 10 and was characterized by constant low-level ash emissions from the summit vent (plume heights <4 km asl), emplacement of pyroclastic flows on the north flank that generated clouds of elutriate ash, and discrete explosions generating ash plumes between 3 and 7 km asl (Schneider and others, 2006). Persistent north winds dispersed ash to the south-southeast over this 2-week time period and ash fall occurred in communities on Afognak and Kodiak Islands, as far as 185 km from Augustine, on February 1 and 3 (fig. 1). Proximal tephra deposits blanketed all sectors of the volcano, but predominated on its northern flank.

Photographs taken during observational overflights on January 29 and 30 show a continuous plume of ash and steam rising from the summit of the volcano (fig. 12). The plume was light colored, which suggests low concentrations of ash compared to plumes of the explosive phase. Discrete explosions during this phase have durations and plume heights similar to those produced during the explosive phase (table 1), and we infer by analogy that such plumes contained higher concentrations of ash than at other times during this phase. Photographs taken on January 30 and February 3 show tephra fallout from two sources. The first is a plume extending downwind from the vertical eruption column rising from the summit vent (labeled A in fig. 12). The second is a cloud of elutriated ash generated during emplacement of pyroclastic flows on the north flank of the volcano (labeled B in fig. 12) (Coombs and others, this volume). This second ash cloud was distinctly brownish pink compared to the light gray, ash-poor plume originating at the vent. Observations of fall deposits on the island during overflights were hindered by the lack of visibility owing to the haze of suspended fine ash surrounding the erupting volcano.

Distal ash reportedly fell as a mixture of ash and snow during a snowstorm. Distal tephra deposits were light gray and contained minor amounts of ash. Cumulative ash fall on Kodiak Island was less than 1 mm thick. Distal samples contain brown, clear, and hybrid glass. Glass compositions range from 75 to 77 wt. percent SiO_2 for clear glass and from 66 to 69.5 wt percent SiO_2 for brown glass (table 2 and fig. 7).

Proximal fall deposits were widely distributed over Augustine Island. Coarse-grained tephra (lapilli) deposits, presumably originating from discrete explosions or from the continuous plume generated at the vent, are located mainly in the southern sector of the island where they overlie elutriate deposits (fig. 3, stations KW030 and KW032; fig. 4). Coarse tephra deposits range from 1 to 5 cm in thickness and contain 60 percent high-silica andesite, 13 percent dense low-silica andesite, 6 percent low-silica andesite scoria, 13 percent banded clasts, and 8 percent lithic fragments (table 3). Light gray fine ash associated with pyroclastic flows was deposited on all sectors of the volcano but is thickest (as much as 2 cm) on the north and south flanks (figs. 4 and 12). Elutriated fine ash deposits grade upward to overlying effusive phase deposits, which can be distinguished by their pale pinkish-orange color (figs. 12 and 13).

Origin of Continuous Phase Tephra

Steady extrusion of a high-silica andesite dome, numerous column- and dome-collapse pyroclastic flows and rock falls (Coombs and others, this volume), continuous low-level ash emissions (<4 km asl), and occasional discrete vent explosions characterized the continuous phase (January 28–Feburary 10, 2006). Seismicity during this time is consistent with steady magma ascent and extrusion at the surface (Power

and Lalla, this volume). Discrete explosions produced plumes as high as 7.2 km asl and large pyroclastic flows (Coombs and others, this volume). Transient overpressures from sealing of the vent by high-silica andesite lava may have caused such bursts of energetic activity. High-silica andesite is the most common lithology in the fall deposits—consistent with explosive disruption of a high-silica andesite dome (table 2). Numerous continuous-phase pyroclastic flows generated low-level plumes of fine ash that drifted downwind and draped surroundings with fine-grained tephra deposits.

Continuous-phase fine-grained elutriated ash deposits contain a high proportion of clear glass shards, whose composition is consistent with the high-silica andesite dome and flows.

Effusive Phase Tephra Deposits (March 3–16, 2006)

Distribution and Character of Effusive Phase Tephra

On March 3, eruptive activity resumed after a brief hiatus (21 days) with the effusion of a low-silica andesite summit lava dome and lava flows that descended to the north and northeast, together with a coincidental increase in rock-fall activity (Coombs and others, this volume; Power and Lalla, this volume). Time-lapse photography and aerial observations revealed that elutriation of fine ash from rockfalls and small pyroclastic flows generated low-level ash clouds (<3 km asl). Fall deposits include localized fine ash on the north flank of

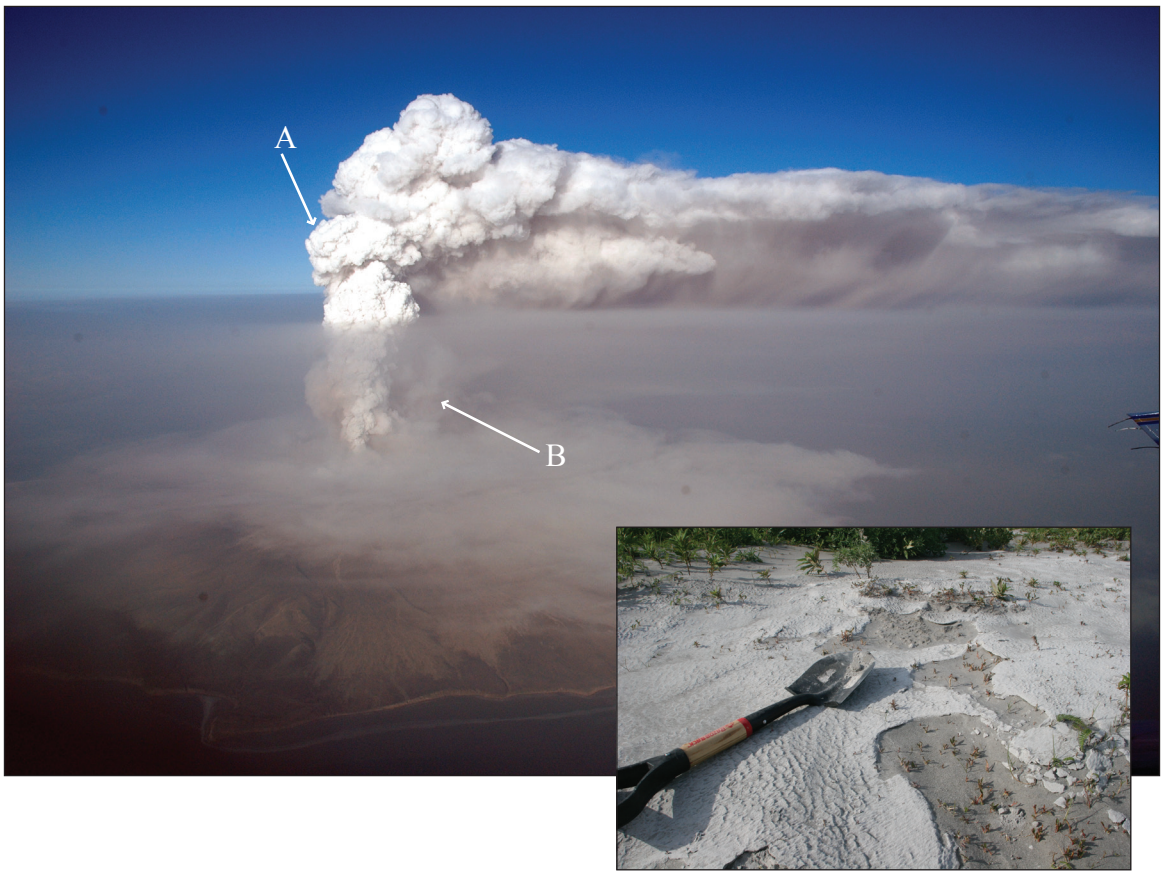


Figure 12. Photograph from an observation flight on January 30, 2006, showing tephra from two sources: *A*, a plume 10-15 km asl extending northeast from the vertical eruption column rising from the summit vent, and *B*, clouds of elutriated ash generated from newly emplaced pyroclastic flows on the north flank of the volcano. View from south. Photo by R.G. McGimsey. Inset photograph shows a typical exposure of a fine-ash deposit elutriated from pyroclastic flows on the north side of the island (fig.3-KW071). Shovel is 60 cm long. Photo by Kristi Wallace, August 6, 2006.

the volcano. Although radar or satellite imagery identified no significant ash clouds, on March 11 and 20, during a period of high easterly winds, minor ash fall was reported at the village of Pope Vanoy, near Lake Iliamna, 85 km west-northwest of Augustine (fig. 1).

Distal deposits were reportedly fine dustings of ash, clearly visible on fresh snow. A distal sample contains brown, clear (abundant), and hybrid glass shards. Glass compositions range from 68 to 78 wt. percent SiO_2 (appendix 2, sample AT-770). Proximal deposits are as much as 2 cm thick and contain fine, pinkish brown, well-sorted ash (fig. 13) with glass compositions ranging from 64 to 75 wt. percent SiO_2 (table 2 and fig. 7). Proximal tephra contains brown (abundant), clear, and hybrid glass shards. No explosions from the vent are thought to have occurred during this time.

Origin of Effusive Phase Tephra

Low-level plumes were generated from small pyroclastic flows and rock falls from the actively growing low-silica andesite lava dome and lava flows (Coombs and others, this volume; Power and Lalla, this volume). Tephra deposits are minor and were caused by the elutriation of fine ash from these small, gravitational collapses of the dome and from lava-flow fronts, either as minor rockfalls or block-and-ash flows. The pinkish brown color of elutriate ash deposits probably results from its more mafic composition (and higher proportion of brown glass shards) and possibly from oxidation. Clear, silicic glass shards, however, predominate in distal tephra deposits, which is inconsistent with the composition of the low-silica andesite dome being extruded during this time. Strong easterly winds reported during this interval likely remobilized unconsolidated fine material from the voluminous high-silica andesite pyroclastic-flow deposits on the north flank that were generated during the late explosive phase (Coombs and others, this volume) and carried it westward to the Iliamna area.

Mass of Select Tephra Deposits

Ideally, the total mass of tephra-fall deposits can be used to estimate the volume of magma that was explosively erupted and transported as ash clouds. Such data could not be obtained for all ash clouds generated during the Augustine 2005-6 eruption because of deposition (1) into Cook Inlet, (2) onto uninhabited and sparsely inhabited areas, and (3) of small volume, fine-grained ash onto seasonal snow pack and subsequent reworking. In addition, mixing of successive layers presented a problem for the six ash clouds generated on January 13 and 14, which fell onto land northeast of the volcano. Of the 13 tephras generated during the explosive phase, only that of January 17 was suitable for mass and volume calculation. Our estimates are based on 10 mass-per-unit-area measurements from this single deposit (figs. 14 and 15). On the basis of similarities in scale and assumed eruption mechanism to the other discrete ash clouds generated during the explosive phase, we use mass values from the January 17 deposit to extrapolate mass and volume values for the other events of the explosive phase (table 1 and 4). We do not estimate volumes of elutriated ash fall from pyroclastic flows.

The total mass for the January 17 tephra-fall deposit is estimated at 1.73×10^9 kg (fig. 14), with a bulk volume of 1.73×10^6 m^3 and a DRE volume of 6.65×10^5 m^3 (table 4). Total mass of tephra fall from the 13 discrete plumes generated during the explosive phase is calculated by multiplying the cumulative seismic duration by the mass eruption rate (calculated from the January 17 plume), which results in 2.2×10^{10} kg. Total bulk volume is 22×10^6 m^3 and total dense-rock equivalent (DRE) volume is 8.5×10^6 m^3 (table 4). These values are modest in comparison to tephra-fall volumes from previous historical eruptions of Augustine (Pyle, 2000; Venzke and others, 2002).

Significance and Hazards of Tephra-Fall Events

Although eruption parameters such as timing, magma composition, and total volume of erupted products for this eruption are much like those observed in past eruptions of Augustine, total vent explosion tephra-fall volume is about one order of magnitude smaller than estimates for the 1976 and 1986 eruptions (Pyle, 2000; Venzke and others, 2002). Historical eruptions of Augustine had a Volcanic Explosivity Index (VEI) of 4 (Venzke and others, 2002), but we assign the 2005–6 eruption a VEI of 3 on the basis of maximum plume height of 13.5 km (event 7 and 9). A VEI is typically weighted on both plume height and volume of tephra fall, but because of the overall lack of volume data for this eruption, we assign a VEI of 3 based on the explosion with the highest plume (L. Siebert, Smithsonian Institute, Global Volcanism Program, written commun., 2006). The 2005–6 eruption of Augustine produced about one order of magnitude less tephra fall than recent eruptions of Cook Inlet volcanoes Redoubt and Spurr (see, for example, Miller and others, 1998; Scott and McGimsey, 1994; McGimsey and others, 2001). Other volcanoes with similar Vulcanian-style eruption mechanisms, such as Unzen, Soufriere Hills, Vulcano, Ngauruhoe, Irazu, and Sakurajima, have tephra-fall volumes (individual events as well as cumulative over an eruptive episode) that are comparable within one order of magnitude (Bonnadonna and others, 2002; Herd and others, 2005; Venzke and others, 2002) to the 2005–6 eruption of Augustine.

Although the potential threat of ash fall was a significant concern during the eruption, the end result was that ash fall was not a significant problem in communities surrounding the volcano (fig. 1). Tephra fall was one of AVO's main concerns for surrounding communities, and the public

mirrored these concerns through consultation of AVO's Web site and public communications (Adleman and others, this volume). Satellite imagery, NOAA HYSPLIT wind-model data, and ash-plume and fall modeling aided AVO in tracking and projecting ash-plume movement and, furthermore, assisted us in briefing the public about the likelihood and nature of tephra fall throughout the eruption. The only reports of health effects from ash fall were as a minor eye irritant on two occasions (aircraft encounters on January 14) and as a nose irritant on one occasion (January 17, Iliamna). Air-quality samplers of fine particulate matter (PM) operated by the Municipality of Anchorage (MOA) and the Department of Environmental Conservation (DEC) detected elevated levels of PM_{10} and $PM_{2.5}$ (<10 and 2.5 microns, respectively) in Anchorage, Soldotna, and Homer during the eruption. Nevertheless, fine particulate levels never exceeded Environment Protection Agency (EPA) air quality standards (fig. 16). Particles 10 microns (that is, PM_{10}) in diameter and smaller can be inhaled into the respiratory tract, where they can cause harm (C. Cahill, oral commun., 2006). On January 13, ash accumulation as thick as 1 mm in Homer probably exceeded the amounts for all other days when instruments were deployed. The small volumes of individual ash-fall deposits make it unlikely that ash caused environmental impacts to water supplies, and no such impacts were reported.



Figure 13. Photograph from an observation flight on March 6, 2006, showing generation of an ash cloud from a small block-and-ash flow associated with dome collapse during the effusive phase. Photo courtesy of Guy Tytgat. Inset photograph (fig.3, KW049) shows, (A), a fine pinkish-brown ash deposit associated with the effusive phase, (B), a fine gray oxidized ash deposit associated with the continuous phase, and (C), a coarse proximal tephra-fall deposit associated with the continuous phase. Both A and B were generated from pyroclastic flows, while C was generated from a vent explosion. Photo from the upper northwest flank of the volcano. Trowel is 25 cm long. Photo by Kristi Wallace, August 2006.

Table 4. Summary of mass and volume data for explosive-phase plumes from Augustine Volcano, January 11–28, 2006.

[Events 1 and 2 contain little juvenile material, so mass and volume calculations likely represent pre-2006 ejecta. Duration of seismic signal at distal seismic station Oil Point (OPT) (fig. 1; Power and Lalla, this volume) used as a proxy for time of plume generation. Mass of tephra fall is based on mass eruption rate for event 9 on January 17, 2006: 6.9×10^6 kg/sec. Bulk volume in cubic meters (m^3) calculated using a density of 1,000 kg/m^3. Dense-rock-equivalent (DRE) volume in cubic meters calculated using a density of 2,600 kg/m3.]

Event date, in AKST (UTC)	Event no.	Seismic duration at OPT, in min:sec	Mass, in 10^9 kg	Bulk volume, in 10^6 m^3	Dense-rock-equivalent volume, in 10^6 m^3
1/11/06	1	01:18	0.5	0.5	0.2
1/11/06	2	03:18	1.4	1.4	0.5
1/13/06	3	11:00	4.6	4.6	1.8
1/13/06	4	04:17	1.8	1.8	0.7
1/13/06	5	03:24	1.4	1.4	0.5
1/13/06 (01/14/06)	6	04:00	1.7	1.7	0.6
1/13/06 (01/14/06)	7	03:00	1.2	1.2	0.5
1/14/06	8	03:00	1.2	1.2	0.5
1/17/06	9	04:11	1.7	1.7	0.7
1/27/06 (01/28/06)	10	09:00	3.7	3.7	1.4
1/27/06	11	01:02	0.4	0.4	0.2
1/28/06	12	02:06	0.9	0.9	0.3
1/28/06	13	03:00	1.2	1.2	0.5
Total			**21.7**	**21.7**	**8.4**

Conclusions

Tephra fall from the 2005–6 eruption of Augustine occurred during each of four eruption phases. Phreatic explosions during the late precursory phase produced little ash fall and posed no hazard to local communities. Initial eruption of low-silica andesite mixed with subordinate high-silica andesite magma initiated a series of 13 discrete Vulcanian explosions during the explosive phase, which generated plumes from 4 to14 km asl and distributed ash 25–185 km from the volcano in all directions. Minor ash fall of ≤1 mm resulted and posed little hazard to local communities. The hazard to aviation was mitigated by monitoring efforts of the AVO and NWS. During the late explosive phase and continuous phase, a dome of high-silica andesite composition was extruded. Subsequent collapses of the dome generated voluminous pyroclastic flows (Coombs and other, this volume), which generated ash clouds (<4 km asl) by elutriation. The resulting tephra deposits are localized to and distributed all over the island (fig. 4). Tracking ash during this phase was hindered by the continuous, long-duration emission of fine-grained low-volume ash clouds. A return to the eruption predominantly of low-silica andesite magma during the effusive phase (Coombs and others, this volume) resulted in the emplacement of a dome and lava flows. Local ash fall associated with small collapses of the lava dome and lava flows was of limited extent and posed no hazard to local communities. Fall deposits from the 2005–6 eruption are not likely to be well-preserved in the geologic record on or off island, because of their small volume, deposition into Cook Inlet, and reworking by wind and water. Total eruption volume (Coombs and other, this volume) is comparable with past eruptions of Augustine, yet tephra-fall volumes are about an order of magnitude smaller because flowage deposits (pyroclastic flows, lava flows/domes, block and ash flows) make up the bulk of erupted products (Coombs and others, this volume). Magma heterogeneity observed throughout the eruption (fig. 7) in both whole-rock and glass compositions, and overall similarity to recent eruptions, will present challenges for future tephrostratigraphers aiming to distinguish among these and other deposits from Augustine.

Acknowledgments

We would like to thank the many residents of communities surrounding Augustine for their keen observations and sampling efforts made during this eruption. Many thanks to AVO staff for their samples and excellent, well-documented photography throughout the eruption. We thank Evan Thoms for his help with GIS map preparation. We thank Manny Nathenson for his significant contributions and helpful discussion of our mass and volume calculations. We thank Barbara Stunder of the National Weather Service for providing the HYSPLIT model, forward trajectories, and GDAS Meteorological Data shown in figure 2. We thank Rick Farrish for safely transporting us all over Augustine Island during our field campaign. We appreciate the opportunity to do fieldwork in the Iliamna region and thank the Iliamna region native councils and the National Park Service for access to this land. Special thanks to Judy Fierstein, James Vallance, and Michelle Coombs for their careful reviews and suggestions for revisions to this manuscript, which we think have increased its value significantly.

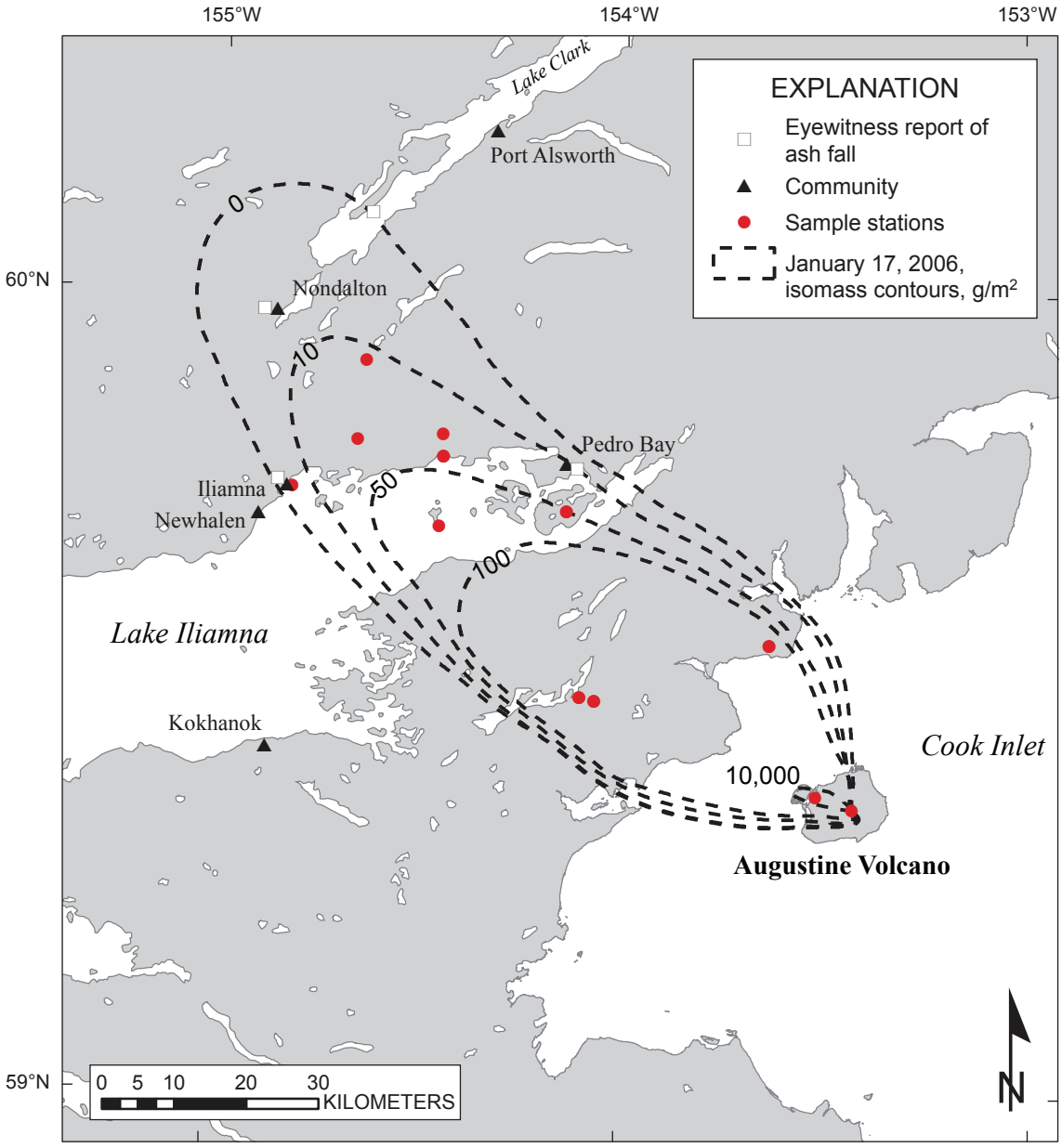


Figure 14. Isomass map of the tephra-fall deposit from Augustine on January 17, 2006. Contours represent lines of equal mass (g/m^2). Mass data were collected using measured-area sampling.

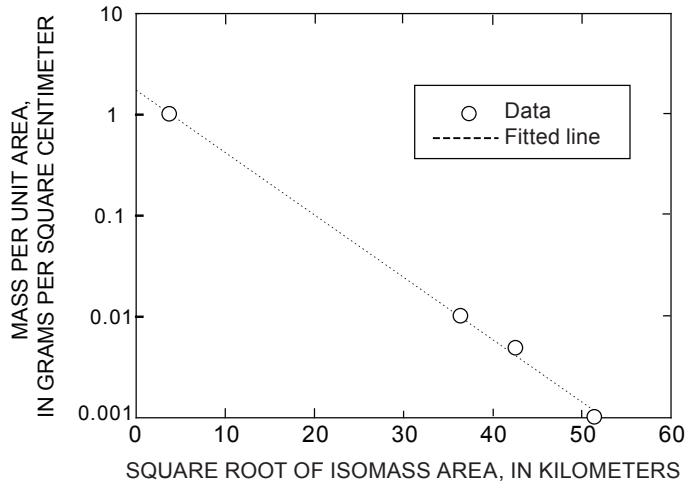


Figure 15. Plot showing mass per unit area (MPUA) versus the square root of isomass area for fall deposits from event 9 on January 17, 2006. The available data are well fitted by a single straight line for the calculation of total mass of the deposit. Tephra volume is calculated from the total mass of the deposit calculated using the root-area method (Pyle, 1989; Fierstein and Nathenson, 1992).

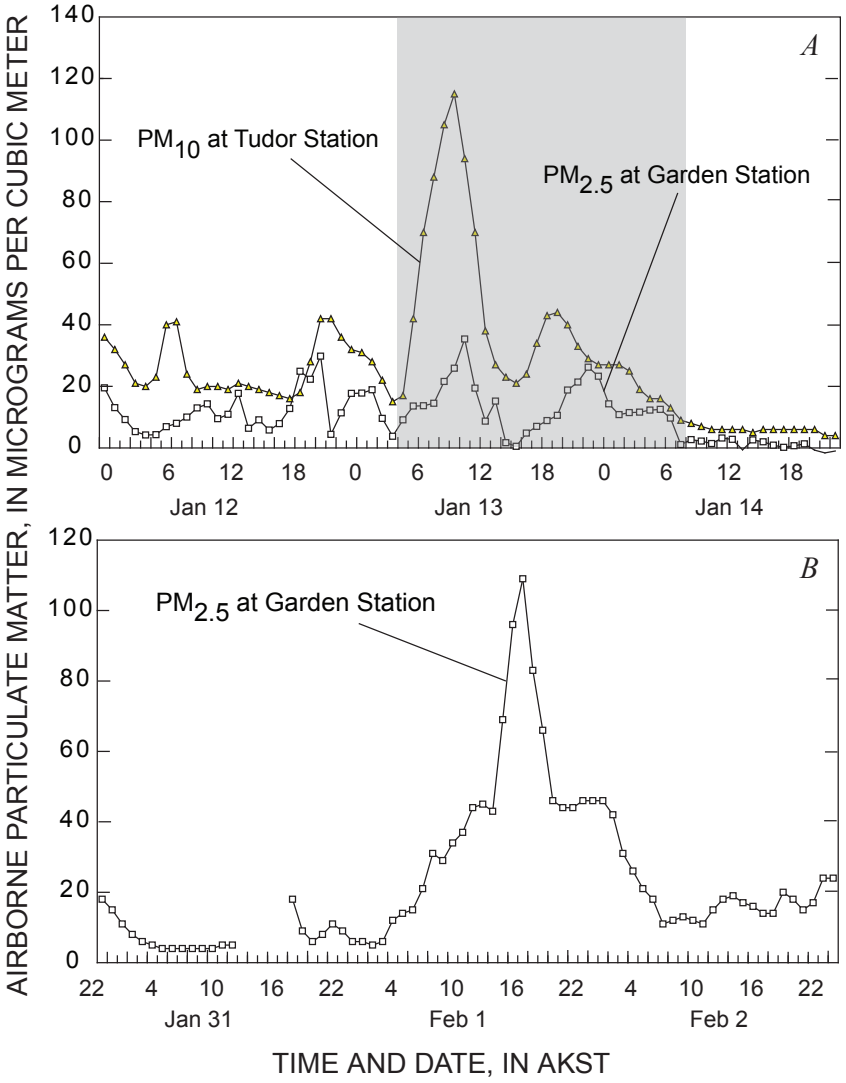


Figure 16. Plots showings airborne particulate matter (PM) in Anchorage, Alaska, on (*A*), January 12–14 and (*B*), January 31–February 2, 2006. Shaded area is the time frame when explosions occurred on January 13 and 14. PM levels however, did not exceed Environmental Protection Agency standards on these days. PM_{10}, aerodynamic diameter <10 microns; $PM_{2.5}$, aerodynamic diameter <2.5 microns. Tudor Station 3335 East Tudor Road; Garden Station, 3000 E 16th Street. Data provided by Steve Morris, Municipality of Anchorage, Environmental Services Division.

References Cited

Adleman, J.N., Cameron, C.E., Snedigar, S.F., Neal, C.A., and Wallace, K.L., 2010, Public outreach and communications of the Alaska Volcano Observatory during the 2005–2006 eruption of Augustine Volcano, *in* Power, J.A., Coombs, M.L., and Freymueller, J.T., eds., The 2006 eruption of Augustine Volcano, Alaska: U.S. Geological Survey Professional Paper 1769 (this volume).

Bailey, J.E., Dean, K.G., Dehn, J., and Webley, P.W., 2010, Integrated satellite observations of the 2006 eruption of Augustine Volcano, *in* Power, J.A., Coombs, M.L., and Freymueller, J.T., eds., The 2006 eruption of Augustine Volcano, Alaska: U.S. Geological Survey Professional Paper 1769 (this volume).

Bonnadonna, C., Mayberry, G., Calder, E.S., Sparks, R.S.J., Choux, C, Jackson, P., Lejeune, A., Loughlin, S., Norton, G, Rose, W., Ryan, G., and Young, S., 2002, Tephra fallout in the eruption of Soufriere Hills Volcano, Montserrat, *in* Druitt, T.H., and Kokelaar, B., eds., The eruption of Soufriere Hills Volcano, Montserrat, from 1995 to 1999: Geological Society of London Memoir, 21, p. 483–516.

Buurman, H., and West, M.E., 2010, Seismic precursors to volcanic explosions during the 2006 eruption of Augustine Volcano, *in* Power, J.A., Coombs, M.L., and Freymueller, J.T., eds., The 2006 eruption of Augustine Volcano, Alaska: U.S. Geological Survey Professional Paper 1769 (this volume).

Cahill, C.F., Cahill, T.A., Webley, P., Wallace, K.L., Dean, K.G., and Dehn, J., 2006, Size- and time-resolved composition of volcanic ash from Augustine Volcano, Alaska [abs.]: Eos (American Geophysical Union Transactions), v. 87, Fall meeting supp., abs. V22B-05.

Cervelli, P.F., Fournier, T.J., Freymueller, J.T., Power, J.A., Lisowski, M., and Pauk, B.A., 2010, Geodetic constraints on magma movement and withdrawal during the 2006 eruption of Augustine Volcano, *in* Power, J.A., Coombs, M.L., and Freymueller, J.T., eds., The 2006 eruption of Augustine Volcano, Alaska: U.S. Geological Survey Professional Paper 1769 (this volume).

Coombs, M.L., Bull, K.F., Vallance, J.W., Schneider, D.J., Thoms, E.E., Wessels, R.L., and McGimsey, R.G., 2010, Timing, distribution, and volume of proximal products of the 2006 eruption of Augustine Volcano, *in* Power, J.A., Coombs, M.L., and Freymueller, J.T., eds., The 2006 eruption of Augustine Volcano, Alaska: U.S. Geological Survey Professional Paper 1769 (this volume).

Chough, S.K., and Sohn, Y.K., 1990, Depositional mechanics and sequences of base surges, Songaskan tuff rings, Cheju Island, Korea: Sedimentology, v. 37, p. 1115–1135.

Daley, E.E., 1986, Petrology, geochemistry, and the evolution of lavas at Augustine Volcano, Alaska: Fairbanks, University of Alaska Fairbanks, MS thesis, 103 p.

de Fontaine, C.S., Kaufman, D.S., Anderson, R.S., Werner, A., Waythomas, C.F., and Brown, T.A., 2007, Late Quaternary distal tephra-fall deposits in lacustrine sediments, Kenai Peninsula, Alaska: Quaternary Research, v. 68, p. 64–78.

Fierstein, J., and Nathenson, M., 1992, Another look at calculation of fallout tephra volumes: Bulletin of Volcanology, v. 54, p. 156–167.

Fisher, R.V., 1961, Proposed classification of volcaniclastic sediments and rocks: Geological Society of America Bulletin, v. 72, p. 1409–1414.

Herd, R.A, Edmonds, M, and Bass, V.A., 2005, Catastrophic lava dome failure at Soufriere Hills Volcano, Montserrat, 12–13 July 2003: Journal of Volcanology and Geothermal Research, v. 148, p. 234–252.

Johnston, D.A., 1978, Volatiles, magma mixing and the mechanism of eruption of Augustine Volcano, Alaska: Seattle, University of Washington, Ph.D dissertation, 204 p.

Kienle, J., and Swanson, S. E., 1987, The 1986 activity of Mt. St. Augustine; volcanic hazards in the Cook Inlet Basin [abs.]: *in* Geologic Hazards Symposium, Alaska Geological Society Symposium Agenda and Abstracts, Anchorage, Alaska, May 12-15, 1987, unpaged.

Larsen, J.F., Nye, C.J., Coombs, M.L., Tilman, M., Izbekov, P., and Cameron, C., 2010, Petrology and geochemistry of the 2006 eruption of Augustine Volcano, *in* Power, J.A., Coombs, M.L., and Freymueller, J.T., eds., The 2006 eruption of Augustine Volcano, Alaska: U.S. Geological Survey Professional Paper 1769 (this volume).

McGee, K.A., Doukas, M.P., McGimsey, R.G., Neal, C.A., and Wessels, R.L., 2010, Emission of SO_2, CO_2, and H_2S from Augustine Volcano, 2002–2008, *in* Power, J.A., Coombs, M.L., and Freymueller, J.T., eds., The 2006 eruption of Augustine Volcano, Alaska: U.S. Geological Survey Professional Paper 1769 (this volume).

McGimsey, R.G., Neal, C.A., and Riley, C.M., 2001, Areal distribution, thickness, mass, volume, and grain size of tephra-fall deposits from the 1992 eruptions of Crater Peak Vent, Mt. Spurr volcano, Alaska: U.S. Geological Survey Open-File Report 01-0370, 38 p.

McNutt, S.R., Tytgat, G., Estes, S.A., and Stihler, S.D., 2010, A parametric study of the January 2006 explosive eruptions of Augustine Volcano using seismic, infrasound, and lightning data, *in* Power, J.A., Coombs, M.L., and Freymueller, J.T., eds., The 2006 eruption of Augustine Volcano, Alaska: U.S. Geological Survey Professional Paper 1769 (this volume).

Miller, T.P., McGimsey, R.G., Richter, D.H., Riehle, J.R., Nye, C.J., Yount, M.E., and Dumoulin, J.A., 1998, Catalog of the historically active volcanoes of Alaska: U.S. Geological Survey Open-File Report, 98-0582, 104 p.

Morrissey, M., and Mastin, L, 2000, Vulcanian eruptions, *in* Sigurdsson, H., Houghton, B.F., McNutt, S.R., Rymer, H., Stix, J., eds., Encyclopedia of volcanoes: Academic Press, p. 463–475.

Petersen, T., De Angelis, S., Tytgat, G., and McNutt, S., 2006, Local infrasound observations of the large ash explosions at Augustine Volcano, Alaska, during January 11–28, 2006: Geophysical Research Letters, v. 33, L12303, p. 1–5, doi: 10.1029/2006GL026491.

Power, J.A., Nye, C.J., Coombs, M.L., Wessels, R.L., Cervelli, P.F., Dehn, J., Wallace, K.L., Freymueller, J.T., and Doukas, M.P., 2006, The reawakening of Alaska's Augustine Volcano: Eos (American Geophysical Union Transactions), v. 87, no. 37, p. 373, 377.

Power, J.A., and Lalla, D.J., 2010, Seismic observations of Augustine Volcano, 1970–2007, *in* Power, J.A., Coombs, M.L., and Freymueller, J.T., eds., The 2006 eruption of Augustine Volcano, Alaska: U.S. Geological Survey Professional Paper 1769 (this volume).

Pyle, D.M., 1989, The thickness, volume, and grainsize of tephra-fall deposits: Bulletin of Volcanology, v. 51, p. 1–15.

Pyle, D.M., 2000, Sizes of volcanic eruptions, *in* Encyclopedia of volcanoes, Sigurdsson, H., Houghton, B.F., McNutt, S.R., Rymer, H., Stix, J., eds.: Academic Press, p. 263–269.

Riehle, J.R., 1985, A reconnaissance of the major Holocene tephra deposits in the upper Cook Inlet region, Alaska: Journal of Volcanology and Geothermal Research, v. 26, p. 37–74.

Roman, D.C., Cashman, K.V., Gardner, C.A., Wallace, P.J., and Donovan, J.J., 2005, Storage and interaction of compositionally heterogeneous magmas from the 1986 eruption of Augustine Volcano, Alaska: Bulletin of Volcanology, v. 68, p. 240–254, doi: 10.1007/s00445-005-0003-z.

Rowe, M.C., Thornber, C.R., and Kent, A.J.R., 2008, Identification and evolution of the juvenile component in 2004–2005 Mount St. Helens ash, *in* Sherrod, D.R., Scott, W.E., and Stauffer, P.H., eds. A volcano rekindled; The renewed eruption of Mount St. Helens, 2004–2006: U.S. Geological Survey Professional Paper 1750, p. 269–646.

Sarna-Wojcicki, A.M., Meyer, C.E., Woodward, M.J., and Lamothe, P.J., 1981, Composition of air-fall ash erupted on May 18, May 25, June 12, July 22, and August 7, *in* Lipman, P.W., and Mullineaux, D.R., eds., The 1980 eruptions of Mount St. Helens, Washington: U.S. Geological Survey Professional Paper 1250, p. 667.

Schmid, R. 1981, Descriptive nomenclature and classification of pyroclastic deposits and fragments; recommendations of the IUGS Subcommission on the Systematics of Igneous Rocks: Geology, v. 9, p. 41– 43.

Schiff, C.J., Kaufman, D.S., Wallace, K.L., Werner, A., Ku, T.L., 2008, Modeled tephra ages from lake sediments, base of Redoubt Volcano, Alaska: Quaternary Geochronology, v. 3, p. 56–67.

Schneider, D.J., Scott, C., Wood, J., and Hall, J., 2006, Nexrad weather radar observations of the 2006 Augustine volcanic eruption [abs.]: Eos (American Geophysical Union Transactions), v. 87, Fall meeting supp., abs. V51C-1686.

Scott, W.E., and McGimsey, R.G., 1994, Character, mass, distribution, and origin of tephra-fall deposits of the 1989–1990 eruption of Redoubt Volcano, south-central Alaska: Journal of Volcanology and Geothermal Research, v. 62, p. 251–272.

Vallance, J.W., Bull, K.F., and Coombs, M.L., 2010, Pyroclastic flows, lahars, and mixed avalanches generated during the 2006 eruption of Augustine Volcano, *in* Power, J.A., Coombs, M.L., and Freymueller, J.T., eds., The 2006 eruption of Augustine Volcano, Alaska: U.S. Geological Survey Professional Paper 1769 (this volume).

Venzke, E., Wunderman, R.W., McClelland, L., Simkin, T., Siebert, L., and Mayberry G., eds., 2002, Global Volcanism, 1968 to present: Smithsonian Institution, Global Volcanism Program Digital Information Series GVP-4 [http://www.volcano.si.edu/world/reports/, accessed on February 12, 2007].

Webley, P.W., Dean, K.G., Dehn, J., Bailey, J.E., and Peterson, R., 2010, Volcanic-ash dispersion modeling of the 2006 eruption of Augustine Volcano using the Puff model, *in* Power, J.A., Coombs, M.L., and Freymueller, J.T., eds., The 2006 eruption of Augustine Volcano, Alaska: U.S. Geological Survey Professional Paper 1769 (this volume).

Webster, J.D., Mandeville, C.W., Goldoff, B., Coombs, M.L., and Tappen, C., 2010, Augustine Volcano—The influence of volatile components in magmas erupted A.D. 2006 to 2,100 years before present, *in* Power, J.A., Coombs, M.L., and Freymueller, J.T., eds., The 2006 eruption of Augustine Volcano, Alaska: U.S. Geological Survey Professional Paper 1769 (this volume).

Appendix 1. Proximal Tephra Sample Station Locations on Augustine Island

Table 5. Proximal sample station locations on Augustine Island.

[All locations shown in datum WGS-1984; latitude and longitude are given in decimal degrees. The prefix "06AU" has been removed from all station names for brevity. PF, pyroclastic flow]

Station Name	Date Visited	Latitude	Longitude	Location Description
KLW020	7/31/2006	59.3857	-153.5154	NW Lagoon (south side west lands)
KLW021	7/31/2006	59.3872	-153.5156	NW Lagoon (south side west lands)
KLW022	7/31/2006	59.3867	-153.5190	NW Lagoon (south side west lands)
KLW023	8/1/2006	59.3683	-153.3670	1986 PF surface above Mound
KLW024	8/1/2006	59.3747	-153.3823	Northeast sector; south of seismic station AU14
KLW025	8/1/2006	59.3758	-153.3835	Feather edge of PF or lahar deposit
KLW026	8/1/2006	59.3718	-153.3929	Near ridge just below seismic station AU14
KLW027	8/1/2006	59.3469	-153.3810	Uphill of SE Point
KLW028	8/2/2006	59.3453	-153.4861	Reworked surge deposit in stressed alder
KLW029	8/2/2006	59.3382	-153.4591	Ridge south of Augustine Creek PF (tephra with abundant black dense juvenile clasts)
KLW030	8/2/2006	59.3367	-153.4565	Valley imediatly south of 06AUKW029
KLW031	8/2/2006	59.3358	-153.4173	Ridge south of AVO2/AV1
KLW032	8/2/2006	59.3244	-153.4147	South Point bluff
KLW033	8/2/2006	59.3484	-153.4797	Feather edge of SW PF finger (lower slopes);surges
KLW034	8/4/2006	59.3642	-153.3748	Near East Chute PF
KLW035	8/4/2006	59.3391	-153.3906	East Side
KLW036	8/4/2006	59.3999	-153.4494	Rocky Point PF
KLW037	8/4/2006	59.3628	-153.4446	Seismic station AUH
KLW038	8/4/2006	59.3284	-153.4006	SE coast near seal haul out (near South Point)
KLW039	8/5/2006	59.3786	-153.3475	NE Point Exactly
KLW040	8/5/2006	59.3569	-153.3420	East Point Bluff
KLW041	8/5/2006	59.3491	-153.3514	Between SE Point and S Point east of 2006 flowage deposits that enter the sea
KLW042	8/5/2006	59.3311	-153.4408	Between South Point and Augustine Creek PF
KLW043	8/5/2006	59.3221	-153.4947	Flats near West Lagoon
KLW044	8/5/2006	59.3471	-153.5305	West Lagoon
KLW045	8/5/2006	59.3835	-153.5509	West Island
KLW046	8/6/2006	59.3599	-153.4320	Summit-west
KLW047	8/6/2006	59.3596	-153.4285	Summit-east
KLW048	8/6/2006	59.3609	-153.4326	Summit-northwest side
KLW049	8/6/2006	59.3601	-153.4358	Ballistic field
KLW050	8/7/2006	59.3590	-153.4827	West side, upper alder stand
KLW051	8/7/2006	59.3594	-153.4840	West side transect
KLW052	8/7/2006	59.3600	-153.4856	West side transect
KLW053	8/7/2006	59.3608	-153.4865	West side transect
KLW054	8/7/2006	59.3615	-153.4869	West side transect
KLW055	8/7/2006	59.3616	-153.4869	West side transect
KLW056	8/7/2006	59.3618	-153.4870	West side transect
KLW057	8/7/2006	59.3702	-153.4879	West side transect

Table 5. Proximal sample station locations on Augustine Island.—Continued

[All locations shown in datum WGS-1984; latitude and longitude are given in decimal degrees. The prefix "06AU" has been removed from all station names for brevity. PF, pyroclastic flow]

Station Name	Date Visited	Latitude	Longitude	Location Description
KLW058	8/7/2006	59.3817	-153.4665	West side transect
KLW059	8/7/2006	59.3825	-153.4672	West side transect
KLW060	8/7/2006	59.3850	-153.4681	West side transect
KLW061	8/7/2006	59.3857	-153.4676	West side transect
KLW062	8/7/2006	59.3865	-153.4671	West side transect
KLW063	8/7/2006	59.3907	-153.4734	West side transect
KLW064	8/8/2006	59.3929	-153.4442	East side of ridge above Rocky Point PF
KLW065	8/8/2006	59.3935	-153.4449	West side of ridge above Rocky Point PF
KLW066	8/8/2006	59.3944	-153.4452	Ridge above Rocky Point PF, near surge
KLW067	8/8/2006	59.3955	-153.4457	Surge deposit western side of Rocky Point PF
KLW068	8/8/2006	59.3955	-153.4454	Surge deposit western side of Rocky Point PF
KLW069	8/8/2006	59.4040	-153.4467	Edge of Rocky Point PF, coastwise
KLW070	8/8/2006	59.4072	-153.4434	Just north of Rocky Point in hummocky topography
KLW071	8/8/2006	59.4081	-153.4438	Coastward of KW070 just north of Rocky Point
KLW072	8/8/2006	59.4077	-153.3949	Burr Point vicinity
KLW073	8/8/2006	59.4065	-153.3988	Burr Point vicinity
KLW074	8/8/2006	59.3858	-153.3818	North of NE Point where larger of 2006 lahars nears the coast
KLW075	8/9/2006	59.3405	-153.3991	East side near seismic station AUSE
KLW076	8/9/2006	59.3584	-153.3709	Upper Alder between East Point and SE Point, lahar visible to north
KLW077	8/9/2006	59.3584	-153.3719	Very near 06AUKW076
KLW078	8/9/2006	59.3642	-153.3751	East side; in high alder
KLW079	8/9/2006	59.3780	-153.4766	NW sector, west of Windy PF; in willow
KLW080	8/9/2006	59.3792	-159.4799	NW sector, west of Windy PF; in alder
KLW081	8/9/2006	59.3577	-153.5259	West sector, in low alder
KLW082	8/10/2006	59.3773	-153.5193	AVO field camp location
KW083	8/10/2006	59.3702	-153.3538	Benchmark Mound
KW084	9/25/2006	59.3254	-153.4667	SSW coast
KW085	9/25/2006	59.3248	-153.4667	SSW coastal bluff (prehistoric Augustine tephra fall)
TP001	12/20/2005	59.3486	-153.4216	Lower south flank
MC001	1/12/2006	59.3694	-153.4730	West flank of Augustine. Ash collection site AAW (seismic station AUW)
MC002	1/12/2006	59.4118	-153.4161	Burr Point. Ash collection site AAN

Appendix 2. Raw Electron Microprobe Geochemical Analyses of Glass from Augustine 2005–2006 Tephra

[This appendix appears only in the digital version of this work—in the DVD-ROM that accompanies the printed volume and as a separate file accompanying this chapter on the Web at: http://pubs.usgs.gov/pp/1769]

Table 6 is a Microsoft Excel file that contains the data used to derive table 2 and figure 7 after analyses were filtered to eliminate the inclusion of mineral data and other bad data points.

This page intentionally left blank

The 2006 Eruption of Augustine Volcano, Alaska
Power, J.A., Coombs, M.L., and Freymueller, J.T., editors
U.S. Geological Survey Professional Paper 1769

Chapter 10

Pyroclastic Flows, Lahars, and Mixed Avalanches Generated During the 2006 Eruption of Augustine Volcano

By James W. Vallance,[1] Katharine F. Bull,[2] and Michelle L. Coombs[3]

Abstract

Each of the three phases of the 2006 eruption at Augustine Volcano had a distinctive eruptive style and flowage deposits. From January 11 to 28, the explosive phase comprised short vulcanian eruptions that punctuated dome growth and produced volcanowide pyroclastic flows and more energetic hot currents whose mobility was influenced by efficient mixing with and vaporization of snow. Initially, hot flows moved across winter snowpack, eroding it to generate snow, water, and pyroclastic slurries that formed mixed avalanches and lahars, first eastward, then northward, and finally southward, but subsequent flows produced no lahars or mixed avalanches. During a large explosive event on January 27, disruption of a lava dome terminated the explosive phase and emplaced the largest pyroclastic flow of the 2006 eruption northward toward Rocky Point. From January 28 to February 10, activity during the continuous phase comprised rapid dome growth and frequent dome-collapse pyroclastic flows and a lava flow restricted to the north sector of the volcano. Then, after three weeks of inactivity, during the effusive phase of March 3 to 16, the volcano continued to extrude the lava flow, whose steep sides collapsed infrequently to produce block-and-ash flows.

The three eruptive phases were each unique not only in terms of eruptive style, but also in terms of the types and morphologies of deposits that were produced, and, in particular, of their lithologic components. Thus, during the explosive phase, low-silica andesite scoria predominated, and intermediate- and high-silica andesite were subordinate. During the continuous phase, the eruption shifted predominantly to high-silica andesite and, during the effusive phase, shifted again to dense low-silica andesite. Each rock type is present in the deposits of each eruptive phase and each flow type, and lithologic proportions are unique and consistent within the deposits that correspond to each eruptive phase.

The chief factors that influenced pyroclastic currents and the characteristics of their deposits were genesis, grain size, and flow surface. Column collapse from short-lived vulcanian blasts, dome collapses, and collapses of viscous lavas on steep slopes caused the pyroclastic currents documented in this study. Column-collapse flows during the explosive phase spread widely and probably were affected by vaporization of ingested snow where they overran snowpack. Such pyroclastic currents can erode substrates formed of snow or ice through a combination of mechanical and thermal processes at the bed, thus enhancing the spread of these flows across snowpack and generating mixed avalanches and lahars. Grain-size characteristics of these initial pyroclastic currents and overburden pressures at their bases favored thermal scour of snow and coeval fluidization. These flows scoured substrate snow and generated secondary slurry flows, whereas subsequent flows did not. Some secondary flows were wetter and more laharic than others. Where secondary flows were quite watery, recognizable mixed-avalanche deposits were small or insignificant, and lahars were predominant. Where such flows contained substantial amounts of snow, mixed-avalanche deposits blanketed medial reaches of valleys and formed extensive marginal terraces and axial islands in distal reaches. Flows that contained significant amounts of snow formed cogenetic mixed avalanches that slid across surfaces protected by snowpack, whereas water-rich axial lahars scoured channels.

Correlations of planimetric area (A) versus volume (V) for pyroclastic deposits with similar origins and characteristics exhibit linear trends, such that $A=cV^{2/3}$, where c is a constant for similar groups of flows. This relationship was tested and

[1]U.S. Geological Survey, Cascades Volcano Observatory, 1300 SE Cardinal Court, Vancouver, WA 98683.

[2]Alaska Volcano Observatory, Alaska Division of Geological and Geophysical Surveys, 3354 College Road, Fairbanks, AK 99709.

[3]Alaska Volcano Observatory, U.S. Geological Survey, 4200 University Drive, Anchorage, AK 99508.

calibrated for dome-collapse, column-collapse, and surgelike flows using area-volume data from this study and examples from Montserrat, Merapi, and Mount St. Helens. The ratio $A/V^{2/3} = c$ gives a dimensionless measure of mobility calibrated for each of these three types of flow. Surgelike flows are highly mobile, with $c \approx 520$; column-collapse flows have $c \approx 150$; and dome-collapse flows have $c \approx 35$, about that of simple rock avalanches. Such calibrated mobility factors have a potential use in volcano-hazard assessments.

Introduction

The 2006 eruption of Augustine Volcano spanned less than 4 months, yet the snowclad, unglaciated Alaskan island volcano erupted in a range of eruptive styles characterized by diverse deposit types, each with distinctive morphology, grain size, and lithologic composition. Within 3 months, three eruptive phases produced at least four lava domes and two lava flows, ranging in composition from low- to high-silica andesite (57.3–63.2 weight percent SiO_2; Larsen and others, this volume). During each eruptive phase, pyroclastic flows produced deposits with the same four predominant rock types; however, the flow deposits of each phase had distinctive morphology and proportions of lithologic components. Only the initial explosive phase generated lahars and mixed-rock-and-snow avalanches.

The morphology, lithologic composition, and areal extent of deposits were initially estimated during the eruption by utilizing onsite Web cameras, satellite imagery, aerial surveillance, and occasional field-based observations (Coombs and others, this volume). These early estimates provided important groundwork for later, field-based mapping, as well as for understanding the eruption chronology. Later field investigations revealed that the deposits were uniformly more abundant, widespread, and varied than suggested by preliminary estimates.

This chapter describes the flow deposits of the 2006 eruption of Augustine Volcano in terms of their morphology, lithologic composition, and sedimentology and discusses possible mechanisms for their flow generation and transport. Our study complements other chapters in this volume that discuss the eruption chronology, seismic interpretation of flow timing, tephra falls, and petrogenesis (Coombs and others, McNutt and others, Wallace and others, and Larsen and others). In particular, this chapter is a companion to that by Coombs and others, which presents a detailed chronology of the events that produced the on-island deposits, as well as a 1:20,000-scale map of the 2006 deposits. The detailed monitoring of Augustine Volcano enabled us to establish a fairly accurate chronology of flowage events (Coombs and others, McNutt and others, Power and Lalla, this volume), allowing us to show how composition and texture of erupted material and morphology of deposits changed during the course of the eruption. We show that lithologic components of clastic deposits, distinct in composition and texture, were produced throughout the eruption, though in proportions that varied systematically with eruptive phase and style. In addition, the distinctive morphologies and relations between pyroclastic-current, lahar, and mixed-avalanche deposits of the initial, explosive phase suggests that deposition on and incorporation of snow were primary controlling factors in the sheetlike morphology of the initial pyroclastic currents, the production of mixed avalanches, and the release of melted ice and snow to produce lahars.

Flowage Phenomena and Recognition of Their Deposits

"Pyroclastic current" is defined here as a general term meaning any pyroclastic density current, regardless of origin, mechanism of transport, or particle concentration. Genesis may be plume-column collapse, or fracturing and collapse of a dome or lava flow. A pyroclastic current is a hot mixture of rock (lithics, pumice, or both lithics and pumice), ash, and gas that flows rapidly away from its source. In this study, the high-solids-fraction end member of the pyroclastic-current spectrum is a pyroclastic flow, and the dilute end member is a pyroclastic surge. In pyroclastic currents, both dense and dilute, the fluid phase, gas, provides at least partial support for the particulate phase and lends such flows their mobility. We define "block-and-ash flows" as pyroclastic flows derived from fracturing and collapse of lava domes or lava flows.

A "lahar" is defined here as a rapidly flowing, gravity-driven mixture of rock debris and water from a volcano. A lahar event may include, in order of increasing proportion of water, debris-flow, hyperconcentrated-flow, and stream-flow or flood phases, but the term "lahar" itself includes only sediment-rich debris flow and intermediate hyperconcentrated flows (Vallance, 2000). The fluid at least partly supports the solid particles in lahar flows.

We define volcanic "mixed avalanche" as a flow or avalanche of rock particles, water, and snow or ice in which snow and ice provide partial support for the solid particles. Such flows, variously termed "mixed avalanches" (Pierson, 1994) and "hybrid flows" (Waitt, 1995) are most common where pyroclastic currents sweep across the extensive snow and ice covering the flanks of a volcano. These phenomena are transitional between snow-rich avalanches and debris flow and commonly behave partly as sliding and partly as flowing mixtures. Waitt and others (1994) describe genetically related sequences of such flows generated by pyroclastic eruptions comprising initial relatively dry debris and snow flows, followed by debris-rich slushy flows and, finally, by watery laharic flows. We report similar sequences of pyroclastic currents, mixed avalanches, and lahars during the 2006 eruption of Augustine Volcano.

At Augustine deposits of pyroclastic flows and lahars are distinctive and commonly well preserved, whereas those of pyroclastic-currents emplaced on snow, mixed avalanches of snow and debris, and lahars that contained substantial snow are ephemeral and can be difficult to distinguish as little as

2 years after the 2006 eruption. Archetypal pyroclastic-flow deposits display coarse levees and digitate margins, and individual flow units are as thick as 2 m. Some more energetic flow deposits thicken to many meters on gentle axial slopes but may thin or be absent on steep slopes and commonly thin to a fine-grained featheredge at deposit margins. In contrast, lahar deposits at Augustine commonly comprise isolated blocks on scoured surfaces bounded by low-aspect blocky levees. Where they funnel into drainages, lahars leave scoured surfaces with faintly stratified deposits, as much as 2 m thick in favorable pockets. Both pyroclastic-current deposits emplaced on snow and mixed-avalanche deposits display soft irregular surfaces crisscrossed with cracks and have thin margins containing lapilli and blocks and commonly lack prominent levees, but ephemeral features like irregular surfaces and cracks disappear in a few years time. Each type of deposit commonly drapes large blocks and vegetation at its margins, suggesting flows that were of greater depth than thin remnants might suggest. These two types of deposit are more distinctive where the flows moved into vegetation. Pyroclastic currents stripped and singed vegetation above the snow level but left it unaffected below, whereas mixed avalanches broke exposed vegetation into uncharred stem and branch fragments but similarly preserved lush vegetation below the emplacement snow surface. In addition, mixed-avalanche deposits are emplaced downslope of cogenetic pyroclastic currents but commonly form genetically related marginal levees for lahars. In such cases, the marginal mixed-avalanche deposits form thick, poorly sorted fills with abundant scattered wood fragments, and the lahar deposits consist of scattered blocks and debris remnants on a scoured, axial channel surface that commonly has vegetation battered and bent over in the flow direction.

Geologic Background and Eruptive History

Augustine is an island volcano, approximately 8 by 11 km, in lower Cook Inlet, 280 km south-southwest of Anchorage, Alaska (fig. 1). The volcano, which is one of the more active volcanoes in Alaska, has had six major eruptions in the 2 centuries before 2006 (1812, 1883, 1935, 1963–64, 1976, 1986; Coats, 1950; Johnstone, 1978; Miller and others, 1998). It has a central vent and comprises a series of domes, lava flows, pyroclastic flows, and debris-avalanche deposits that overlie Jurassic and Cretaceous sedimentary rocks of the Naknek Formation exposed on the south side of the island (Dettermen and Reed, 1980; Waitt and Begét, 1996 and 2009). Johnston (1978) suggests that the onset of volcanism was during the Moosehorn glacial advance, 19.0–15.5 ka. Hummocky topography along the north coastline is evidence for numerous catastrophic collapses of the summit dome, the most recent of which, in 1883, generated a tsunami that reached the east shores of Cook Inlet (Begét and Kienle, 1992; Siebert and others, 1995; Begét and Kowalik, 2006; Waitt, this volume).

Recent historical eruptions of Augustine have followed sequences similar to that in 2006. Eruption sequences have typically begun with explosive activity that produced ash plumes to higher than 10 km above mean sea level (asl) and pyroclastic flows, followed by effusive activity that built lava domes and lava flows and caused block-and-ash flows (Kienle and Forbes, 1977; Johnston, 1978; Kienle and Swanson, 1985; Swanson and Kienle, 1988). Lavas and juvenile clasts have consistently been crystal-rich, vesicular to dense, two-pyroxene±amphibole±olivine, low- through high-silica andesite and dacite (56–64 weight percent SiO_2), with banded clasts of the same rock types (Johnston, 1978; Daley, 1986; Harris and others, 1987; Miller and others, 1998, p. 14).

The well-studied 1976 and 1986 eruptions of Augustine were particularly similar to the 2006 eruption in terms of sequence, deposit distributions, and magma compositions (Swanson and Kienle, 1988; Power and others, 2006; Coombs and others, this volume). Before the 1976 eruption, precursory seismic activity began in May 1975, and the volcano erupted explosively on January 22. Explosions continued for about 3 days, produced ash plumes as high as 14 km asl, and generated pyroclastic flows and lahars on all flanks of the volcano (Kienle and Forbes, 1977; Johnston, 1978). At least one of the pyroclastic flows burned and damaged a research station on the northern tip of the island, and another reached the sea to the east of there. Activity resumed on February 6, and the volcano erupted almost continuously until February 16. Pyroclastic flows also occurred during the continuous phase of ash emission. A lava dome emerged February 11–12. After a

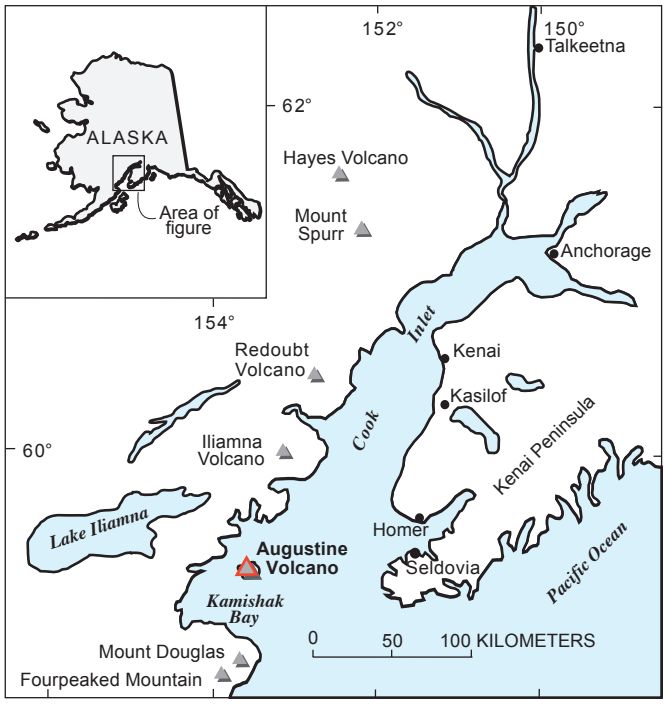


Figure 1. Index map of southern Alaska, showing location of Augustine Volcano in lower Cook Inlet.

repose period, renewed effusion occurred in August. The total volume of pyroclastic-flow deposits from the 1976 eruption was estimated at 0.05 km^3 (Kienle and Swanson, 1985).

Seismic activity precursory to the 1986 eruption began in July 1985, and the explosive phase began in late March 1986. Ash plumes rose as high as 12 km asl but, unlike during previous eruption, pyroclastic flows moved only northward, some reaching the sea (Swanson and Kienle, 1988). Ash reached surrounding communities, including Anchorage, March 27–31. During April 23–28, the continuous phase was marked by effusion and resulted in a short, blocky lava flow. Encroachment of the lava flow and a growing dome on steep slopes generated scattered block-and-ash flows. A 4-month repose followed the April activity. Renewed effusion August 30–31 accelerated dome growth and sent block-and-ash flows down the north flank of the volcano.

The 2006 Eruption Sequence

Slowly escalating, shallow seismicity (increasing from ~4–8 to 20–35 earthquakes per day) initiated precursory activity at Augustine in late April 2005 (Jacobs and McNutt, this volume; Power and Lalla, this volume). Seismicity increased through fall 2005. Inflation at the volcano began in midsummer 2005, marked by lengthening along a north-south baseline between stations located at 100 and 200 m asl, and continued at a steady rate until late November (Cervelli and others, 2006). Inflation reached a maximum by mid-December, suggesting intrusion of a northwest-striking dike at shallow levels (Cervelli and others, 2006; Cervelli and others, this volume). In mid-December, phreatic explosions produced a thin layer of ash on the winter snowpack within about 1 km of the vent (Power and others, 2006; Wallace and others, this volume). Small explosions continued through December.

From January to March 2006, distinct eruptive styles and deposits characterized each of the three eruptive phases (table 1). During the explosive phase, from January 11 to 28, 13 discrete vulcanian explosions, from 1 to 11 minutes in duration, initiated pyroclastic flows, and during quiescent intervals between explosions, three lava domes effused (Coombs and others, this volume). Initial pyroclastic currents of the explosive phase were widespread and deposited onto snow. Varying amounts of snow incorporated by the flows, or that underlay their still hot deposits, produced mixed avalanches and lahars (fig. 2*A*). Subsequent pyroclastic flows moved across previous deposits rather than snow and did not generate secondary flows (figs. 2*A*, 2*B*). None of the pyroclastic flows reached the sea, although near Rocky Point the last explosive-phase pyroclastic flow came within 100 m of the water (fig. 2*B*). During the continuous phase, from January 28 to February 10, continuous rapid effusion and nearly constant collapse of a high-silica-andesite lava dome punctuated by small explosions caused countless pyroclastic flows restricted to the north flank of the volcano (fig. 2*C*). After a pause in eruptive activity from February 10 to March 3, the effusive phase, from March 3 to March 16, generated blocky, dark-gray to black, low-silica andesite lava flows north and northeast of the summit and generated block-and-ash flows on steep flanks of the upper edifice (fig. 2*D*). After effusion ceased on March 16, the lava flows continued to shed rockfall and block-and-ash flows until at least late May. In October 2006, remobilization of pinkish-gray ash deposits during rainy weather resulted in water-rich lahar deposits, primarily on the north flank of the volcano (Coombs and others, this volume).

Methods

Field Methods

We conducted limited geologic fieldwork on Augustine Island (fig. 1) during the eruption and continued with more detailed investigations during 3 weeks in August 2006 and 1 week in July 2008. We noted pyroclastic-current, mixed-avalanche, and lahar deposits at more than 500 sites and collected 72 representative bulk samples for grain-size and lithologic analyses (table 2).[4] Where recognizable, distinct layers or facies present within each flow deposit were also sampled, and samples were taken at multiple sites along a longitudinal section of single flow units of at least two pyroclastic-flow deposits. As described below, all units contained clasts of multiple, distinct rock types, identifiable on the basis of color, morphology, and vesicularity. At 20 sites we performed "clast counts" to determine the proportions of various rock types within a given deposit. We conducted clast counts by picking a patch of ground at each site that contained at least 50 to 100 clasts, and counting the clasts that were 10 to 30 cm in diameter.

Methods for Analyzing Grain-Size Distributions

A total of 60 samples were submitted for grain-size analysis to the sediment-processing laboratory at the Cascades Volcano Observatory (table 3). All samples were sieved, using the visual-accumulation method, in one-ϕ intervals, from –6 ϕ (32 mm diam) to 4 ϕ ($\geq$0.063 mm diam). Of the 60 samples, 17 samples had the fine-ash (<0.063 mm diam) portion analyzed on a Sedigraph to calculate the weight percentage of each size class between 5 ϕ and 10 ϕ (0.063 and 0.001 mm diam, respectively). Standard statistics for grain-size distributions were calculated for each bulk sample (table 4).

Methods for Analyzing Flow Components

Preliminary clast counts in the field were refined after grain-size analysis by performing lithologic analysis on representative size classes from explosive- and continuous-phase samples. Lithologic categories were initially defined in the

[4]Note that tables 2, 3, 4, 6 and 8 are grouped at the back of this chapter, after References Cited.

Table 1. Summary of 2006 eruption and resulting deposits at Augustine Volcano, Alaska.

[Phases, event dates and times, and unit names from Coombs and others (this volume). Seismic duration from McNutt and others (this volume). Plume height from Wallace and others (this volume). Units are defined in figure 2]

Phase	Event	Date (2006)	Time of onset (AST)	Seismic duration (mm:ss)	Plume height (km)	Units emplaced		Comments
						Lava flows and domes	Flowage deposits	
Explosive January 11–28	1	1/11	4:44	1:18	6.5		Mixed avalanches (Exma).	Mixed avalanches of rock and snow were observed after these initial explosions, but were later covered. No lahars were observed.
	2	1/11	5:12	3:18	10.2			
		1/12				Ephemeral dome		
	3	1/13	4:24	11:00	10.2		Pyroclastic flows and currents (Expct); mixed avalanches (Exma) and lahars (Exlh).	Most widespread pyroclastic currents (Expct); mixed avalanches (Exma) and lahars (Exlh) in the east sector occurred during this interval.
	4	1/13	8:47	4:17	10–16			
	5	1/13	11:22	3:24	10–16		Pyroclastic flows (Expf); mixed avalanche (Exma); lahar (Exlh).	Widespread pyroclastic flows (Expf); mixed avalanches (Exma) and lahars (Exlh) in the northern sector occurred during this interval. Thick pyroclastic flows with coarse levees (Expf) were common to the east and north.
	6	1/13	16:40	4:00	9–11			
	7	1/13	18:58	3:00	13.5		Pyroclastic flows (Expf); mixed avalanche (Exma); lahar (Exlh).	Widespread pyroclastic flows (Expf); mixed avalanches (Exma) and lahars (Exlh) in the south sector occurred during this interval. Thick pyroclastic flows with coarse levees (Expf) were likely on all flanks.
	8	1/14	0:14	3:00	10.2			
						Dome (Exd1)		
	9	1/17	7:58	4:11	13.5		Pyroclastic flows (Expf)	A pyroclastic flow (Expf) emplaced to the southwest, possibly other pyroclastic flows elsewhere.
						Dome (Exd2)		
	10	1/27	20:24	9:00	10.5		Pyroclastic current (Expc); Rocky Point pyroclastic flow (RPpf).	A pyroclastic current and the voluminous Rocky Point pyroclastic flow were emplaced to the north during this event. Transitional composition between other explosive-phase deposits (rich in scoriaceous low-silica andesite) and continuous-phase deposits (rich in high-silica andesite).
	11	1/27	23:37	1:02	3.8			Seismic signal indicates that this event was gas rich and mass poor.
	12	1/28	2:04	2:06	7.2			No observations of deposits from these events, but seismic signals suggest pyroclastic flows (McNutt and others, this volume).
	13	1/28	7:32	3:00	7–11			
Continuous January28–February 10	14	1/28	14:31	--	8–9	Lava lobes	Pyroclastic flows and currents (Cpf, Cpc, Cpfw).	Thick, voluminous pyroclastic flows (Cpf, Cpfw, Cpc) were emplaced on the north flanks. High-silica andesite was predominant in deposits; scoriaceous low-silica andesite was rare. No lahar or mixed-avalanche deposits were emplaced. Lava flows began to effuse at the end of the continuous phase.
	--	1/29	11:17	--	--			
	--	1/30	--	--	--			
	--	2/3						
	--	2/10						
Hiatus								
Effusive March 3–16	--	3/3				Lava flow (Eflf)	Block-and-ash flows (Efba).	Dark-gray to black block-and-ash flows, predominantly containing dense low-silica andesite, traveled 0.5 to 2 km beyond the north and northeast lava lobes, lava flows to the east and north fractured and collapsed. Rockfall formed talus aprons around lava-lobe fronts.
	--							
	--							
	--	3/16						

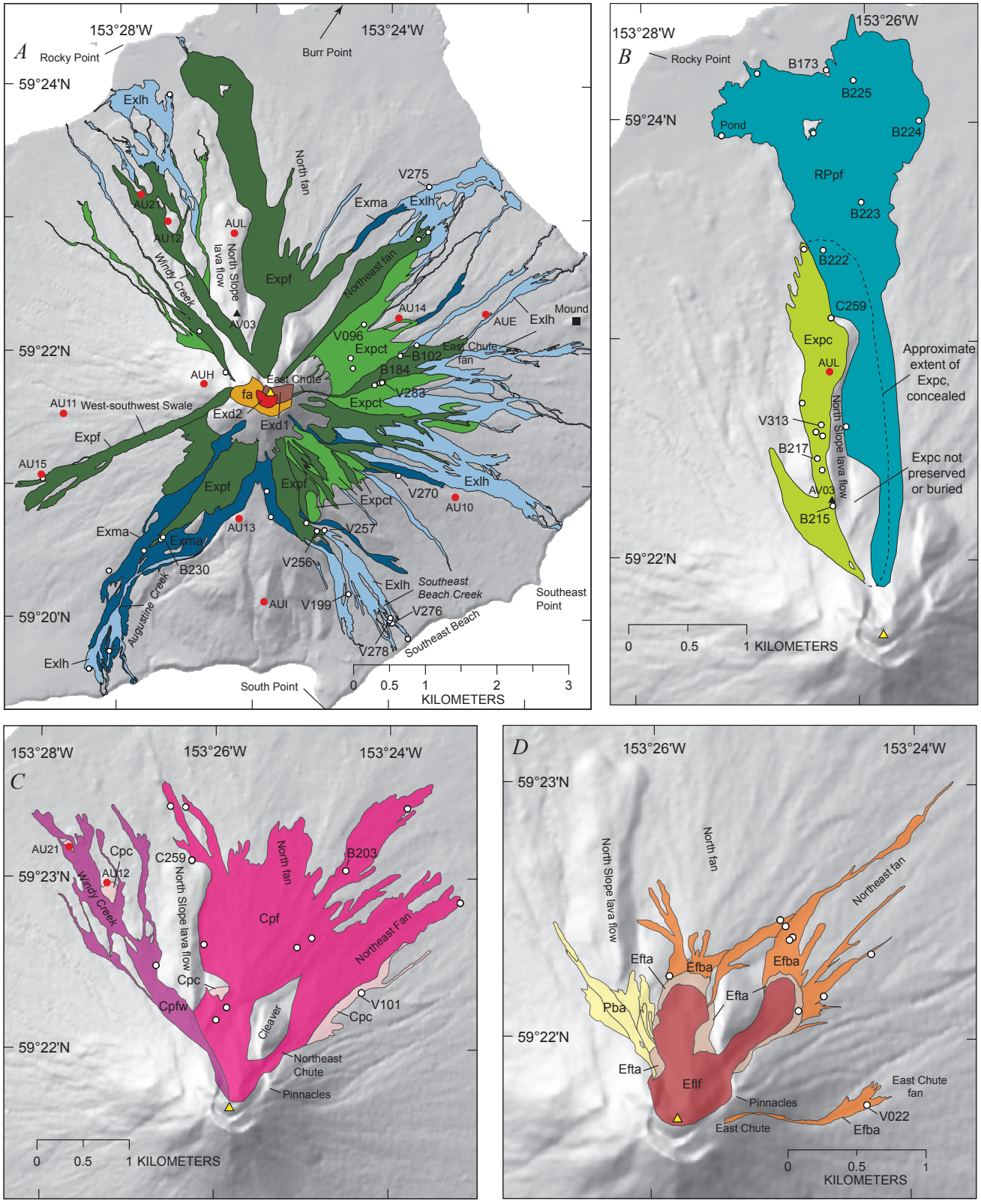
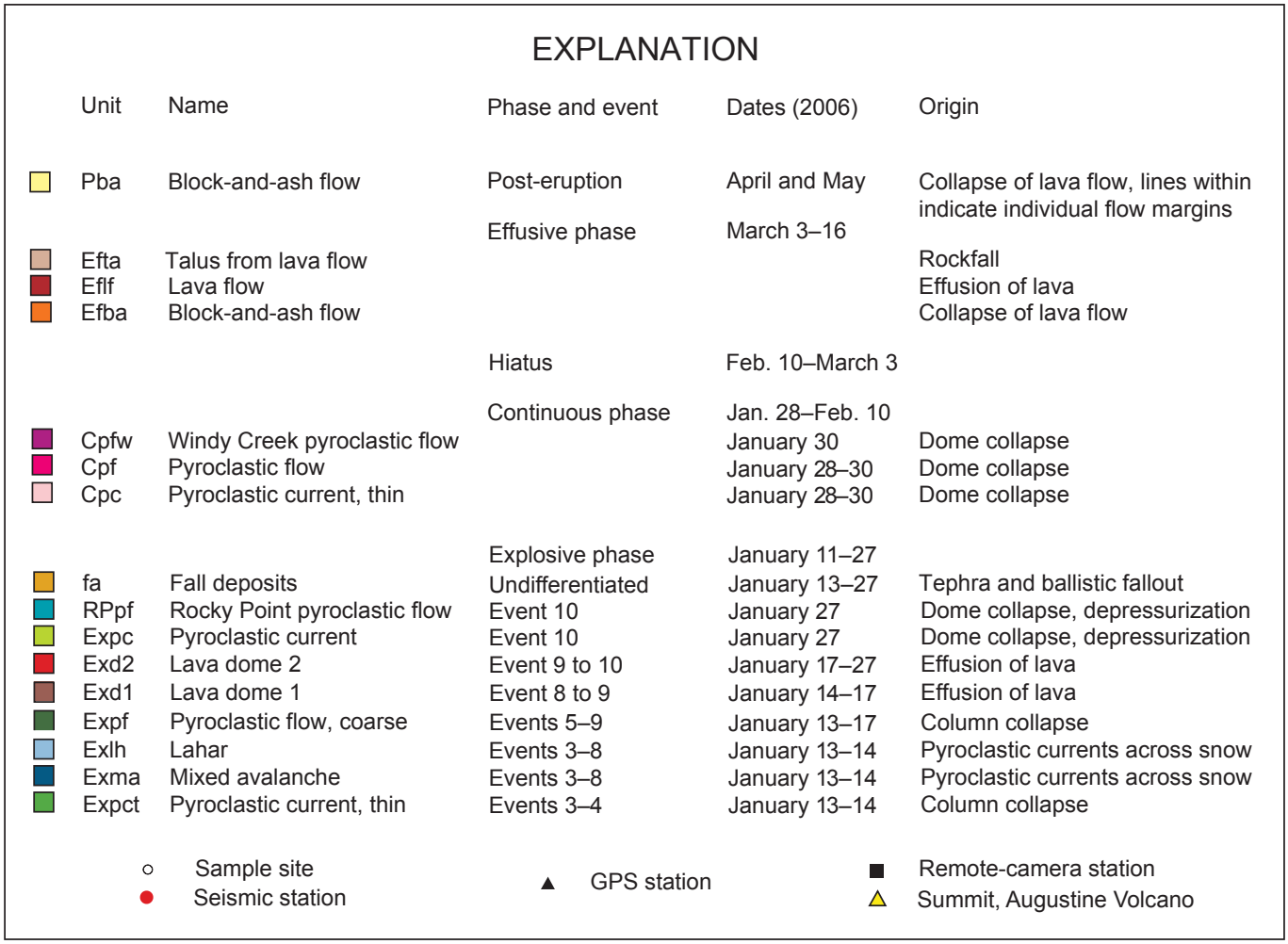


Figure 2. Time sequence of geologic maps of Augustine Volcano showing distribution of 2006 Augustine deposits and select sample locations (after Coombs and others, this volume). *A*, Explosive-phase deposits of events 1 through 9. *B*, Explosive-phase deposits of event 10. *C*, Continuous-phase deposits. *D*, Effusive-phase deposits. All place names associated with Augustine Volcano are informal except Augustine Creek, Augustine Island, and Burr Point.



field and later modified slightly after whole-rock compositional analysis and petrography (fig. 3; table 5). For a few samples, each size fraction was sorted into lithologic categories, and then clast populations for each rock type were counted and weighed (table 6). For most samples, however, we limited the lithologic analysis to the 4- and 8-mm size fractions.

2006 Flows and Flowage Deposits

Our results include emplacement chronology and detailed descriptions of the 2006 Augustine flowage deposits. We also summarize the detailed geologic mapping by Coombs and others (this volume). We use deposit characteristics, distribution, and timing to interpret emplacement and eruption mechanisms during each of the three eruptive phases.

Explosive-phase deposits include pyroclastic currents, lahars, and mixed avalanches on all flanks of the volcano. Pyroclastic deposits range from widely distributed, thin surge deposits to thick, lobate, flow deposits confined to drainages. In contrast, numerous pyroclastic flows of the continuous phase formed a thick fan restricted to the north side of the volcano and no lahars or mixed avalanches. Effusive-phase lava flows on steep slopes collapsed to form block-and-ash-flow deposits of limited extent north and east of the vent.

Explosive-Phase Deposits, January 11–28

The explosive phase comprised 13 discrete explosions, each lasting 1–11 minutes (table 1). Each explosion produced tephra plumes, and most explosions produced flowage deposits that together draped all flanks of the volcano. Flowage deposits included those emplaced by pyroclastic currents, lahars, and mixed avalanches.

Events 1 and 2, January 11: Vulcanian Explosions and Mixed Avalanches

Two explosions on January 11 cleared the vent, released plumes 6 to 9 km asl, deposited ash on the volcano's flanks, and produced small flowage deposits on the upper flanks of the volcano (table 1) (Schneider and others, 2006; Bailey and



others, this volume). Seismicity suggests that the first short explosion was primarily a gas-release, vent-clearing event (McNutt and others, this volume). The second explosion probably produced the flowage deposits. After these explosions and before those of January 13, an ephemeral lava dome grew (table 1).

Alaska Volcano Observatory geologists on an overflight, plus Web- and fixed-camera images, documented mixed avalanches of rock and snow on the flanks of the volcano the afternoon after these explosions. Lobate deposits of the flows underlay upper drainages around the volcano (Coombs and others, this volume). The lobes were 50 to 300 m wide, confined to gullies, extended from 1 to 2 km down the flanks of the volcano from 300 to 700 m asl, and were at least several meters thick. Close examination of aerial photographs showed that the flows contained abundant snow, as well as rock debris. We observed little evidence of melting in the photographs; surface water was not released beyond the lobe fronts, although water rivulets formed on the flow surface. As a result, we infer that the flows were not particularly hot. These deposits were subsequently covered or destroyed by later events and so were not visited or sampled. Samples of the January 11 ash deposits contained altered, dense clasts and no juvenile material (Wallace and others, this volume). We therefore infer that these mixed-avalanche deposits contained little or no juvenile rock either.

Events 3 through 9, January 13–17: Widespread Pyroclastic Currents, Lahars, and Mixed-Avalanches

Seven explosions, five on January 13, one on January 14, and one on January 17, lasted 3–11 minutes. The explosions produced widespread pyroclastic currents, mixed avalanches, lahars, and tephra falls, and all deposits contained juvenile material (table 1, fig. 2*A*). The short duration of these events, their pyroclastic nature, and their seismic characteristics indicate that they were vulcanian. McNutt and others (this volume) infer that the short duration and the dominantly emergent characteristics of events 3–9 (table 1) indicate a moderately uniform distribution of gas within the magma as it exited the vent. The high proportions of vesicular, high- and low-silica andesite within pyroclastic products of the eruption are consistent with short-term, explosive release of gas-rich magma (fig. 4).

Figure 3. Photographs of clastic rock types ejected during 2006 eruption of Augustine Volcano, Alaska. *A*, Low-silica andesite scoria. *B*, Dense low-silica andesite. *C*, High-silica andesite, friable and vesicular with a cinderblock-like texture. *D*, Dense intermediate-silica andesite. *E*, Banded scoria with end members of high-silica andesite (HSA) and low-silica andesite scoria (LSAS).

Table 5. Rock types in flow deposits from the 2006 eruption of Augustine Volcano, Alaska.

Lithology (acronym)	Description	Vesicularity[1]
Low-silica andesite scoria (LSAS)	Reddish-brown to black vesicular porphyritic andesite with distinctive, pale- to olive-green rinds. Smaller lapilli are wholly olive green. Clasts commonly are cauliform. Abundant phenocrysts of plagioclase and less abundant pyroxene visible in hand specimen.	33±5
Dense low-silica andesite (DLSA)	Dark-gray to black, poorly vesicular andesite. Some groundmass is glassy, and clasts are commonly angular. Phenocrysts include plagioclase, clinopyroxene, and orthopyroxene. Some lapilli and blocks have breadcrust rinds.	20±4
High-silica andesite (HSA)	Light- to medium-gray, moderately vesicular, crystal-rich high-silica andesite. Phenocrysts include plagioclase, pyroxene, and amphibole. Clasts are lower in density than DLSA and commonly rounded owing to friable, cinderblock-like texture. Clast interiors may be variably oxidized.	37±8
High-silica andesite pumice (HSAP)	White to cream-colored porphyritic andesite, moderately to highly vesicular. Phenocrysts include plagioclase, pyroxene, and amphibole.	~42
Dense intermediate-silica andesite (DIA)	Light- to medium-gray, poorly vesicular porphyritic andesite. Some groundmass is glassy, and clasts are commonly angular.	22±3
Banded	Banded clasts; any combination of lithologies above.	39±9
Oxidized	Red, pink, orange, and yellow tinted clasts. Includes glassy, dense, vesicular clasts and crystals. May not all be juvenile.	Not determined
Crystals	Crystals, singly or in clots (with little to no groundmass attached; crystals more abundant than groundmass). Consistently present in the 2-mm and smaller size classes, increasing in proportion with decreasing size class.	Not applicable
High-silica inclusions[2]	Lavender patches and veinlets within HSA clasts in continuous-phase pyroclastic-flow deposits. In thin section, the patches are monocrystalline and polycrystalline masses in a groundmass of quartz, feldspar, clear glass, and vesicles. Masses are predominantly plagioclase (mostly sieve textured) but also include orthopyroxene and biotite. Micrographic textures are relatively common.	Not determined
Fine-grained gabbroic inclusions[2]	Salt-and-pepper, equigranular blocks or inclusions within dense low-silica andesite blocks of effusive-phase deposits. Crystals are ≤2 mm-diameter skeletal plagioclase, amphibole, and two-pyroxene.	Not determined

[1] As determined by point count by Larsen and others (this volume); errors are plus and minus 1σ.

[2] Lithology recognized in the field but not observed in the laboratory.

Explosive-Phase Pyroclastic Currents

Aerial reconnaissance on January 12, 16, and 18, time-lapse photographs, and seismic data constrain the emplacement of pyroclastic currents during the sequence of events 3 through 9 (table 1). Seismic signals from stations downslope of flows or beside flowpaths include 10–30-minute-long, cigar-shaped codas and increases in amplitude on temporary broadband stations 10–20 minutes after each explosion. Such distinctive signals on instruments below or next to flows, and their absence in other quadrants, delineate flowpaths (McNutt and others, this volume). Comparison of signals from instruments on all flanks of Augustine suggests that the longest-lasting flow occurred in a time-staggered sequence around the volcano. Signals indicating large flows were first recorded on east-side seismometers during events 3 through 5, on north-side seismometers during events 5 and 7, and on south-side seismometers during event 8 (Coombs and others, this volume; McNutt and others, this volume). Smaller flows occurred during the other events (table 1). Coombs and others (this volume), using time-lapse images from stations north and east of the volcano, report pyroclastic currents on the east and northeast flanks during events 4 and 5 and on the north flank during event 5 and smaller flows on the east and north flanks of the volcano after event 5. Aerial reconnaissance on January 16 indicated pyroclastic flowage deposits on all flanks of the volcano. An aerial survey revealed that an explosion on January 17 produced a pyroclastic flow on the Southwest flank, and seismicity suggests flows on the Northwest flank as well.

The deposits from these pyroclastic currents include two main types: a pyroclastic unit, typically 5 to 30 cm thick and widespread on the aprons of the volcano that is named the "thin, explosive-phase pyroclastic-current deposit" (map unit Expct); and an overlying unit, commonly 50–200 cm thick, lobate and with prominent blocky margins that is named the "explosive-phase pyroclastic-flow deposit" (map unit Expf) (fig. 2*A*).

The first voluminous pyroclastic currents to descend the volcano swept across steep, snow-covered slopes and spread widely on volcano aprons to form thin deposits (unit Expct, fig. 2*A*). These deposits blanket much of the upper slopes of the volcano down to about 300 m asl (fig. 2*A*)—a horizontal runout of 2 to 3 km and an elevation drop of 900 m. In August 2006, typical 5- to 30-cm-thick deposits commonly overlay snow but elsewhere thinned to a featheredge against pre-2006 surfaces to form complex tonguelike margins (fig. 5). Islands of pre-2006 deposits formed where this pyroclastic deposit lapped against gentle rises, ridges, and knolls.

Deposits of the first pyroclastic currents (unit Expct) commonly are poorly sorted, massive, and ungraded; however, near distal margins the deposits overlie graded and crudely bedded facies rich in dense clasts, as large as 1 m across. (fig. 6). Typical deposits have a bimodal size distribution with modes in lapilli- and ash-size and very fine ash components

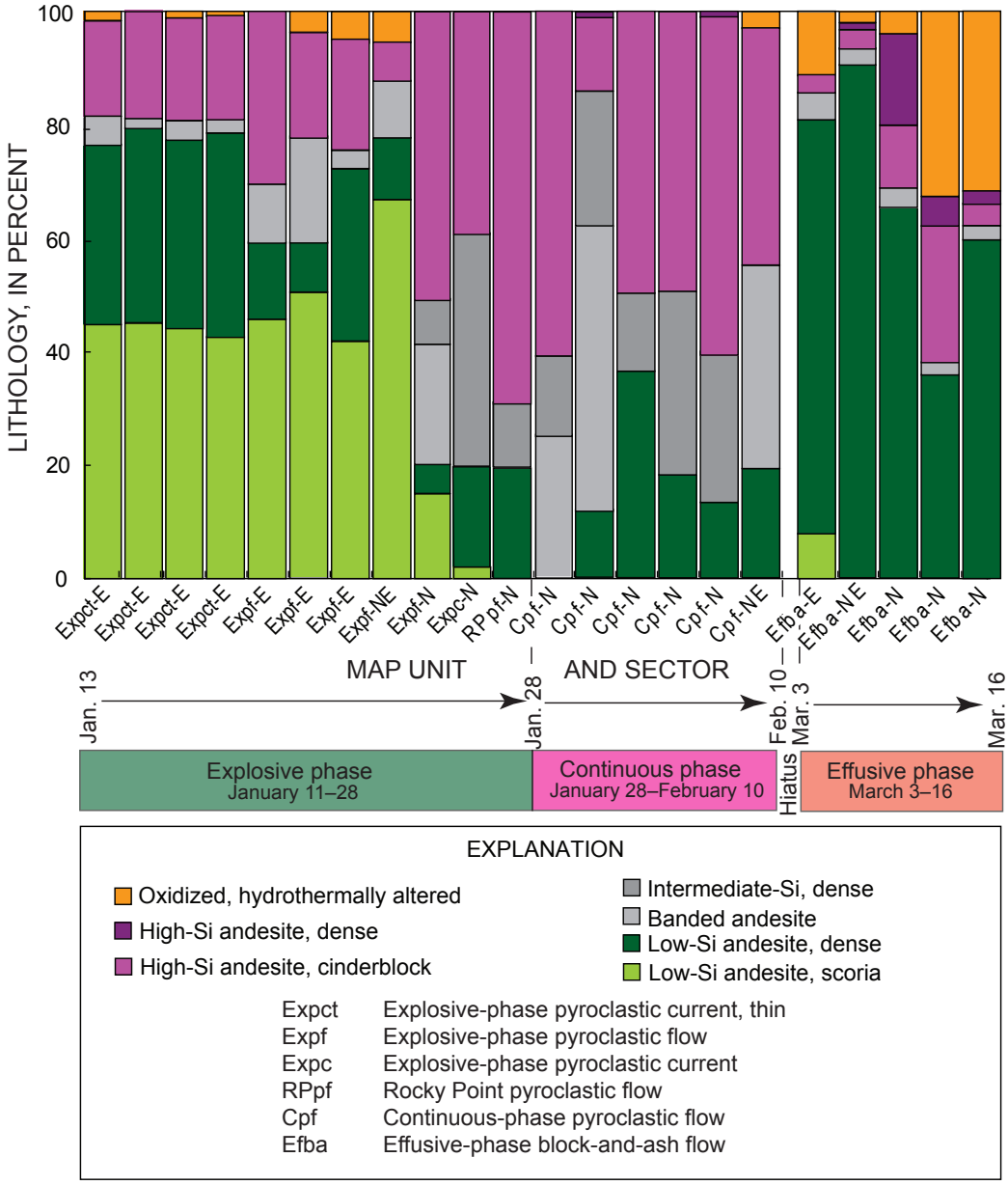


Figure 4. Plot of lithologic components versus flow type and quadrant for pyroclastic-current deposits, as determined by clast counts in the field (lithologies described in table 5).

ranging from 8 to 15 percent (figs. 6, 7). In contrast, basal stratified facies have stunted or absent lapilli-size modes and very fine ash components of less than 5 percent. Bedding within the fines-deficient facies nearly parallels bedding planes or dips at low angles toward source, and grading, if present, is inverse and coarse tailed (fig. 6). The stratified basal facies grades upward to the more common massive facies above within 1 or 2 cm.

After the initial widespread pyroclastic currents, multiple lobate pyroclastic flows (unit Expf), fig. 2*A*) funneled into valleys on all flanks of the volcano and produced deposits with archetypal morphology, including blocky, lobate margins and levees (fig. 8). The coarse pyroclastic-flow deposit (unit Expf) invariably overlies thin pyroclastic deposits (unit Expct) and thus postdates events 3 and 4 in drainages to the east and north and event 7 to the south and southwest. The largest flows moved as far as 3 to 4 km from source and typically moved farther along narrower valley axes than did initial widespread flows. The complex digitate margins of these distal flows thus now overlie pre-2006 surfaces (fig. 8). Deposit lobes are 5 to 30 m across and 1 to 2 m thick at distal or levee margins, although some thin toward their interiors and upslope to as little as 20 cm (fig. 9).

Coarse pyroclastic-flow lobes form overlapping sequences that indicate multiple episodes of deposition (fig. 9). Longitudinal cross sections of overlapping flow lobes indicate that subsequent flows plowed up and incorporated sediment from previous lobes even on gentle slopes. In adjacent areas, such lobes comformably overlie pre-2006 substrate with little evidence of erosion. Erosion of older 2006 pyroclastic-flow deposits by younger ones and an absence of such erosion on pre-2006 surfaces suggest that the older deposits remained somewhat fluid when subsequent flows inundated them.

The coarse pyroclastic-flow deposit (unit Expf, fig. 2) is poorly sorted, massive, and ungraded to inversely graded (fig. 9). Typical deposits have a bimodal size distribution, with lapilli and medium-to-coarse-ash modes (figs. 7, 9). Fine-grained basal layers may lack lapilli and blocks and have large fine-ash components. Inverse coarse-tail grading is common where blocks and large lapilli concentrate near the surface behind flow-lobe margins (fig. 9).

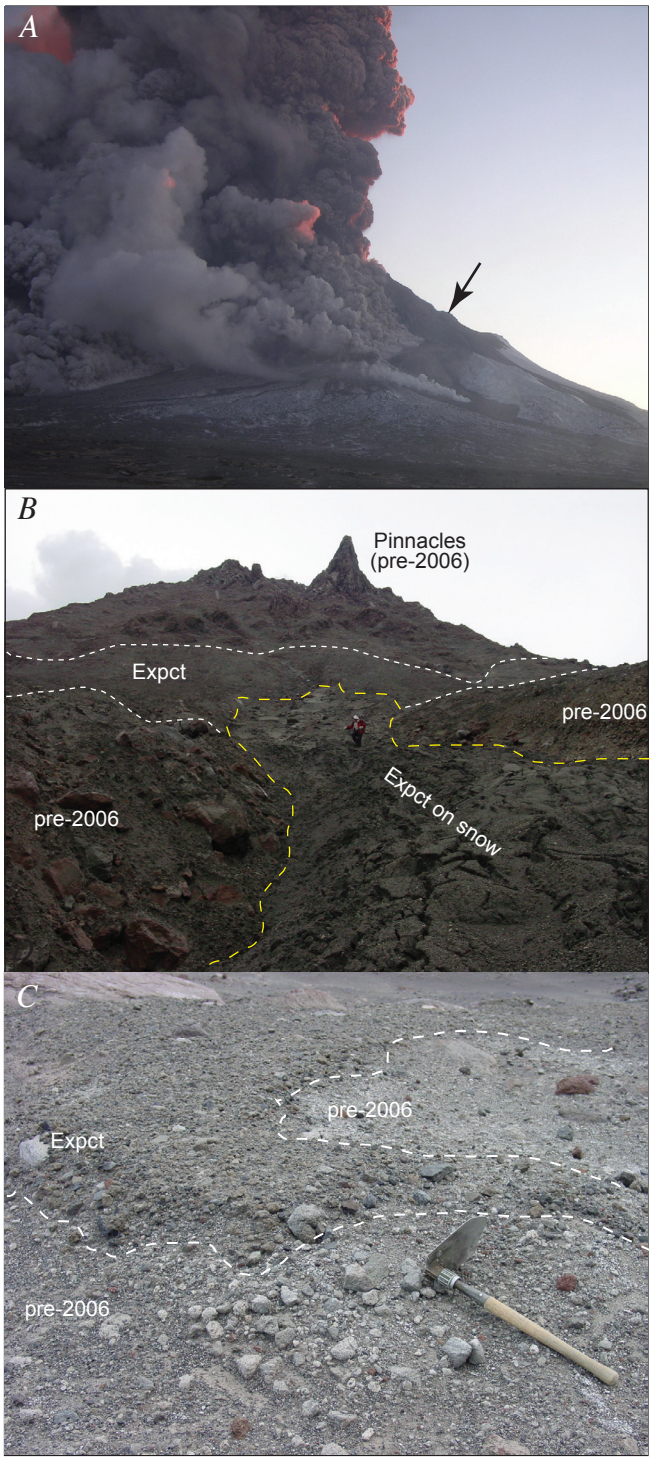


Figure 5. Photographs of thin explosive-phase pyroclastic-current deposit (unit Expct). *A*, Time-lapse photograph taken at 1645 AKST January 13, 2006, from Burr Point showing a pyroclastic current of event 6 moving down north slope of volcano toward camera. Arrow denotes blanket of debris already in place across the upper flanks, inferred to be unit Expct. *B*, Unit Expct deposit on east slope of volcano below Pinnacles (~1 km northeast of vent). Deposit is absent on steep, pre-2006 outcrops, including Pinnacles in background. In foreground, deposits in a gully were emplaced on snow. Later melting of snow caused deposits to become cracked and lumpy. *C*, Initial explosive-phase pyroclastic deposits (unit Expct) emplaced on pre-2006 moss- and lichen-covered surface, which was probably windswept of snow at time of deposition. Leading edge of 2006 flow is in middle of photograph. Flow drapes pre-2006 surface in a way typical of this deposit.

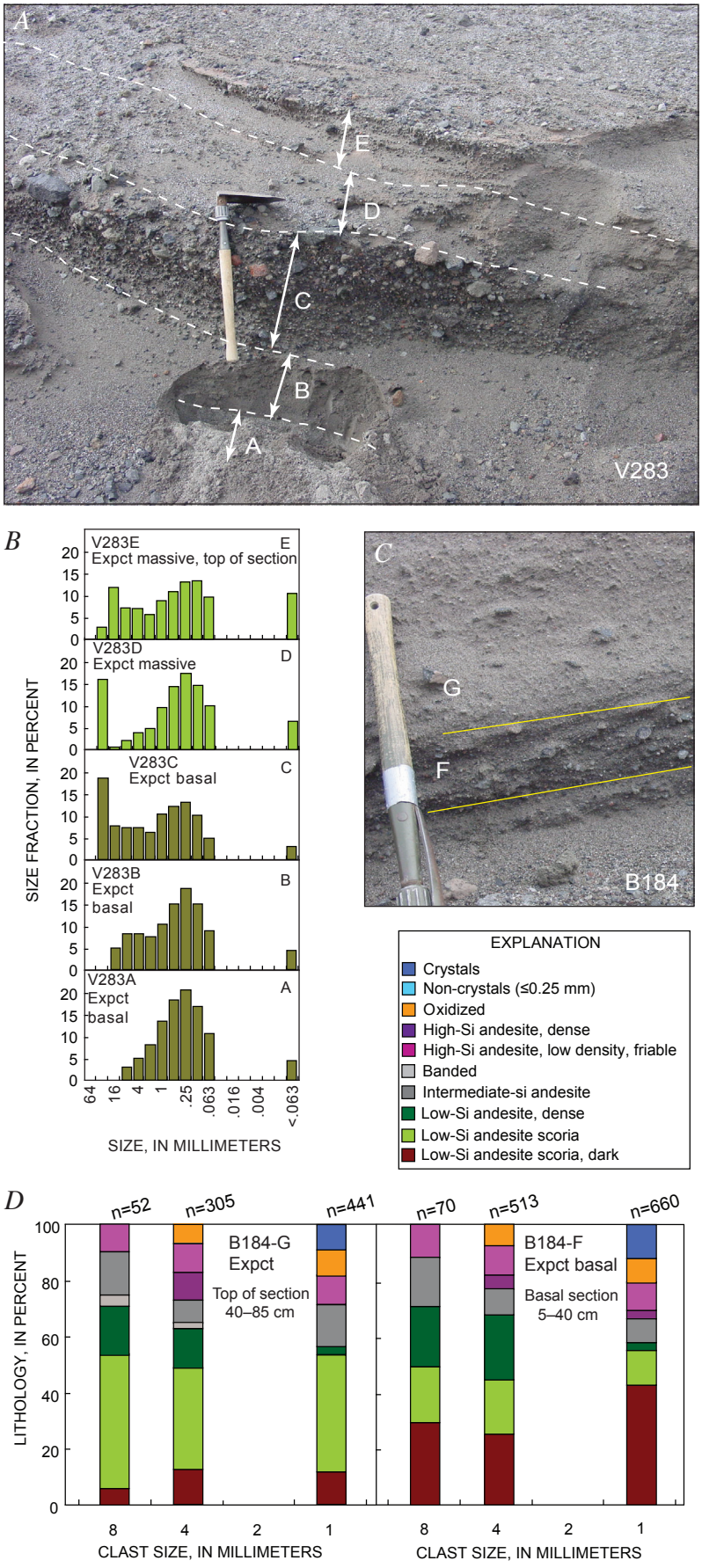


Figure 6. Basal stratified facies of thin explosive-phase pyroclastic-current deposit (unit Expct) on east flank of Augustine Volcano at station V283 (fig. 2*A*; table 3). *A,* Photograph of inversely graded, faintly stratified facies (layers A–C) overlain by ubiquitous, massive blanketing facies of deposit (layers D, E). Shovel is 50 cm long. *B*, Grain-size histograms of layers designated in figure 6A. *C,* Photograph of outcrop at station B184, approximately 50 m upslope of that shown in figure 6A, showing two 2006 layers on top of pre-2006 surface. Layer F is faintly crossbedded, and, like layers A through C at station V283, is friable. Layer G is typical blanketing facies of deposit. *D,* Plots of lithologic components of sample B184-F of basal facies and typical sample B184-G of deposit. Basal facies contains greater proportions of dark scoria and dense clasts than overlying deposit and other explosive-phase pyroclastic deposits. Sample locations are shown in figure 2*A* and table 2.

All pyroclastic deposits of the early explosive phase (events 3–9) contain similar proportions of lithologic components (figs. 4, 10; table 7). Low-silica andesite is the dominant rock type, and scoria is more common than dense rock (fig. 10). Subordinate rock types include high-silica andesite and dense, intermediate-silica andesite. Size- and density-segregation processes selectively sorted numerous blocks and lapilli of greenish-gray low-silica andesite scoria to the surface of pyroclastic flows as they slowed, lending deposits an easily distinguishable greenish gray hue. In fine-grained fractions, the three key constituents become more difficult to recognize, and we identify increasing proportions of phenocrysts (fig. 10).

Explosive-Phase Mixed Avalanches and Lahars

Mixed avalanches and lahars were generated by the first widespread pyroclastic currents (generally unit Expct) that moved across winter snowpack during events 3 through 8 on January 13 and 14; no such flows occurred thereafter. Aerial reconnaissance on January 12 and 16 constrains the emplacement of these flows. Flowline patterns along drainages are visible in oblique aerial photographs of January 16 but not in those of January 12. Scoured slopes and vegetation, as well as striations along northward-, eastward-, and southward-oriented streampaths, caused the patterns. These features were most conspicuous downslope of fresh pyroclastic-current deposits, and farther downstream in several drainages as far as the coast. Later observations showed that mixed-avalanche and lahar tracks caused the patterns (fig. 2*A*).

We infer that one or more of the six events on January 13–14 generated both mixed avalanches and lahars and, more specifically, that the first widespread pyroclastic currents to descend any particular valley during January 13–14 generated these flowage deposits (fig. 2*A*). Time-lapse photographs taken from the Mound camera (fig. 2*A*) suggest that east-side lahars had moved into several drainages downstream of the informally named East Chute during event 3 or 4 (Coombs and others, this volume, fig. 4*C*). Time-lapse photographs taken from Burr Point show fresh coarse pyroclastic-flow deposits (unit Expf) that descended the Northeast fan (fig. 2*A*; Coombs and others, this volume, figs. 5*C*, 5*D*). These pyroclastic-flow deposits overlap lahar deposits and one mixed-avalanche deposit, downstream along Northeast fan, suggesting that the

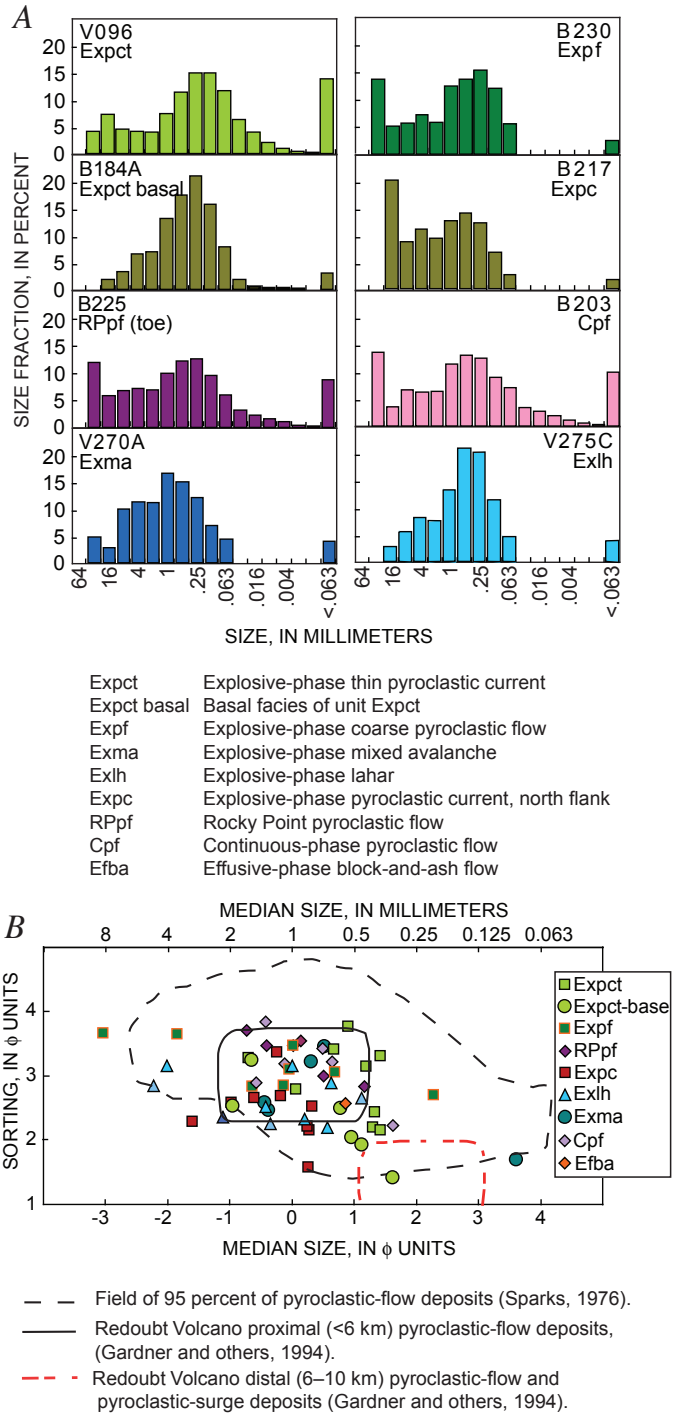


Figure 7. Summary of results from grain-size analyses of 2006 flowage deposits at Augustine Volcano. *A*, Histograms showing grain-size distribution of each clastic-flow type. Pyroclastic deposits with high fines content include deposits from initial thin, and subsequent coarse, explosive-phase pyroclastic deposits, the Rocky Point pyroclastic-flow deposit, and most continuous-phase pyroclastic-flow deposits. Some explosive-phase pyroclastic deposits are fines deficient. Bimodality with modes in lapilli and coarse-ash fractions, though present in some samples, is not conspicuous. *B,* Sorting versus median grain size for 2006 pyroclastic-flow deposits. Most samples fall within region of worldwide pyroclastic-flow deposits (dashed line; after Sparks, 1976) and 1989–90 proximal pyroclastic-flow deposits of Redoubt Volcano (solid line; after Gardner and others, 1994). Sample locations are shown in figure 2 and table 2; grain-size data are listed in tables 3 and 4.

lahar and mixed-avalanche deposits were emplaced during events 3 through 5.

Seismic signals provide further clues about the timing of lahar and mixed-avalanche emplacement (in this volume: Coombs and others; McNutt and others). Seismic stations adjacent to flowpaths recorded high-frequency, cigar-shaped codas following explosions, whereas other stations far from flowpaths recorded only explosion signals (McNutt and others, this volume). Broadband stations downstream of flows also showed increased seismicity as long as 20 minutes after initial explosion signals. The postexplosion timing and characteristics of these seismic signals suggest that they were produced by pyroclastic flows, mixed avalanches, and lahars that flowed toward the stations (Coombs and others, this volume). For example, station AUE, located between East Chute and Mound (fig. 2*A*) within about 100 m of a lahar path, recorded dominant, long-duration flowage signals, the longest of which lasted more than 30 minutes during event 3 and was partly caused by lahars passing near the station, rather than by pyroclastic flows upslope (McNutt and others, this volume). Stations AUE and AU14 also recorded signals consistent with flowage phenomena during events 4 and 5. The signal during event 5, in particular, could plausibly include lahars. Stations AUL and AU12 both recorded

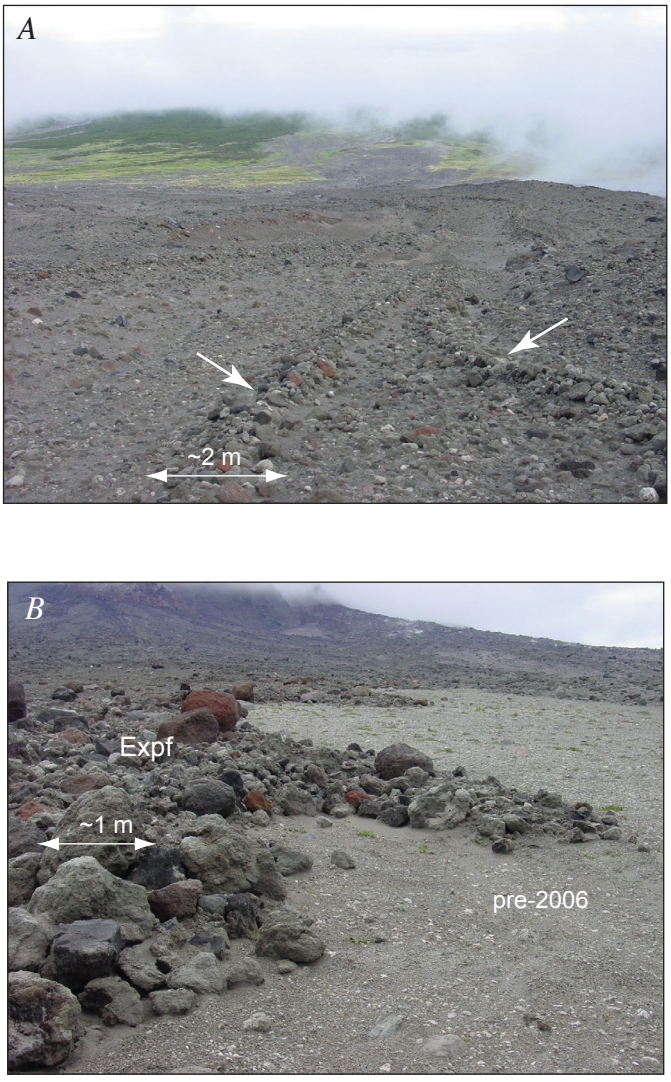


Figure 8. Photographs of coarse explosive-phase pyroclastic-flow deposits (unit Expf). *A,* Medial levees (arrows), approximately 50 cm high concentrate large lapilli and blocks and define margins of lobate deposits. *B*, Digitate, distal margin of coarse pyroclastic-flow deposit.

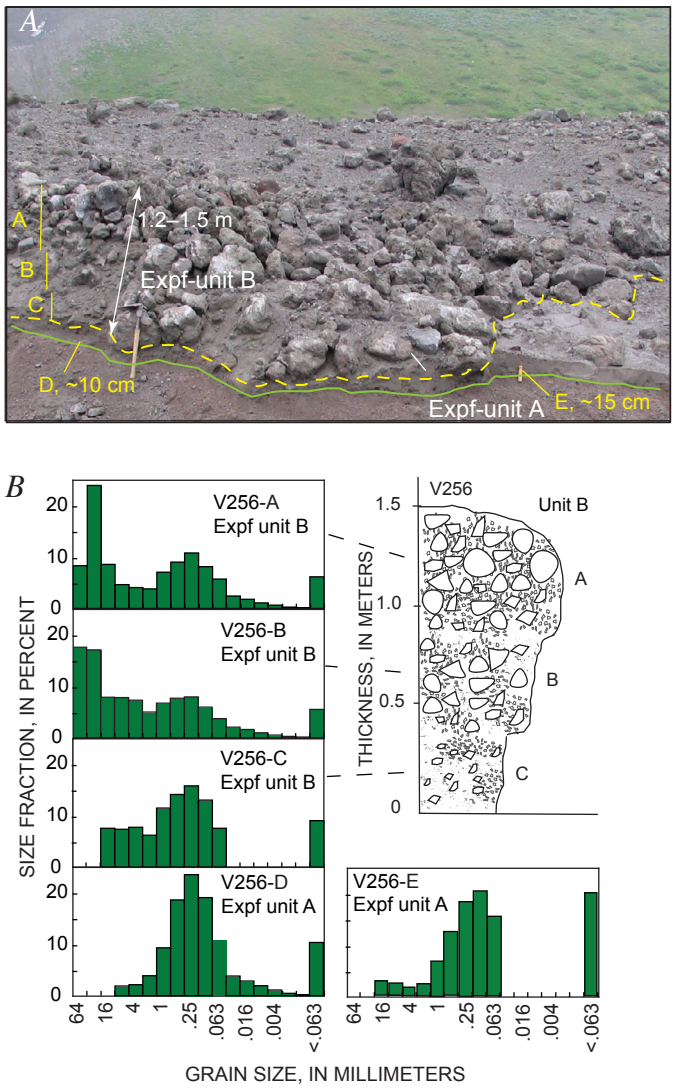


Figure 9. Overlapping explosive-phase pyroclastic-flow deposits (unit Expf) at station V256 (fig. 2*A*). *A,* Photograph showing distal margin of pyroclastic-flow unit B where it has overrun and partially eroded pyroclastic-flow unit A. Sampling sites are denoted in yellow as A through E. *B,* Unit B is inversely graded, as shown by histograms of grain-size distribution and by graphic log to right. Sample locations are shown in figure 2*A* and table 2.

flows during event 5 but not during earlier events. These deposits, which were the first widespread pyroclastic flows of the 2006 eruption, probably generated the lahars that moved downstream of North Fan and within Windy Creek drainage to the coast (fig. 2*A*). On the basis of the protracted seismic signals recorded at stations AU15, AU13, and AUI (fig. 2*A*), to the southwest and south of the volcano, pyroclastic flows and the mixed avalanches and lahars that they generated in Augustine Creek and Southeast Beach Creek probably occurred during event 8.

Mixed-Avalanche Deposits

Mixed-avalanche deposits (unit Exma) crop out south and east of the volcano, from upper slopes downstream as far as the coast, and extend from near the margins of some thin explosive-phase pyroclastic-flow deposits (fig. 2*A*). Mixed-avalanche deposits are most widespread in drainages on the southwest to southeast flanks of the volcano (fig. 2*A*). In the upper parts of Augustine Creek drainage, mixed-avalanche deposits occupy wide swaths of the valley, interrupted only by younger coarse pyroclastic-flow lobes (fig. 2*A*). In medial and distal reaches of valley systems, such as Augustine Creek, mixed-avalanche deposits crop out next to lahars (figs. 11–13). In areas where mixed-avalanche and lahar deposits mingle, the mixed-avalanche deposits occupy flow margins and commonly form islands surrounded by lahar deposits (fig. 13). On the east side of Augustine Island, mixed-avalanche deposits of more limited extent commonly are confined to upper-slope gullies and span a few minor drainages downslope (fig. 2*A*).

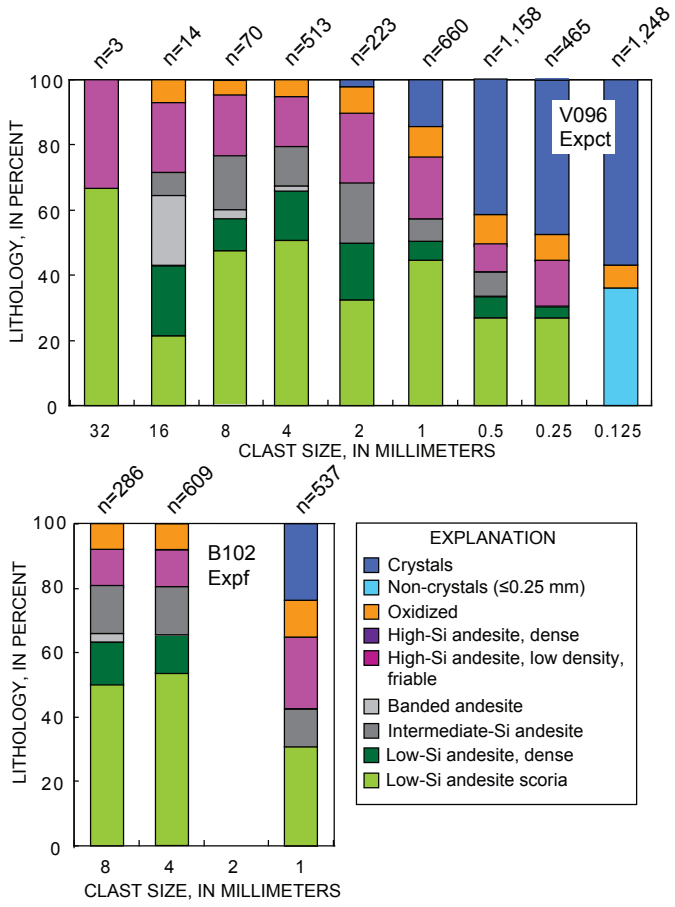


Figure 10. Plots showing lithologic components versus clast size for pyroclastic deposits of explosive-phase events 3 through 9. Above, initial explosive-phase pyroclastic deposit (unit Expct) and below, subsequent explosive-phase pyroclastic-flow deposit (unit Expf). Sample locations are shown in figure 2*A* and table 2.

Mixed-avalanche deposits have distinctive irregular surfaces crisscrossed with cracks. These cracks cut through the soft sediment that forms the deposits, and in August 2006, several months after the eruption, the cracks locally exposed snow. In protected, proximal reaches during August 2006, we observed that some deposits contained snow, some overlay snow, and others had distinctive, extremely uneven, lumpy surfaces due to the melting of both underlying and contained snow (figs. 11, 12). Along vegetated slopes at lower elevations, deposit surfaces were littered with uncharred alder and willow branches that had been broken to pieces and denuded small stems and twigs. Nearby such littered surfaces, deposit remnants were also scattered on top of large boulders and throughout patches of alder and willow whose upper branches were commonly denuded and broken but not charred. Apparently, the brush in mixed-avalanche paths was commonly buried and protected under snowpack when snow and debris mixtures slid across it. As a result, the vegetation, whose tops were generally clipped and destroyed, were irregularly draped with debris. Deposit margins, which are broadly lobate and do not form levees themselves, are common as levees of axial lahar flows (fig. 12).

The thickness of explosive-phase mixed-avalanche deposits ranges from 0.2 to 3 m and averages about 0.5 m. Poorly sorted, ungraded deposits typically have modes in gravel- and sand-size ranges (fig. 11). The deposits contain proportions of juvenile rock types similar to those of explosive-phase pyroclastic-flow debris. Locally, the lumpy surfaces are rich in fines (<0.063 mm diam) and cracked where snowmelt had pooled, collected the fines, and subsequently dried (fig. 11).

Lahar Deposits

Explosive-phase lahar deposits (unit Exlh) underlie the middle to lower parts of most drainages around the volcano, except those to the west (fig. 2*A*). Generally, lahar deposits are downstream of pyroclastic-flow deposits and adjacent to, or downstream of, mixed-avalanche deposits (figs. 2*A*, 13). Watery lahars and floods reached the coast on most flanks of the volcano (fig. 2*A*).

The variation in the areal extent of lahar inundation suggests a variation in water content among lahars. The most widespread lahar deposits are also those with characteristics most suggestive of high water content. The deposits

Table 7. Overview of lithologic components in key deposits of the three phases of the 2006 eruption of Augustine Volcano, Alaska.

[Phases, events, and units (after Coombs and others, this volume). Component values are 8-mm data averaged from table 6 and recalculated to 100 percent. Components are low-silica andesite scoria (LSAS), dense low-silica andesite (DLSA), dense intermediate-silica andesite (DIA), high-silica andesite (HSA), and mixtures (banded), defined in table 5. Units are defined in figure 2. Mixed-avalanche (Exma) and lahar (Exlh) data are not included in "Average for unit" column]

Phase	Date	Event	Unit(s) emplaced (map designation): Lavas, lithology	Unit(s) emplaced (map designation): Flowage deposits	Lithologic components (in percent): Expct						Expf						Expct base (above) Expc (below)						RPpf						Exma (above) Exlh (below)							Cpf						Efba						Average for unit		
					LSAS	DLSA	DIA	Banded	HSA	Oxidized	LSAS	DLSA	DIA	Banded	HSA	Oxidized	LSAS	DLSA	DIA	Banded	HSA	Oxidized	LSAS	DLSA	DIA	Banded	HSA	Oxidized	LSAS	DLSA	DIA	Banded	HSA	Exotic [1]	LSAS	DLSA	DIA	Banded	HSA	Oxidized	LSAS	DLSA	DIA	Banded	HSA	Oxidized	LSA [2]	IA [3]	HSA
Explosive, January 11–28	1/11	1		Mixed avalanches (destroyed)																																												
		2																																													
	1/11–1/13		Ephemeral dome, LSA																																													
	1/13-1/14	3		Pyroclastic current, thin (Expct); mixed avalanche (Exma); lahar (Exlh)	45	16	14	4	16	6	Expf possible, no data						51	20	16	2	11	0							47	11	7	3	18	14													68	18	14
		4																																												
		5		Pyroclastic flow (Expf); mixed avalanche (Exma); lahar (Exlh)							62	11	10	2	11	4													41	19	14	1	16	9											75	13	12
		6																																												
		7																																												
		8																																												
	1/14–1/17		Dome (Exd1), LSA																																												
	1/17	9		Pyroclastic flow (Expf)							49	10	12	8	16	5																													62	21	17
	1/17–1/27		Dome (Exd2) HSA, IA																																												
	1/27	10		Pyroclastic current (Expc)													8	29	23	3	34	3																							38	27	35
				Rocky Point pyroclastic flow (RPpf)																			9	11	14	1	62	3																	21	15	64
	1/27–1/28	11		Pyroclastic flows? (buried)																																												
		12																																												
		13																																													
Continuous	1/28–2/3	14		Pyroclastic flow (Cpf, Cpfw, and Cpc)																																	0	18	41	5	29	7							19	50	31
		--																																												
		--																																												
	2/3–2/10	--	Lava lobes, LSA																																												
		--																																												
Hiatus																																														
Effusive	March 3–16		Lava flow (Eflf); LSA	Block-and-ash flow (Elba)																																							9	63	9	0	4	15	85	10	5

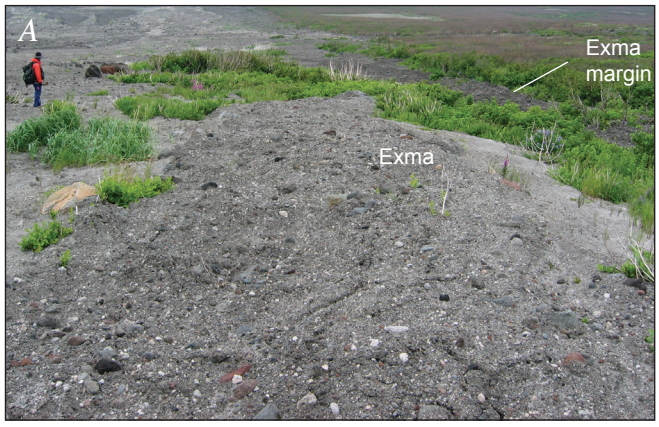
[1] Oxidized + pumice.

[2] LSA = LSAS+DLSA.

[3] IA = DIA+banded.

downvalley of East Chute are the best examples of these water-rich flows (figs. 12*B*, 14*A*). On the east flank of the volcano, between about 500 and 100 m asl, long linear lahar levees, 2 to 10 m wide and about 20 cm high, consist of cobble and boulder accumulations littered with sand and silt. The levees trace along vegetated terraces and mossy surfaces upstream of the youngest explosive-phase coarse pyroclastic-flow deposit (unit Expf), toward their apparent source, the older, thin pyroclastic-current deposit (unit Expct; figs. 2*A*, 12). In between levees, large lahars were water rich and erosional. Boulders as large as 3 m in diameter, commonly of low-silica andesite scoria, dot eroded and scoured surfaces. In this scoured regime, willows and alders are commonly battered on their upstream sides, denuded, and bent downslope into bayonet-stick forms (fig. 14*A*). Downstream, levees lead into channels where the water-rich debris mixture flowed and deposited 30- to 100-cm-thick channel facies (fig. 14*B*). In outcrop, the channel facies has characteristics typical of transitional or hyperconcentrated-flow deposits, such as intermediate sorting, crude bedding, and both inverse and normal grading (fig. 14*B*). Where exposed, inversely graded strata underlie crudely stratified, normally graded sediment. In distal reaches, levees range in size and character from linear trains of scattered cobbles and boulders to boulder-cobble-rich accumulations, as thick as 50 cm.

Areally extensive lahar deposits commonly have margins bordered by mixed-avalanche deposits, suggesting



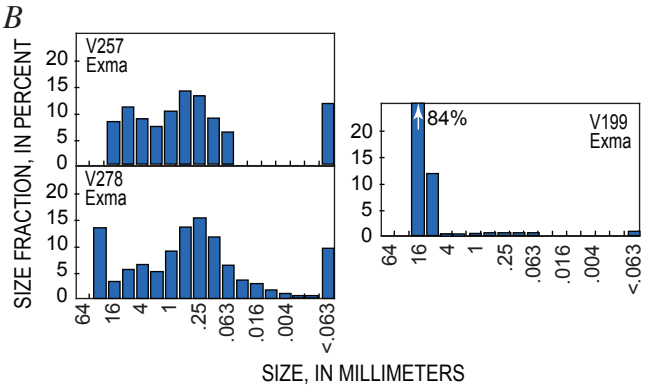


Figure 11. Photograph and grain-size plots of explosive-phase mixed-avalanche deposits (unit Exma). *A*, View downstream of mixed-avalanche deposit showing irregular, lumpy surface texture. Cracks formed after incorporated snow had melted, and wet, compacted fines had dried and contracted. Margin of deposit, cutting across upper right of photo, drapes vegetation. Apparently, much debris in this area was emplaced on top of snow that covered and protected vegetation, then melted into place, partly burying small alder trees. *B*, Histograms of grain-size distribution of mixed-avalanhce deposits, illustrating variability of size distribution. Sample locations are shown in figure 2*A* and table 2.





Figure 12. Photographs of lahar levees; view downstream. *A,* Boulders, cobbles, and sparse matrix that have accumulated along right margin of lahar. *B,* Mixed avalanche deposit (unit Exma) forms left-marginal levee-terrace, 2 m high, of lahar flow to right. Lahars denude alders and willows, forming bayonetlike stems that are battered and bent downstream. Green vegetation was protected from flow by burial under snow.



Figure 13. Photographs of explosive-phase lahar deposits. *A,* Aerial view down Augustine Creek on lower south-southwest flank of volcano, showing lahar deposit (unit Exhl; light-blue dashed outline and flow-direction arrows). Mixed-avalanche deposit (unit Exma) forms terraces lateral to, and islands within, lahar deposit. Lahar channels are scoured. *B,* Photograph of small-scale (~5 m across) lahar deposits. Lahar deposits in foreground (dashed lines) were generated by explosive-phase pyroclastic-flow deposit (unit Expf; solid lines) that came to rest on snow. *C,* Aerial view of bouldery mixed-avalanche and lahar deposits in Augustine Creek, bordering scoured lahar channels that cut seacliff. Lahar transport formed bouldery delta as far as 100 m offshore.

a genetic relation between these two types of deposit. South-southwest of the volcano, mixed-avalanche deposits are situated in intermediate valley reaches between source pyroclastic-flow deposits and lahars. Farther downstream, along intermediate to distal reaches of Augustine Creek, terraces of lumpy-surfaced mixed-avalanche deposits border lahar deposits rather than boulder-cobble levees (fig. 12*B*). In between these mixed-avalanche terraces are scoured lahar surfaces with scattered boulders, much like the scoured surfaces of the large lahars described above (fig. 12*A*). Downstream of the marginal mixed-avalanche deposits, boulder-cobble levees become evident. Near the coastline in Augustine Creek, bouldery mixed-avalanche and lahar deposits are situated on either side of a scoured channel incised in a low seacliff (fig. 13*C*). Lahars carried boulders as large as 1 m in diameter through the channel, and carried other boulders as far as 100 m into the ocean. We observed similar relations between mixed avalanches and lahars that moved to the coast along drainages on the south and southeast sides of the island.

The smallest-volume lahar deposits appear to have originated at the coarse margins of explosive-phase the pyroclastic-flow deposit (unit Expf, fig. 13*B*); fluid breakaways are visible at the toes and margins of some of the younger coarse pyroclastic-flow-deposit lobes. The lahar deposits, which are typically only few meters wide and no more than a few tens of meters long, have cobble-rich margins that become progressively less distinct with distance downslope (fig. 13*B*). These deposits are present where the pyroclastic flow deposit (unit Expf) evidently came to rest on top of snowpack.

The lithologic composition of lahar deposits (unit Exlh) is similar to that of explosive-phase pyroclastic currents (units Expct, Expf) and virtually identical to that of mixed-avalanche deposits (unit Exma). The greenish-gray, low-silica andesite scoria that is common in all explosive-phase deposits is also diagnostic in lahar deposits (tables 6, 7). A combination of size and density segregation has concentrated greater than 50 percent scoria in lahar-levee deposits. The channel facies of lahar deposits contain scoria proportions typical of other explosive-phase deposits, but also oxidized lithic clasts and pumice from pre-2006 deposits (table 6). These rock types are present in the lahars owing to progressive entrainment of sediment along the flowpath. At Augustine, lahar flowpaths rarely exceed 2 km in length, and so bulking factors in deposits are rarely much greater than 10 percent.

Grain-size characteristics of Augustine lahar deposits are similar to those of the transitional to hyperconcentrated flows documented at other volcanoes (Scott, 1988; Vallance, 2000). The sorting index ranges from 2.2 to 3.2, typical of transitional flows (table 2; Scott, 1988). The upper, crudely bedded deposits are moderately well sorted, have the finest mean grain size, and have grain-size distributions with a mode of about 0.5 mm (figs. 14*A*, 14*B*). Underlying, more massive deposits have the greatest proportions of coarse particles, the poorest sorting, and grain-size distributions with a weak bimodality (figs. 14*A*, 14*B*).

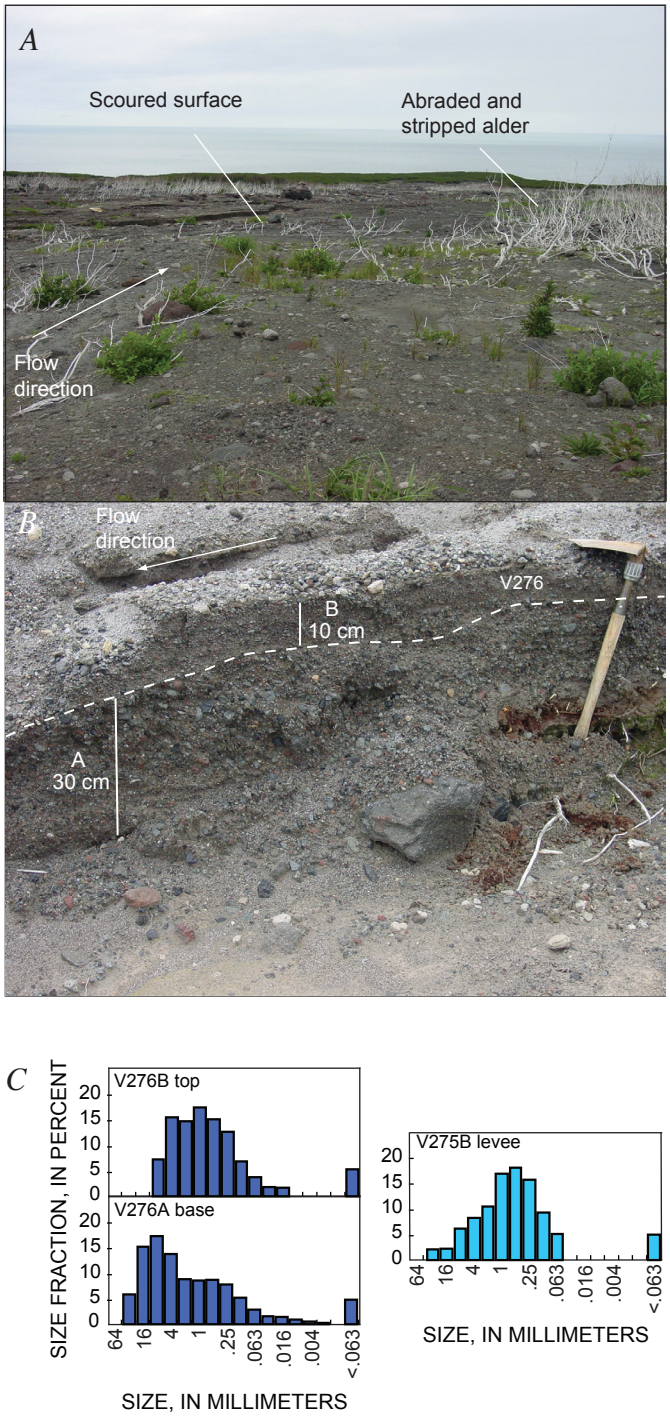


Figure 14. Photographs of scoured lahar surface (*A*) and nearby vertical section (*B*) at sample location V276, with histograms of deposit grain-size characteristics (*C*). *A*, Lahar surface is not only scoured but also displays willows and alders stripped of vegetation and bent in flow direction to form bayonetlike sticks. *B*, Normally graded lahar deposit where it funneled into distal channel and began to deposit its sediment load. Layer B is faintly stratified. Shovel is 50 cm long. *C*, Basal layer A contains a larger proportion of large clasts and also more fines than layer B. Nearby levee deposit (sample V275B) is relatively fines poor. Sample locations are shown in figure 2*A* and table 2.

Events 10 through 13, January 28–29: Pyroclastic Flows to the North and the Transition to the Continuous Phase

The 9-minute-long explosion of event 10 produced the largest-volume pyroclastic output of the explosive phase and sent pyroclastic currents northward. Events 11 through 13 either generated no pyroclastic currents or produced no deposits distinguishable from those of the subsequent continuous phase. Two distinctive pyroclastic currents occurred in rapid succession during event 10 (McNutt and others, this volume; Coombs and others, this volume). The first deposit contains large proportions of dense, nonvesicular andesite (unit Expc, fig. 2*B*). The second more widespread deposit, named the "Rocky Point pyroclastic flow," overlies the first deposit and covers an area of about 3 km^2 from the volcano's summit northward toward Rocky Point (unit RPpf, fig. 2*B*).

Stratigraphy, the destruction of monitoring devices, and the characteristics of seismic signals constrain the timing of the two large pyroclastic flows on the north flank to event 10. At 2024 AKST January 27, 2006 (0524 UTC, Jan. 28, 2006), a forceful blast destroyed seismic station AUL and GPS station AV03, both then located on the prehistoric North Slope lava flow (fig. 2*B*). Lithologically distinct pyroclastic deposits at these sites and battered fragments of the stations within deposits downstream (fig. 15*A*) shows that the initial flow (unit Expc) destroyed the stations. The Rocky Point pyroclastic flow overlies this pyroclastic-current deposit and underlies pyroclastic-flow deposits correlated to the continuous phase (unit Cpf; figs. 15*B*, 15*C*), suggesting that the flows occurred between 2024 AKST January 27 (event 10) and aerial observations midday on January 29 during the early part of the continuous phase. Coombs and others (this volume) infer that the Rocky Point flow occurred during event 10, on the basis of deposit size (largest of the 2006 eruption), the extent of the postexplosion seismic signal (~30 minutes), the relative size of the ash signal on radar (largest of the 2006 sequence, Schneider and others, 2006), and the number of lightning strikes (most recorded strikes during the 2006 eruption; Thomas and others, this volume). We accept their interpretation that the largest flow should correspond to an event with a long seismic coda, an ash-rich plume, and numerous lightning strikes. Event 10 is the only likely eruptive pulse during the time interval in question with these characteristics.

Explosive-Phase Pyroclastic-Current Deposit

The pyroclastic-current deposit (unit Expc) drapes the conspicuous North Slope lava flow (Waitt and Begét, 2009) and spills onto gentler slopes, a distance of 3.3 km northward from its source at the summit to its distal margin (fig. 2*B*). The limited distribution of this flowage deposit along the top of a ridge 50–100 m high is likely an artifact of the deposit's unknown extent: eastward, beneath pyroclastic-flow deposits of Rocky Point and the continuous phase; and westward, beneath younger deposits of the adjacent, upper-eastern Windy Creek drainage (figs. 2*B*, 2*C*). The thickness of the deposit varies. Along the steep eastern margin of the prominent lava flow, it is 20 to 150 cm thick; on the lava flow's western edge, it thins irregularly to zero, revealing patches of pre-2006 deposits. Under varying thicknesses of continuous-phase pyroclastic flow deposits (unit Cpf) and the Rocky Point pyroclastic-flow deposit (unit RPpf), it is 5 to 50 cm thick to the east (fig. 15). North to north-northwest of the North Slope lava flow, it thins to a few centimeters and extends downslope as irregular patches within tracts of alder. In this area, the alders are singed and stripped of leaves above 1 to 2 m above ground and unaffected below, suggesting that margins of the flow were gas rich and contained insufficient heat either to melt underlying snowpack fully or to burn vegetation. Snow melting during spring and summer thaw subsequently emplaced the patches.

Outcrops of the pyroclastic-current deposit commonly are inversely graded, massive to faintly bedded, and loose or friable (figs. 15, 16). Some parts appear to be ungraded, especially those overlain by and, possibly eroded by younger pyroclastic flows. Grain size ranges from fine ash to lapilli, has a mode in the coarse-ash-size fraction and, where coarser overall, has another faint mode in the lapilli-size fraction (fig. 16*C*).

The pyroclastic-current deposit is lithic rich and varies somewhat in the proportions of lithologic components intermediate between those of previous explosive-phase deposits and those of subsequent continuous-phase deposits (fig. 16*D*). Like previous pyroclastic deposits of the explosive phase, angular, dense, low- and intermediate-silica andesite clasts make up 25 to 50 percent of the rock types in the deposit. In contrast, however, the pyroclastic-current deposit contains greater proportions of high-silica andesite than all previous explosive-phase deposits (fig. 16; tables 6, 7).

The pyroclastic-current (unit Expc) and the Rocky Point (unit RPpf) deposits originated during the same 9-minute event, and so we considered their possible genetic relation but rejected that hypothesis for the following reasons. First, the pyroclastic-current deposit crops out in extensive areas where evidence of the Rocky Point pyroclastic flow is absent. Second, where the two deposits crop out together their contact is abrupt, sharp, and commonly erosionally unconformable. Third, grain-size characteristics of the two deposits differ where they overlap; for example, thin, fine-ash edges of the Rocky Point deposit overlie much coarser ash and lapilli deposits of the pyroclastic-current deposit (fig. 15*B*). These observations are inconsistent with a cogenetic origin, and so we conclude that these two units followed one another successively within a few minutes during event 10.

Explosive-Phase Rocky Point Pyroclastic Flow

The most voluminous and widespread pyroclastic flow of the 2006 eruption also occurred during event 10. The Rocky Point pyroclastic flow originated near the summit of the

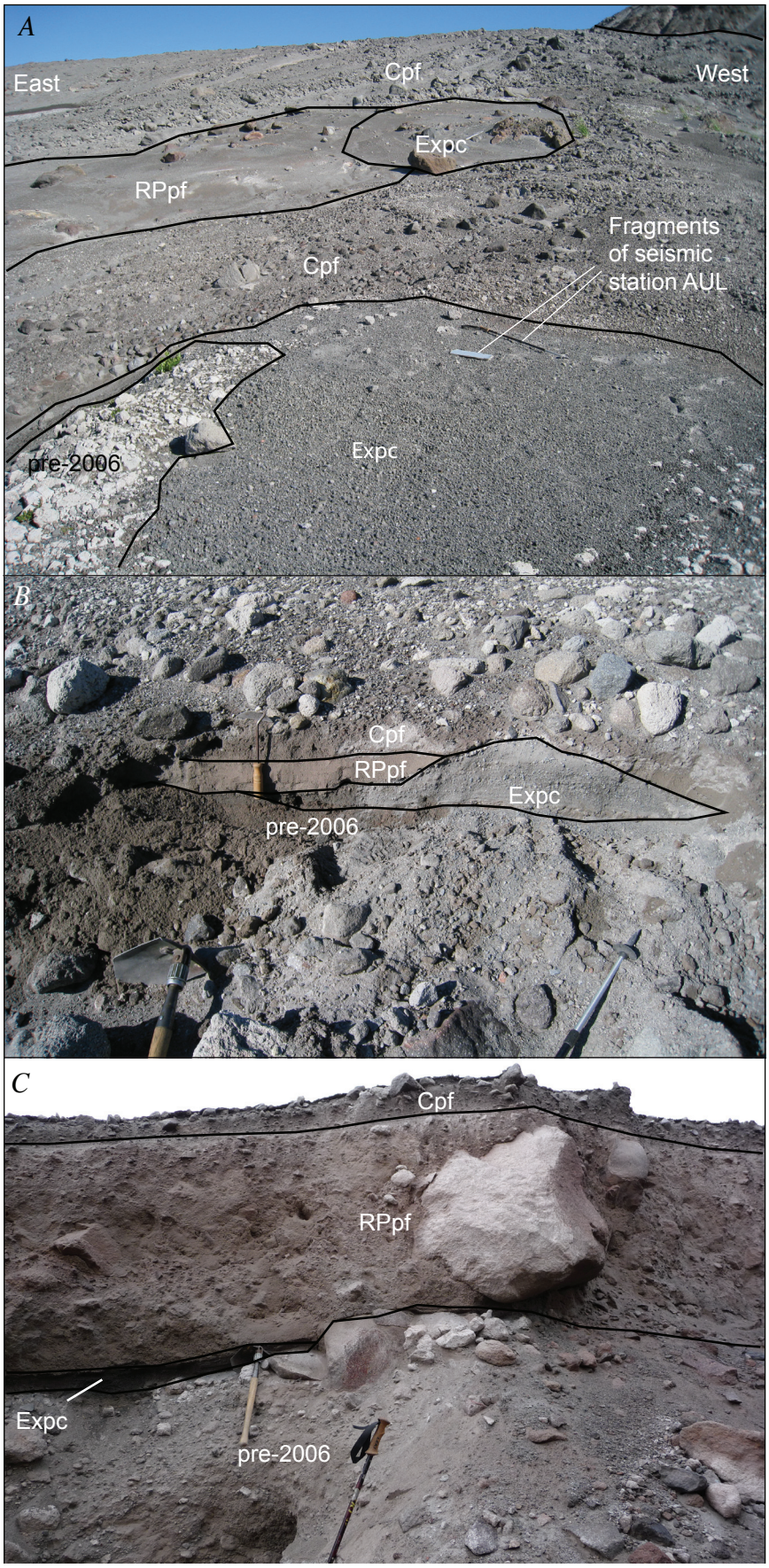
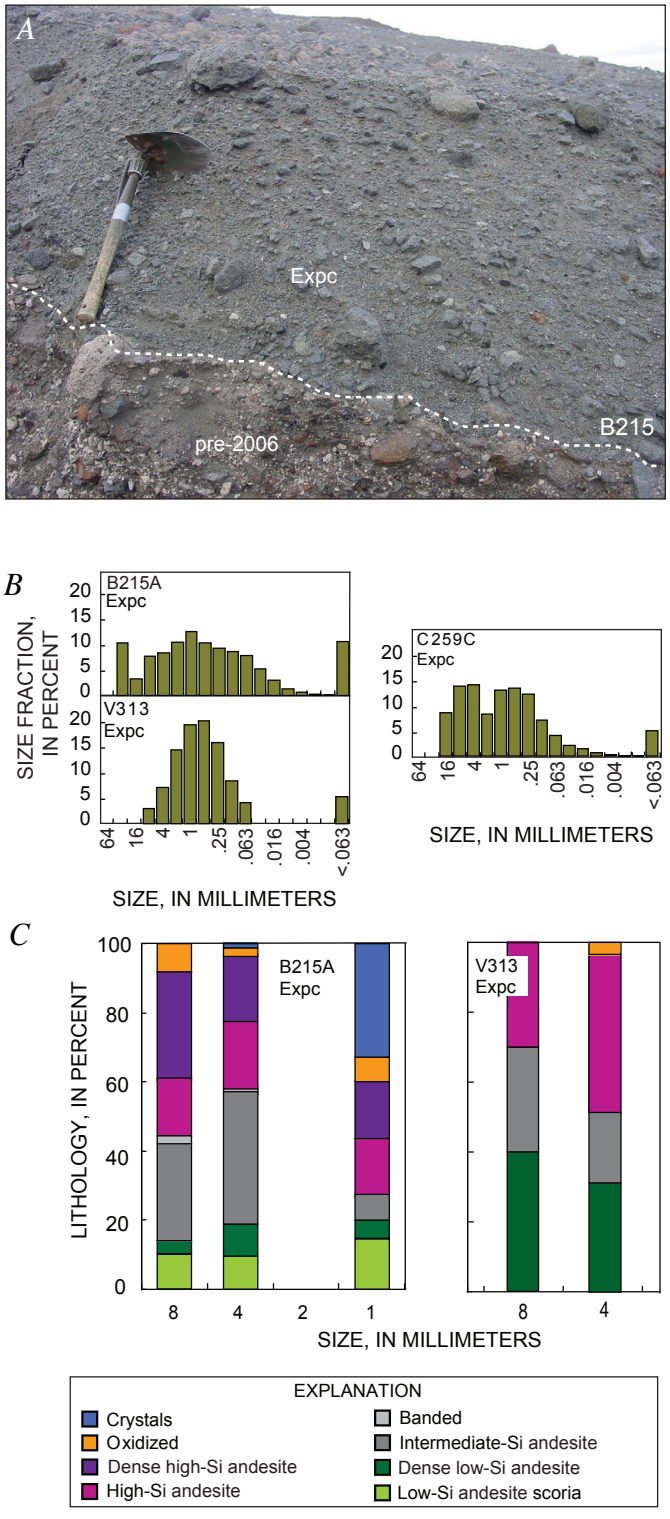


Figure 15. Photographs illustrating relations between 2006 explosive- and continuous-phase pyroclastic deposits on north flank of Augustine Volcano. *A,* Surface of pyroclastic-current deposit (unit Expc), oldest of 2006 deposits at this locality, with scattered fiberglass fragments, 40 and 90 cm long, from upslope seismic station AUL and GPS station AV03. Rocky Point pyroclastic-flow deposit (unit RPpf) thins from left to right (east to west) and disappears, whereas younger, continuous-phase pyroclastic-flow deposit (unit Cpf) drapes over and around gentle slopes. *B*, Thin, fine-grained Rocky Point deposit (unit RPpf) underlies continuous-phase pyroclastic-flow deposit (unit Cpf) and overlies friable, light-gray deposit (unit Expc). *C*, Rocky Point deposit (unit RPpf), 1 m thick, is in same stratigraphic position as in figure 15*B*.

volcano; traveled northward about 4 km, where a low ridge system, capped by a 50-m-high hill, divided the flow into two large and one small parts; and, finally, spread out to form several lobes across a nearly flat surface (figs. 2*B*, 17*C*). The flow moved just more than 5 km from its source and stopped less than 1 km from the shoreline near Rocky Point.

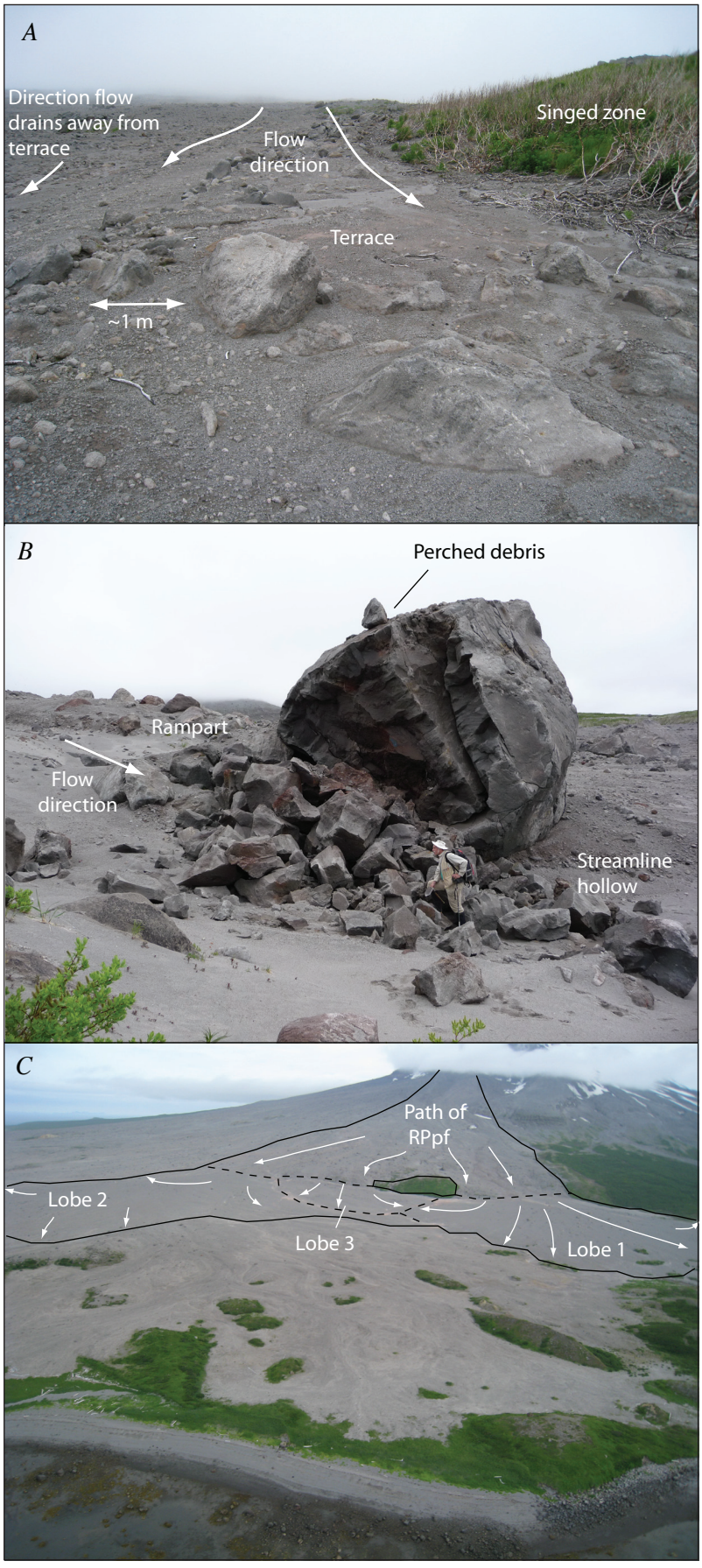


The Rocky Point pyroclastic-flow deposit (unit RPpf; fig. 2*B*) is distinctive, not only because of its size and distribution north of the volcano but also because of its physical characteristics. The deposit widens from about 0.3 to 1.8 km from south to north, averages 5 to 6 m in thickness, has maximum thicknesses of 10 to 15 m, and has a volume of about 1.6×10^7 m^3 (Coombs and others, this volume). Continuous-phase pyroclastic-flow lobes overlie proximal parts of the deposit (compare figs. 2*B*, 2*C*). Axial parts of the deposit thicken to as much as 15 m but thin to less than 1 m where the flow moved across steep slopes, locally revealing pre-2006 deposits on especially steep scarps. Narrow, blocky marginal terraces are present where a ridge to the west and a 50-m-high hill to the east funneled part of the flow (fig. 17*A*). The terraces, which apparently formed at ephemeral levels during the receding stage of the passing flow, are thus marginal relics of a fluid flow whose mass largely drained away and accreted downslope. Dozens of large blocks, 3 to10 m in diameter, dot the axial medial surfaces but are absent near lateral or distal deposit margins. Such blocks commonly have pyroclastic-debris aprons that ramp up on their stoss sides and streamline hollows on their lee sides (fig. 17*B*). Many blocks have patches of fine material, centimeters to a few tens of centimeters thick, with scattered lapilli and blocks perched on their tops (fig. 17*B*).

Along its eastern margin, the Rocky Point pyroclastic-flow deposit thins to a few centimeters and divides into numerous small tongues. These features were distinguishable in August 2006 from the subdued features of pre-2006 deposits only by the absence of moss and lichens. The western margin of the deposit is more readily delineated because there the flow lapped up on a prominent ridge, leaving behind not only deposits a few centimeters thick but also a fringe of scorched, broken, and denuded alders (fig. 17*A*).

Three distinct lobes of the Rocky Point pyroclastic-flow deposit fan across a flat surface north of an east-west ridgeline (fig. 17*C*). These lobes, which are about 10 m thick where flows debouched onto the plain, and thin to a few centimeters

Figure 16. Explosive-phase pyroclastic-current deposit (unit Expc) on north-slope lava flow (fig. 2*A*). *A,* Photograph of cross section, 80 cm thick, from the site of samples V303 and B215 near GPS station AV03, destroyed during event 10. Shovel is 50 cm long. *B,* Grain-size distribution plots of deposits at site illustrated in figure 16*A* and at two other sites. Relatively high fines content of sample B215A is unlike that of other samples from this deposit. *C,* Plots of lithologic components of fines-poor deposit. Deposit is more like those of continuous phase than those of explosive phase and proportion of dense clasts is greater than in other deposits, suggesting a lithologic transition from explosive-phase to continuous-phase magma composition. Sample locations are shown in figure 2*A* and table 2.



near margins, coalesce to form nearly continuous deposit along about 1.8 km of the plain from east to west (fig. 17*C*). Lobes exhibit radiating systems of low ridges and swales. Like those Cole and others (2002) describe in large dome-collapse pyroclastic flows at Montserrat, these linear features parallel flow directions. In cross section, ridges have gentle slopes and broad axes spaced 5 to 20 m apart transverse to flow directions. Swales anastomose in the downflow direction, such that individual ridgelines are rarely traceable more than a few tens of meters. The large blocks that protrude 2 to 5 m above the surface are concentrated within thick axial parts of the lobes and poke through both ridges and swales described previously. These large blocks are absent where deposits thin and thus rarely appear within 100 m of lobe margins. Like the axial blocks upslope, such large blocks commonly preserve accumulations of fine matrix and lapilli, 5 to 20 cm thick, on their tops. Lobe margins thin to a few centimeters and commonly concentrate broken and slightly singed alder branches (figs. 18*A*, 18*B*).

As the westernmost lobe spread westward, it buried a shallow pond, resulting in several openwork depressions surrounded by accumulations of fine ash on the surface of the deposit where the pond had been. The interaction of hot pyroclastic debris and underlying water must have generated steam that migrated through the deposits, winnowing fine ash to form elutriation pipes. The openwork depressions are the surface manifestation of these elutriation pipes, which are not exposed in cross section.

Figure 17. Photographs illustrating features of the Rocky Point pyroclastic-flow deposit (unit RPpf). *A,* Terrace formed shortly after peak flow, with subsequent channel drainaway during waning flow. *B*, Perched debris, debris rampart, and streamline hollow on this 8-m-high block suggest the following sequence: (1) flow was thick and energetic enough to move block 3 km into place; (2) subsequent flow was high enough over top of large block to leave debris; (3) waning flow formed a debris rampart and streamline hollow around block; and (4) highly fluid, waning flow drained downstream away from steep slopes, leaving thin deposits, locally less than 1 m thick. *C*, Flowpath illustrates approximate overall streamlines and three depositional lobes on low-lying apron north of volcano.

Thick fill deposits did not crop out by July 2008, intermediate ones have characteristics typical of pyroclastic flows, and thin ones have characteristics of surgelike flows. Deposits from about 0.3 to to more than 1 m thick are predominantly massive, though faintly inversely graded within their basal few centimeters (fig. 15*C*). Deposits not only thin toward lateral and distal margins but also fine (figs. 15*B*, 18*C*). Coarse deposits have modes in the coarse-ash to lapilli range, and fine marginal deposits have modes in the coarse-ash range (fig. 18*C*). Overall, the Rocky Point pyroclastic-flow deposit is relatively fines rich, containing 7 to 13 percent very fine ash, with the most fines rich parts at distal margins (fig. 18*C*).

The Rocky Point pyroclastic-flow deposit shows even more striking lithologic variations compared with earlier explosive-phase flows (units Expct and Expf) than does the coeval deposit (unit Expc). Friable high-silica andesite constitutes as much as 80 percent of clasts (excluding crystals) in most size classes, and low-silica andesite scoria generally less than 10 percent of the total (fig. 18*D*). White, high-silica andesite pumice is also a significant constituent, constituting as much as 20 percent of coarse to very coarse ash. Lapilli include significant proportions of both dense and scoriaceous low- to intermediate-silica andesite (fig. 18*D*).

Large blocks, 3 to 10 m in diameter, differ markedly in composition from lapilli and blocks smaller than about 1 m in diameter scattered on the surface of the deposit. The larger blocks that we examined consisted of uniform, intermediate-silica andesite or banded andesite. In contrast, in many areas, especially on distal fans, lapilli and smaller blocks at the surface consist predominantly of high-silica andesite. The huge blocks are probably too large to have been ejected from the vent during event 10, suggesting that this rock type originated by disruption of a dome that had grown between events 9 and 10. Smaller clasts carried on the surface to distal margins would have been emplaced last and therefore indicate the composition of the rock ejected from the vent during the last stages of event 10, after the capping domerock had been removed explosively. If these arguments are valid, event 10 disrupted a dome composed predominately of intermediate silica andesite, then tapped progressively deeper in the conduit and magma chamber to erupt high silica andesite, typical of late-stage event 10 and of the continuous-phase events that followed.

Continuous-Phase Deposits, January 28–February 10

The continuous phase began January 28 and lasted until February 10 (table 1). The first half of this phase, until about February 3, was marked by continuous emission of ash to heights below 4 km asl, punctuated by explosions that injected ash to 5 to 8 km asl (Schneider and others, 2006; Wallace and others, this volume). Direct observations of the volcano were hindered during this interval by poor weather and ashy haze, especially on the north flank (Coombs and others, this volume). Seismicity was dominated by flowage signals, which recorded the movement of pyroclastic flows down the north flanks (Power and Lalla, this volume). Fine, light-gray, massive ash deposits on the island likely represent elutriation from pyroclastic flows generated during this interval (Wallace and others, this volume). These observations, coupled with volume estimates (Coombs and others, this volume), suggest that rapid effusion of lava and dome collapse leading to numerous block-and-ash-flows dominated the early part of the continuous phase. From February 3 to 10, magma-flux rate waned, and a coherent lava flow and summit lava dome grew (Coombs and others, this volume).

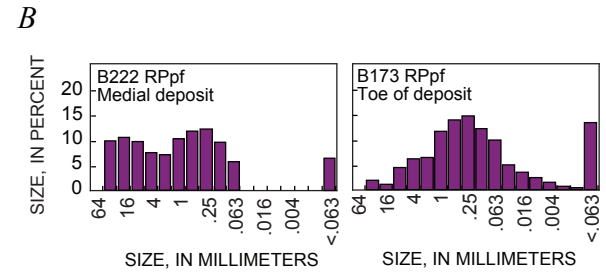
The early part of the continuous phase generated pyroclastic-flow deposits (units Cpf and Cpfw) and thin pyroclastic-current deposits (unit Cpc, fig. 2*C*). Secondary flowage deposits, such as avalanches and lahars, were not identified. Lava effusion during the second half of the continuous phase probably generated small block-and-ash flows, but these were likely covered by, and indistinguishable from, subsequent effusive-phase block-and-ash flows.

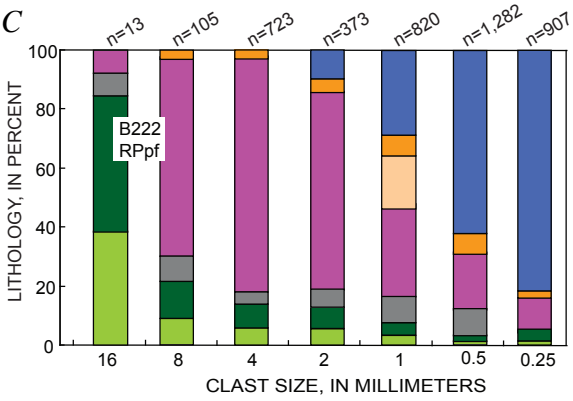
Flow Morphology and General Characteristics

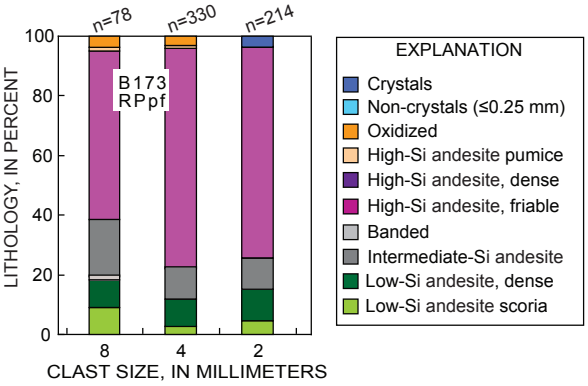
All pyroclastic-flow deposits of the continuous phase have similar composition, grain-size distribution, and outcrop characteristics but differ in morphology. Continuous-phase pyroclastic flows constitute thick, composite fans to the northeast and north of the summit (unit Cpf, fig. 2*C*). The Windy Creek pyroclastic-flow deposit (unit Cpfw, fig. 2*C*), however, is an anastomosing deposit on the northwest flank, which, on the basis of the timing of destruction of a seismometer on that flank (Coombs and others, this volume, fig. 15), we surmise was emplaced during a particularly large single-flow event. The continuous-phase pyroclastic current (unit Cpc) is a thin marginal facies emplaced coevally with the two pyroclastic-flow deposits described above. Unlike explosive-phase flows, continuous-phase flows were all restricted to the north quadrant of the volcano (fig. 2*C*).

The north and northeast fans of continuous-phase pyroclastic flows reach from the summit to about 100 m asl. Flows in the north fan traveled downslope between a cleaver and a prehistoric lava-dome remnant, and those in the northeast fan flowed down the Northeast Chute (fig. 2*C*). Prominent lateral-flow levees, rich in large blocks, define dozens of overlapping flow lobes, especially in the upper reaches of the fans (fig. 19*A*). The lower halves of these two fans spread out and overlap downslope of the cleaver. The lower edges consist predominantly of multiple, lobate fingers, as far as 4 km from the summit. Subdued levees define some flow margins, but elsewhere the distal lobes fan out with indistinct edges (fig. 19*B*). Although most flows traveled over unvegetated terrain, some lobes struck and singed alders near their termini. Comparison of digital terrain models of the volcano's edifice from before and after the continuous phase suggests that the two fans are as much as 20 m thick in their









upper reaches (Coombs and others, this volume), whereas individual lobes are generally only as much as 2 m thick.

The Windy Creek pyroclastic flow (unit Cpfw, fig. 2*C*) was the only continuous-phase flow to travel northwestward; it fanned out over the northwest flank in a series of channels as it followed topographic lows over the somewhat-hummocky topography (fig. 19*C*), finally stopping about 50 m asl. The destruction of seismic station AU12 (fig. 2*C*) within its pathway pinpoints its emplacement at 03:24 AKST January 30 (Coombs and others, this volume). The deposit contains abundant blocks, as large as several meters across, that commonly form lateral levees alongside wide, flat-bottomed channels.

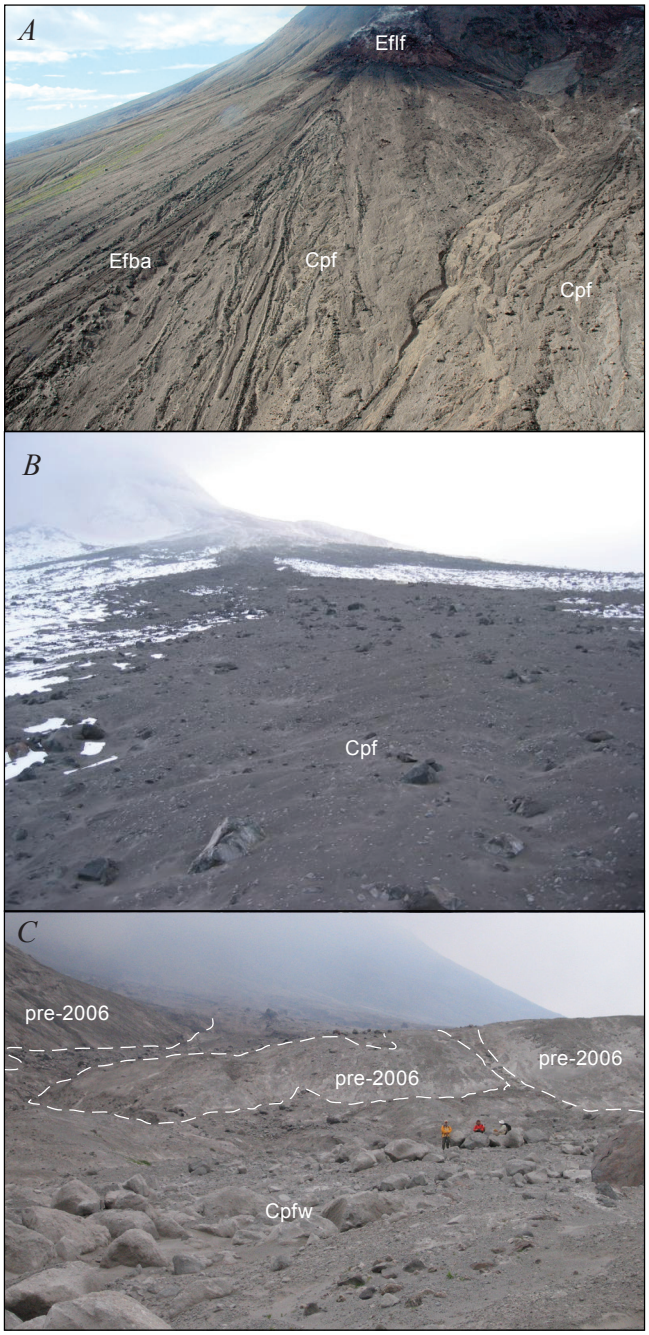
The thin pyroclastic-current deposit (unit Cpc, fig. 2*C*) is mapped in several locations as a featheredge facies of continuous-phase flows alongside margins of thicker flows, or where continuous-phase flows lap onto topographic highs. The deposit is generally less than 0.2 m thick and in some places consists only of scattered clasts of friable high-silica andesite atop the pre-2006 surface (Coombs and others, this volume, fig. 15).

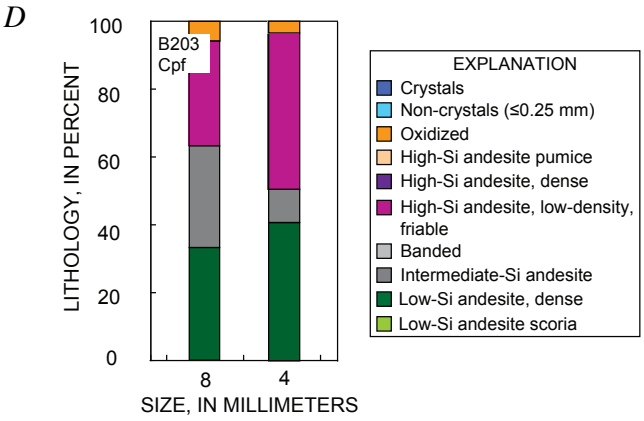
Grain-size distributions in continuous-phase pyroclastic-flow deposits are similar to those in earlier pyroclastic-flow deposits, particularly the coarse explosive-phase deposits. Grain-size distribution in continuous-phase flow deposits is moderately bimodal, with modes in lapilli and medium-ash size classes (fig. 7*A*).

Continuous-Phase Compositions

The shift in eruptive style that began during event 10 continued during the continuous phase and corresponds with a shift in lithologic composition. As revealed in pebble counts and lithologic analysis, continuous-phase composition vary somewhat among individual deposits but generally the deposits are rich in high-silica andesite, dense intermediate-silica andesite, and banded clasts, with slightly less dense low-silica andesite and basically no low-silica andesite scoria (figs. 4, 19*D*; tables 6, 7).

Figure 18. Rocky Point pyroclastic-flow deposit (unit RPpf), with grain-size characteristics and lithologic components. *A,* Photograph of distal-lobe margins marked by scorched willow branches and large lapilli (sample location B173). Arrow denotes the flow direction. Shovel is 50 cm long. *B*, Histograms of grain-size distribution of medial and distal deposit. Toe of deposit, which was not overlain by lobes of later flow pulses, is finer than more proximal deposits. *C*, Plots of lithologic components of the Rocky Point pyroclastic-flow deposit. Deposit contains abundant friable, high-silica andesite, a rock type also characteristic of subsequent continuous-phase deposits. Sample locations are shown in figure 2*B* and table 2.





The appearance of continuous-phase deposits shows the shift toward more silicic clast compositions: the deposits are characteristically pale brownish-pink to gray, lighter colored than the explosive- and effusive-phase deposits.

Effusive-Phase Deposits, March 3–16

The effusive phase began after an eruptive hiatus from about February 10 to March 3 (table 1). Whereas effusion of coherent lava lobes northward and northeastward began at the summit near the end of the continuous phase in early February, these lobes were enlarged during the effusive phase, and block-and-ash-flow deposits from February were buried by the products of March activity.

Effusion ultimately produced low-silica andesite in the form of a summit lava dome and two lava flows, descending northward and northeastward from the vent. As the lava emerged and became unstable, blocky material dislodged to form talus deposits, and caused rockfalls and gas release. The release of gas from the fragmenting lava generated block-and-ash flows that traveled down the north, northeast, and east flanks of the volcano (fig. 2*D*).

Talus Deposits

Aprons of rockfall deposits skirt the front of the northern and northeastern lava flows (unit Efta, fig. 2*D*). The deposits are highly oxidized, blocky, and unstable, and extend approximately 75 to 100 m beyond the lava flows (figs. 20*A*, 20*B*). These deposits were not sampled, owing to their instability and proximity to the oversteepened lava-flow fronts. We estimate the thickness of these talus aprons at 5 to 20 m.

Block-And-Ash-Flow Deposits

Block-and-ash flows were initiated from four areas: (1) the effusive-phase lava dome, (2) the front of the northern lava flow, (3) the front of the northeastern lava flow, and (4)

Figure 19. Photographs and lithogic components of continuous-phase pyroclastic-flow deposits (units Cpf and Cpfw). *A*, Continuous-phase deposit (unit Cpf) below effusive-phase lava flow (unit Eflf) on northeast flank of volcano. Thin, dark fingers of effusive-phase block-and-ash-flow deposit (unit Efba) sit atop overlapping, leveed lobes that compose deposit (unit Cpf). *B*, Distal toe of farthest-reaching part of deposit (unit Cpf) on north fan. Some distal parts of deposit lack levees and instead have featheredges. *C*, Windy Creek pyroclastic-flow deposit (unit Cpfw). Flow swept around and over topographic highs on northwest flank, with little deposition on steep lee slopes. *D*, Plot of lithologic components of deposit. Sample locations are shown in figure 2*C* and table 2.

the top and margin of the northeastern lava flow, which then traveled down East Chute (fig. 2*D*). The block-and-ash flows formed distinctive black, blocky, narrow tongues that are visible beyond the apron of varying and jumbled talus blocks (unit Efba, figs. 2*D*, 20*C*, 20*D*). The long, lobate deposits commonly have blocky levees. The northeastern block-and-ash-flow deposit is estimated to average 6 m in thickness, whereas the others average less than 3 m. Grain-size characteristics of this block-and-ash-flow deposit suggest concentrations of coarse lapilli and coarse ash and an absence of fine ash (fig. 2*E*).

Lithologic analyses indicate that effusive-phase pyroclastic-flow deposits contain significantly more low-silica andesite clasts than do either explosive- or continuous-phase deposits (figs. 4, 20*F*). Very few of these low-silica andesites are scoriaceous. The effusive-phase deposits also contain small to modest proportions of intermediate- and high-silica andesite (figs. 4, 20*F*). Hydrothermally altered and oxidized clasts are more common in effusive-phase block-and-ash-flow deposits than in the pyroclastic-flow deposits of other phases. Huge blocks of oxidized material, as large as several meters across, are common in outcrop.

Discussion

Lithologic Composition and the Three Eruptive Phases

Our field observations in August 2006 quickly revealed that the three eruptive phases were unique, not only in terms of style of volcanism, including associated seismicity, geodetic response, and ash emissions, but also in terms of the types and morphologies of deposits that were produced and, in particular, of their lithologic composition (fig. 4). Two important characteristics were revealed through lithologic analysis of the 2006 flowage deposits: (1) each lithology is present in the deposits of each eruptive phase and in each flow type, and (2) the lithologic proportions are unique to and consistent in the deposits of each eruptive phase.

Lithologic analysis reveals systematic changes in magma composition and clast texture during the 2006 Augustine eruption. Deposits of the three eruptive phases varied in composition and clast type, although a single rock type or group of rock types dominated each phase (figs. 4, 21, table 7). Thus, the explosive phase predominantly produced low-silica andesite, mostly as scoria, but also as 10–20 percent dense clasts; the continuous phase predominantly produced high-silica andesite and lesser intermediate-silica andesite and banded clasts, with clasts of all compositions varying in vesicularity; and the effusive phase produced an even higher proportion of low-silica andesite than the explosive phase, mostly as nonvesicular to sparsely vesicular clasts. Most clasts larger than 1 cm in diameter in effusive-phase block-and-ash flows are low-silica andesite (fig. 21).

Lithologic transitions coincided generally, but not exactly, with shifts in style of volcanism as marked by the three eruptive phases. Explosive-phase deposits of events 3 through 9 (Jan. 13–17) are lithologically similar, whereas event 10 (Jan. 28) yielded two flows whose lithologic composition differed from that of flows erupted earlier. The 9-minute explosion generated the pyroclastic-current that draped the north-slope lava flow and the voluminous Rocky Point pyroclastic flow, marking not only a transition from intermittent vulcanian explosions to continual dome collapses, but also a compositional transition within pyroclastic deposits from primarily scoriaceous, low-silica andesite to primarily friable, high-silica andesite (table 5). This compositional shift began the transition from the explosive to the continuous phase.

Disruption of two lava domes that had grown before event 10 (between Jan. 13 and 27) probably influenced the compositional shift, particularly in dense rock types, within event 10 pyroclastic deposits, but the tapping of a deeper, more silicic magma caused the most striking lithologic shift (figs. 4, 21, table 7; Larsen and others, this volume). The older dome (unit Exd1, fig. 2*A*), emplaced January 14–17, and shallow residual magma in the conduit are two possible sources of the dense, low-silica andesite clasts within the event-10 deposits, the pyroclastic current (unit Expc) and Rocky Point pyroclastic-flow (unit RPpf. A younger, explosive-phase lava dome (unit Exd2, figs. 2*A*, 21), composed of intermediate- to high-silica andesite and banded andesite, was extruded between events 9 and 10 (Jan. 17 and 27). Disruption of this younger dome may have generated the huge intermediate-silica andesite blocks within the Rocky Point pyroclastic flow and partly caused the increases in dense high-silica andesite within the deposits of both event 10 pyroclastic deposits. We conclude that pulverization of the domes caused increases in nonvesicular magma, resulting in inclusion of dense clasts in event 10 ejecta. Concentrations of more vesicular high-silica andesite within the Rocky Point pyroclastic-flow deposit, especially in distal areas and on the deposit surfaces, originated from the vent last and indicate the tapping of a deeper, more silicic magma body during event 10 that continued during the continuous phase (Larsen and others, this volume).

The proportions of low- to intermediate- to high-silica andesite in clastic deposits changed abruptly during event 10, at the start of the continuous phase, and again after the hiatus that preceded the effusive phase (figs. 4, 21). These trends heralded changes in eruption rate, magma composition, and gas content. During the explosive phase before event 10, proportions were about 70:15:15. During event 10 proportions showed a rapid change to 38:27:35 and then to 20:15:65. Subsequently, pyroclastic-flow deposits emplaced during the continuous phase contained no scoria, but enough dense low-silica andesite to change proportions to approximately 25:35:40. Probably, the magma had become sufficiently gas poor and had extruded slowly enough that no vesicular low-silica andesite ejecta formed, and fewer than a third of the ejecta were composed of dense, low-silica andesite. During

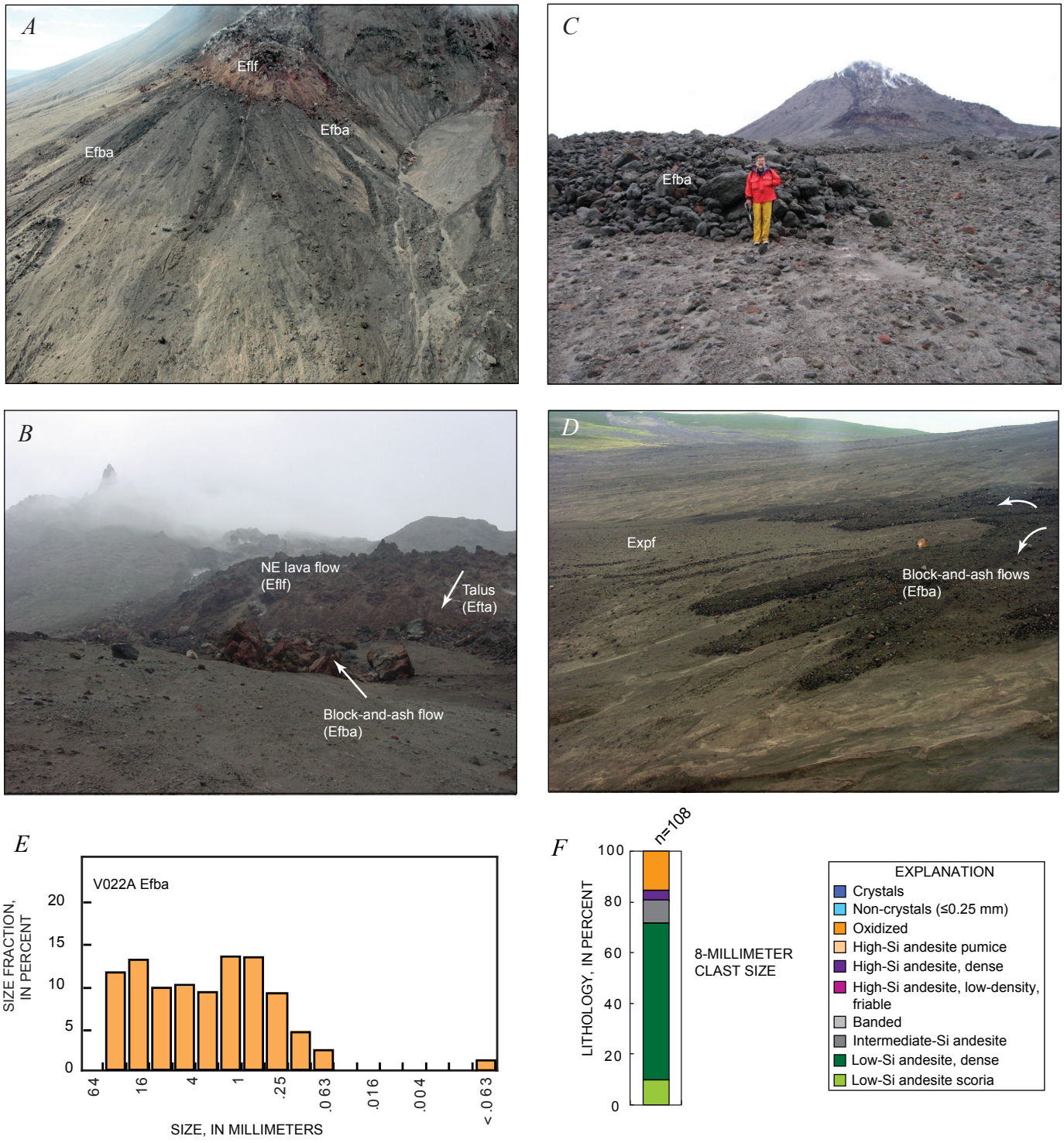


Figure 20. Photographs, plot of grain-size distribution, and lithologic components of effusive-phase block-and-ash-flow deposit (unit Efba). *A*, Aerial view south towards effusive-phase block-and-ash-flow deposit (unit Efba) and lava flow (unit Eflf). *B*, View of the northeast lava flow (unit Eflf), rockfall talus apron (unit Efta) below lava, and short block-and-ash-flow deposit (unit Efba). *C*, Distal margin of block-and-ash-flow deposits (unit Efba). *D*, Oblique aerial view of distinctive black block-and-ash-flow deposits in East Chute area. These deposits resulted from fracturing and collapse of parts of new lava flow. *E*, Grain-size distribution of block-and-ash-flow deposits. *F*, Plot of lithologic components of block-and-ash-flow deposit. Sample locations are shown in figure 2*D* and table 2.

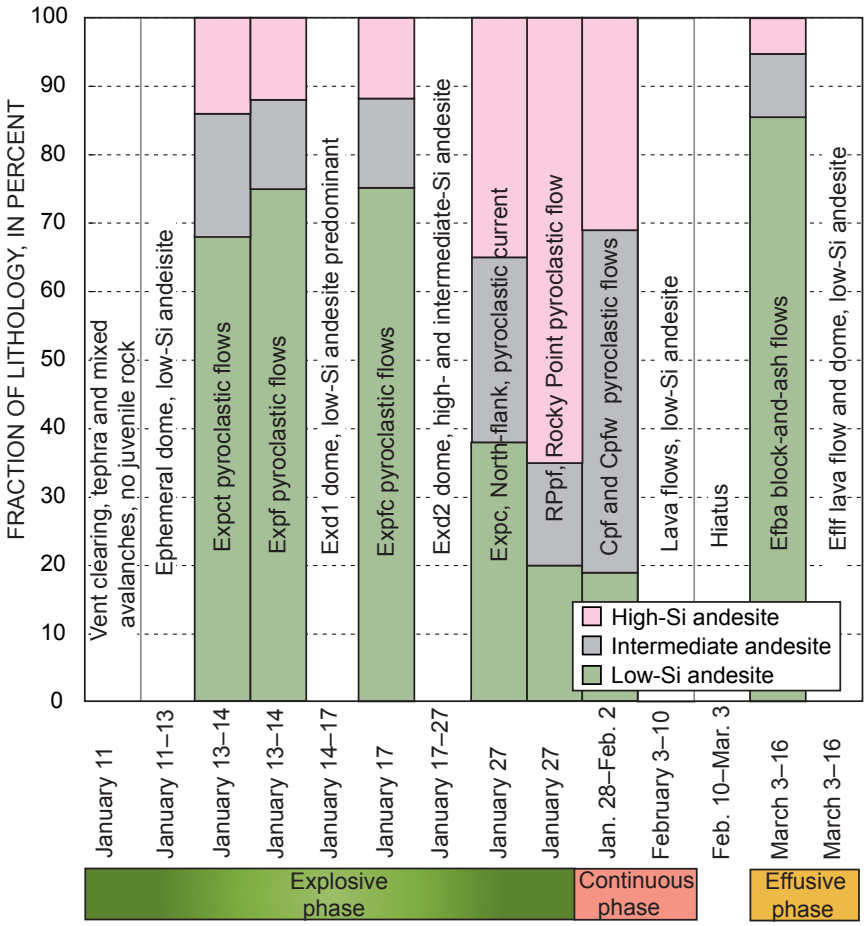


Figure 21. Plot summarizing chronologic changes in chief lithologic components in deposits of 2006 eruption of Augustine Volcano. Proportion of low-silica andesite, initially high, diminished at end of explosive phase and during continuous phase as proportion of intermediate- and high-silica andesite increased. These trends reverse from continuous phase to effusive phase. Low-silica andesite increased during the effusive phase and changed from being predominantly scoriaceous during the explosive phase, to predominantly dense during the effusive phase.

the continuous phase, proportions of both intermediate- and high-silica andesite increased significantly.

Banded clasts, which include any combination of compositions, most commonly compose bands of high- and low-silica andesite (table 4; Larsen and others, this volume). The proportions of banded clasts in the deposits varied widely but were largest in continuous-phase deposits (fig. 4), suggesting that mixing of low- and high-silica andesite magmas was common throughout the eruption but probably greatest during the continuous phase. Larsen and others (this volume), interpret the intermediate-silica andesite to be the product of complete mixing between high- and low-silica andesitic magmas.

Effusion of low-silica andesite lava began before the end of the continuous phase and continued during the effusive phase, producing block-and-ash flows predominantly composed of dense, low-silica andesite, sparse scoria, and about 13 percent high-silica andesite (figs. 4, 21, table 7). Larsen and others (this volume) suggest that the waning stages of the continuous and the effusive phase extruded the last dregs of eruptible high-silica andesite magma along with low-silica andesite lavas. High-silica andesite clasts in block-and-ash flows derive from inclusions of such material within the lava flow itself or from erosion and incorporation from underlying, continuous-phase pyroclastic-flow deposits.

Origin and Downslope Behavior of Pyroclastic Currents and Flows

During the 2006 eruption of Augustine Volcano, the chief factors that influenced pyroclastic-flow behavior and the nature of their deposits were genesis, grain size, and the characteristics of the surface over which they flowed. Column collapse from short-lived vulcanian blasts, dome collapse, and the collapse of viscous lavas on steep slopes caused the pyroclastic currents documented in this study.

Column-collapse flows during the explosive phase spread widely and probably were dilute and laterally mobile where they overran snowpack. Subsequent flows had similar fines content but were confined to drainages. This change in flow morphology occurred once previous pyroclastic flows had either melted the snowpack or coated the snow with layers of pyroclastic debris sufficiently thick to insulate new flows from the underlying snow. In contrast, the dome-collapse Rocky Point pyroclastic flow and the continuous-phase flows involved neither column collapse nor the influence of underlying snow. Only the Rocky Point pyroclastic flow, possibly because it was more voluminous and finer grained than subsequent flows, showed evidence of appreciable dilution as it moved. The dome failure that generated the large-volume

Rocky Point pyroclastic flow may have been deeper seated than subsequent dome-collapse flows, thereby unloading incompletely degassed lava that decompressed explosively to inflate the initial pyroclastic mass. The subsequent continuous-phase flows behaved as partially fluidized granular flows. In contrast, effusive-phase block-and-ash flows were caused exclusively by collapses of andesite lava-flow margins. These block-and-ash flows, though hot, were sufficiently coarse and permeable that gas escaped rapidly and lapilli and blocks were mostly supported by particle-to-particle contacts. These flows behaved basically as rock avalanches because their ash-and-gas mixture provided little fluidization to ameliorate their frictional-granular characteristics.

Formation of Levees and Digitate Margins During Pyroclastic-Flow Emplacement

Scoria-rich column-collapse flows of the explosive phase, dome-collapse flows of the continuous phase, and block-and-ash flows of the effusive phase all behaved similarly, regardless of their diverse origins, to produce deposits with coarse blocky levees and digitate distal margins, a morphology indicative of partially fluidized, granular flows with high solids fractions (fig. 22). Some of these pyroclastic flows may have been highly energetic on steep slopes near their source, but as they descended the volcano's slopes, hot particle and gas mixtures settled to form granular basal flows that moved across intermediate and gentler slopes of the volcano's apron. Overriding, elutriate ash clouds (fig. 5*A*) would have obscured basal granular flows. Once the pyroclastic flows began to decelerate, large, low-density particles began to migrate to the surfaces of the basal granular flows (figs. 9, 22*A*). The surface velocities of such granular flows are greater than those of propagating flow fronts; thus, particles at the surface migrate toward distal and lateral margins, where they accrete particle by particle, and then lag behind the moving flow to form levees (fig. 22*B*; for example, Lube and others, 2007). Fines-poor aggregations of outsize low-density particles that accrete at active flow fronts influence the behavior of the granular flow in two ways. First, because the largest particles in natural grainflows are commonly more angular than smaller ones, the coarse mixture at the front of flows may develop a greater Coulomb friction than in the finer following flows (Pouliquen and others, 1997). Second, coarse mixtures that form at flow margins are generally more permeable than finer interior flows. Because fluid, in this case gas, can more readily escape from the coarse and, therefore, permeable flow fronts than from the relatively less permeable ash-rich flows that follow, flows evolve Coulomb-friction-dominated perimeters that encompass fluidized or partially fluidized interiors, for example, in debris-flow systems (Iverson, 1997). More mobile debris that pushes a perimeter of less mobile debris results in unstable flow and the formation of large-particle-rich clefts and lobes at propagating flow fronts (Pouliquen and Vallance, 1999). When such partially fluidized, granular pyroclastic flows come to rest, they preserve clefts, lobes, and finger-shaped bifurcations as digitate deposit margins that are relics of granular-flow instabilities (fig. 22*A*).

A similar segregation process can occur with low-density particles and cause cleft-and-lobe structures. Vallance and Savage (2000) show that density segregation, though dependent on a different sorting mechanism than size segregation, is highly efficient in the upper parts of granular flows. Thus, if a flow contains large, low-density particles, such as pumice or scoria, these particles will migrate to the surface, where velocities are highest, and then move toward flow margins. If the perimeter thus formed is more frictional than the interior flow, a flow instability results, and the flow breaks into clefts and lobes. Again, the mechanism depends on the granular character of the flow; however, optimal density segregation occurs in more energetic granular flow than does optimal size segregation (Vallance, 1994; Vallance and Savage, 2000).

In such natural phenomena as pyroclastic flows, the granular material traps gas, which, if it cannot readily escape, partially supports the weight of the particles. The medium is then partially fluidized and thus flows more easily downslope. Pouliquen and Vallance (1999) modeled such flows in the laboratory by pouring aerated 500°C ash or sand down an inclined surface. The granular, sediment-rich basal avalanches control the behavior of these flows. Segregation of large, low-density particles that initially move upward and then toward flow fronts, as well as elutriation of small particles at flow fronts, ultimately forms coarse, permeable perimeters that are dominated by Coulomb friction (Pouliquen and Vallance, 1999). Consolidation of solids and entrapment of gas generate fines-rich flow interiors that are partially fluidized (Pouliquen and Vallance, 1999, fig. 7). As the flows slow and eventually come to rest, frictional contrasts with the bed—large at the flow perimeter and small in the fluid flow interior—cause flow instabilities that commonly result in digitate deposits similar to the flow fingers observed at Augustine Volcano in 2006 (fig. 22).

Behavior of Energetic Pyroclastic Currents—Implications for the Generation of Their Deposits

The initial pyroclastic-flow deposits of the explosive phase, and those from a vigorous dome collapse during event 10, share characteristics which indicate that they were energetic and diluted by gas ingestion as they moved. Such features include widespread, but thin, deposits; gradual thinning of deposits at lateral and distal margins and an absence of lateral or distal levees; the presence of large blocks in thick axial deposits and the absence of such blocks near margins; the presence of deposits on topographically high areas; evidence of vigorous elutriation, such as fines-deficient "lag" deposits and cogenetic fine marginal deposits; and temperatures insufficient to burn vegetation or completely melt underlying snow. On the basis of the deposits that these dilute, energetic flows produced, the most important processes are settling of large and dense blocks into thick, fluid axial parts

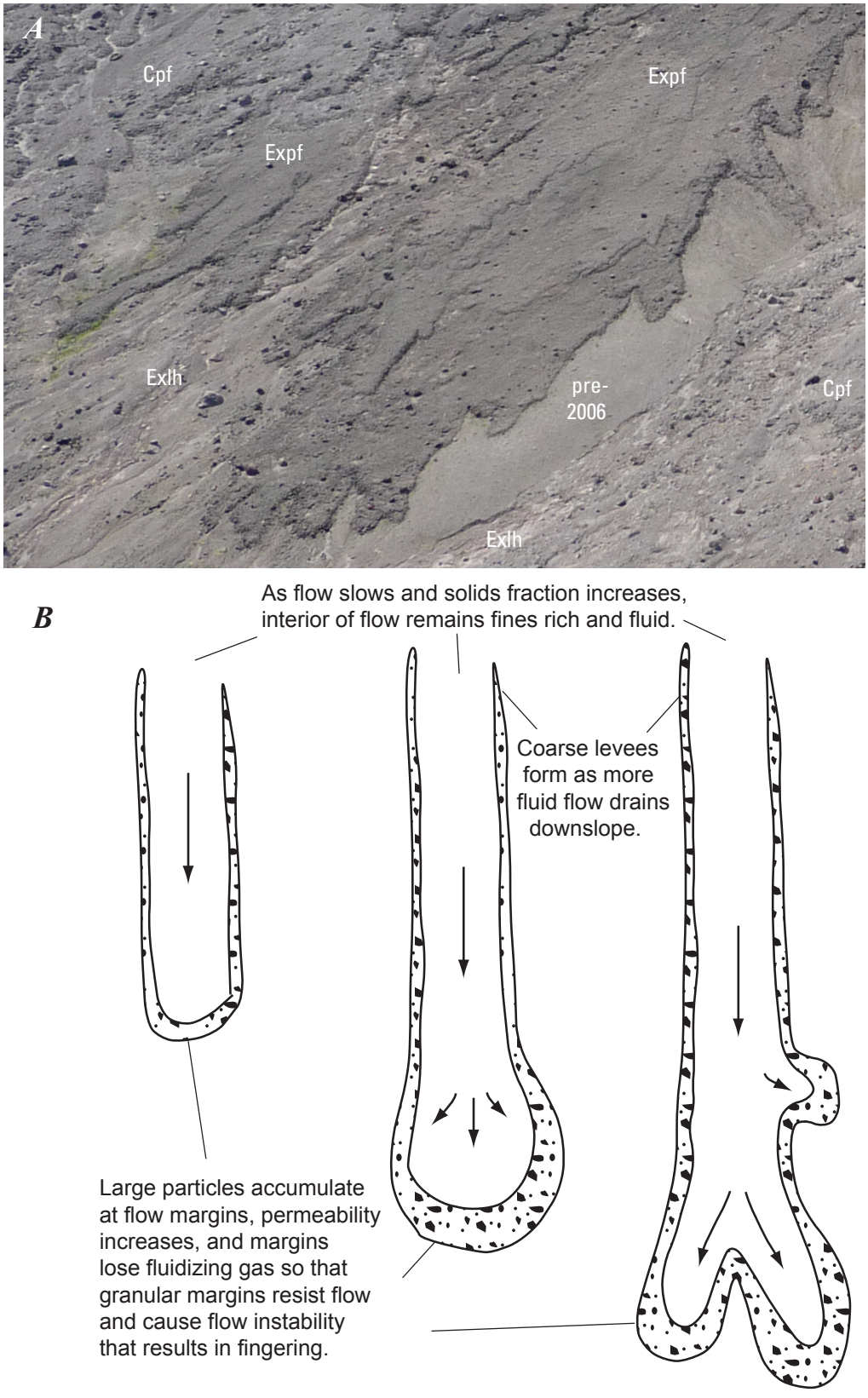


Figure 22. *A,* Oblique aerial photograph of part of northeast fan, showing coarse blocky digitate margins of explosive- and continuous-phase pyroclastic-flow deposits (units Expf and Cpf). *B*, Line drawing illustrating evolution of fingering in moving pyroclastic flow.

of the flow; elutriation of fine ash to form proximal lag facies and marginal fine surges, and a propensity to spread laterally, especially across snow-covered slopes. Each of the three types of explosive-phase deposit documented in this study exhibit some, but not all, of these features.

The Rocky Point pyroclastic flow originated as a large dome collapse that probably caused a sudden depressurization of deep-seated lava; it then evacuated the entire conduit and must have tapped into a magma "chamber" at 4- to 6-km depth. The collapse and decompressively vesiculated conduit magma generated a surge-like flow whose deposits fine and taper to thin margins, despite the enormous blocks contained in axial zones. The deposit shows notable drainaway features, such as stranded terraces (fig. 17*A*), matrix debris perched on blocks whose tops reach 8 m above the deposit surface (fig. 17*B*), and pre-2006 scarp surfaces that protrude through axial, meters-thick deposits lying on gentler slopes in adjacent areas. Cole and others (2002) described voluminous pyroclastic-flow deposits at Montserrat that originated from dome collapse and share many characteristics with the Rocky Point pyroclastic-flow deposit. For example, the Montserrat deposits also contain large blocks with matrix debris perched on their tops, indicating flow depths greater than local deposit thicknesses. Similarly, ridge-and-swale features, concentrations of low-density clasts, and tree fragments characterize distal zones. In the Rocky Point pyroclastic-flow deposit, we additionally noticed pyroclastic debris ramparts piled up on the stoss sides, and streamline hollows on the lee sides, of large blocks that had been grounded on steep slopes early in the depositional sequence (fig. 17*B*). Cole and others (2002, fig. 22) inferred that as these sheetlike flows decelerated, the upper parts of the flow drained downslope to form tapering, distal deposits with concentrations of low-density particles at their surface. On gently sloping fans, swales (inappropriately called furrows by Cole and others) are radially oriented parallel to flow but exhibit subordinate anastomosing patterns that divide and truncate the gently sloping ridges parallelling them. The large blocks are distributed 100 to 500 m inboard of the deposit margins situated both on ridges and in swales. We infer that the complex anastomosing swale patterns were paths followed by the most fluid pyroclastic debris as it drained away from material slightly more resistant to flow along ridges, while simultaneously following predominantly radial flow directions. On the basis of their characteristics, we concur with Cole and others (2002) that large dome-collapse pyroclastic flows like those at Montserrat and Rocky Point moved as a sheetlike body that drained away downslope, stranding huge blocks along slopes and fan apices. When it reached low-gradient slopes, the flow accreted incrementally at fan apices to form ~10-m-thick accumulations, and the overriding flow pushed downslope to produce fines-rich deposits, rich in low-density particles, that thin gradually toward distal margins.

The distribution and characteristics of the pyroclastic-current deposit (unit Expc, fig. 2*B*) suggest that it was the energetic product of laterally directed explosions at the beginning of event 10. Its deposit is similar to initial explosive-phase pyroclastic currents (unit Expct), but differs notably in its ubiquitous friability, mostly lacking fine matrix particles, and its distribution across the axis of a 50- to 100-m-high ridge. Even though it flowed across snowy slopes, the pyroclastic current did not generate lahars. The deposit at distal margins fines and tapers to thin edges. We infer that this deposit was emplaced by a surge-like flow because of its distribution on a high ridge and its lack of fine particles. Explosions directed northward at the beginning of event 10 probably initiated the pyroclastic current.

Initial pyroclastic flows of the explosive phase (unit Expct, fig. 2*A*) invariably flowed across snowpack, scoured it, and commonly came to rest on snow; thus, this underlying snow, rather than conditions at the vent, chiefly controlled both flow behavior and deposit characteristics (fig. 23). Deposits preserved on top of snow suggest that flows had cooled significantly to near-ambient temperatures during transit. This observation implies considerable heat transfer because pyroclasts exited the vent at temperatures in excess of the solidus temperature (Larsen and others, this volume). We infer that ingestion and vaporization of snow fluidized the flows so that the resulting deposits are widespread, commonly thin, and thin toward their lateral margins but do not fine there. Unlike the Rocky Point pyroclastic-flow deposit, these deposits rarely are more than 1 m and commonly only 10 to 20 cm thick (fig. 5*B*). Because the flows originated by column collapse of short-lived vulcanian plumes rather than by dome collapse, they did not carry outsize blocks. Blocks smaller than 1 m across are scattered across deposit surfaces, even near margins (fig. 5*C*). Where emplaced on windswept snow-free terrain, the deposits are smooth surfaced and thin toward margins. These deposits' distal margins rarely are preserved because distal parts of the deposits generated lahars and mixed avalanches. The evolution and behavior of these flows across snow are discussed in more detail below.

Behavior of Pyroclastic Flows Across Snow and the Evolution of Mixed Avalanches and Lahars

Theoretical analysis and experimental results by Walder (2000a,b) suggest a mechanism whereby initial pyroclastic flows can spread across snowpack and generate mixed avalanches and lahars. Pyroclastic flows can erode substrates formed of snow or ice through a combination of mechanical and thermal processes at the bed. Walder shows both theoretically (2000a) and experimentally (2000b) that thermal scour can effectively incorporate snow at the base of a pyroclastic flow. The fundamental cause of thermal scour is unstable fluidization of the pyroclast layer by a brief, intense burst of vapor at the instant when hot grains contact snow that involves vapor bubbling and particle convection which disrupt the snow surface (Walder, 2000b). The analysis shows that an upward flux of water vapor immediately upon pyroclastic-flow contact with snow can be great enough to fluidize the pyroclastic layer efficiently under the proper conditions. Those conditions are

a function of emplacement temperature, overburden pressure or pyroclastic-flow thickness, and grain size, as illustrated in figures 24*A* and 24*B*. If vaporization is sufficient, hot pyroclastic material is efficiently mixed with underlying snow, and melting is enhanced. The tendency toward fluidization at the interface can enhance both the mobility of a pyroclastic flow and its ability to form slurries of snow, water, and pyroclastic material that may later coalesce and flow downstream. Increase in temperature and decrease in grain size favor fluidization at the interface, but the relation to overburden pressure is more complex. Overburden pressure at the interface enhances fluidization to a point where total load is too great and then suppresses the process (fig. 24*A*).

We can approximately constrain the overburden pressure P for Augustine flows by using deposit thickness, solids fraction, and rock density as proxies in calculating values for the actual flow, such that $P = \nu\rho_{rock}gh$, where the solids fraction ν of the deposit is about 0.4 to 0.5, the density of the rock ρ_{rock}

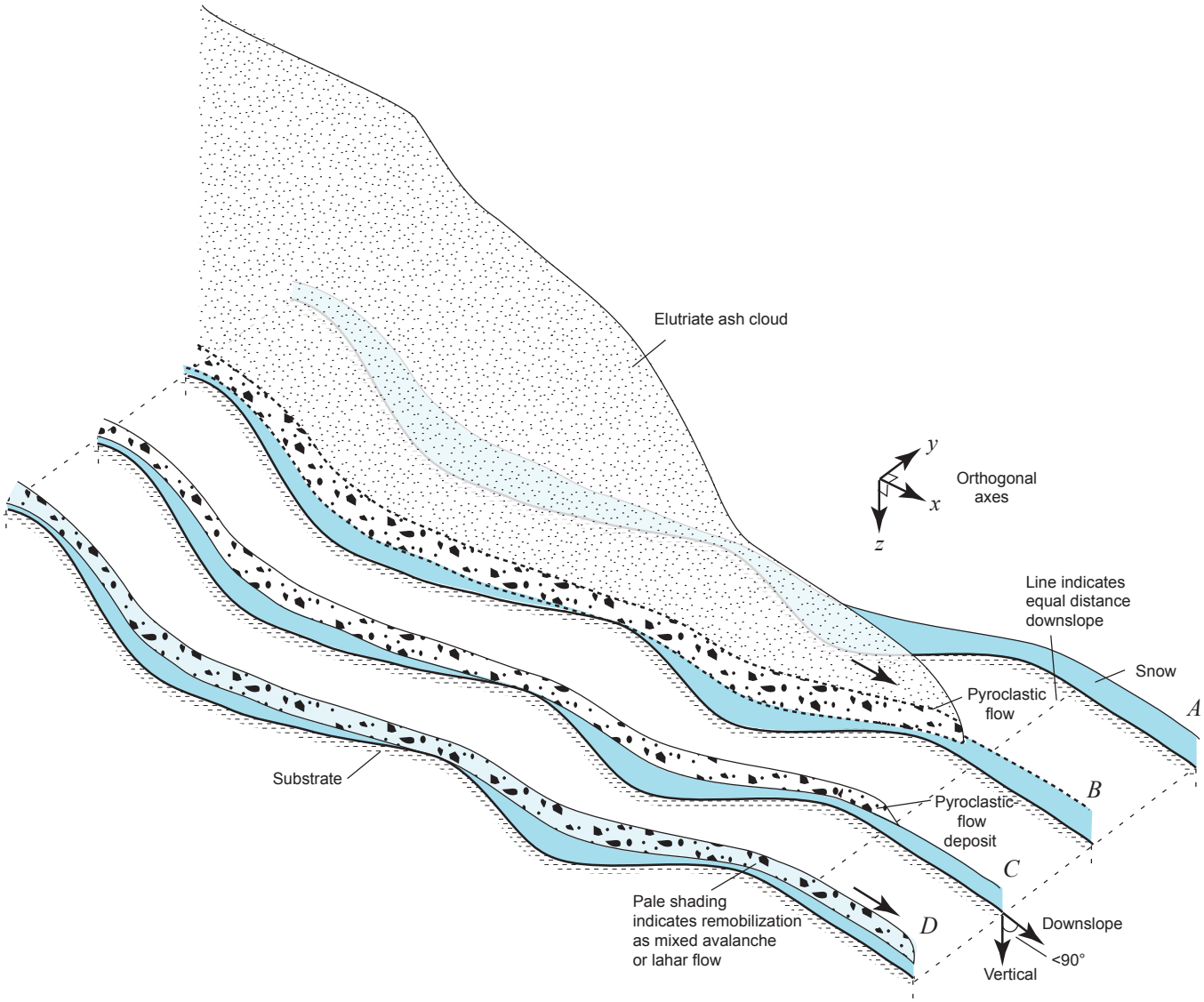
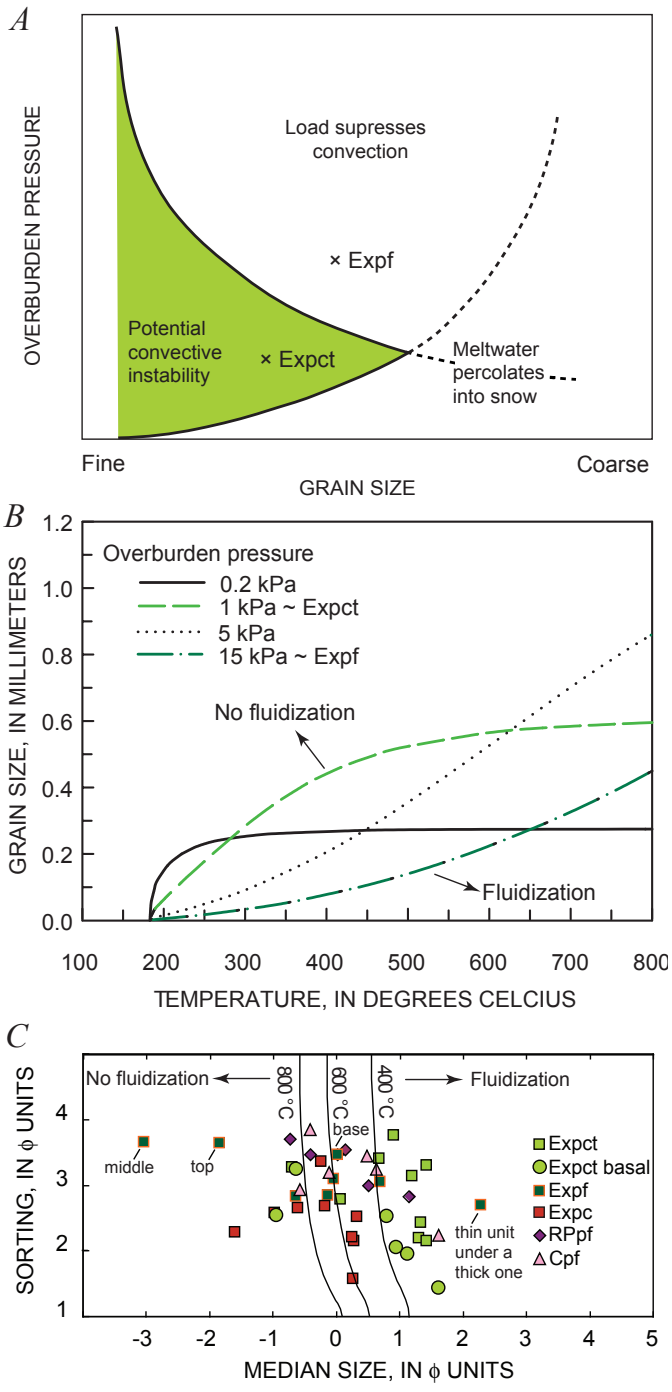


Figure 23. Schematic sketches of successive stages in the interaction of a pyroclastic flow with snow. *A,* Initial snow-covered slope. *B*, How a pyroclastic flow might move across snow, partially eroding and incorporating it. *C,* The pyroclastic flow stops briefly or decelerates almost to a stop. *D*, Finally, a mixture of snow, water, and pyroclastic debris begins to move and forms mixed avalanches (or lahars). Field evidence supports either sequence *A–B–D* or *A–B–C–D* but cannot distinguish whether pyroclastic flows come to a complete stop before initiating mixed avalanches or merely decelerates. Once in motion, mixed flows likely contain hot or warm pyroclastic debris, especially large particles, which can continue to convert snow to water through heat exchange, allowing the mixture to become progressively wetter with distance downstream.

is 1,600 to 2,600 kg/m^3, g is the gravitational constant, and h is the deposit thickness. Vaporization of snow dilutes moving flows, so that flow depth would have been greater than the thickness of deposits, but the solids fraction would probably have been correspondingly smaller, and so our simple calculation is not unreasonable. A further assumption is that the gas phase largely supports the pyroclasts, so that hydrostatic and total pressures are approximately equal. This assumption implies that the flow is fully fluidized—basal fluid pressure would diminish in the degree to which fluidization is partial. Our estimated P values for the initial thin pyroclastic current (unit Expct, fig. 2*A*) that initiated mixed-avalanche and lahar flows, using h = 0.1–0.2 m, are about a tenth (0.6–2.5 kPa) of those for subsequent flows; they appear to lie in the field where fluidization is favored (figs. 24*A*, 24*B*). The subsequent flows (unit Expf, fig. 2*A*) yield estimated overburden pressures that may fall in the field of suppressed fluidization where P = 8–20 kPa and h = 1–2 m (fig. 24*B*). Fine-grained pyroclastic flows are more apt to fluidize snow substrates than are coarse-grained flows—in fact, within reasonable, pyroclastic-flow temperature ranges of 300–800°C, grain size is a more important factor than temperature for inducing thermal scour (figs. 24*A*, 24*C*). Our grain-size data show that the initial thin pyroclastic current (unit Expct), which was generally finer grained than those that followed, falls in a field favorable to thermal scour of snow and coeval fluidization (fig. 24*C*). Lastly, we note that tephra-fall and pyroclastic debris from previous eruptions insulated underlying snow from subsequent flows (fig. 5*A*), greatly diminishing their facility for efficient thermal scour or fluidization.

Initial pyroclastic flows of the explosive phase invariably generated lahars and mixed avalanches, but some of these secondary flows were wetter and more laharic than others. Apparently, the resulting mixtures were sensitive to the available proportions of hot pyroclast material and snow. On the east side of the volcano, secondary flows were quite watery, and recognizable mixed-avalanche deposits are small or absent. In contrast, on the south side of the volcano, mixed-avalanche deposits predominate in medial reaches and form extensive marginal terraces and axial islands in distal reaches, as illustrated in Augustine Creek (figs. 2*A*, 13).

On the basis of field observations, our conception of how pyroclastic flows moving over snow generate slurries of snow, water, and pyroclastic material and how these mixtures behave downstream is illustrated in figures 23 and 25. Once a pyroclastic flow is in motion, it scours substrate snow thermally and mechanically, converting some snow to vapor and some to water. Our field data cannot constrain whether slurry mixtures begin to move while pyroclastic flows remain in motion (sequence *A–B–D*, fig. 23) or whether pyroclastic flows come to a complete stop, and then the wettest parts of slurries break away (sequence *A–B–C–D*, fig. 23)—each scenario is possible, given local conditions. We envision that moving slurries contain hot pyroclastic blocks and lapilli that transfer their heat more slowly than smaller particles and continue to melt remaining snow in slurries as they move. Thus, slurries that contain significant amounts of snow are likely to become progressively more water-rich downstream. The wettest parts of the slurries will be the most mobile, and such parts will coalesce where drainages join downstream. Flows that contain little snow will behave like lahars, segregating both large and low-density particles to their surfaces and margins and forming bouldery levees as they flow downstream (fig. 12*A*); however, those flows that contain significant amounts of snow will also segregate low-density snow toward their margins (fig. 25). By this process, mixtures that contain substantial



amounts of snow and move significant distances downstream can generate both snow-rich, marginal flows that slide across surfaces protected by snowpack, and water-rich axial flows that scour channels and are mainly laharic (fig. 25). The sliding marginal flows, like those in Augustine Creek (fig. 13*A*), preserve vegetation under snowpack, destroy exposed vegetation, and form marginal mixed-avalanche deposits that become draped over vegetation and are littered with shattered branches (figs. 11*A*, 12*A*). The cogenetic, water-rich axial flows scour their beds and leave trails of stripped vegetation and scattered boulders in their wakes (fig. 12*A*).

Relation Between Volume and Planimetric Area for Pyroclastic Flows and Surges—Implications Concerning Mobility

On the basis of simple dimensional analysis, we expect that planimetric area, A, will scale with deposit volume, V, to the two-thirds power for granular mass flows of similar origin with sudden onset. We see that $V = h_{ave}A$, where h_{ave} is the average deposit thickness. For lahars Iverson and others (1998) argued that $h_{ave} \approx \varepsilon A^{1/2}$, where ε is a constant and the deposits are dominantly tabular and thin relative to their lateral dimensions (that is, ε is a small constant). Substituting this approximation into the first equation gives the desired relation, $A = cV^{2/3}$, where c is a hypothetical constant, such that $c = \varepsilon^{-2/3}$ (Iverson and others, 1998). Iverson and others demonstrated the validity of this relation statistically by calibrating c with data from lahars. Dade and Huppert (1998) showed a similar relation to be true for debris avalanches, and Griswold and Iverson (2007) demonstrated such relations for nonvolcanic debris flows and rock avalanches. Finally, Calder and others (1999) and Widiwijayanti and others (2009) suggested such a relation for pyroclastic flows from the recent eruptions of Montserrat and Merapi.

We hypothesize here that log-log plots of planimetric area versus volume for pyroclastic-current deposits with similar origins and characteristics will fall along linear trends, such that $A = cV^{2/3}$, where c is a constant for similar groups of flows. To test and calibrate this relation, we analyzed trends in pyroclastic-current inundation data from Soufrière Hills Volcano, Montserrat (Calder and others, 1999; Druitt and others, 2002 a), Mount St. Helens in 1980 (Rowley and others, 1981), Merapi Volcano, Indonesia, in 2006 (Charbonnier and Gertisser, 2008), and Augustine Volcano in 2006 from this study (fig. 26*A*). We find considerable scatter among the data for pyroclastic-current deposits relative to those for lahars, rockfall avalanches, and volcanic debris avalanches (fig. 26*B*). Pyroclastic currents generally yield more widely varying data because such currents have diverse origins and behavior. Some currents, such as surges (Druitt and others, 2002a; Loughlin and others, 2002), are dilute and more mobile than others that are granular. Some currents have highly energetic origins at the vent, and others begin as simple gravitational collapses of domes and lava flows (Druitt and others, 2002b). Finally, some currents have a sudden onset, and others erupt continuously over significant time periods. In our analysis, we consider only currents that have a sudden onset, because the condition of continuous pyroclastic-current production violates the assumptions in the model presented here (Iverson and others, 1998). Our plot (fig. 26*A*) suggests grouping pyroclastic-currents into three flow types on the basis of mobility and, coincidentally, origin: (1) dome-collapse flows, (2) column-collapse flows, and (3) energetic surge-like flows. We obtain regression-line and two-thirds-slope correlations with large coefficients of determination, meaning positive correlations between planimetric area and deposit volume, for each flow types; however, we consider the correlation for the third type to be quite tentative because it includes only four data pairs (table 8). We tested whether best-fit regressions differ significantly from specified two-thirds-slope fits and observed that they do not differ significantly (table 8). In contrast, best-fit regressions do differ significantly from zero-slope fits for all three types, implying that the null hypothesis of no correlation between planimetric area and deposit volume must be rejected. Our statistical analyses of data for dome-collapse and column-collapse flows support our hypothesis that planimetric area A

Figure 24. Plots that show how overburden pressure, temperature, and grain size influence potential for convective instability that favors erosion and entrainment of snow by pyroclastic flows moving across snowpack (from Walder, 2000b). *A*, Schematic plot of overburden pressure versus grain size, showing how decrease in grain size favors convective instability. Relation of overburden pressure to such instabilities is more complex. Increasing pressure increases likelihood of snow entrainment until load becomes too great and instability is suppressed. *B*, Isobaric plots of grain size versus temperature, showing field of snow fluidization and suppressed fluidization. We estimated likely overburden pressures of 2006 Augustine pyroclastic flows on their substrate by using explosive-phase-deposit parameters as proxies. Thus, pressure $P \approx \nu\rho gh$, where ν is solids fraction of deposit, ρ is rock density, g is gravitational constant, and h is deposit thickness. Such a calculation assumes that fluidizing gas supports weight of particles. Incomplete fluidization would diminish actual overburden pressure. Our estimated P values for initial thin pyroclastic-current deposit (unit Expct) that initiated mixed-avalanche and lahar flows are about a tenth of those for subsequent pyroclastic-flow deposits (unit Expf) and appear to lie in field where fluidization is favored. Subsequent flows yield estimated overburden pressures that may suppress fluidization. *C*, Isothermic boundaries between fluidization and its inverse on our sorting-versus-median-ϕ-size data for 2006 Augustine pyroclastic flows. Grain-size characteristics of initial flows (unit Expct) plot in field where fluidization is more likely than for those of subsequent flows.

varies with $V^{2/3}$. We tentatively advance a similar relation for energetic surgelike flows but suggest that such a relation needs further testing with data.

The ratio $A/V^{2/3} = c$ gives a dimensionless measure of mobility calibrated for similar types of pyroclastic currents, and such calibrated mobility factors have a potential use in volcanic hazard assessments. Genesis, energy, and grain-size characteristics, all of which influence mobility among pyroclastic-currents, vary too widely for all flows to fall along similar trends (fig. 26*A*). As we might expect, surgelike flows are highly mobile and have a mobility factor of $c \approx 520$ that is greater than that of lahars, with $c \approx 200$ (fig. 26*B*; Iverson and others, 1998). The column-collapse flows studied here have a moderate mobility factor of $c \approx 150$, only slightly less than that

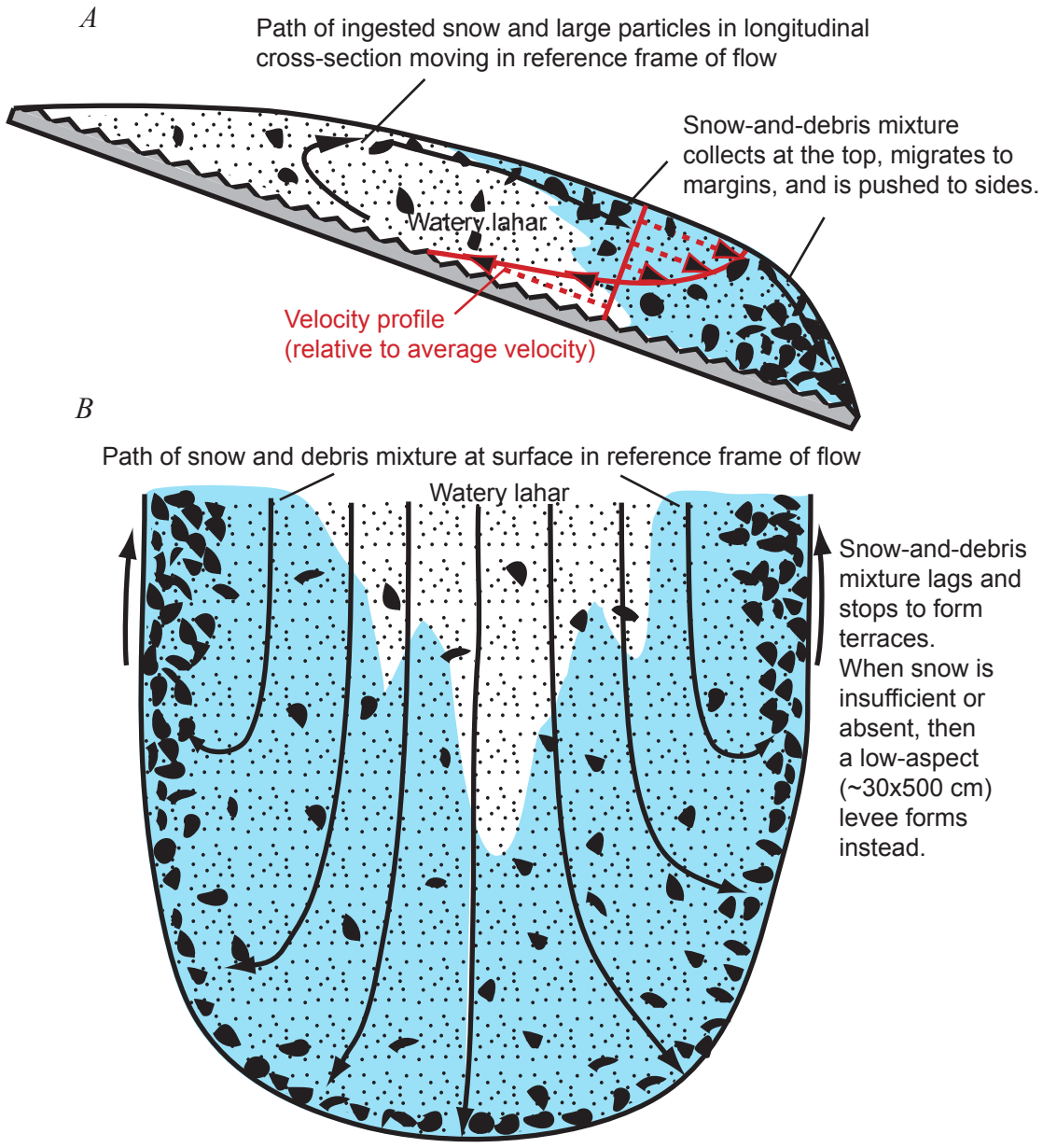


Figure 25. Schematic diagrams showing how simultaneous segregation of low-density snow and entrained coarse particles to surface of a mixed flow (simultaneous mixed avalanche and lahar) results in segregation of both snow and debris mixture to front (*A*) and margins (*B*) of flow. Whether such flows produce boulder-cobble levees or marginal mixed-avalanche deposits depends on amount of snow entrained at any particular time and place downstream while flow is in motion. Frame of reference advects downstream at average speed of flow (that is, at propagation velocity of flow front).

for lahars. Dome-collapse flows have a mobility factor of $c \approx 37$, a result similar to that of Widiwijayanti and others (2009), suggesting that they are no more mobile than volcanic debris avalanches and only slightly more mobile than nonvolcanic rockfall avalanches (fig. 26*B*). Mobilities of similar types of pyroclastic currents, as measured with our ratio $A/V^{2/3}$, yield more consistent results than H/L ratios, where H is the fall height and L is the runout distance (for example, Hayashi and Self, 1992; Calder and others, 1999). However, appropriate data are sparse, and our mobility relations could benefit by testing with additional data. Widiwijayanti and others (2009) present data illustrating the relation of cross-sectional area versus volume for dome-collapse flows and obtain the result: cross-sectional area = $0.05–0.1V^{2/3}$. Their data allow hazard zones for dome-collapse flows to be drawn in a consistent, repeatable way at any volcano, using the LAHARZ procedure of Iverson and others (1998). Cross-sectional areas for more energetic and dilute pyroclastic currents have proved difficult to measure, and data are needed to assess and calibrate the utility of the LAHARZ method for such flows. Indeed, mobile pyroclastic surges commonly accompany even the least mobile types of pyroclastic flow, such as those generated by the collapse of lava domes and flows.

Conclusions

The 2006 eruption of Augustine Volcano provided an opportunity to observe explosions, map and characterize pyroclastic and other flowage deposits, and test hypotheses concerning the origins and behavior of these flows. In particular, this study provided us with an unusual opportunity to observe the interaction of pyroclastic currents with winter snowpack. We summarize below our chief conclusions drawn from our data, and the methodologies that generated it.

1. Each of the three phases of the 2006 eruption had a distinctive style of volcanism and distinctive flowage deposits. The explosive phase comprised short vulcanian explosions that punctuated dome growth and produced pyroclastic currents on all flanks of the volcano. Initial pyroclastic currents spread widely across winter snowpack and generated slurries that coalesced to form mixed avalanches and lahars, whereas the final pyroclastic currents of the explosive phase involved explosive disruption and decompression of a lava dome. Continuous-phase activity consisted of rapid lava-dome growth and frequent dome-collapse pyroclastic flows restricted to the north sector of the volcano, followed by an andesite lava flow. After a 3-week pause, activity resumed with the extrusion of lava and a dome, accompanied by periodic block-and-ash flows, during the final, effusive phase of the eruption.

2. The three eruptive phases were unique—not just in terms of style of volcanism, including its associated seismicity, geodetic response, and ash emissions—but also in terms of the types and morphologies of deposits that were produced, and, in particular, of their basic lithologic components—low-, intermediate-, and high-silica andesite. Overall, during the three phases, lithologic compositions trended from low-silica andesite to high-silica andesite and back to low-silica andesite. However, each rock type is present in the deposits of each eruptive phase and each flow type.

3. The chief factors that influenced pyroclastic-current behavior and the morphology of their deposits were genesis, grain size, and the characteristics of the surfaces over which they flowed. Column collapse from short-lived vulcanian blasts, dome collapse, and the collapse of viscous lavas on steep slopes caused the pyroclastic flows documented in this study. Column-collapse flows during the explosive phase spread widely where they overran snowpack. Subsequent, similar flows were confined to drainages because previous pyroclastic currents had melted the snowpack, or coated it with ash or debris sufficient to insulate the later flows from the underlying snow. In contrast, later dome-collapse flows involved neither column collapse nor the influence of underlying snow. Because it was voluminous, the dome failure that generated the Rocky Point pyroclastic flow may have been sufficiently deep seated that unloading of incompletely degassed lava caused explosive decompression which initiated an energetic flow. High proportions of juvenile high-silica andesite within the deposits suggest that the Rocky Point explosion opened the conduit to the magma chamber and made way for continuous output of magma during the next phase. The subsequent, continuous-phase flows behaved as partially fluidized granular flows. Effusive-phase block-and-ash flows were caused exclusively by collapses of andesite lava flows.

4. Pyroclastic flows can erode and incorporate substrates formed of snow or ice through a combination of mechanical and thermal processes at the bed. Conversion of snow to vapor by hot pyroclast material fluidized such flows and thus enhanced their spread across snowpack and the resulting production of mixed avalanches and lahars. Walder's hypothesis (2000a,b) that thermal scour can effectively incorporate snow into a pyroclastic current, given proper pressure, temperature, and grain-size conditions at the pyroclastic layer's interface with substrate snow, is consistent with field observations during this study. Grain-size characteristics of initial pyroclastic flows, and estimates of overburden pressure at their base, are conditions that are favorable to thermal scour of snow and coeval fluidization. These flows scoured substrate snow and generated secondary slurry flows, whereas subsequent flows did not.

5. Initial pyroclastic flows of the explosive phase invariably generated lahars and mixed avalanches, but some of these secondary flows were wetter and more laharic than others. Where secondary flows were quite watery, mixed-avalanche

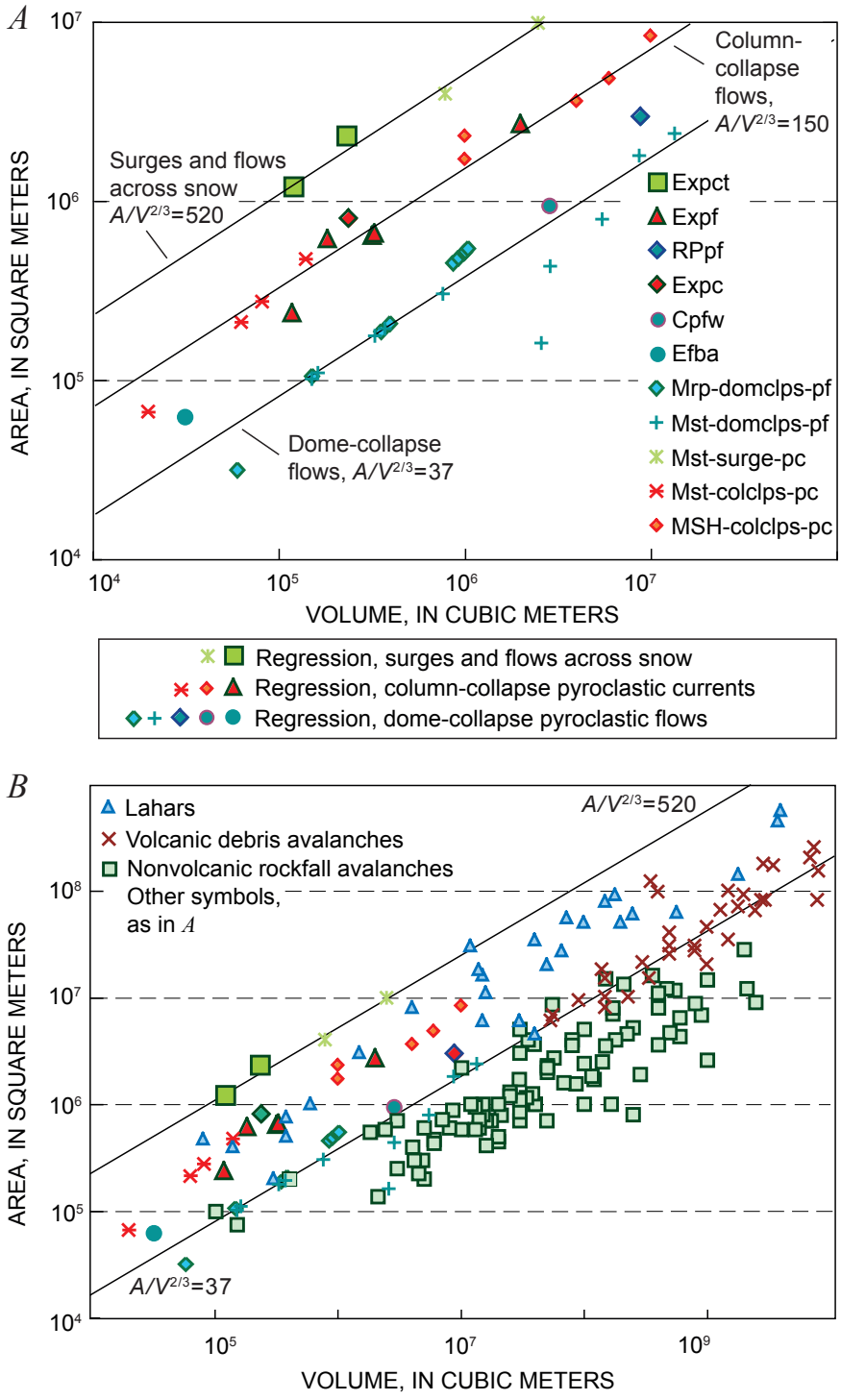


Figure 26. Plots of planimetric area versus volume for pyroclastic-current deposits of the 2006 eruption of Augustine Volcano relative to other pyroclastic currents, lahars, and debris avalanches. *A*, Augustine pyroclastic currents plotted with data of Charbonnier and Gertisser (2008) for Merapi pyroclastic currents (Mrp), of Calder and others (1999) for Montserrat currents (Mst), and of Rowley and others (1981) for Mount St. Helens currents (MSH). *B*, Area versus volume for worldwide occurrences of lahars (Iverson and others, 1998) and nonvolcanic debris flows and rock avalanches (Griswold and Iverson, 2007). Best fits to data of specified two-thirds-slope models are plotted in figure 26*A* for 21 dome-collapse flows, 14 column-collapse flows, and 4 surgelike flows. Same abbreviations for Augustine units as in figure 2; domclps-pf, dome-collapse pyroclastic flows; colcops-pc, column-collapse pyroclastic currents; and surge-pc, surgelike flows. Parameters and analysis of variance statistics for these models and for best-fit regression-line models are listed in table 8.

deposits were small or insignificant. Mixed-avalanche deposits that contained substantial snow blanketed medial reaches of valleys and had associated extensive marginal terraces and axial islands in distal reaches. Flows that incorporated significant amounts of snow formed cogenetic mixed avalanches that slid across surfaces protected by snowpack and water-rich axial lahars that scoured channels.

6. Plots of planimetric area (A) versus volume (V) for pyroclastic currents with similar origins and characteristics exhibit linear trends, such that $A = cV^{2/3}$ where c is a constant for similar types of flow. This relation was tested and calibrated for dome-collapse, column-collapse, and surgelike flows, using inundation-volume data from Montserrat (Calder and others, 1999), Mount St. Helens in 1980 (Rowley and others, 1981) and Augustine in 2006. The ratio $A/V^{2/3} = c$ gives a dimensionless measure of mobility, calibrated here for each of the three types of pyroclastic current. Energetic flows like surges are highly mobile and have an apparent dimensionless mobility factor of $c \approx 520$; column-collapse flows have a moderate mobility factor of $c \approx 150$; and dome-collapse flowss have an approximate mobility factor of $c \approx 35$, suggesting that these flows are not much more mobile than rock avalanches. Such calibrated mobility factors have a potential use in volcanic hazard assessments.

Acknowledgments

The entire staff of Alaska Volcano Observatory generously shared observations, ideas, and data that greatly helped us improve and refine this study. Numerous people set up and maintained the field camp during summer of 2006, without which this study would have been difficult or impossible. We especially thank Game McGimsey, Tina Neal, Evan Thoms, Cheryl Cameron, and Dan Jones for logistical field support. Our helicopter pilot, Rick Farrish transported us safely around the island, often in difficult conditions. Tim Druitt and Kristi Wallace provided careful reviews that helped us improve many defects in the manuscript.

References Cited

Bailey, J.E., Dean, K.G., Dehn, J., and Webley, P.W., 2010, Integrated satellite observations of the 2006 eruption of Augustine Volcano, *in* Power, J.A., Coombs, M.L., and Freymueller, J.T., eds., The 2006 eruption of Augustine Volcano, Alaska: U.S. Geological Survey Professional Paper 1769 (this volume).

Begét, J.E., and Kienle, J., 1992, Cyclic formation of debris avalanches at Mount St. Augustine volcano: Nature, v. 356, no. 6371, p. 701–704.

Begét, J.E., and Kowalik, Z., 2006, Confirmation and calibration of computer modeling of tsunamis produced by Augustine Volcano, Alaska: Science of Tsunami Hazards, v. 24, no. 4, p. 257–267.

Calder, E. S., Cole, P.D., Dade, W.B., Druitt, T.H., Hoblitt, R.P., Huppert, H.E., Ritchie, L., Sparks, R.S.J., and Young, S.R., 1999, Mobility of pyroclastic flows and surges at the Soufrière Hills Volcano, Montserrat: Geophysical Research Letters, v. 26, p. 537–540.

Cervelli, P.F., Fournier, T., Freymueller, J.T., and Power, J.A., 2006, Ground deformation associated with the precursory unrest and early phases of the January 2006 eruption of Augustine Volcano, Alaska: Geophysical Research Letters, v. 33, no. L18304, doi:10.1029/2006GL027219, p. 1–5.

Cervelli, P.F., Fournier, T.J., Freymueller, J.T., Power, J.A., Lisowski, M., and Pauk, B.A., 2010, Geodetic constraints on magma movement and withdrawal during the 2006 eruption of Augustine Volcano, Alaska, *in* Power, J.A., Coombs, M.L., and Freymueller, J.T., eds., The 2006 eruption of Augustine Volcano, Alaska: U.S. Geological Survey Professional Paper 1769 (this volume).

Charbonnier, S.J., and Gertisser, R., 2008, Field observations and surface characteristics of pristine block-and-ash flow deposits from the 2006 eruption of Merapi Volcano, Java, Indonesia: Journal of Volcanology and Geothermal Research, v. 177, p. 971–982.

Coats, R.R., 1950, Volcanic activity in the Aleutian Arc: U.S. Geological Survey Bulletin 974-B, p. 35–49.

Cole, P.D., Calder, E.S., Sparks, R.J.S., Clarke, A.B., Druitt, T.H., Young, S.R., Herd, R.A., Harford, C.L., and Norton, G.E., 2002, Deposits from dome-collapse and fountain-collapse pyroclastic flows at Soufrière Hills Volcano, Monserrat, *in* Druitt, T.H., and Kokelaar, B.P., eds., The eruption of Soufrière Hills Volcano, Montserrat, from 1995 to 1999: London Geological Society Memoirs, p. 231–262.

Coombs, M.L., Bull, K.F., Vallance, J.W., Schneider, D.J., Thoms, E.E., Wessels, R.L., and McGimsey, R.G., 2010, Timing, distribution, and volume of proximal products of the 2006 eruption of Augustine Volcano, Alaska, *in* Power, J.A., Coombs, M.L., and Freymueller, J.T., eds., The 2006 eruption of Augustine Volcano, Alaska: U.S. Geological Survey Professional Paper 1769 (this volume).

Dade, W.B., and Huppert, H.E., 1998, Long runout rockfalls: Geology, v. 26, p. 803–806.

Daley, E.E., 1986, Petrology, geochemistry, and the evolution of lavas at Augustine Volcano, Alaska: Fairbanks, University of Alaska, 106 p.

Dettermen, R.L., and Reed, B.L., 1980, Stratigraphy, structure, and economic geology of the Iliamna Quadrangle, Alaska: U.S. Geological Survey Bulletin 1368-B, 86 p.

Druitt, T.H., Calder, E.S., Cole, P.D., Hoblitt, R.P., Loughlin, S.C., Norton, G.E., Ritchie, L.J., Sparks, R.J.S., and Voight, B., 2002a, Small-volume, highly mobile pyroclastic flows formed by rapid sedimentation from pyroclastic surges at Soufrière Hills Volcano, Monserrat; an important hazard, *in* Druitt, T.H., and Kokelaar, B.P., eds., The eruption of Soufrière Hills Volcano, Monserrat, from 1995 to 1999: London Geological Society Memoirs, p. 263–279.

Druitt, T.H., Young, S.R., Baptie, B., Bonadonna, C., Calder, E.S., Clarke, A.B., Cole, P.D., Harford, C.L., Herd, R.A., Luckett, R., Ryan, G., and Voight, B., 2002b, Episodes of cyclic Vulcanian explosive activity with fountain collapse at Soufrière Hills Volcano, Montserrat, *in* Druitt, T.H., and Kokelaar, B.P., eds., The eruption of Soufrière Hills Volcano, Montserrat, from 1995 to 1999: London Geological Society Memoirs, p. 281–306.

Gardner, C.A., Neal, C. A., Waitt, R.B., and Janda, R.J., 1994, Proximal pyroclastic flow deposits from the 1989-1990 eruption of Redoubt Volcano, Alaska—stratigraphy, distribution, and physical characteristics: Journal of Volcanology and Geothermal Research, v. 62, p. 213–250.

Griswold, J.P., and Iverson, R.M., 2007, Mobility statistics and automated hazard mapping for debris flows and rock avalanches: U.S. Geological Survey Scientific Investigations Report 2007-5276, 49 p.

Harris, G.W., Swanson, S.E., and Nye, C.J., 1987, Comparative petrology and petrography of the 1976 and 1986 ejecta of Augustine Volcano [abs.]: Geological Society of America Abstracts with Programs, v. 19, p. 387.

Hayashi, J.N., and Self, S., 1992, A comparison of pyroclastic flow and debris avalanche mobility: Journal of Geophysical Research, v. 97, p. 9063–9071.

Iverson, R.M., 1997, The physics of debris flows: Reviews in geophysics, v. 35, p. 245–296.

Iverson, R.M., Schilling, S.P., and Vallance, J.W., 1998, Objective delineation of lahar-inundation hazard zones: Geological Society of America Bulletin, v. 110, p. 972–984.

Jacobs, K.M., and McNutt, S.R., 2010, Using seismic *b*-values to interpret seismicity rates and physical processes during the preeruptive earthquake swarm at Augustine Volcano 2005–2006, *in* Power, J.A., Coombs, M.L., and Freymueller, J.T., eds., The 2006 eruption of Augustine Volcano, Alaska: U.S. Geological Survey Professional Paper 1769 (this volume).

Johnston, D.A., 1978, Volatiles, magma mixing and the mechanism of eruption of Augustine Volcano, Alaska: Seattle, University of Washington, Ph.D. thesis, 204 p.

Kienle, J., and Forbes, R.B., 1977, Augustine—evolution of a volcano: Fairbanks, University of Alaska, Geophysical Institute Annual Report 1975–76, p. 26–48.

Kienle, J., and Swanson, S.E., 1985, Volcanic hazards from future eruptions of Augustine Volcano, Alaska: Geophysical Institute, University of Alaska Fairbanks, Rep. UAG R-275, 2nd ed., 122 p.

Larsen, J.F., Nye, C.J., Coombs, M.L., Tilman, M., Izbekov, P., and Cameron, C., 2010, Petrology and geochemistry of the 2006 eruption of Augustine Volcano, Alaska, *in* Power, J.A., Coombs, M.L., and Freymueller, J.T., eds., The 2006 eruption of Augustine Volcano, Alaska: U.S. Geological Survey Professional Paper 1769 (this volume).

Loughlin, S.C., Calder, E.S., Clarke, A.B., Cole, P.D., Luckett, R., Mangan, M.T., Pyle, D.M., Sparks, R.J.S., Voight, B., and Watts, R.B., 2002, Pyroclastic flows and surges generated by the 25 June 1997 dome collapse, Soufrière Hills Volcano, Montserrat, *in* Druitt, T.H., and Kokelaar, B.P., eds., The eruption of Soufrière Hills Volcano, Montserrat, from 1995 to 1999: London Geological Society Memoirs, p. 191–210.

Lube, G., Cronin, S.J., Platz, T., Freundt, A., Proctor, J., Henderson, C., and Sheridan, M.F., 2007, Flow and deposition of pyroclastic granular flows; a type example from the 1975 Ngauruhoe eruption, New Zealand: Journal of Volcanology and Geothermal Research, v. 161, p. 165–186.

McNutt, S.R., Tytgat, G., Estes, S.A., and Stihler, S.D., 2010, A parametric study of the January 2006 explosive eruptions of Augustine Volcano, Alaska, *in* Power, J.A., Coombs, M.L., and Freymueller, J.T., eds., The 2006 eruption of Augustine Volcano, Alaska: U.S. Geological Survey Professional Paper 1769 (this volume).

Miller, T.P., McGimsey, R.G., Richter, D.H., Riehle, J.R., Nye, C.J., Yount, M.E., and Dumoulin, J.A., 1998, Catalog of the historically active volcanoes of Alaska: U.S. Geological Survey Open-File Report 98-0582, 104 p.

Pierson, T.C., 1994, Volcanic mixed avalanches; a distinct eruption-triggered mass-flow process at snow-clad volcanoes: Geological Society of America Bulletin, v. 106, p. 1351–1358.

Pouliquen, O., Delour, J., and Savage, S.B., 1997, Fingering in granular flows: Nature, v. 386, p. 816–817.

Pouliquen, O., and Vallance, J.W., 1999, Segregation induced instabilities of granular fronts: Chaos, v. 9, p. 621–630.

Power, J.A., and Lalla, D.J., 2010, Seismic observations of Augustine Volcano, 1970–2007, *in* Power, J.A., Coombs, M.L., and Freymueller, J.T., eds., The 2006 eruption of Augustine Volcano, Alaska: U.S. Geological Survey Professional Paper 1769 (this volume).

Power, J.A., Nye, C.J., Coombs, M.L., Wessels, R.L., Cervelli, P.F., Dehn, J., Wallace, K.L., Freymueller, J.T., and Doukas, M.P., 2006, The reawakening of Alaska's Augustine

Volcano: Eos (American Geophysical Union Transactions), v. 87, no. 37, p. 373, 377.

Rowley, P.D., Kuntz, M.A., and McCleod, N.S., 1981, Pyroclastic-flow deposits, *in* Lipman, P.W., and Mullineaux, D.R., eds. The 1980 eruptions of Mount St. Helens: U.S. Geological Survey Professional Paper 1250, p. 489–512.

Schneider, D.J., Scott, C., Wood, J. and Hall, T., 2006, NEXRAD weather radar observation of the 2006 Augustine volcanic eruption clouds [abs.]: Eos (American Geophysical Union Transactions), v. 87, abstract V51C-1686.

Scott, K.M., 1988, Origins, behavior, and sedimentology of lahars and lahar-runout flows in the Toutle-Cowlitz River system: U.S. Geological Survey Professional Paper 1447-A, 78 p.

Siebert, L., Begét, J.E., and Glicken, H., 1995, The eruptive history of Augustine Volcano, Alaska: Journal of Volcanology and Geothermal Research, v. 66, no. 1, p. 367–395.

Sparks, R.S.J., 1976, Grain-size variations in ignimbrites and implications for the transport of pyroclastic flows: Sedimentology, v. 23, p. 147–188.

Swanson, S.E., and Kienle, J., 1988, The 1986 eruption of Mount St. Augustine; field test of a hazard evaluation: Journal of Geophysical Research, v. 93, no. 85, p. 4500–4520.

Thomas, R.J., McNutt, S.R., Krehbiel, P.R., Rison, W., Aulich, G., Edens, H.E., Tytgat, G, and Clark, E., 2010, Lightning and electrical activity during the 2006 eruption of Augustine Volcano, *in* Power, J.A., Coombs, M.L., and Freymueller, J.T., eds., The 2006 eruption of Augustine Volcano, Alaska: U.S. Geological Survey Professional Paper 1769 (this volume).

Vallance, J.W., 1994, Experimental and field studies related to the behavior of granular mass flows and the characteristic of their deposits: Houghton, Michigan Technological University, Ph.D.dissertation, 197 p.

Vallance, J.W., 2000, Lahars, *in* Sigurdsson, H., Houghton, B.F., McNutt, S.R., Rymer, H., and Stix, J., eds., Encyclopedia of volcanoes: San Diego, Calif., Academic Press, p. 601–616.

Vallance, J.W., and Savage, S.B., 2000, Particle segregation in granular flows down chutes, *in* Rosato, A.D., and Blackmore, D.L., eds. Segregation in granular flows: Dordrecht, Kluwer, p. 31–51.

Waitt, R.B., 1995, Hybrid wet flows formed by hot pyroclasts interacting with snow during the 1992 erupton of Crater Peak, Mount Spurr Volcano, Alaska, *in* Kieth, T.E.C., ed., U.S. Geological Survey Bulletin 2139, p. 107–118.

Waitt, R.B., 2010, Ejecta and landslides from Augustine Volcano before 2006, *in* Power, J.A., Coombs, M.L., and Freymueller, J.T., eds., The 2006 eruption of Augustine Volcano, Alaska: U.S. Geological Survey Professional Paper 1769 (this volume).

Waitt, R.B., and Begét, J.E., 1996, Provisional geologic map of Augustine Volcano, Alaska: U.S. Geological Survey Open-File Report 96-0516, 44 p.

Waitt, R.B., and Begét, J.E., 2009, Volcanic processes and geology of Mount Augustine, Alaska: U.S. Geological Survey Professional Paper 1762, 78 p.

Waitt, R.B., Gardner, C.A., Pierson, T.C., Major, J.J., and Neal, C. A., 1994, Unusual ice diamicts emplaced during the December 15, 1989 eruption of Redoubt Volcano, Alaska: Journal of Volcanology and Geothermal Research, v. 62, p. 409–428.

Walder. J.S., 2000a, Pyroclast/snow interactions and thermally driven slurry formation; part 1, theory for monodisperse grain beds: Bulletin of Volcanology, v. 62, p. 105–118.

Walder. J.S., 2000b, Pyroclast/snow interactions and thermally driven slurry formation; part 2, experiments and theoretical extension to polydisperse tephra: Bulletin of Volcanology, v. 62, p. 119–129.

Wallace, K., Neal, C.A., and McGimsey, R.G., 2010, Timing, distribution and character of tephra fall from the 2005-2006 eruption of Augustine Volcano, Alaska, *in* Power, J.A., Coombs, M.L., and Freymueller, J.T., eds., The 2006 eruption of Augustine Volcano, Alaska: U.S. Geological Survey Professional Paper 1769 (this volume).

Widiwijayanti, C., Voight, B., Hidayat, D., and Schilling, S.P., 2009, Objective delineation of areas at risk from block-and-ash pyroclastic flows and surges: Bulletin of Volcanology, v. 71, p. 687–703, doi:10.1007/s00445-008-0254-6.

Table 2. Samples taken and analyses performed for pyroclastic-flow, lahar, and mixed-avalanche deposis of the 2006 eruption of Augustine Volcano, Alaska.

[Samples are sorted by event and sector]

Sample Number	Latitude (decimal degrees)	Longitude (decimal degrees)	Sector 1=ESE-ENE 2=NE-WNW 3=SSE-SW	Unit	Phase	Emplacement Date	Event	Sample Type	Grain size	Sedi-graph	Com po nen try
V021A	59.366	-153.410	1	Expct	Explosive	1/13/06	3-4	Bulk	X		
V033A	59.368	-153.394	1	Expct	Explosive	1/13/06	3-4	Bulk	X		X
V096	59.371	-153.407	1	Expct	Explosive	1/14/06	3-4, 6-7	Bulk	X	X	X
V281A	59.363	-153.404	1	Expct	Explosive	1/13/06	3-4	Bulk	X		
V281B	59.363	-153.404	1	Expct	Explosive	1/13/06	3-4	Bulk	X		
V283A	59.363	-153.402	1	Expct basal	Explosive	1/13/06	3-4	Bulk	X		
V283B	59.363	-153.402	1	Expct basal	Explosive	1/13/06	3-4	Bulk	X		
V283C	59.363	-153.402	1	Expct basal	Explosive	1/13/06	3-4	Bulk	X		
V283D	59.363	-153.402	1	Expct top	Explosive	1/13/06	3-4	Bulk	X		
V283E	59.363	-153.402	1	Expct top	Explosive	1/13/06	3-4	Bulk	X		
V330	59.367	-153.382	1	Exlh	Explosive	1/13/06	3-4	Bulk	X		
B096A	59.366	-153.410	1	Expct	Explosive	1/13/06	3-4	Bulk			
B096B	59.366	-153.410	1	Expct	Explosive	1/13/06	3-4	Hand-picked juvenile clasts			
B106	59.365	-153.409	1	Expf	Explosive	1/13/06	3-4	Bulk	X		X
B184A	59.363	-153.403	1	Expct	Explosive	1/13/06	3-4	Bulk	X	X	X
B184B	59.363	-153.403	1	Expct	Explosive	1/13/06	3-4	Bulk	X	X	X
B184C	59.363	-153.403	1	Expct	Explosive	1/13/06	3-4	Bulk	X		
B102	59.346	-153.429	1	Expf	Explosive	1/13-14/06	3-7	Bulk	X		X
C120	59.351	-153.406	3	Expct	Explosive	1/13-14/06	3-8	Bulk	X		
V117	59.369	-153.447	2	Expf	Explosive	1/13/06	5	Bulk	X		
B176	59.404	-153.449	2	Expf	Explosive	1/13-14/06	5	Bulk	X	X	
V270A	59.384	-153.399	2	Exma	Explosive	1/13-14/06?	7?	Bulk	X		
V270B	59.384	-153.399	2	Exlh	Explosive	1/13-14/06	7	Bulk	X		
V272	59.386	-153.397	2	Exlh	Explosive	1/13-14/06	7	Bulk	X		
V275A	59.387	-153.391	2	Exlh	Explosive	1/13-14/06	7	Bulk	X		X
V275B	59.387	-153.391	2	Exlh	Explosive	1/13-14/06	7	Bulk	X		X
V275C	59.387	-153.391	2	Exlh	Explosive	1/13-14/06	7	Bulk	X		
V237	59.388	-153.385	2	Exlh	Explosive	1/14/06	7	Bulk	X		
V258	59.366	-153.398	3	Exma	Explosive	1/13-14/06	7	Bulk	X		
V199	59.336	-153.410	3	Exma	Explosive	1/14/06	8	Bulk	X		
V256A	59.344	-153.418	3	Expf-top	Explosive	1/14/06	8	Bulk	X	X	
V256B	59.344	-153.418	3	Expf-mid	Explosive	1/14/06	8	Bulk	X	X	
V256C	59.344	-153.418	3	Expf-base	Explosive	1/14/06	8	Bulk	X		
V256D	59.344	-153.418	3	Expf-base	Explosive	1/14/06	8	Bulk	X	X	
V256E	59.344	-153.418	3	Expf	Explosive	1/14/06	8	Bulk	X		
V257	59.344	-153.416	3	Exma	Explosive	1/14/06	8	Bulk	X		
V264	59.345	-153.420	3	Expf-reworked	Explosive	1/13-14/06	8	Bulk			

Table 2. Samples taken and analyses performed for pyroclastic-flow, lahar, and mixed-avalanche deposis of the 2006 eruption of Augustine Volcano, Alaska.—Continued

[Samples are sorted by event and sector]

Sample Number	Latitude (decimal degrees)	Longitude (decimal degrees)	Sector 1=ESE-ENE 2=NE-WNW 3=SSE-SW	Unit	Phase	Emplacement Date	Event	Sample Type	Grain size	Sedi-graph	Com po nen try
V276A	59.333	-153.399	3	Exlh-base	Explosive	1/13-14/06	8	Bulk	X	X	X
V276B	59.333	-153.399	3	Exlh-top	Explosive	1/13-14/06	8	Bulk	X	X	
V278	59.333	-153.400	3	Exma	Explosive	1/13-14/06	8	Bulk	X	X	X
V280	59.333	-153.400	3	Exlh	Explosive	1/13-14/06	8	Bulk	X		
B230	59.343	-153.455	3	Expf	Explosive	1/13-14/06	8	Bulk	X		X
C025A	59.329	-153.468	3	Exlh	Explosive	1/13-14/06	8	Bulk			
B129	59.360	-153.436	3	Expf	Explosive	1/17/09	9	Bulk			
V254	59.350	-153.487	3	Expf	Explosive	1/17/06	9	Bulk	X		
V019	59.352	-153.477	2	Expf	Explosive	1/17/06	9	Bulk	X		X
V297	59.386	-153.442	2	Expc	Explosive	1/27/06	10	Bulk	X		
V311	59.376	-153.439	2	Expc	Explosive	1/27/06	10	Bulk			
V312A	59.376	-153.440	2	Expc	Explosive	1/27/06	10	Bulk	X		
V312B	59.376	-153.440	2	Expc	Explosive	1/27/06	10	Bulk	X		
V312C	59.376	-153.440	2	Expc	Explosive	1/27/06	10	Bulk			
V312D	59.376	-153.440	2	Expc	Explosive	1/27/06	10	Bulk	X		
V313	59.377	-153.439	2	Expc	Explosive	1/27/06	10	Bulk	X		X
V315	59.379	-153.442	2	Expc	Explosive	1/27/06	10	Bulk	X		
B215A	59.371	-153.437	2	Expc	Explosive	1/27/06	10	Bulk	X	X	X
B216	59.373	-153.439	2	Expc	Explosive	1/27/06	10	Bulk	X		
B217	59.374	-153.440	2	Expc	Explosive	1/27/06	10	Bulk	X		
C259C	59.385	-153.438	2	Expc	Explosive	1/27/06	10	Bulk	X	X	X
B173	59.404	-153.439	2	RPpf	Explosive	1/27/06	10	Bulk	X	X	X
B222	59.390	-153.439	2	RPpf	Explosive	1/27/06	10	Bulk	X		X
B223	59.394	-153.434	2	RPpf	Explosive	1/27/06	10	Bulk	X		
B224	59.400	-153.425	2	RPpf	Explosive	1/27/06	10	Bulk	X	X	
B225	59.403	-153.435	2	RPpf	Explosive	1/27/06	10	Bulk	X	X	
C259B	59.385	-153.438	2	RPpf	Explosive	1/27/06	10	Bulk	X		
B218	59.377	-153.436	2	Cpf	Continuous	>1/27/2006	>14	Bulk	X		
V224	59.383	-153.395	2	Cpf	Continuous	>1/28/06	>14	Bulk	X		
LC259A	59.385	-153.438	2	Cpf	Continuous	>1/28/06	>14	Bulk	X	X	
B143	59.369	-153.446	2	Cpf	Continuous	>1/28/06	>14	Hand-picked juvenile clasts			
B149A	59.371	-153.432	2	Cpf	Continuous	>1/28/06	>14	Hand-picked juvenile clasts			
B155A	59.376	-153.429	2	Cpf	Continuous	>1/28/06	>14	Bulk			
B203	59.384	-153.409	2	Cpf	Continuous	>1/28/06	>14	Bulk	X	X	X
V101	59.372	-153.405	2	Cpc	Continuous	>1/28/06	>14	Bulk	X		X
C294	59.375	-153.445	2	Cpfw	Continuous	1/30/06	Windy	Bulk	X		
V022A	59.363	-153.405	1	Efba	Effusive	3/3-16/06	>14	Bulk	X		X

Table 3. Grain-size distribution for samples of clastic-flow deposits of the 2006 eruption of Augustine Volcano, Alaska.

[Samples sorted by map unit[1]. Data are obtained by sieve analysis and given in weight percent. Data for grain sizes <0.063 mm obtained by sedigraph. Fine-ash totals from sedigraph-measured smaples are calculated from sedigraph data, not weighed. All samples analyzed at the Cascades Volcano Observatory]

Sample Number	Unit	31.5 mm	16.0 mm	8.0 mm	4.0 mm	2.0 mm	1.0 mm	0.50 mm	0.25 mm	0.125 mm	0.063 mm	Fine ash (<0.063 mm)	31 µm	16 µm	8 µm	4 µm	2 µm	1 µm
V021A	Expct	0.0	5.4	10.0	7.1	4.7	8.8	11.4	14.6	15.6	10.2	12.2						
V033A	Expct	16.4	9.0	8.0	7.9	6.0	9.8	11.3	12.4	9.4	4.9	4.9						
V096	Expct	4.2	7.4	4.6	4.2	4.0	7.5	11.5	15.1	15.1	11.8	14.0	6.3	4.0	2.1	1.0	0.4	0.2
V281A	Expct	0.0	0.0	2.2	2.6	6.3	12.4	18.3	19.1	19.1	12.9	6.9						
V315	Expct	2.5	10.9	9.5	9.4	6.8	10.0	13.9	15.6	12.2	6.6	2.5						
V283D	Expct	16.0	0.6	2.1	3.9	4.9	9.6	14.4	17.4	14.7	10.0	6.4						
V283E	Expct	2.8	11.7	7.1	6.9	5.6	8.8	10.8	13.0	13.3	9.6	10.3						
V283A	Expct-basal	0.0	0.0	3.0	4.9	8.1	13.4	18.2	20.6	16.8	10.6	4.4						
V283B	Expct-basal	0.0	4.9	8.0	8.0	7.5	10.3	14.9	18.4	14.9	8.7	4.3						
V283C	Expct-basal	18.5	7.6	7.2	7.2	6.1	10.4	12.1	13.1	10.0	4.8	3.0						
B184A	Expct	0.0	1.9	3.4	6.7	7.2	13.6	18.0	21.6	16.3	8.1	3.2	1.9	0.6	0.3	0.2	0.1	0.0
B184B	Expct	1.9	2.7	3.0	5.1	6.0	9.9	15.1	19.5	18.1	11.0	7.7	3.9	1.7	1.0	0.7	0.3	0.2
B184C	Expct	0.0	0.0	0.3	1.0	3.2	10.5	19.1	26.1	24.1	11.9	4.0						
C120	Expct	0.0	3.9	21.6	16.5	7.7	8.3	11.6	12.8	9.1	5.0	3.6						
V117	Expf	7.7	14.0	8.4	8.0	8.3	11.0	13.9	14.5	9.1	3.7	1.3						
B102	Expf	3.8	9.1	10.3	9.1	8.7	10.6	13.2	14.6	10.2	5.5	4.8						
B176	Expf	0.0	1.3	3.5	5.5	7.5	10.8	15.6	19.7	18.7	10.9	6.3	2.6	1.5	1.1	0.7	0.3	0.1
V256A	Expf-top	23.8	8.5	4.6	4.1	3.8	7.0	9.0	10.7	8.1	5.7	6.2	2.4	1.8	1.1	0.6	0.2	0.1
V256B	Expf-middle	17.0	7.8	7.8	7.2	5.0	6.7	7.6	7.9	6.0	3.7	5.5	2.0	1.6	1.0	0.5	0.2	0.1
V256C	Expf-base	0.0	7.5	7.4	7.7	6.2	11.5	14.1	15.8	13.1	7.6	9.0						
V256D	Expf-base	0.0	0.0	1.9	2.1	3.9	9.3	18.6	23.5	19.0	10.8	10.3	3.8	2.8	2.0	1.1	0.5	0.2
V256E	Expf	0.0	2.3	1.8	1.3	1.8	6.6	12.2	18.4	20.4	15.3	19.9						
V019	ExPf	2.5	3.6	4.0	6.3	9.5	13.7	15.6	14.4	12.3	8.0	10.1						
B230	Expf	13.9	5.1	5.8	7.2	5.9	12.6	13.9	15.4	12.1	5.5	2.6						
V237	Exlh	3.1	5.6	9.2	11.8	11.8	14.8	15.3	13.0	8.0	3.7	3.7						
V270B	Exlh	0.0	7.8	12.2	10.8	8.2	11.0	12.0	12.0	9.5	6.5	10.0						
V275B	Exlh	2.1	2.2	6.3	8.3	10.5	17.1	18.2	15.8	9.4	5.1	5.0						
V275C	Exlh	0.0	2.8	5.8	8.1	7.7	13.6	21.0	20.4	11.7	4.8	4.1						
V280	Exlh	0.0	16.8	22.0	11.2	6.3	7.6	8.6	9.5	7.0	5.1	5.8						
V330	Exlh	0.0	4.0	8.4	9.1	8.6	11.9	12.8	14.9	14.3	9.4	6.5						

V276A	Exlh-hcf	5.9	15.3	17.5	13.9	8.9	8.7	8.8	7.9	5.2	2.9	4.8	1.6	1.4	1.0	0.5	0.2	0.1
V276B	Exlh-hcf	0.0	0.4	7.3	15.7	14.8	17.5	15.2	12.7	6.9	3.8	5.3	1.8	1.7	1.0	0.5	0.2	0.1
V272	Exlh-hcf	0.0	3.6	4.4	5.0	5.7	12.8	16.5	17.0	15.1	10.7	9.2						
V275A	Exlh-hcf	0.0	3.2	16.8	17.7	13.8	12.9	12.0	10.2	6.4	3.4	3.6						
V199	Exma	0.0	84.1	11.9	0.2	0.2	0.4	0.6	0.6	0.6	0.6	0.8						
V257	Exma	0.0	8.2	11.1	8.8	7.2	10.3	14.2	13.3	9.0	6.2	11.7						
0V258	Exma	5.6	5.3	6.2	7.2	3.0	48.7	6.0	6.1	4.1	3.2	4.6						
V254	Exma	0.0	0.0	0.0	0.0	0.7	0.7	2.3	9.5	23.0	22.4	41.4						
V270A	Exma	4.8	2.9	10.0	11.4	11.3	16.8	15.2	12.2	7.0	4.5	4.0						
V278	Exma	13.5	3.2	5.5	6.4	5.1	9.1	13.6	15.4	11.8	6.3	9.6	3.6	2.8	1.7	0.9	0.3	0.3
V297	Expc	3.9	9.5	12.6	8.3	7.7	10.1	14.3	15.8	12.0	4.9	1.0						
V312A	Expc	0.0	1.0	6.8	9.8	8.8	18.2	20.4	16.1	10.4	5.0	3.5						
V312B	Expc	0.0	0.0	0.0	9.7	13.9	20.0	25.8	19.4	7.7	2.4	1.1						
V312C	Expc	0.0	0.0	16.4	29.0	11.2	10.7	8.8	9.1	7.6	4.3	2.9						
V313	Expc	0.0	0.0	3.0	7.3	14.9	19.9	20.6	16.2	8.6	4.2	5.4						
B215A	Expc	10.4	3.2	7.7	8.4	10.5	12.6	10.4	9.4	8.7	7.9	10.7	5.3	3.1	1.3	0.6	0.3	0.1
B216	Expc	2.5	8.3	5.6	6.7	8.4	13.2	17.0	18.5	13.0	6.1	0.8						
B217	Expc	0.0	20.3	8.8	11.1	9.5	12.7	14.2	12.3	6.8	2.7	1.7						
C259C	Expc	0.0	8.6	13.9	14.1	8.3	13.0	13.4	12.2	7.2	4.2	5.0	2.3	1.5	0.7	0.3	0.1	0.1
B173	RPpf	2.0	1.2	4.6	6.4	6.6	12.1	14.4	15.3	12.7	10.3	13.9	5.1	3.7	2.5	1.6	0.7	0.4
B222	RPpf	9.8	10.5	9.6	7.4	6.9	10.2	11.7	12.1	9.5	5.6	6.7						
B223	RPpf	17.1	9.6	7.2	7.1	6.5	9.8	10.8	10.5	7.6	5.7	8.1						
B224	RPpf	0.0	9.7	8.9	8.2	4.9	11.4	13.8	15.6	11.8	7.9	7.5	2.6	2.0	1.4	0.9	0.4	0.2
B225	RPpf	12.2	6.0	6.9	7.3	7.1	10.2	12.4	12.8	9.7	6.1	8.9	3.2	2.4	1.6	1.1	0.5	0.3
C259B	RPpf	0.0	0.0	1.9	5.1	6.1	8.5	15.0	21.7	21.3	14.3	6.1						
B218	Cpf	2.7	10.5	6.1	8.1	10.6	13.4	14.1	12.0	8.4	6.4	7.4						
B203	Cpf	13.6	3.5	6.8	6.3	6.4	11.4	13.2	12.6	9.0	7.0	9.9	3.4	2.7	1.9	1.0	0.6	0.2
C259A	Cpf	10.2	10.9	8.4	7.5	8.4	11.5	13.9	14.2	9.6	4.0	1.3	0.7	0.2	0.2	0.1	0.0	0.0
V224	Cpf	9.7	1.5	3.8	5.9	8.3	11.7	14.4	14.9	12.3	9.9	7.8						
C294	Cpf	24.9	7.6	4.0	4.0	5.5	7.4	10.5	11.2	10.0	8.3	6.5						
V101	Cpc	6.8	9.4	5.2	5.4	5.7	11.2	13.4	15.2	12.9	8.5	6.3						
V022A	Efba	11.7	13.4	10.0	10.6	9.7	14.1	14.0	9.0	4.6	1.8	1.2						

[1] Map units defined in figure 2. Expct, Explosive-phase pyroclastic-current deposit, thin; Expf, pyroclastic-flow deposit; Expc, pyroclastic-current deposit; Exlh, lahar deposit (hcf,hyperconcentrated flow deposit); Exma, mixed-avalanche deposit; RPpf, Rocky Point pyroclastic-flow deposit; Cpf, Continuous-phase pyroclastic-flow deposit; Cpfw, pyroclastic-flow of Windy Creek; Cpc, pyroclastic-current deposit; Efba, Effusive-phase block-and-ash-flow deposit.

Table 4. Statistics of grain-size analyses for samples of pyroclastic-flow, lahar, and mixed-avalanche deposits from the 2006 eruption of Augustine Volcano, Alaska.

[All values in phi units. Statistics calculated by using software courtesy of Sebastien Dartevelle, Los Alamos National Laboratories. Units defined in figure 2]

Sample	Unit	Mean	Median	Sorting	Mode	Skewness	Kurtosis
V021A	Expct	0.60	1.19	3.14	2.5	-0.16	0.96
V033A	Expct	-1.14	-0.70	3.27	-5.5	-0.11	0.70
V096	Expct	0.72	1.42	3.31	1.5	-0.25	1.08
V281A	Expct	1.38	1.42	2.15	2.5	0.05	1.23
V315	Expct	-0.42	0.07	2.78	1.5	-0.20	0.75
V283D	Expct	-0.36	0.91	3.76	1.5	-0.30	1.22
V283E	Expct	0.08	0.68	3.41	2.5	-0.13	0.85
V283A	Expct-basal	1.01	1.12	1.94	1.5	-0.12	0.97
V283B	Expct-basal	0.31	0.78	2.52	1.5	-0.24	0.87
V283C	Expct-basal	-1.24	-0.64	3.23	-5.5	-0.17	0.67
B184A	Expct-basal	0.73	0.96	2.04	1.5	-0.18	1.03
B184B	Expct-basal	1.05	1.33	2.44	1.5	-0.20	1.18
B184C	Expct-basal	1.56	1.61	1.43	1.5	-0.06	0.94
V117	Expf	-1.07	-0.64	2.83	1.5	-0.16	0.70
B102	Expf	-0.48	-0.14	2.84	1.5	-0.13	0.79
B176	Expf	1.06	1.30	2.20	1.5	-0.16	1.05
V256A	Expf-top	-1.66	-1.85	3.64	-5.5	0.12	0.64
V256B	Expf-mid	-2.41	-3.04	3.65	-6.5	0.28	0.71
V256D	Expf-base	-0.48	0.02	3.46	1.5	-0.12	0.89
V256E	Expf	2.83	2.28	2.70	2.5	0.09	1.28
B230	Expf	-0.77	-0.04	3.09	1.5	-0.27	0.80
V019	Expf	1.34	1.64	2.07	3.5	-0.28	0.94
V256C	Expf-base	0.30	0.70	3.05	1.5	-0.09	1.07
V297	Expc	-0.60	-0.18	2.69	1.5	-0.19	0.71
V312A	Expc	0.11	0.27	2.15	0.5	-0.08	1.04
V312B	Expc-base	0.15	0.26	1.58	0.5	-0.08	0.97
V312C	Expc-top	-0.92	-1.60	2.29	-2.5	0.42	0.82
V313	Expc	0.30	0.25	2.21	0.5	0.18	1.34
B215A	Expc	-0.20	-0.24	3.36	-0.5	0.01	0.91
B216	Expc	-0.16	0.33	2.53	1.5	-0.27	0.93
B217	Expc	-1.24	-0.97	2.58	-4.5	-0.04	0.68
C120	Expc	-0.75	-0.95	2.53	-3.5	0.16	0.69
C259C	Expc	-0.67	-0.60	2.65	-2.5	0.03	0.83
B173	RPpf	1.07	1.17	2.82	1.5	-0.02	1.10
B222	RPpf	-0.75	-0.41	3.47	1.5	-0.02	0.89
B223	RPpf	-1.05	-0.73	3.70	-5.5	0.02	0.81
B224	RPpf	0.05	0.51	2.99	1.5	-0.14	0.88
B225	RPpf	-0.48	0.02	3.46	1.5	-0.12	0.89
V022A	Efba	0.46	0.78	2.55	3.5	-0.22	0.86
V237	Exlh	-0.56	-0.42	2.51	0.5	-0.05	0.91
V270B	Exlh	-0.09	0.00	3.16	-3.5	0.06	0.91
V275B	Exlh	0.07	0.20	2.34	0.5	-0.06	1.06
V275C	Exlh	0.27	0.57	2.20	0.5	-0.17	1.09
V280	Exlh	-1.27	-2.01	3.16	-3.5	0.43	0.88
V330	Exlh	0.34	0.64	2.88	1.5	-0.04	1.01
V276A	Exlh-hcf[1]	-1.65	-2.23	2.85	-3.5	0.32	0.86
V276B	Exlh-hcf[1]	-0.27	-0.34	2.25	-0.5	0.13	0.96
V272	Exlh-hcf[1]	1.00	1.12	2.65	1.5	-0.03	1.28
V275A	Exlh-hcf[1]	-0.88	-1.12	2.35	-2.5	0.20	0.84
V199	Exma	-4.40	-4.49	0.43	-4.5	0.47	3.34
V257	Exma	0.09	0.31	3.21	0.5	0.00	0.93
V258	Exma	-0.74	-0.38	2.47	-0.5	-0.15	2.21
V254	Exma	3.91	3.61	1.69	5.5	0.12	0.56
V270A	Exma	-0.55	-0.43	2.58	-0.5	-0.06	0.99
V278	Exma	-0.23	0.53	3.45	1.5	-0.22	0.93
B218	Cpf	-0.32	-0.11	3.18	0.5	0.02	1.08
B203	Cpf	-0.35	0.14	3.54	-5.5	-0.12	0.92
C259A	Cpf	-1.04	-0.58	2.89	1.5	-0.18	0.72
V224	Cpc	0.34	0.65	3.22	1.5	-0.11	1.23
C259B	RPpf	1.42	1.62	2.22	1.5	-0.06	1.36
C294	Cpfw	-1.00	-0.43	3.84	-5.5	-0.06	0.68
V101	Cpc	-0.22	0.49	3.42	1.5	-0.17	1.01

[1] Hyperconcentrated-flow lahars

Table 6. Lithologic components in pyroclastic-current, lahar, and mixed-avalanche samples from the 2006 eruption of Augustine Volcano, Alaska.

[All values in weight percent. Components: low-silica andesite scoria (LSAS), dense low-silica andesite (DLSA), dense intermediate-silica andesite (DIA), high-silica andesite (HSA), high-silica andesite pumice (HSAP), and mixtures (banded) and defined in table 5. Phases and units (after Coombs and others, this volume), are defined in figure 2]

Sample	Unit[1]	Event	Size[2] (mm)	Clasts counted[3]	LSAS	DLSA	DIA	Banded	HSA	HSAP	Oxidized	Crystals	Non-crystals
			8	171	43.9	22.2	10.5	2.3	13.5	0.0	7.6	0.0	0.0
V033A	Expct	3–4	4	395	43.3	22.8	11.1	1.8	14.7	0.0	6.3	0.0	0.0
			1	509	46.8	6.3	10.8	0.0	13.9	1.6	5.7	14.9	0.0
			32	3	66.7	0.0	0.0	0.0	33.3	0.0	0.0	0.0	0.0
			16	14	21.4	21.4	7.1	21.4	21.4	0.0	7.1	0.0	0.0
			8	70	47.1	10.0	17.1	2.9	18.6	0.0	4.3	0.0	0.0
			4	513	50.5	15.2	12.3	1.6	15.4	0.0	5.1	0.0	0.0
V096	Expct	3–4	2	223	32.3	17.0	18.8	0.0	21.5	0.0	8.1	2.2	0.0
			1	660	44.7	5.9	6.1	0.0	18.8	0.0	10.2	14.4	0.0
			0.5	1,158	26.2	6.4	7.0	0.0	8.7	0.2	9.9	41.7	0.0
			0.25	465	26.5	3.7	0.0	0.0	13.8	0.0	8.2	48.0	0.0
			0.125	1,248	0.0	0	0	0	0.0	0.0	7.3	56.7	36.0
Average	Expct	--	--	--	40.8	10.9	8.4	6.0	17.6	0.1	6.6	14.8	3.0
			8	51	49.0	21.6	17.6	0.0	11.8	0.0	0.0	0.0	0.0
B184A	Expct basal	3–4	4	728	44.2	23.2	9.5	0.3	15.7	0.1	7.0	0.0	0.0
			1	744	55.2	2.8	8.5	0.0	12.6	0.0	8.9	12.0	0.0
			8	52	53.8	17.3	15.4	3.8	9.6	0.0	0.0	0.0	0.0
B184B	Expct basal	3–4	4	305	48.9	13.8	8.2	1.6	20.0	0.7	6.9	0.0	0.0
			1	441	53.3	2.9	14.7	0.2	10.4	0.0	9.3	9.1	0.0
Average	Expct basal	--	--	--	50.7	13.6	12.3	1.0	13.4	0.2	5.3	3.5	0.0
			8	286	50.0	13.3	14.7	2.1	11.9	0.0	8.0	0.0	0.0
B102	Expf	3–7	4	609	53.5	11.8	14.4	0.0	11.2	0.8	8.2	0.0	0.0
			1	537	30.9	1.5	11.0	0.0	21.4	0.0	11.4	23.8	0.0
			8	72	73.6	8.3	5.6	2.8	9.7	0.0	0.0	0.0	0.0
B230	Expf	8	4	703	56.8	5.3	16.4	0.1	15.4	2.4	3.7	0.0	0.0
V019	Expf	9	8	147	48.3	9.5	12.2	7.5	17	0	5.4	0	0.0
Average	Expf	--	--	--	53.0	8.0	12.4	13.0	13.9	0.8	6.3	--	0.0
			8	76	47.4	10.5	6.6	2.6	18.4	9.2	5.3	0.0	0.0
V278	Exma	8	4	649	47.8	10.9	12.3	1.7	13.3	2.2	11.9	0.0	0.0
			8	138	40.6	29.7	7.2	0.0	12.3	0.0	10.1	0.0	0.0
V275A	Exlh	7	4	705	38.2	15.5	14.6	0.0	20.4	0.0	11.3	0.0	0.0
			1	344	39.0	0.3	9.0	--	19.5	0.0	13.1	19.2	0.0
			8	131	58.8	11.5	5.3	0.8	19.1	0.0	4.6	0.0	0.0
V275B	Exlh-levee	7	4	352	53.7	9.9	10.5	0.3	17.0	0.0	8.5	0.0	0.0
			1	671	31.0	2.5	6.7	0.0	20.0	0.0	14.2	25.6	0.0

Table 6. Lithologic components in pyroclastic-current, lahar, and mixed-avalanche samples from the 2006 eruption of Augustine Volcano, Alaska.—Continued

[All values in weight percent. Components: low-silica andesite scoria (LSAS), dense low-silica andesite (DLSA), dense intermediate-silica andesite (DIA), high-silica andesite (HSA), high-silica andesite pumice (HSAP), and mixtures (banded) and defined in table 5. Phases and units (after Coombs and others, this volume), are defined in figure 2]

Sample	Unit[1]	Event	Size[2] (mm)	Clasts counted[3]	LSAS	DLSA	DIA	Banded	HSA	HSAP	Oxidized	Crystals	Non-crystals
V276A	Exlh	8	8	250	24.0	17.2	29.6	1.2	15.6	0.0	12.4	0.0	0.0
			4	327	38.8	15.9	15.9	0.9	15.9	0.0	12.5	0.0	0.0
			1	402	43.0	3.7	10.9	0.0	12.9	0.0	15.2	14.2	0.0
Average	Exlh	--	--	--	42.0	11.6	11.7	0.9	16.8	1.0	10.8	5.4	0.0
B215A	Expc	10	8	114	9.6	3.5	28.1	1.8	48.2	0.0	8.8	0.0	0.0
			4	959	9.7	9.2	38.5	0.0	39.0	0.0	2.5	1.1	0.0
			1	808	14.5	5.3	7.3	0.0	32.9	0.0	7.1	32.9	0.0
C259C	Expc	10	8	279	13.6	44.4	9.7	6.8	24.0	0.0	1.4	0.0	0.0
			4	2,080	35.3	39.3	9.8	1.2	11.4	0.0	2.9	0.0	0.0
V313	Expc	10	8	10	0.0	40.0	30.0	0.0	30.0	0.0	0.0	0.0	0.0
			4	179	0.0	29.6	20.1	0.6	44.1	1.7	3.9	0.0	0.0
Average	Expc	--	--	--	11.8	24.5	20.5	1.7	32.8	0.2	3.8	4.9	0.0
B173	RPpf	10	8	78	9.0	9.0	19.2	1.3	56.4	1.3	3.8	0.0	0.0
			4	330	2.4	9.1	10.6	0.0	73.9	0.9	3.0	0.0	0.0
			2	214	4.2	10.7	9.8	0.0	71.5	0.0	0.5	3.3	0.0
B222	RPpf	10	32	2	0.0	100.0	0.0	0.0	0.0	0.0	0.0	0.0	0.0
			16	13	38.5	46.2	7.7	0.0	7.7	0.0	0.0	0.0	0.0
			8	105	8.6	12.4	8.6	0.0	67.6	0.0	2.9	0.0	0.0
			4	723	5.8	7.9	3.3	0.0	79.8	0.0	3.0	0.1	0.0
			2	373	5.4	6.7	5.9	0.3	67.6	0.0	4.6	9.7	0.0
			1	820	2.7	3.9	8.3	0.0	31.7	18.0	7.0	28.4	0.0
			0.5	1282	0.9	1.6	9.2	0.0	19.6	0.0	6.9	61.8	0.0
			0.25	907	0.7	4.0	0.0	0.0	11.1	0.0	2.5	81.7	0.0
Average	RPpf				7.1	19.2	7.5	0.2	44.3	2.2	3.1	16.8	0.0
B203	Cpf	≥14	8	95	0.0	33.7	31.6	0.0	28.4	0.0	6.3	0.0	0.0
			4	641	0.0	42.6	7.2	0.0	46.6	0.0	3.6	0.0	0.0
V101	Cpc	≥14	8	73	0.0	1.4	50.7	11.0	28.8	0.0	8.2	0.0	0.0
			4	589	0.0	4.9	40.6	0.2	45.7	0.0	8.7	0.0	0.0
Average	Cpf				0.0	20.6	32.5	2.8	37.4	0.0	6.7	0.0	0.0
V22A	Efba		8	108	9.0	63.1	9.0	0.0	3.6	0.0	15.3	0.0	0.0

[1] Units after Coombs and others (this volume), same as in table 1.

[2] Size is defined as particles remaining on sieve indicated; for larger size classes (≥1.0 mm), grains were sorted by using a hand lens and binocular microscope, and commonly the lithologic differences were best determined by using wetted clasts (which represented the most common field conditions). Clast-type groups were then dried, counted, weighed, and normalized to 100 percent. For smaller size classes (≤0.50 mm), sorting was done by using a single paintbrush hair under a binocular microscope. Clast types were sorted by lithology or oxidation for most size classes. The samples whose small grains were sorted had them divided among crystals, noncrystals, and oxidation. Lithologies are described in table 3.

[3] Not all size classes were counted for all samples. Clasts from each size class were initially sorted from 32 mm to 0.125 mm to assess the similarity in clast-type proportions between size classes. The 4- and 8-mm size classes were deemed representative of the proportions of lithologies for many samples.

Table 8. Parameters and analysis-of-variance statistics for alternative linear models of log-transformed volume versus planimetric area for pyroclastic-current deposits worldwide and those from the 2006 eruption of Augustine Volcano, Alaska.

Variable	Best-fit regression	Specified 2/3 slope	Specified zero slope
	Dome-collapse pyroclastic flows		
Slope of line	0.659	0.667	0
Intercept of line at log V=0	1.612	1.5661 = log 37	5.530
Number of data pairs (N)	21	21	21
Residual degrees of freedom (DF)	19	20	20
Residual sum of squares (SS)	0.800	0.801	5.133
Residual mean square (MS)	0.042	0.042	0.257
Standard error of model (sigma)	0.205	0.200	0.507
Coefficient of determination (r^2)	0.844	0.844	0
F statistic comparison to best-fit regression	Not applicable	0.017	102.9
Null hypothesis	Not applicable	Accepted, 0.99-confidence level	Rejected
	Column-collapse pyroclastic currents		
Slope of line	0.736	0.667	0
Intercept of line at log V=0	1.779	2.1717 = log 150	5.943
Number of data pairs (N)	14	14	14
Residual degrees of freedom (DF)	12	13	13
Residual sum of squares (SS)	0.110	0.151	4.731
Residual mean square (MS)	0.009	0.012	0.364
Standard error of model (sigma)	0.095	0.108	0.603
Coefficient of determination (r^2)	0.977	0.968	0
F statistic comparison to best-fit regression	Not applicable	4.493	547.9
Null hypothesis	Not applicable	Accepted, 0.99-confidence level	Rejected
	Surge-like pyroclastic currents		
Slope of line	0.653	0.667	0
Intercept of line at log V=0	2.794	2.718 = log 520	6.509
Number of data pairs (N)	4	4	4
Residual degrees of freedom (DF)	2	3	3
Residual sum of squares (SS)	0.008	0.008	0.444
Residual mean square (MS)	0.004	0.003	0.148
Standard error of model (sigma)	0.064	0.053	0.385
Coefficient of determination (r^2)	0.981	0.981	0
F statistic comparison to best-fit regression	Not applicable	0.045	105.5
Null hypothesis	Not applicable	Accepted, 0.99-confidence level	Rejected

This page intentionally left blank

The 2006 Eruption of Augustine Volcano, Alaska
Power, J.A., Coombs, M.L., and Freymueller, J.T., editors
U.S. Geological Survey Professional Paper 1769

Chapter 11

Characterizing Pyroclastic-Flow Interactions with Snow and Water Using Environmental Magnetism at Augustine Volcano

By James E. Begét[1]

Abstract

In-place measurements of environmental magnetic susceptibility of pyroclastic flows, surges and lahars emplaced during the 2006 eruption of Augustine Volcano show that primary volume magnetic susceptibilities of pyroclastic materials decreased where the flows encountered water and steam. The Rocky Point pyroclastic flow, the largest flow of the eruption sequence, encountered a small pond near the north coast of Augustine Island where local interactions with water and steam caused susceptibilities to decrease from $1{,}084\pm128\times10^{-5}$ SI to $615\pm114\times10^{-5}$ SI. Ash produced during phreatic explosions and pyroclastic surges that crossed snow also produced deposits with reduced susceptibilities, while lahar deposits derived from pyroclastic flows showed even greater reductions in susceptibility ($430\pm129\times10^{-5}$ SI). The susceptibility reductions are probably largely attributable to oxidation of iron in magnetite and other minerals within the pyroclastic flows, although other physiochemical processes may play a role. Measurements of the magnetic properties of pyroclastic flows, surges, and lahar deposits can be a useful tool in understanding the processes that occur when pyroclastic flows encounter ice, snow, and water and interact with water and steam on the slopes of active volcanoes.

Introduction

The interactions that occur between pyroclastic flows and snow, ice, and water are of considerable interest to volcanologists because these processes sometimes generate floods and lahars that cause destruction and fatalities in areas far beyond the maximum extent of the pyroclastic flows themselves. For instance, the 1985 eruption at Nevado del Ruiz Volcano in the Andes Mountains of Colombia generated pyroclastic flows and surges that were restricted to the upper reaches of the volcano, far from any human habitation. However, the pyroclastic eruption melted snow and ice over part of the summit ice cap and generated devastating mudflows that traveled as far as 100 kilometers down stream valleys. These lahars traveled down the Río Lagunillas and caused an estimated 23,000 fatalities at the town of Armero, where local people had had little comprehension of the risks from the Ruiz eruption (Pierson and others, 1990).

The lahar and flood deposits produced by interactions between pyroclastic flows and glaciers, snowfields, and bodies of water have attracted much attention since the catastrophic Ruiz eruption. For instance, during the eruptions of Ruapehu Volcano in New Zealand in 1994–95 and 2005–6, interactions of pyroclastic material and snow became a focus of concern. Lahars that traveled downslope after explosive events at the summit were observed during emplacement, and their deposits were intensively studied (Cronin and others, 1997). Unfortunately, once again it proved difficult to observe and study active surges and pyroclastic flows and the processes that occur during their encounters with snow and ice, because the active vents are extremely hazardous to approach during eruptions, and because these kinds of eruptions and processes typically produce large clouds of ash, gas, and steam that hide the ground-level interactions. As a result, the processes involved in the generation of lahars and floods by pyroclastic flows are still poorly understood.

The 2006 eruption of Augustine Volcano provided an excellent opportunity to study pyroclastic-flow and surge deposits that had encountered ice, snow, and water, as well as associated lahar deposits resulting from those interactions. Comprehensive sedimentological and stratigraphic studies of the pyroclastic-flow and lahar deposits produced in 2006 at Augustine Volcano showed that such interactions were complex and varied. Some pyroclastic flows traveled across snowfields with little obvious effect on the sedimentology of

[1]Alaska Volcano Observatory, Department of Geology and Geophysics, University of Alaska Fairbanks, 900 Yukon Drive, Fairbanks, AK 99775.

the pyroclastic flow deposits, while others crossed areas of snow and were locally modified and transformed into mixed rock-and-snow avalanches, lahars, and water-rich floods (Vallance and others, this volume).

In this paper, we present tests of a new geophysical technique that we believe has great promise as a means to identify and characterize pyroclastic-flow and surge deposits that have interacted with snow, ice, and water. Environmental magnetism is the study of interactions between environmental processes and the magnetic properties of sediments (Evans and Heller, 2003). Studies of environmental magnetism often focus on changes in magnetic susceptibility, because this geophysical characteristic of sediments is relatively easily measured and has been shown to undergo significant changes in response to various environmental factors and depositional processes (Maher and Thompson, 1999). We have followed this approach and focused on magnetic susceptibility in this study.

Pyroclastic-flow deposits that have interacted with snow, ice, and water are good candidates for this kind of study, because the initial magnetic susceptibility of volcanic rocks and volcanic ash deposits produced by explosive eruptions elsewhere in Alaska have been shown to be relatively high, indicating the presence of abundant susceptible iron-bearing minerals (Begét and others, 1994). However, to our knowledge, no prior studies of the changes in magnetic susceptibility of pyroclastic deposits due to interactions with water and steam have ever been undertaken. Searches on Google Scholar and GeoRef found no record of scientific papers on this subject, and recent academic textbooks on environmental magnetism (Evans and Heller, 2003) and volcanology (Schmincke, 2004) contain no references to this kind of investigation.

This paper presents the results of several hundred measurements of magnetic susceptibility on fresh, in place, deposits of the 2006 pyroclastic flows on the flanks of Augustine Volcano, as well as measurements on more areally restricted surge and lahar deposits. The purpose of this paper is not to descriptively characterize the magnetic mineralogy and magnetic characteristics of the 2006 deposits, but to report on the initial development and field-testing of a new geophysical approach that can quickly and quantitatively characterize a key geophysical property of pyroclastic-flow deposits that records evidence of past interactions with water and snow.

2006 Pyroclastic Flows and Related Deposits on the North Flank of Augustine Island

The 3-month-long eruption at Augustine Volcano in 2006 involved a variety of different eruptive mechanisms and produced a wide array of pyroclastic and secondary deposits (Coombs and others, this volume; Vallance and others, this volume). Explosive activity began on January 11, 2006, and more than a dozen discrete Vulcanian blasts occurred in the next 20 days, generating ash fall, pyroclastic flows, mixed avalanches of snow, ice, and rock, and lahars. On January 28, the eruption moved into a more continuous eruptive phase as rapid effusion of lava led to vigorous block-and-ash-flows. A summit lava dome began to form in early February, and, after a pause from February 10 to March 2, two short, blocky lava flows were emplaced by late March. The initial period of explosions, lasting from January 11 to January 28, is referred to as the explosive phase, while eruptive events occurring from January 28 to February 10 are considered to be part of the continuous phase, and all subsequent activity is part of the effusive phase (Power and others, 2006; Coombs and others, this volume).

On January 27, 2006, near the end of the explosive phase, a discrete several-minute-long explosive event (event 10 in the nomenclature of Vallance and others, this volume) deposited the Rocky Point pyroclastic flow on the north flank of the volcano (fig. 1). This flow is the most voluminous of any single flow produced during the eruptive sequence, totalling 17 million m^3 (Coombs and others, this volume). It traveled almost to sea level on the north side of Augustine Island and buried earlier 2006 pyroclastic flows on the north flank of the volcano (fig. 2).

The distal portion of the Rocky Point pyroclastic flow nearly reached the coast, traveling over a small pond of water. The pond lay at 25 m above sea level (asl) and was approximately 50 m in diameter. The pond is partly surrounded by hummocks of the late 19th century Burr Point debris-avalanche deposit and the older Rocky Point debris-avalanche deposit (Begét and Kienle, 1992; Siebert and others, 1995) and likely was formed during one of these events. The 2006 Rocky Point pyroclastic flow completely filled the lake basin with pyroclastic debris. This pyroclastic flow also generated small, relatively dilute ash-cloud surges that traveled short distances beyond the lateral margins of the pyroclastic flow and singed alders and other vegetation around the former shoreline of the pond, leaving well-sorted sandy ash deposits.

The initial magmatic explosive events early in January that marked the beginning of the explosive phase occurred when Augustine Volcano was completely covered with winter snow. These explosions generated pumiceous pyroclastic flows, snow avalanches, and lahars that moved down all sides of the volcano (Vallance and others, this volume). By the time the Rocky Point pyroclastic flow was emplaced on January 28, much of the winter snowpack on the volcano had been removed or buried by the earlier pyroclastic flows. The snow was almost completely gone when block-and-ash flows, emplaced during the later continuous phase, subsequently buried the uppermost parts of the Rocky Point pyroclastic flow (Coombs and others, this volume).

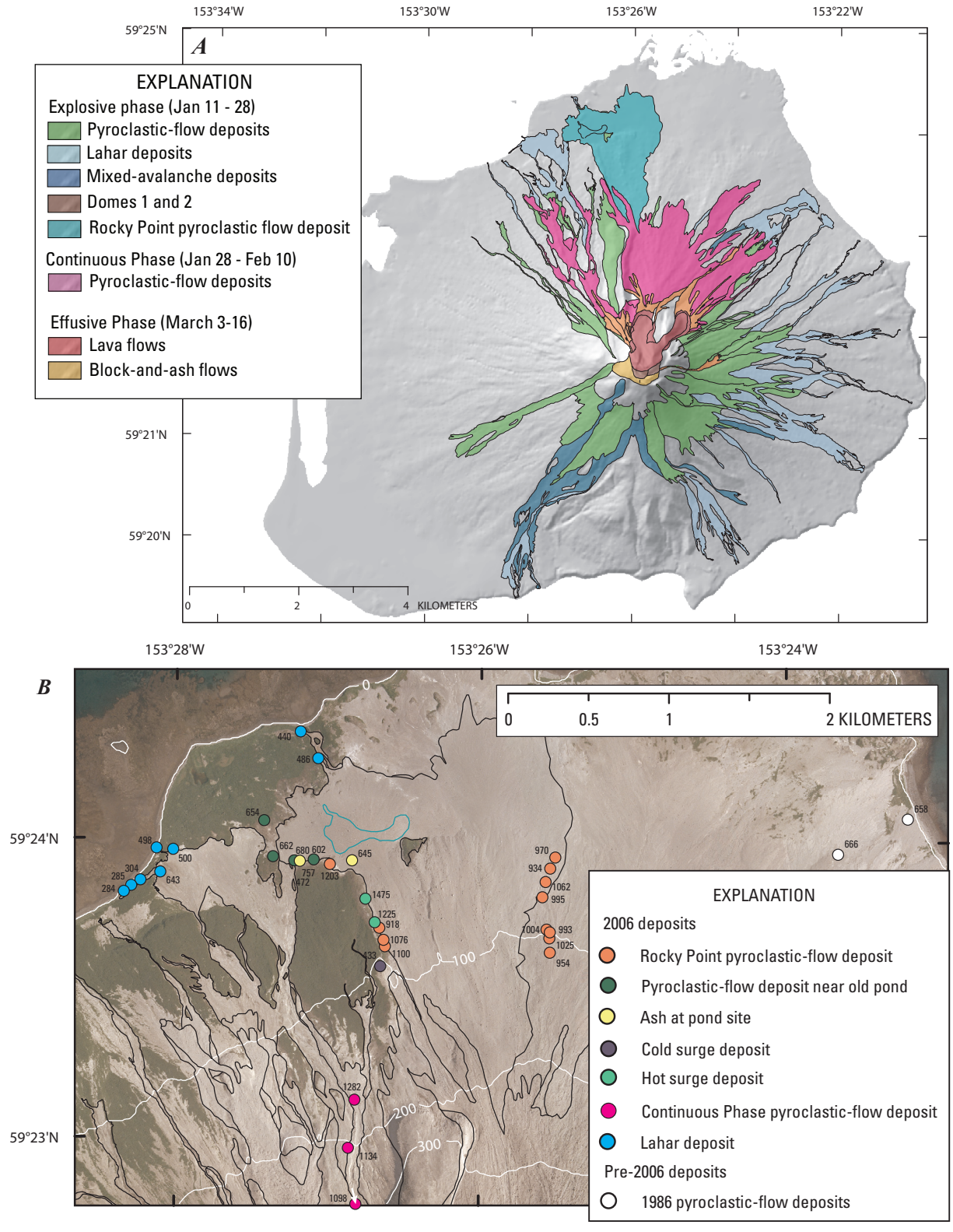
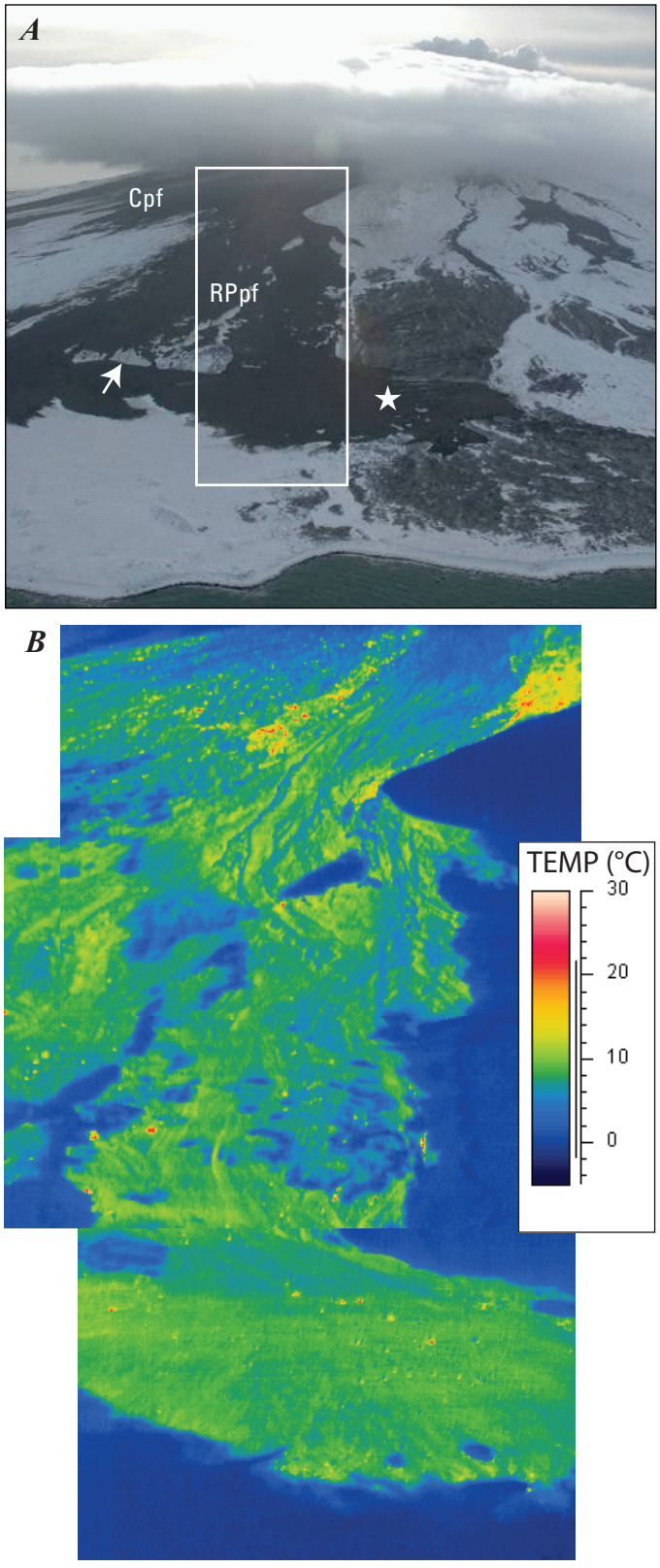


Figure 1. Generalized maps showing deposits from the 2006 eruption of Augustine Volcano on Augustine Island. *A,* Distribution of deposits from the 2006 eruption draped over shaded-relief map of Augustine Island, modified from Coombs and others (this volume). *B,* Sample locations for this study on the north flank of Augustine Volcano, overlain on an orthophoto taken July 12, 2006. Outlines of contiguous 2006 deposits are shown in black. The general outline of the small pond buried by the Rocky Point pyroclastic flow, as mapped in July 2006 by Begét, is shown in light blue, and100-m contours shown in white. Some 2006 deposits were sampled in fresh exposures in a small channel 170 m east of the region of contiguous flows and a few sites were sampled on 1986 pyroclastic flows (see text for detailed discussion).



Magnetic Susceptibility of Pyroclastic Flows, Surges and Lahars at Augustine Volcano

Augustine Volcano produced a wide range of pyroclastic deposits during the 2006 eruption. This study targets the Rocky Point pyroclastic flow deposit because it provides an almost ideal opportunity to test the hypothesis that measurements of magnetic susceptibility can provide a quantitative tool for identifying and characterizing pyroclastic deposits that have been in contact with snow, ice, and water. We also present some results from lahars, from pyroclastic flows on the north flank that were produced during the later continuous phase of the eruption and from 1986 Augustine pyroclastic flow deposits.

Magnetic susceptibility is a basic geophysical property of all rocks and sediments. Magnetic susceptibility can be measured on a mass, molar, or volume basis. It is determined by measuring the effect of an applied magnetic field of known strength on a sample. The ease of magnetization of the sample is a complex function of the concentration, size, shape, and mineralogy of magnetizable material in the sample. Most of the susceptibility signal in volcanic rocks typically reflects the presence of common ferromagnetic minerals, such as magnetite, hematite, and iron-titanium oxides, with a minor contribution from other ferromagnesian minerals that contain relatively small amounts of Fe^{2+}, Fe^{3+}, or Mn^{2+} such as olivine, amphiboles, and pyroxenes.

Field measurements of volume magnetic susceptibility of the 2006 deposits at Augustine Volcano were made with a Bartington MS2 susceptibility meter and an MS2F microprobe. A small amount of sample preparation, including the excavation of small pits, was done in this study to standardize the sampling process, but the volume magnetic susceptibility measurements themselves are nondestructive. When measuring volume susceptibility, the MS2 meter has a sensitivity of 2×10^{-6} SI, with a range from $1–9999\times10^{-5}$ SI, and a resolution of 2×10^{-6} SI in standard mode. The Bartington instrument has become an international standard for environmental susceptibility measurements and records data in dimensionless volume susceptibility units, which are multiplied by 10^{-5} to convert susceptibilities into SI units (Bartington Corporation, 2004).

◀**Figure 2.** Views of recently emplaced pyroclastic flow deposits, February 8, 2006. *A,* Oblique aerial photograph of Augustine's north flank, showing the Rocky Point pyroclastic flow (RPpf) and the overlying Continuous Phase pyroclastic flow fan (Cpf). The Rocky Point flow was bifurcated by a low ridge (white arrow). Westernmost lobe of the Rocky Point flow crossed and filled in a small lake (star). Box shows approximate area of panel B. Photo by M. Coombs, USGS. *B,* Thermal infrared image mosaic showing close up of Rocky Point deposit. Images by D.J. Schneider, AVO.

The Bartington M2SF microprobe is designed for use in geologic studies. The probe has a diameter of 15 mm and measures volume susceptibility in a small region of the sample immediately beneath the probe. In order to take a measurement the probe is placed on the sample and activated. The instrument then applies a magnetic field and measures the sample response, with about 90 percent of the susceptibility signal coming from the upper few millimeters of the sample, where the magnetic field projected by the probe is strongest (fig. 3). The MS2F microprobe proved to be ideal for field studies of the pyroclastic-flow deposits because the knowledge that 90 percent of the susceptibility response is obtained from a restricted area within a few millimeters of the MS2F probe allows the operator to precisely control what the instrument is measuring, even in field settings. For this study the goal was to effectively measure the susceptibility of the matrix of pyroclastic-flow deposits, so the probe was placed directly on exposures of the well-sorted and finer grained pyroclastic flow matrix visible between clasts in the pyroclastic flow deposits. Voids or lithic clasts hidden beneath the surface of the area chosen for the matrix sampling have a negligible influence on volume susceptibility measurements, as long as they were buried more than approximately 2 cm below the surface, or if they were more than 1 cm away from the outside edges of the MS2F microprobe (fig. 3).

Several different sampling methods were tested during this study. Initially, shallow pits and trenches approximately 50 cm deep were excavated into the tops of pyroclastic flow deposits and into the sides of associated levees, and the MS2F microprobe was then inserted into the pit for the measurement. Subsequent measurements were taken on smoothed surfaces cut only a few centimeters into the surface of massive pyroclastic flow deposits and levees to expose the matrix of the deposits, and in some cases directly on the hardpan surface of indurated pyroclastic flow deposits. After each measurement, the surface was excavated to check if voids or blocks were present just below the surface of the prepared site. No significant differences in susceptibility were observed among any of the various sampling strategies as long as the excavations and natural surfaces measured were flat and smooth.

Component analysis of the 2006 pyroclastic flow deposits revealed that they contain several different lithologies and that the relative percentages of the different lithologies changed through the course of the 2006 eruption (Vallance and others, this volume). All of the magnetic susceptibility values discussed in this paper, unless specifically noted otherwise, are from the Rocky Point pyroclastic flow, which was erupted during a short time interval and has broadly similar proportions of lithic components throughout its extent (Vallance and others, this volume). The susceptibility of the two major lithic components in the Rocky Point pyroclastic-flow deposit was measured directly on representative lithic blocks and showed that different rock types produced during the 2006 eruption have dramatically different susceptibilities (table 1). Low-silica andesite scoria and dense clasts have susceptibilities between 1,200–1,700×10^{-5} SI, while friable and moderately vesicular high-silica andesite "cinderblock" clasts (Vallance and others, this volume) have volume susceptibilities of 700–1,200×10^{-5} SI. The Rocky Point pyroclastic flow deposit consists mainly of high-silica andesite, with clasts of low-silica andesite being present as a secondary component. The large difference in the susceptibility measured between the two principal lithologies suggests that the volume susceptibility of the pyroclastic flow will be strongly influenced by the relative proportion of these two major components within the deposit. Component analysis of different size fractions of the Rocky Point pyroclastic flow found that similar percentages of the major components were present from the coarsest to the finest grain sizes of the pyroclastic flow (Vallance and others, this volume), suggesting that susceptibility measurements of the matrix of the pyroclastic flow deposit are a good approximation of the susceptibility of the entire pyroclastic flow deposit.

The Rocky Point pyroclastic flow traveled down the volcano's north flank, where previous explosive events had deposited pyroclastic flows and cleared the surface of snow (Coombs and others, this volume; Vallance and others, this volume). Measurements taken from different places on the Rocky Point deposit yielded generally similar magnetic susceptibilities of 900–1,400×10^{-5} SI. The repeatability of the susceptibility measurements taken at each site was good, with values of one standard deviation from the mean typically falling no more then 10–20 percent from the average value for the entire group of susceptibility measurements. The

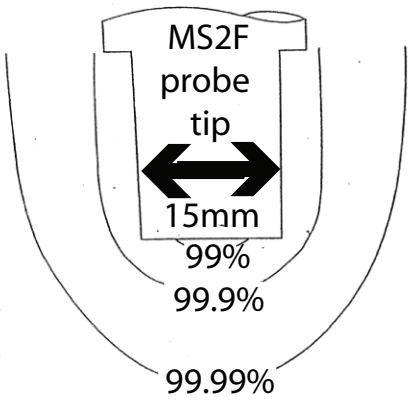


Figure 3. An isomagnetic field plot showing the rapid decrease in sensitivity of the M2SF field probe with distance from the tip of the instrument. The probe tip is 15 mm in diameter and has a maximum sensing distance of 15-20 mm, but the instrument is highly sensitive to the magnetic susceptibility of sample material just below and within a few millimeters of the center of the probe tip, so that 99% of the measured signal comes from material directly beneath the probe, and 99.9% of the signal is measured within a few millimeters of the probe. This property of the instrument makes it feasible to accurately measure the volume susceptibility of pyroclastic flow deposit matrices, as long as no voids or large lithic clasts are present within a few millimeters of the base of the probe. Figure modified from the Bartington M2S system operating manual (Bartington Corporation, 2004).

Table 1. Magnetic susceptibility measurements of the Rocky Point pyroclastic flow and associated deposits from the 2006 eruption of Augustine Volcano.

Station Number	Elevation (meters)	Latitude (north)	Longitude (west)	Magnetic susceptibility[1]	1σ [2]	N[3]	Deposit type
Rocky Point pyroclastic-flow deposit							
06AUJEB45	84	59.394	153.444	1100	63	10	PF[4] 1evee ridge with pink top
06AUJEB46	79	59.394	153.444	1076	82	9	PF body
06AUJEB47	76	59.395	153.444	918	83	5	Pink top in PF body
06AUJEB40	52	59.398	153.426	1062	83	4	PF body matrix
06AUJEB41	40	59.398	153.426	934	42	3	PF matrix
06AUJEB42	34	59.399	153.425	970	49	4	Flow terminus lobe
06AUJEB35	116	59.394	153.426	954	91	4	PF matrix
06AUJEB36	91	59.395	153.426	1025	1	5	PF matrix
06AUJEB37	88	59.395	153.426	1004	211	4	PF matrix
06AUJEB38	85	59.395	153.426	993	9	5	PF matrix
06AUJEB39	61	59.397	153.427	995	49	5	PF matrix
06AUJEB52	23	59.399	153.450	1203	30	6	PF matrix upslope of pond
06AUJEB40A	49	59.401	153.429	1240	119	6	Fines-depleted matrix
Rocky Point pyroclastic-flow deposit, in or adjacent to pond							
06AUJEBJA	30	59.399	153.454	472	43	5	Pink oxidized phreatic ash
06AUJEBJ	23	59.399	153.454	757	35	6	Pink oxidized PF matrix
06AUJEB51	23	59.399	153.448	645	84	6	Fine pink ash in collapse pit
06AUJEB51A	23	--	--	443	95	4	Fine pink ash in pond phreatic explosion pits
06AUJEB51B	23	59.399	153.456	662	49	8	PF matrix
06AUJEB51C	23	59.401	153.457	654	19	11	PF matrix, thin in bushes
06AlJ.JEB88	21	59.399	153.452	802	50	5	Pinkish PF in pond
06AUJEB89	19	59.399	153.452	602	37	7	Reddish oxidized PF in pond
06AUJEB90	14	59.399	153.453	680	24	5	Pink phreatic ash in pond
06AUJEB40B	46	59.3995	153.453[5]	907	55	6	Lower PF beside pond
06AUJEB40C	46	59.3995	153.453[5]	1200	14	2	PF around burned spruce
06AUJEB42A	30	--	59.399[5]	1299	25	5	PF 100 m from pond
Surge deposits associated with Rocky Point pyroclastic flow							
06AUJEB44	109	59.393	153.444	433	41	7	Cold surge
06AUJEB44A	101	59.3935	153.444[5]	1025	94	3	Distal ash cloud
06AUJEB44B	87	59.3935	153.444[5]	1166	127	6	Intermediate surge depos
06AUJEB48	71	59.395	153.445	1225	63	6	Proximal surge deposit
06AUJEB49	49	59.397	153.446	1475	308	4	Coarse proximal surge
06AUJEB51	23	59.399	153.448	1084	33	3	Ash cloud from surge
06AUJEB51A	14	59.3995	153.448[5]	827	45	3	Gray surge deposit
Continuous phase pyroclastic-flow deposit on northwest flank							
06AUJEB2	278	59.379	155.447	1098	8	2	PF matrix
06AUJEB2A	287	59.379	155.447	989	9	2	PF matrix
06AUJEB2B	314	59.379	155.447	1058	134	4	PF matrix
06AUJEB3	213	59.383	153.448	1134	30	2	PF matrix
06AUJEB4	170	59.385	153.447	1282	35	2	PF levee

Table 1. Magnetic susceptibility measurements of the Rocky Point pyroclastic flow and associated deposits from the 2006 eruption of Augustine Volcano.——Continued

Station Number	Elevation (meters)	Latitude (north)	Longitude (west)	Magnetic susceptibility[1]	1σ [2]	N[3]	Deposit type
2006 lahar deposits							
06AUJEB59	14	59.398	153.468	643	21	3	Lahar clasts
06AUJEB91	12	59.399	153.467	500	18	7	Lahar matrix
06AUJEB53	6	59.404	153.451	486	17	10	Lahar matrix
06AUJEB60	2	59.398	153.470	304	54	11	Lahar matrix
06AUJEB93	1	59.399	153.469	498	23	8	Lahar matrix
06AUJEB55	1	59.406	153.453	440	23	10	Lahar matrix
06AUJEB61	1	59.397	153.472	284	22	10	Lahar matrix
06AUJEB62	0.5	59.397	153.472	285	114	10	Lahar matrix
Individual clasts from 2006 pyroclastic-flow deposits							
06AUJEB45	84	59.394	153.444	1517	93	6	Low-silica andesite
06AUJEB35	116	59.394	153.426	1288	56	3	Low-silica andesite bomb
06AUJEB35	116	59.394	153.426	761	28	3	High-silica andesite
06AUJEB2A	287	59.379	155.447	1203	0	1	High-silica andesite
06AUJEB2A	287	59.379	155.447	989	9	2	Boulder in PF matrix
06AUJEB2B	314	59.379	155.447	1150	0	1	Prismatic boulder
1986 pyroclastic-flow deposits							
06AUJEB57	26	59.399	153.394	666	50	8	1986 PF
06AUJEB58	9	59.401	153.387	658	18	11	1986 PF matrix samples
06AUJEB58A	6	59.401	153.387	672	94	11	1986 PF matrix

[1]Reported magnetic susceptibility values are averages of N measurements.

[2]σ is the standard deviation of the averaged magnetic susceptibility measurements.

[3]N is the number of individual magnetic susceptibility measurements at each station.

[4]PF is an abbreviation for pyroclastic-flow deposit.

[5]Measurements made on traverses downhill from the first station in the series.

variation in the entire data set of susceptibility measurements for the Rocky Point pyroclastic flow deposit is somewhat larger (table 1), and is thought to reflect variations in the initial componentry of these deposits.

Susceptibility Measurements Along a Traverse at the Margin of the Rocky Point Pyroclastic Flow Deposit

The pyroclastic flow deposits emplaced in 2006 on the north side of Augustine Volcano partially buried a preexisting pyroclastic fan that has been developing since 1883 (Waitt and Begét, 2009). On the lower part of the pyroclastic fan, the Rocky Point pyroclastic flow deposit is bordered on its western edge by a much older lava flow. On its western margin against the lava flow, the Rocky Point pyroclastic flow developed flat terraces and a levee that could be traced for hundreds of meters downslope. Alder trees and soil buried by the Rocky Point pyroclastic flow were charred and incinerated, showing that the pyroclastic flow was hot in this area (fig. 4).

In order to better understand the sources of variation in magnetic susceptibility, measurements were made at eight separate sites during a 1-km-long traverse along the western margin of the Rocky Point pyroclastic flow (fig. 1). The averages of all of these measurements ranged from 937 to $1{,}061\times10^{-5}$ SI, indicating that much less variability in magnetic susceptibility occurs in this particular region of the pyroclastic flow than was seen in the complete data set from the Rocky Point pyroclastic flow and the subsequent flows of the continuous phase (fig. 5). The small range of susceptibilities measured from this one part of the Rocky Point pyroclastic flow supports our suggestion that the susceptibility within the lithic components of each flow strongly influences the matrix magnetic susceptibility. The greater variability within the entire set of susceptibility measurements for the Rocky Point pyroclastic flow and later pyroclastic-flow deposits is therefore thought to reflect a small amount of variability in the relative abundances

of the constituent components occurring through the entire pyroclastic flow (fig. 6).

Continuous-Phase Pyroclastic Flow Deposits

Measurements of magnetic susceptibility were also made on pyroclastic flow deposits produced during the continuous phase of the 2006 eruption (Coombs and others, this volume). Numerous block-and-ash flows, erupted from January 28 to February 10, are found on the upper parts of the pyroclastic fan on the north side of Augustine volcano, where they bury the slightly older Rocky Point pyroclastic flow deposit. Magnetic susceptibility measurements were made on continuous-phase pyroclastic flow deposits on both the east and west sides of the pyroclastic fan. These values ranged between 917×10^{-5} SI and $1{,}282\times10^{-5}$ SI, similar to the susceptibility measurements made on the Rocky Point pyroclastic flow deposits. Studies of the lithic makeup of deposits of the continuous phase found mostly a mixture of high-silica andesite and intermediate andesite clasts and banded clasts, with only minor amounts of greenish porphyritic andesite. The measured susceptibilities in the continuous-phase pyroclastic flow



Figure 4. The 2006 Rocky Point pyroclastic flow traveled down the north side of Augustine Island and flowed into a small pond. Yellow rucksack is 80 cm tall.

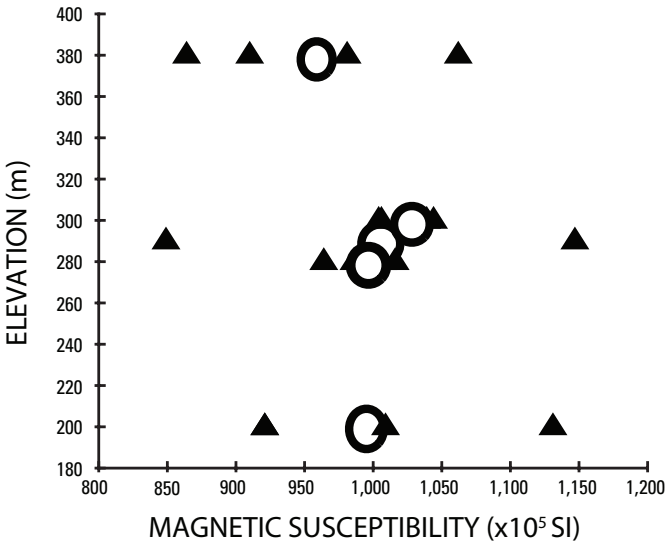


Figure 5. Magnetic susceptibility of the Rocky Point pyroclastic flow measured within a single channel along a 1.5-km-long traverse at five sites between 380 m and 200 m elevation. Multiple measurements were taken at each site. Triangles on the plot show the value of the individual magnetic susceptibility measurement, while large open circles show the mean value calculated for each site. The average susceptibilities were nearly identical at all sites along the traverse.

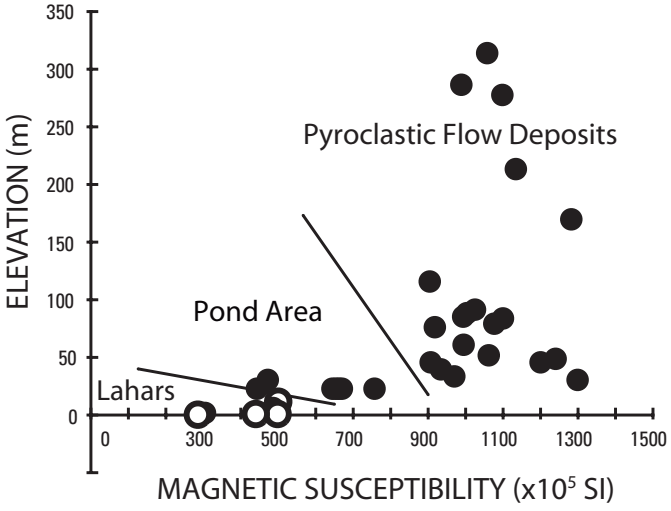


Figure 6. Average volume magnetic susceptibilities of 2006 Rocky Point pyroclastic flow deposits (solid circles), measured on the slopes above the pond site and at the pond site, and lahar deposits (open circles) measured in stream channels. The susceptibilities of the pyroclastic flow deposits in the former pond area were notably lower than those of other pyroclastic flow deposits, and lahar deposits were characterized by similarly low or even lower magnetic susceptibilities.

deposits probably reflect variations in the componentry of the deposits at different localities, just as was seen in the Rocky Point pyroclastic flow deposits.

Interaction of Rocky Point Pyroclastic-Flow Deposits with Water and Steam

The volume magnetic susceptibility of Rocky Point pyroclastic flow deposits decreased significantly where the Rocky Point flow encountered a small pond on the north side of Augustine Volcano (figs. 1, 2). As discussed above, the magnetic susceptibility of pyroclastic flow deposits determined at numerous sites above the pond ranged from ca. 900×10^{-5} SI to 1300×10^{-5} SI. A virtually identical range of susceptibility values was obtained from measurements on the Rocky Point pyroclastic flow deposits in areas immediately adjacent to the pond (table 1). For instance, at a site just 25 m from the pond, where the flow had partially buried alders and burned them (fig. 7), the averaged volume susceptibility of the Rocky Point pyroclastic flow deposit was 1203×10^{-5} SI. This value is indistinguishable from susceptibility measurements taken farther upslope and demonstrates that no significant changes were observed in the susceptibility of the pyroclastic flows as a result of travel distance or elevation loss anywhere throughout the Rocky Point pyroclastic flow deposit above the pond area (fig. 6).

The susceptibility of the Rocky Point pyroclastic flow deposit decreases abruptly where it encountered water at the pond site. During fieldwork in August 2006, the former pond site was found to be filled with the Rocky Point pyroclastic flow deposits but was still easily recognizable as a round, flat local depression in the deposit surface. While rootless fumaroles were rare within the Rocky Point pyroclastic deposit at lower elevations, several small rootless fumaroles were still active in this area, suggesting some moisture might still be present below the former pond surface (fig. 8).

The susceptibility values measured on the flow-deposit matrix around the pond basin ranged from 756×10^{-5} SI to 802×10^{-5} SI, or about 10 to 40 percent lower than the susceptibility of Rocky Point pyroclastic flow deposits or the later, continuous-phase pyroclastic flow deposits found higher on the north side of Augustine Volcano (table 1). The abrupt decrease in magnetic susceptibility observed in Rocky Point pyroclastic flow deposits filling the pond basin suggests that interactions between the hot pyroclastic flow and water and steam produced significant reductions in the initial susceptibility of the pyroclastic flow deposit.

Phreatic Ash and Other Deposits near the Pond

Multiple small craters in the surface of the pyroclastic flow deposits within the pond area, ranging from approximately 1 to 3 m in diameter (fig. 8), show that small phreatic explosions occurred in this area during or soon after the pyroclastic flows entered the pond. These explosion craters are mantled with as much as 10 cm of pink, silt-size ash derived from material elutriated from the 2006 pyroclastic flow



Figure 7. Photograph showing Rocky Point pyroclastic flow deposit on the north flank of Augustine Volcano. The presence of charred alders and soil in a lateral levee of the Rocky Point pyroclastic flow deposit 50 m from the pond area indicates that the flow was still hot when it reached the pond area. Rucksack in photo (indicated by arrow) is 0.8 m in length.

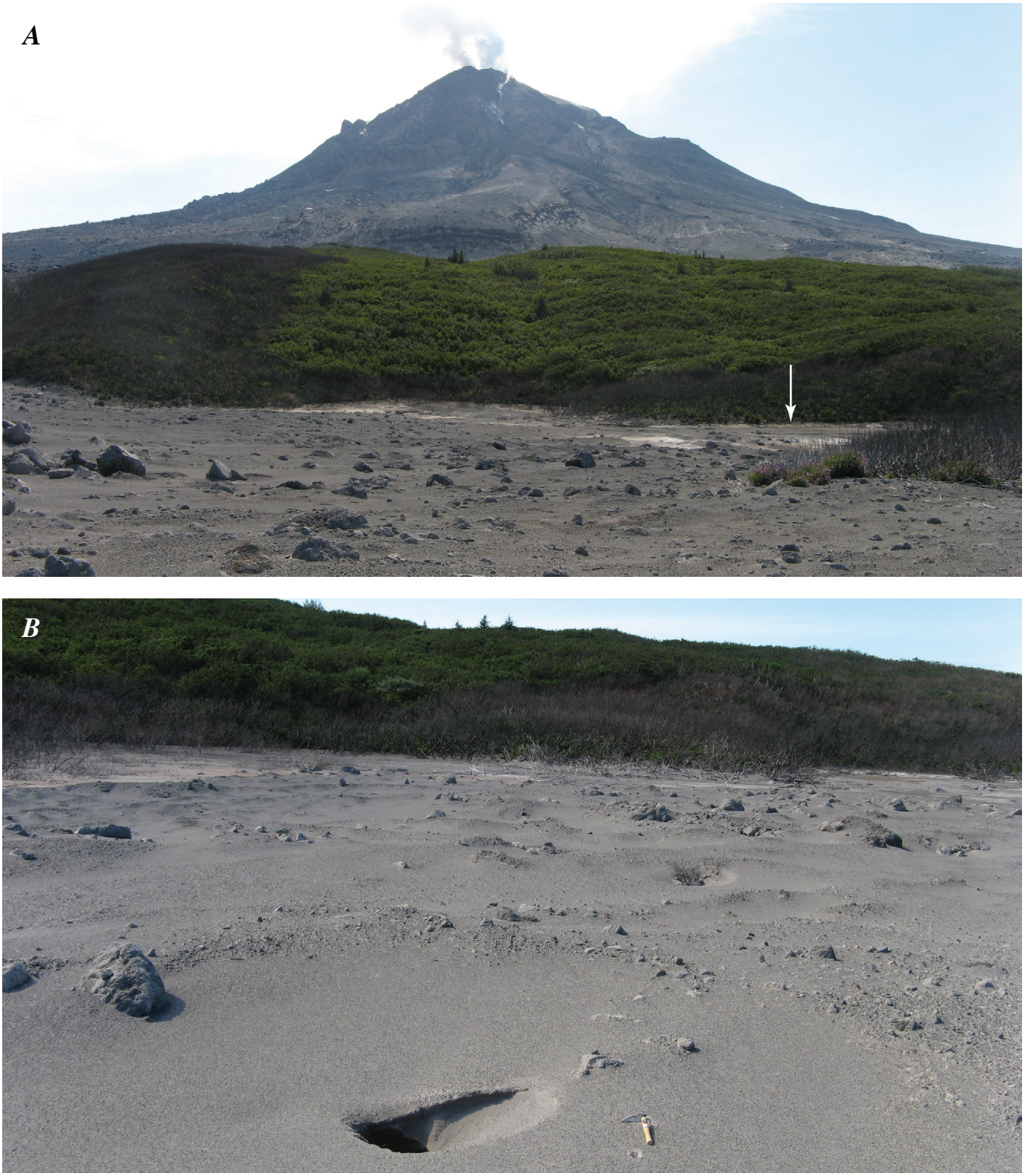


Figure. 8. Photographs of the Rocky Point pyroclastic flow. *A,* View looking south at the area of the pond filled by deposits of the 2006 Rocky Point pyroclastic flow. The Rocky Point pyroclastic flow traveled downslope alongside the ridge at the left of the image, and filled a pond (arrow) at the base of the ridge. Note the area of dead alders along the ridge caused by ash-cloud surges from the pyroclastic flows. Two traverses through the deposits left by the ash-cloud surges were made about 800 m upslope. *B,* Small phreatic explosion craters (pseudocraters) and rootless fumaroles within the pond area. The tool next to the rootless fumarole in the foreground is 28 cm long.

deposits. The magnetic susceptibility of this ash is 482×10^{-5} SI, a value 50 to 70 percent lower than that of the unaltered Rocky Point pyroclastic flow deposits outside the pond area. The low magnetic susceptibility of the phreatic ash deposits in the pond area provides additional evidence that interaction with water and steam can produce significant reductions in the magnetic susceptibility of pyroclastic flow deposits.

The secondary phreatic explosion craters probably formed during very shallow explosions caused by rapid superheating of steam that produced locally overpressured conditions (Shepherd and Sigurdsson, 1982; Sheridan and Wohletz, 1983; Schmincke, 2004). The phreatic ash generated in these explosions was probably originally part of the matrix of the pyroclastic flow that interacted with water and steam as the pyroclastic flow travelled into the pond. The ash underwent an additional period of interaction with steam during the phreatic explosion as local pockets of water flashed to steam and blasted out the small craters. The additional interaction with steam during the phreatic explosions may account for the markedly lower susceptibility of the phreatic ash when compared to the matrix of the Rocky Point pyroclastic flow deposits in the same area.

Vertical Profiles Cut into the 1986 Pyroclastic Flow Deposits

Magnetic susceptibility measurements reported on 2006 pyroclastic flow deposits are from the upper parts of flows and the top and flanks of flow levees. These pyroclastic flow deposits, even in distal areas, were at least 1 m thick and were still hot 4–7 months after the eruption, so that it was not possible to safely excavate a trench completely through a 2006 pyroclastic flow deposit during this study in order to make susceptibility measurements from the top to the bottom of a pyroclastic flow deposit.

Eroded sections through 1986 pyroclastic flow deposits were found in three places beyond the limits of the 2006 pyroclastic flow deposits. Susceptibility measurements were made at 10-cm intervals from the top to the bottom through the three different 1986 pyroclastic flow deposits in order to investigate the possible variations in susceptibility with depth within pyroclastic flows (fig. 1). No significant variations in susceptibility with depth were found in any of the three 1986 pyroclastic flow deposits we studied (fig. 9). This suggests that the susceptibility measurements made in shallow surface trenches excavated into pyroclastic flow deposits are reasonably representative of the magnetic susceptibility of the matrix of the entire pyroclastic flow at any given site.

The 1986 pyroclastic flow deposits were characterized by significantly lower susceptibilities than all the 2006 pyroclastic flow deposits above the pond area.The field setting of the 1986 pyroclastic flow deposits indicated they had not interacted with water (table 1). Light gray dacite clasts make up the main variety of lithic blocks found in the 1986 pyroclastic flows (Waitt and Begét, 2009; Roman and others, 2006), and susceptibility measurements showed that these blocks were characterized by lower susceptibilities than either of the major lithic components of the 2006 Rocky Point pyroclastic flow deposits. This finding is consistent with the hypothesis presented above that the volume susceptibility of a pyroclastic flow deposit matrix primarily reflects the susceptibility and relative abundance of its major lithic components.Because component analyses of the 2006 Augustine pyroclastic flow deposits showed that their fine-grained matrix material consisted of comminuted rock material derived from the major coarse-grained components (Vallance and others, this volume), the susceptibility measurements on the 1986 deposits comprise a rapid proxy measurement of their componentry. Therefore, the significant differences in susceptibility found between the 1986 and 2006 deposits are an indication that susceptibility data can be used to map and differentiate separate groups of pyroclastic flow deposits.

2006 Rocky Point Pyroclastic Surge Deposits

Magnetic susceptibility measurements of surge deposits that had decoupled from the Rocky Point pyroclastic flow and traveled up a slope adjacent to the main pyroclastic fan were made along two traverses spaced about 50 m apart at a site ca. 800 m inland and 175 m higher than the pond area. At this locality the surge had singed alders within a few meters of the western margin of the Rocky Point pyroclastic fan, but it was unable to burn alders after traveling 100 m and 20–30 m

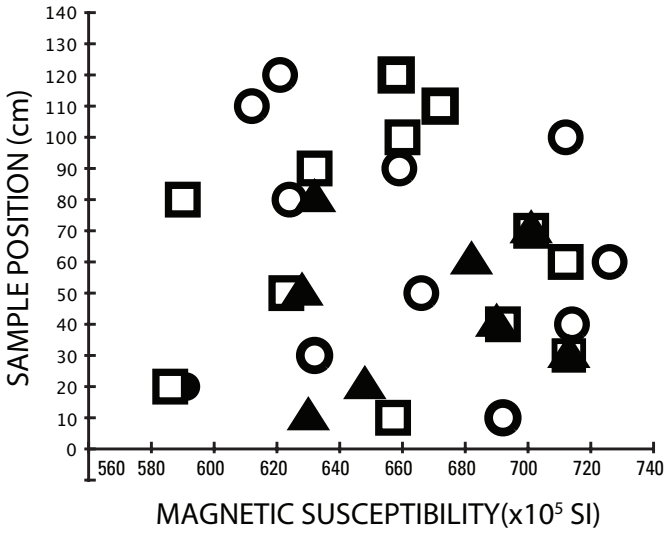


Figure 9. Vertical magnetic susceptibility profiles measured though three 1986 pyroclastic flow deposits.The measurements were taken at 10-cm intervals from the bottom to the top, with two flows (open circle and open square symbols) being ca. 1.3 m thick and one flow (solid triangle symbol) being ca. 1 m thick. No progressive changes or systematic pattern of susceptibility was noted in any of the three measured vertical profiles.Note that although the susceptibility measurements from each pyroclastic flow deposit showed small variations through the sections, the average susceptibilities (658×10^{-5} SI, 665×10^{-5} SI, and 671×10^{-5} SI) of the three 1986 flows were essentially identical.

higher up the slopes (table 1).These slopes were not affected by pyroclastic flows or floods before the Rocky Point eruptive event, and snow was probably present on these slopes and interacted with the pyroclastic surge as it traversed this slope up into the alder grove (Coombs and others, this volume). The ash-cloud surge deposits consisted of weakly bedded coarse sandy beds as much as 10 cm thick that thinned quickly and disappeared within 100 m of the western margin of the Rocky Point pyroclastic flow.

The susceptibility of the surge deposits immediately adjacent to the Rocky Point pyroclastic fan, in an area where the surge had burned alders, averaged $1{,}166\times10^{-5}$ SI, while the average volume susceptibility of deposits from the same surge at higher elevations, where they had cooled enough to not singe alders, was only 433×10^{-5} SI. The observed decrease in susceptibility is greater then 60 percent, i.e. much larger than the decrease in susceptibility observed downslope, where the Rocky Point pyroclastic flow traveled into the pond. The rapid and significant decrease in susceptibility measured over short distances in the ash cloud surge deposits adjacent to the Rocky Point pyroclastic flow deposit shows that the magnetic characteristics of pyroclastic surge deposits can change very rapidly. This contrasts strongly with the susceptibility data from the pyroclastic flows themselves, which showed no progressive changes with travel distance.

2006 Lahar Deposits

Lahar deposits were preserved in several small stream channels downstream from the pyroclastic flow deposits on the north flank (figs. 1, 10). Repeat photography and field observations during the 2006 eruption indicate that these lahars formed during the earliest explosive phase, when low-silica andesite-rich pyroclastic flows produced widespread flooding and lahars that reached the north coast of Augustine Island (Coombs and others, this volume).

The thin lahar deposits are composed of silt- and sand-rich diamictons that form flat terraces along narrow stream channels that are often no more than 2 to 10 m wide. The deposits are all less than 1 m thick, and often only 20–30 cm thick, with porphyritic greenish andesite boulders and rounded cobbles being the primary coarse lithic component (fig. 10). The greenish andesite boulders in pyroclastic flows had high susceptibilities (table 1), but volume susceptibility measurements on the matrix of the lahar deposits were much lower, with values ranging from 284×10^{-5} SI to 643×10^{-5} SI (fig. 6). These susceptibility values measured on lahars are lower than those measured on any of the pyroclastic flow deposits except those deposited within the pond basin.There is some overlap between highest susceptibility values measured on the lahar deposits and the susceptibility values measured for Rocky Point pyroclastic flow and phreatic ash deposits at the pond, but the lowest susceptibility values for the lahars are notably lower than any of the pyroclastic flow deposits from the 2006 eruption.

Interpretation of the Magnetic Susceptibility Data

Magnetic susceptibility is a measure of the relative amounts of different kinds of magnetic minerals present in samples. The changes in magnetic susceptibility documented in this study where pyroclastic flows encountered water and snow therefore record changes in the characteristics of the magnetic minerals in the pyroclastic flow deposits (Evans and Heller, 2003). It is well known that environmental factors, such as soil development or hydrothermal activity, can cause the alteration



Figure 10. Photograph of thin, fine-grained lahar deposits preserved in small stream channels just downslope from the terminal zone of the Rocky Point pyroclastic flow deposits. Also shown is the Bartington MS2F microprobe used in this study. Entrenching tool handle is 40 cm long.

or destruction of the existing magnetic minerals and the generation of new magnetic minerals (Liu and others, 1999). An important finding of this study is that the magnetic susceptibility of pyroclastic flow and surge deposits erupted by Augustine Volcano in 2006 were reduced in areas where encounters with water, snow, and steam occurred. Water-mediated lahar deposits derived from the pyroclastic flows had still lower susceptibilities. Our finding that interactions with water caused susceptibility variations in 2006 pyroclastic flow and lahar deposits at Augustine Island suggest that measurement of magnetic susceptibility variations can provide a new tool for evaluating interactions between pyroclastic flows and water.

Pyroclastic flows typically contain collections of different lithologies or components. Our data show that the susceptibilities of pyroclastic flow deposits erupted at Augustine Volcano in 2006 are somewhat variable but are all higher than pyroclastic flow deposits erupted in 1986. This reflects the higher susceptibilities of the major lithologic components of the 2006 pyroclastic flows and demonstrates that different assemblages of pyroclastic flow deposits produced during separate eruptive events can be differentiated by their magnetic susceptibility. This finding suggests that magnetic susceptibility data may be a useful tool for differentiating and mapping pyroclastic deposits at active volcanoes.

The magnetic susceptibility of the 2006 pyroclastic flow deposits showed significant changes in two key areas. At the northwest margin of the 2006 pyroclastic fan, Rocky Point pyroclastic flows filled a small pond basin. The magnetic susceptibilities of the pyroclastic flow deposits were significantly lower within the infilled pond basin, where the flows encountered water and steam, than they were anywhere else in the pyroclastic fan. Similar reductions in susceptibility were also found in ash cloud surge deposits that had traveled across an area where snow covered the ground. Lahar deposits in stream channels downstream from the pyroclastic flow deposits showed even lower volume susceptibility values.

The observed reductions in magnetic susceptibility in these 2006 Augustine deposits may reflect several different geochemical processes, but most of the change is probably attributable to oxidation of the iron-bearing minerals caused by interactions between the hot pyroclastic flows and water and steam. Oxidation is an inevitable consequence of the exposure of hot pyroclastic rocks to water and steam. Generations of volcanologists have noted the creation of oxidized, hematite-rich zones at the tops of pyroclastic flows, known as “pink tops,” and applied this classic criterion to infer the past presence of heat and water (Ross and Smith, 1961; Hildreth, 1983; Tait and others, 1998). Oxidation of iron-bearing minerals from the ferrous to ferric state characteristically results in the production of mineral phases with lower magnetic susceptibility, and we believe this is the main cause of the susceptibility changes we have observed in the 2006 Augustine pyroclastic flow, surge, and lahar deposits that formed by interactions with water, snow, and steam. Other geochemical processes may also be playing a role, including partial disruptions and dislocations of the atomic structure of the ferro-magnesium minerals (Ishikawa, 1958).

Over long periods of time, weathering and soil development can also cause changes in the original susceptibility of sediments (Maher and Thompson, 1999; Singer and others, 1992), but the 2006 pyroclastic deposits at Augustine were only a few months old when this study was made, and so were far too young for weathering to have greatly affected them.

Did Density Fractionation Occur in the 2006 Augustine Pyroclastic Flows, Surges, and Lahars?

In addition to the effect of geochemical processes on magnetic susceptibility, some physical processes produce sorting of sediments and can alter magnetic susceptibility. For instance, the higher density of magnetic minerals causes them to preferentially settle out of wind-blown sediment and water-transported sediment (Begét, 2001; Oldfield, 1991, 1992; Begét and others, 1990; Begét and Hawkins, 1989).

Could pyroclastic flow processes play a role in creating the observed variations in magnetic susceptiblity at Augustine Volcano?As noted above, the highest group of susceptibility values measured on any of the volcaniclastic deposits came from the 2006 pyroclastic flow deposits. The volume susceptibility measurements from the matrix of these flow deposits showed some variability from flow to flow, probably reflecting differences in the mix of the initial lithic components of the numerous pyroclastic flows produced during this part of the eruption. However, when the susceptibility of one area of the Rocky Point pyroclastic flow deposit was measured at multiple sites along its western margin, the susceptibility of the deposit showed little change for hundreds of meters downslope, suggesting that the processes involved in the lateral transit and emplacement of the Rocky Point pyroclastic flow did not produce progressive susceptibility changes along its flow path.

The prevailing modern view is that pyroclastic flows are dominantly turbulent, although locally they may be characterized by laminar or even plug flow (Schmincke, 2004). The finding here that density sorting and depletion by fractionation of heavy magnetic minerals did not occur to any significant degree as the 2006 pyroclastic flows traveled downslope suggests that the flows were sufficiently turbulent during emplacement to suspend all of the fine-grained components and minimize the loss of heavy Fe-bearing minerals. This was true for samples measured in pyroclastic flow deposit channels, recording sedimentation from the base of flow deposits, from pyroclastic flow levees formed by “freezing” of marginal parts of the pyroclastic flows, and also from flat-surfaced pyroclastic fans and terminal lobes that may have undergone plug flow as they decelerated and stopped.

Regeneration and formation of new matrix material by clast-to-clast collisions as the pyroclastic flow travels downslope and produces a deposit along its path probably plays an important role in modulating downslope changes in magnetic susceptibilities in the 2006 pyroclastic flow deposits. The absence of any progressive change in susceptibility in

the Rocky Point pyroclastic flow from the upper slopes to the lower slopes strongly suggests that either density fractionation of the heavier magnetic minerals did not occur to a significant extent during flow, or new magnetic minerals were continually being added to the matrix of the flows by comminution of larger particles.

In contrast, significant reductions in magnetic susceptibility were observed in 2006 surge deposits that traveled only about 100 m beyond the margin of the Rocky Point pyroclastic flow deposit. Surges are typically highly inflated and have much lower particle concentrations than block-and-ash flows, and they would be more likely to be affected by density fractionation. The rapid decrease in susceptibility observed in the local surge deposits formed in 2006 at Augustine Volcano likely reflects some oxidation and alteration of the ferromagnetic minerals produced as the heat of the surge produced water and steam from the underlying snow, but we also suspect that some significant amount of the reduction in susceptibility seen in the distal surge deposits reflects progressive fractionation and removal of the denser magnetic minerals from the turbulent and dilute surge ash cloud as it traveled away from its source in the main Rocky Point pyroclastic flow deposit.

The magnetic susceptibility of lahars found downslope from the Rocky Point pyroclastic flow deposits is lower than that of the hot pyroclastic deposits from which they were derived. Lahars generated during the 2006 Augustine eruption appear to have been mainly produced by interactions between pyroclastic flows and surges and the winter snowpack (Vallance and others, this volume). The sediment in the lahars was in direct and prolonged contact with water, and the low susceptibility of the lahars is thought to reflect sustained geochemical alteration and oxidation of the ferromagnetic minerals. It is possible that some loss of heavy minerals by density fractionation may also have occurred during lahar deposition, but we do not see any progressive evolution in the susceptibility of the lahar deposits with distance away from the pyroclastic flow margin, as occurred in the surge deposits. For this reason, we do not think that density fractionation was an important factor in the evolution of the magnetic susceptibility of the lahar deposits, and we attribute the lower magnetic susceptibility that characterizes these deposits to water-rock interaction as the pyroclastic flows encountered snow and water and transformed into lahars that traveled to the lower flanks of the volcano.

Acknowledgments

This study was supported by the Alaska Volcano Observatory and by a National Science Foundation grant to Begét. We gratefully acknowledge helpful reviews by John Hagstrum and John Power of the U.S. Geological Survey, and by Kate Bull of the Division of Geological and Geophysical Surveys of the State of Alaska. Michelle Coombs and Jim Vallance kindly introduced the author to the complexities of the 2006 Augustine pyroclastic flow deposits during fieldwork on Augustine Island, and Michelle Coombs helped the author with an early draft of the manuscript.

References

Bartington Corporation, 2004, Operation Manual for MS2 Magnetic Susceptibility System: 72 p.

Begét, J.E., 2001, Continuous late Quaternary proxy climate records from loess in Beringia: Quaternary Science Reviews, v. 20, p. 499–509.

Begét, J., and Hawkins, D., 1989, Influence of orbital parameters on Pleistocene loess deposition in central Alaska: Nature, v. 337, p. 151–153.

Begét, J. E., and Kienle, J. 1992, Cyclic formation of debris avalanches at Mt. St. Augustine volcano, Alaska: Nature, v. 356, p. 701–704.

Begét, J., Stone, D., and Hawkins, D., 1990, Paleoclimatic forcing of magnetic susceptibility variations recorded in central Alaskan loess: Geology v. 18, p. 40–43.

Begét, J. E., Stihler, S., and Stone, D. B., 1994, A 500 year long record of tephra falls from Redoubt Volcano and other volcanoes in upper Cook Inlet, Alaska: Journal of Volcanology and Geothermal Research, v. 62, p. 55–67

Coombs, M.L., Bull, K.F., Vallance, J.W., Schneider, D.J., Thoms, E.E., Wessels, R.L., and McGimsey, R.G., 2010, Timing, distribution, and volume of proximal products of the 2006 eruption of Augustine Volcano, *in* Power, J.A., Coombs, M.L., and Freymueller, J.T., eds., The 2006 eruption of Augustine Volcano, Alaska: U.S. Geological Survey Professional Paper 1769 (this volume).

Cronin, S.J., Hodgson, K.A., Neall, V.E., Palmer, A.S., and LeCointre, J.A., 1997, The 1995 Ruapehu lahars in relation to the late Holocene lahars of Whangaehu River, New Zealand: New Zealand Journal of Geology and Geophysics, v. 40, p. 507–520.

Evans, M.E. and Heller, F., 2003, Environmental Magnetism: principles and applications of environmagnetics: Amsterdam, Academic Press, 299 p.

Hildreth, W., 1983, The compositionally zoned eruption of 1912 in the Valley of Ten Thousand Smokes, Katmai National Park, Alaska: Journal of Volcanology and Geothermal Research, v. 18, p. 1–56.

Ishikawa, Y., 1958, An order-disorder transformation phenomenon in the $FeTiO_3$–Fe_2O_3 solid solution series: Journal of the Physics Society of Japan, v. 13, p. 828–837.

Liu, X.M., Hesse, P., Rolph, T. and Begét, J., 1999, Properties of magnetic mineralogy of Alaskan loess, evidence for pedogenesis: Quaternary International, v. 62, p. 93–102.

Maher, B., and Thompson, R., 1999. Quaternary climates, environments and magnetism: Cambridge University Press, 354 p.

Oldfield, F., 1991, Environmental magnetism, a personal perspective: Quaternary Science Review, v. 10, p. 73–85.

Oldfield, F., 1992, The source of fine-grained ‘magnetite’ in sediments: Holocene, v. 2, p. 180-182.

Pierson, T.C., Janda, R.J., Thouret, Jean-Claude, and Borrero, C.A., 1990, Perturbation and melting of snow and ice by the 13 November 1985 eruption of Nevado del Ruiz, Colombia, and consequent mobilization, flow, and deposition of lahars: Journal of Volcanology and Geothermal Research, v. 41, p. 17–66.

Power, J.A., Nye, C.J., Coombs, M.L., Wessels, R.L., Cervelli, P.F., Dehn, J., Wallace, K.L., Freymueller, J.T., and Doukas, M.P., 2006, The reawakening of Alaska's Augustine Volcano: Eos (American Geophysical Union Transactions), v. 87, no. 37, p. 373, 377.

Roman, D.C., Cashman, K.V., Gardner, C.A., Wallace, P.J., and Donovan, J.J., 2006, Storage and interaction of compositionally heterogeneous magmas from the 1986 eruption of Augustine Volcano, Alaska: Bulletin of Volcanology, v. 68, p. 240–254.

Ross, C.S., and Smith, R.L., 1961, Ash-flow tuffs, their origin, geologic relations and identitification: U.S. Geological Survey Professional Paper 366, 81 p.

Schmincke, H-U., 2004, Volcanism: Berlin, Springer Press, 324 p.

Shepherd, J.B., and Sigurdsson, H., 1982, Mechanism of the 1979 explosive eruption of Soufriere Volcano, St. Vincent: Journal of Volcanology and Geothermal Research, v. 13, p. 119–130.

Sheridan, M. and Wohletz, K.H., 1983, Hydrovolcanism, basic considerations and review: Journal of Volcanology and Geothermal Research, v. 17, p. 1–29.

Siebert, L., Begét, J., and Glicken, H., 1995, The 1883 and late-prehistoric eruptions of Augustine volcano, Alaska: Journal of Volcanology and Geothermal Research, v. 66, p. 367–396.

Singer, M.J., Fine, P., Verosub, K.L., and Chadwick, O.A., 1992, Time dependence of magnetic susceptibility on soil chronosequences on the California coast: Quaternary Research, v. 37, p. 323–332.

Tait, S., Thomas, R., Gardner, J., and Jaupart, C., 1998, Constraints on cooling rates and permeabilities of pumice in an explosive eruption jet from colour and magnetic mineralogy: Journal of Volcanology and Geothermal Research, v. 86, no. 1–4, p. 79–91.

Vallance, J.W., Bull, K.F., and Coombs, M.L., 2010, Pyroclastic flows, lahars, and mixed avalanches generated during the 2006 eruption of Augustine Volcano, *in* Power, J.A., Coombs, M.L., and Freymueller, J.T., eds., The 2006 eruption of Augustine Volcano, Alaska: U.S. Geological Survey Professional Paper 1769 (this volume).

Waitt, R.B. and Begét, J.E., 2009, Volcanic processes and geology of Augustine Volcano, Alaska: U.S. Geological Survey Professional Paper 1762, 78 p.

This page intentionally left blank

The 2006 Eruption of Augustine Volcano, Alaska
Power, J.A., Coombs, M.L., and Freymueller, J.T., editors
U.S. Geological Survey Professional Paper 1769

Chapter 12

Remote Telemetered and Time-Lapse Cameras at Augustine Volcano

By John Paskievitch[1], Cyrus Read[1], and Thomas Parker[1]

Abstract

Before and during the 2006 eruption of Augustine Volcano, the Alaska Volcano Observatory (AVO) installed a network of telemetered and nontelemetered cameras in Homer, Alaska, and on Augustine Island. On December 1, 2005, a network camera was installed at the Homer Field Station, a University of Alaska Fairbanks Geophysical Institute (UAF/GI) facility on a bluff near Homer, where telemetered Augustine data are received. The camera placed there provides observations of the volcano from a distance of 126 km (78 miles) in daylight hours during clear sky conditions. On January 9, 2006, a radio-telemetered network camera was installed on the lower eastern flank of the volcano at "Mound," 4.4 km (2.7 miles) from the summit. The proximity of this camera provided for near-field images of the volcano. A nontelemetered camera with onsite recording was installed 3.8 km (2.4 miles) north of the volcano's summit near Burr Point on December 17, 2005. This camera recorded high-resolution images at a rate of 4 images per hour through much of the eruptive sequence. A low-light camera was installed on February 8, 2006, at the Homer facility to augment the extreme low-light camera installed by the UAF/GI (Sentman and others, this volume). On September 10, 2006, a second radio-telemetered network camera was installed at Lagoon camp on the west side of Augustine Island, 5.4 km (3.3 miles) west-northwest of the summit. The installation of these camera systems proved valuable for assessing volcanic activity, determining ground hazards and on-island weather for visiting field teams, and deciphering depositional history after the eruption.

Introduction

Augustine Volcano, in lower Cook Inlet, is one of the most frequently active volcanoes in Alaska, recently erupting in 1976 and 1986 (Miller and others, 1998). Increased seismicity and deformation, starting in April 2005 and escalating in November 2005, indicated that the volcano was likely to become active once again (Power and others, 2006). Therefore, the Alaska Volcano Observatory (AVO) installed a network of telemetered and nontelemetered cameras in Homer, Alaska, and on Augustine Volcano (fig. 1) in anticipation of an eruption. These cameras, similar to ones previously installed by AVO to monitor Veniaminof and Spurr volcanoes, augmented telemetered geophysical data and provided frequent visual observations of this remote volcano. Images from the telemetered cameras were served over the Internet on AVO's Web site for internal and public use. This paper presents a description of the equipment and installation of these cameras, and a chronology of when they were operational. More detailed analysis of the images is presented in Coombs and others (this volume) and Vallance and others (this volume).

Chronology of the 2006 Eruption and Camera Installation

Beginning in mid-2005, AVO detected an increased number of earthquakes beneath Augustine's summit and evidence of inflation of the volcanic edifice (Power and others, 2006). Seismicity increased to higher levels in November 2005. Several phreatic explosions occurred in December 2005. On January 10, 2006, seismicity increased sharply, and this was followed on January 11 by two brief explosive eruptions. From January 13 through 28, 11 more discrete vulcanian blasts produced ash clouds that rose to 16 km above sea level (asl), pyroclastic flows, lahars, and avalanches on the island

[1]Alaska Volcano Observatory, U.S. Geological Survey, 4200 University Drive, Anchorage, AK 99508.

(the "explosive phase"). On January 28, the volcano entered a period of more continuous activity consisting of rapid lava effusion, block-and-ash flows, and ash emission (the "continuous phase"; Coombs and others, this volume). After a pause in activity from February 10 to March 3, activity resumed during the "effusive phase" as two lava flows and a new summit lava dome were emplaced, accompanied by many small block-and-ash flows from the growing lava bodies.

A network camera was installed at the Homer Field Station on December 1, 2005. A nontelemetered camera with onsite storage was installed on the north flank of the volcano near Burr Point on December 17, 2005. On January 9, 2006, AVO installed the first remote radio-telemetered network camera on Augustine Island east-northeast of the summit at a site informally known as "Mound," just two days before the onset of the explosive phase. On February 8, 2006, a low-light camera and network video server were installed at the Homer Field Station. The final network camera was installed on the west side of Augustine Island at the informally named "Northwest Lagoon" on September 10, 2006. Daytime activity during all three phases of the eruption was mostly imaged by both the netcam at Mound and the nontelemetered camera at Burr Point, except when weather clouds or ash obscured the view The image records of both the telemetered and non telemetered

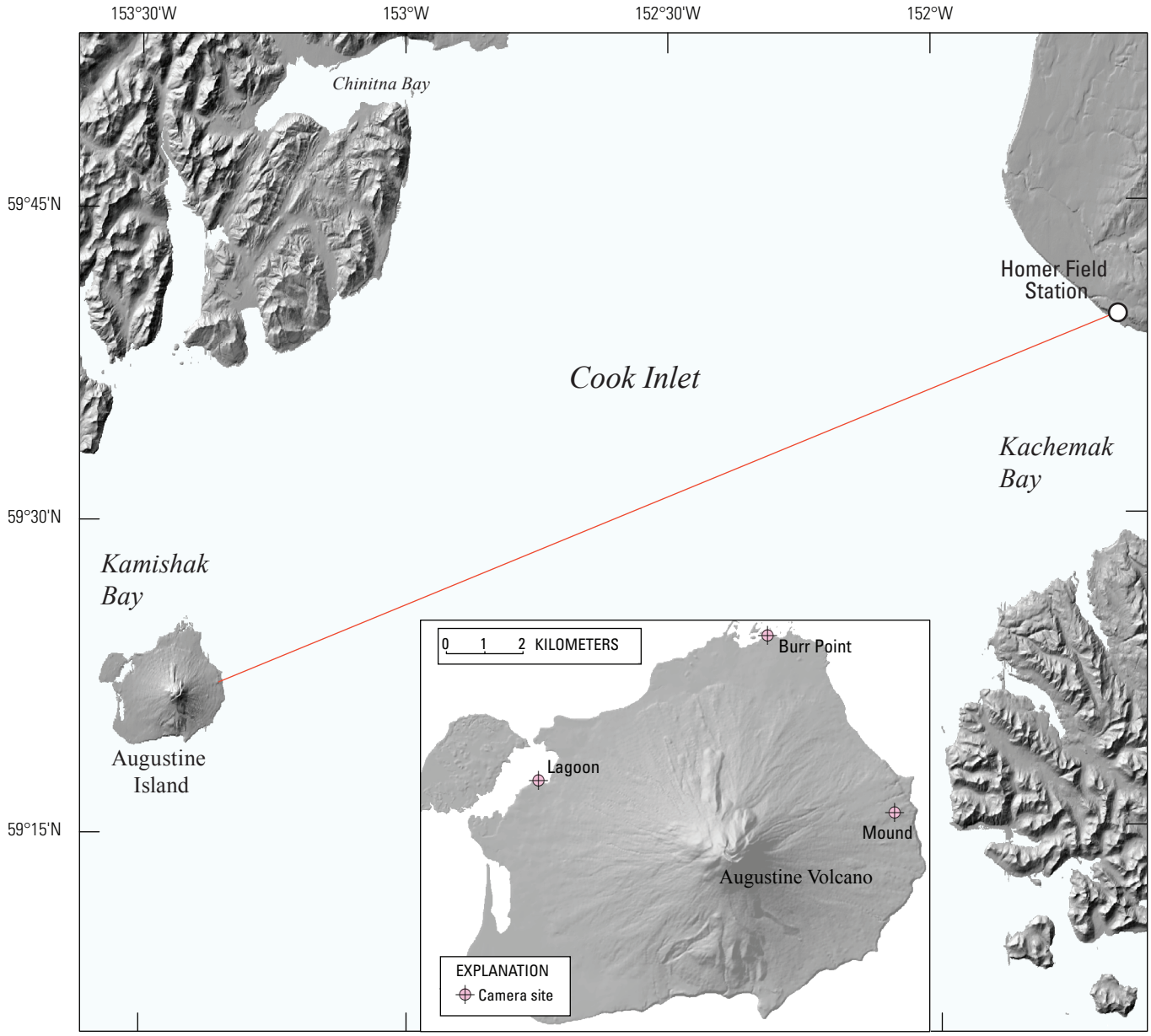


Figure 1. Map of lower Cook Inlet showing Augustine Island and telemetry path (in red) from the Mound camera back to the Homer Field Station. Inset map shows location of cameras on Augustine Island.

telemetered cameras were occasionally interrupted during parts of January and February as a result of various power problems, exceeding on-site recording capacity, and physical damage to the installations. Cameras located in Homer did not image any of the explosive activity because of poor visibility, but they did record much of the activity during the continuous and effusive phases of the eruption.

Cameras Used

A variety of cameras were used to establish the visual monitoring network (table 1). Stardot network cameras were used for telemetered daylight images. The Stardot Netcam MegaPixel is an IP networked camera (appendix 1). Its Web interface allows adjustment and control of various parameters, including those affecting image quality, date and time stamps, text overlays, security, file naming, and image transfer. Near-real-time images can be viewed remotely using http and automatically uploaded to designated servers using ftp.

A Watec 120N analog camera connected through a Stardot video server provided telemetered nighttime images. The Watec 120N is a monochrome low-light camera with sensitivity in the near-infrared (appendix 1). It was used in conjunction with a Watec 120N control box which allows for gain adjustment and image integration. Images from this camera were sampled and transmitted across a Stardot Ethernet-based video server (appendix 1).

A Nikon COOLPIX 8700 configured with a Harbortronics DigiSnap 2000 time-lapse control system was used to take time-lapse images and store them on-site. The Nikon COOLPIX 8700 is an 8 effective megapixel digital camera. The Harbortronics DigiSnap 2000 controls image sampling intervals, and a Harbortronics voltage regulator conditions the power needed by both the camera and DigiSnap 2000. This system was tested, packaged, and provided by the Hawaiian Volcano Observatory (HVO) and is further described in Orr and Hoblitt (2008). Vendor specifications for equipment used in this package are given in appendix 1.

Homer-based Network Camera

A Stardot Netcam MegaPixel camera was installed at the UAF/GI Homer facility on December 1, 2005. It is mounted on a window ledge inside the facility and aimed through a window at Augustine Island. The camera is fixed with a remotely controllable 8 mm to 48 mm motorized zoom lens. It is attached to the Homer-based UAF/GI network and is accessible through the Internet. It sends images at user-defined intervals to an ftp server at AVO facilities in Anchorage. Images were transferred at 5-minute intervals throughout the eruption.

The distance of this camera from the volcano (126 km, or 78 miles) allows for a broader field of view, useful for determining heights and lateral trends of plumes. However, darkness and cloud conditions between camera and target often prevented observation of the volcano, and none of the explosive events in January were imaged. This camera did provide useful images during the continuous and effusive phases of activity at times when clear skies coincided with daylight hours (fig. 2). More proximal cameras that require radio telemetry or onsite storage were decided upon to capture the potential eruptive activity.



Figure 2. Image of Augustine Volcano, 78 miles away, captured by the Homer Field Station netcam on December 1, 2005.

Mound Network Camera

A radio-telemetered Stardot Netcam MegaPixel camera was installed at Augustine Volcano at “Mound” on January 9, 2006, just before the onset of explosive activity. Mound is located on a small hill on the east side of the island at an elevation of about 100 m and 4.4 km from the summit. The camera is mounted within a Stardot enclosure attached to a solar panel mounting structure (fig. 3).

The equipment package (fig. 4) at Mound includes a Trimble NetRS GPS receiver for deformation monitoring, a RefTek ANSS-130 strong-motion accelerometer for seismic monitoring, the Stardot

Table 1. Summary of cameras installed during 2005 and 2006 to monitor Augustine Volcano.

Camera Name	Camera Used	Date of Initial Deployment	Lens Used	Operating Resolution (pixels)	Image Capture Frequency	Camera Outage/ Reduced Capture Rate
Homer Netcam	Stardot Netcam Megapixel	12/1/2005	8-48-mm motorized zoom lens	640×480	1 image every 5 minutes	None
Homer Low-Light Camera	Watec 120N	2/8/2006	n/a	758×494	1 image every 2 minutes	None
Mound Netcam	Stardot Netcam Megapixel	1/9/2006	8-mm zoom lens	640×480	2 images every 30 minutes	1/17/2006 – 2/21/2006: Frequency of image capture reduced during low visibility or darkness to save power.
Burr Point Time- Lapse Camera	Nikon COOLPIX 8700	12/17/2005	Built in Nikon lens	1,024×768 (in TV mode)	1 image every 15 minutes	1/23/06 – 2/24/06: Camera was removed from island for maintenance. 5/13/06: Camera ran out of battery.
Lagoon Netcam	Stardot Netcam	9/10/2006	8-mm zoom lens	320×240	2 images every 60 minutes	Occasional outages due to poor radio telemetry.

camera system, a serial-based power controller, a serial-to-Ethernet device server, and an Intuicom EB-1 wireless Ethernet bridge. All Ethernet devices are part of the Homer-based UAF/GI network and are linked to it using the Intuicom Ethernet Bridge (appendix 1).

The image interval of this camera was decided partly by bandwidth limitations, but mostly by power considerations. The combined power requirement of the equipment at Mound is nearly 12W, which is a heavy load for a small-scale solar power system during the winter months in Alaska. Power use had to be managed to stay within the limits of the reserve and recharge rate of the power system, which was done through a USGS-designed power controller (appendix 2). This is a device that reports site voltage and allows management of four independently controlled power ports through a terminal session. The camera was placed on a power port that is programmable for powering on at user-defined intervals and durations. The Mound camera was typically set to power on at 30-minute intervals for 5-minute durations. The camera was powered on for longer durations during periods of anticipated or actual eruptions. While powered on, the camera was set to transfer images at 2-minute intervals.

One of the advantages of a near-field camera is that it suffers far less obstruction from cloud and fog than a camera (in this comparison) placed 78 miles away in Homer. While the Homer camera failed to image any of January's explosive events, the Mound camera imaged most of them. The most impressive sequence imaged by the Mound camera was during an explosive event on January 13, between 16:35 and 16:45 AKST (fig. 5).

Low-light Camera

A Watec 120N low-light camera was installed at the UAF/GI Homer facility on February 8, 2006, which supplemented a small astronomical CCD camera (Sentman and others, this volume). The low light camera is mounted on a ledge inside the facility and aimed through a window at Augustine Volcano. It is attached to the Homer-based UAF/GI network by a video server. The video server is accessible through the Internet and sends images at user-defined intervals to an ftp server at AVO facilities in Anchorage. Images were transferred at 2-minute intervals through most of the eruption.

This camera allowed viewing of the volcano at night. It imaged much of the summit area activity during the effusive phase of the eruption (fig. 6).

Time-Lapse Camera

A stand-alone 8.0 megapixel Nikon COOLPIX 8700 digital camera system was installed on an old debris-flow deposit on the north side of the volcano at Burr Point on December 17, 2005. The camera enclosure housed the camera,



Figure 3. The Mound camera aimed at Augustine Volcano. The camera's housing has a protective debris- and snow-shedding shield of bent aluminum. The housing is attached to an Alaska Volcano Observatory (AVO) solar-panel mounting structure. AVO photo by M. Coombs, January 12, 2006.

intervalometer, and DC-DC inverter, and it had a lexan window plate through which images were captured. This box was attached to a larger fiberglass box that housed a 100A/hr lead-acid battery. The image interval of 15 minutes and image file size of approximately 600KB allowed for about 70 days of storage on a 4-gigabyte flash card.

The location of this camera allowed imaging of the north side of the volcano, where activity was focused during the continuous and effusive phases of the eruption. The camera captured much of the daylight eruptive activity in high resolution and allowed reconstruction of the sequence of events (Coombs and others, this volume; their fig. 4). In addition, incandescent lava and block-and-ash flows were often visible in nighttime images from this vantage during the effusive phase of the eruption (fig. 7; Coombs and others, this volume; their fig. 17).

Lagoon Camera

A Stardot Netcam system was installed on a wooden hut at the Northwest Lagoon base camp on the west side of Augustine Island on September 10, 2006. This camera used an existing Plate Boundary Observatory (PBO) Intuicom radio

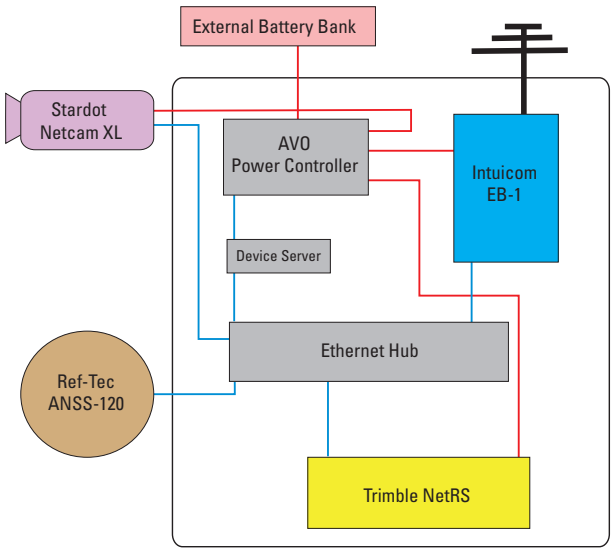


Figure 4. Block diagram of the Mound equipment package. Red lines indicate 12-volt DC power connections to the Alaska Volcano Observatory (AVO) power controller, while blue lines indicate data connections. The thin black line represents a Hardigg Storm Case iM2700, which houses electronic equipment.

network, as described in Pauk and others (this volume). The camera has an 8-mm lens. Image resolution was kept low, set to 320×240, and image upload interval was set to 2 images per hour in order not to impact bandwidth on the PBO network. Although this camera was not installed until after the eruptive activity, it was useful during post-eruption field operations (fig. 8) and is still operational in May 2010.

Image Handling

Images were uploaded from the individual devices to a file server at AVO in Anchorage. Image retention on the file server was limited to allow for frequent synchronization with upstream processing systems. The AVO internal Web server retrieved new images from the file server at a scheduled interval. Once on the

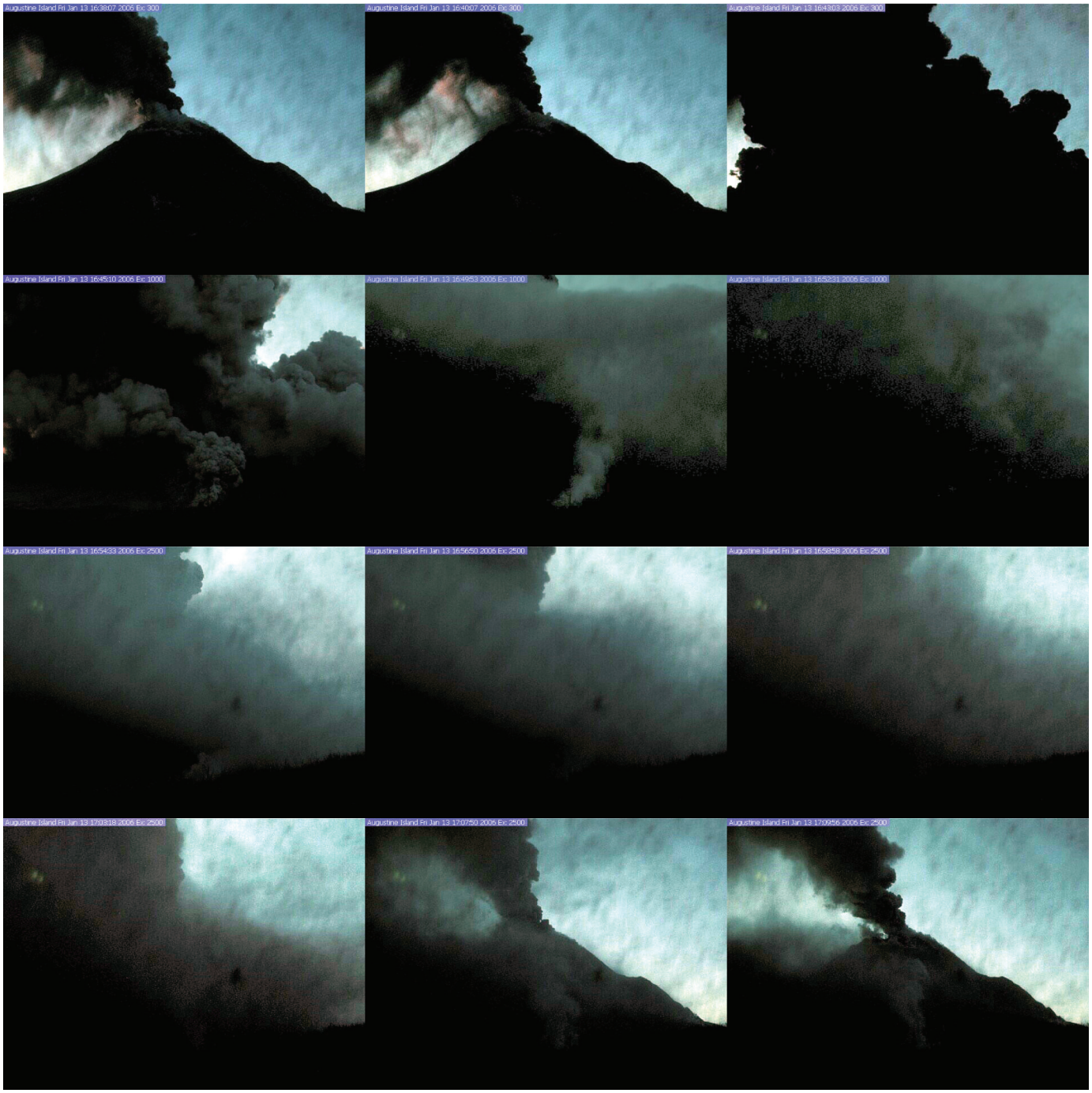


Figure 5. Augustine Volcano eruptive sequence as imaged by the Mound camera. Images cover from 16:38:07 to 17:09:56 AKST on January 13, 2006. The sequence of images is from left to right in each row and top to bottom in rows.



Figure 6. Nighttime image of a lava flow from Augustine Volcano, captured on February 8, 2006, from the Homer Field Station using the Watec 120N low-light camera. The outline of the volcano is seen with the lava dome visible on the right side of the summit. The light colored foreground is snow which has bright spots where moonlight is being reflected.

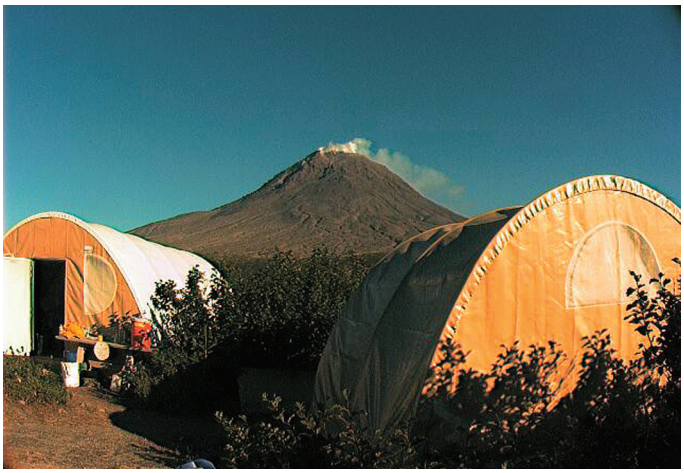


Figure 8. Image captured by the Lagoon camera during field operations on Augustine Island on September 12, 2006, showing an Alaska Volcano Observatory (AVO) base camp.



Figure 7. Image of Augustine Volcano captured by the Burr Point time-lapse camera at 1747 AKST on March 6, 2006, during the effusive phase of the eruption. Incandescence is from growing lava dome and lava flows on the volcano's north flank.

internal Web server, the images were sorted into directories by date for long-term storage and retrieval. A pointer to the most recent image from each camera was maintained to allow it to be downloaded from a static URL. Images were available on the internal Web server within 5 minutes of their acquisition. Rapid creation of simple animations from each camera was made possible by stitching together individual images into an AVI file encoded with MJPEG.

The AVO public Web server retrieved images from each camera's static URL on a set schedule. The public server only maintained the most recent image from each camera. Images were available on the server within 10 minutes of their acquisition.

Conclusions

The use of the Augustine remote camera systems established real-time visual observations of eruptions as a critical aspect of the AVO response. Near and far field cameras at multiple angles capable of imaging in all light conditions allows for critical hazard assessments, estimation of plume heights, accurate depositional chronology, and onsite weather/hazard assessments for field teams visiting an active volcano. The telemetered cameras are still operational as of May 2010 and AVO continues to use them as part of its monitoring repertoire.

References Cited

Coombs, M.L., Bull, K.F., Vallance, J.W., Schneider, D.J., Thoms, E.E., Wessels, R.L., and McGimsey, R.G., 2010, Timing, distribution, and volume of proximal products of the 2006 eruption of Augustine Volcano, *in* Power, J.A., Coombs, M.L., and Freymueller, J.T., eds., The 2006 eruption of Augustine Volcano, Alaska: U.S. Geological Survey Professional Paper 1769 (this volume).

Miller, T.P., McGimsey, R.G., Richter, D.H., Riehle, J.R., Nye, C.J., Yount, M.E., and Dumoulin, J.A., 1998, Catalog of the historically active volcanoes of Alaska: U.S. Geological Survey Open-File Report 98-582, 104 p.

Orr, T.R., and Hoblitt, R.P., 2008, A versatile time-lapse camera system developed by the Hawaiian Volcano Observatory for use at Kilauea Volcano, Hawai'i: U.S. Geological Survey Scientific Investigations Report 2008-5117, 8 p. [http://pubs.usgs.gov/sir/2008/5117/].

Pauk, B.A., Jackson, M., Feaux, K., Mencin, D., and Bohnenstiehl, K., 2010, The Plate Boundary Observatory permanent global positioning system network on Augustine Volcano before and after the 2006 eruption, *in* Power, J.A., Coombs, M.L., and Freymueller, J.T., eds., The 2006 eruption of Augustine Volcano, Alaska: U.S. Geological Survey Professional Paper 1769 (this volume).

Power, J.A., Nye, C.J., Coombs, M.L., Wessels, R.L., Cervelli, P.F., Dehn, J., Wallace, K.L., Freymueller, J.T., and Doukas, M.P., 2006, The reawakening of Alaska's Augustine Volcano: Eos (American Geophysical Union Transactions), v. 87, no. 37, p. 373, 377.

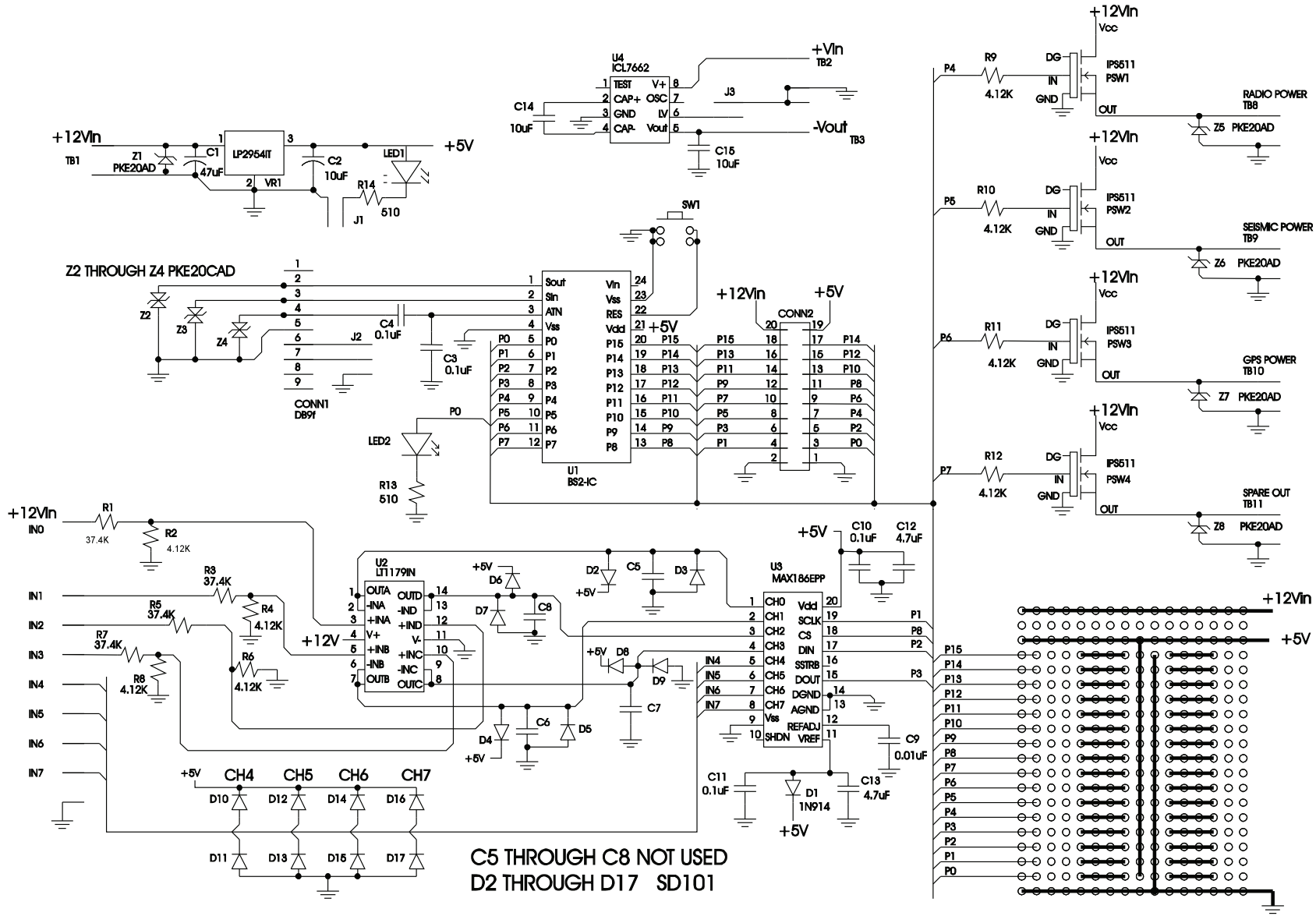
Sentman, D.D., McNutt, S.R., Stenbaek-Nielsen, H.C., Tytgat, G., and DeRoin, N., 2010, Imaging observations of thermal emissions from Augustine Volcano using a small astronomical camera, *in* Power, J.A., Coombs, M.L., and Freymueller, J.T., eds., The 2006 eruption of Augustine Volcano, Alaska: U.S. Geological Survey Professional Paper 1769 (this volume).

Vallance, J.W., Bull, K.F., and Coombs, M.L., 2010, Pyroclastic density currents, lahars, and mixed avalanches generated during the 2006 eruption of Augustine Volcano, *in* Power, J.A., Coombs, M.L., and Freymueller, J.T., eds., The 2006 eruption of Augustine Volcano, Alaska: U.S. Geological Survey Professional Paper 1769 (this volume).

Appendixes 1 and 2

Appendix 1. Product data sheets and manuals.

Equipment	Internet Link for Manual
Stardot Netcam MegaPixel	http://stardot-tech.com/netcam/netcam-brochure.pdf
Watec 120N	http://www.wateccameras.com/products.php?prod_id=124
Stardot video server	http://www.stardot.com/express6/specs.html
Nikon COOLPIX 8700	http://www.nikonusa.com/pdf/manuals/coolpix/CP8700_en.pdf
Harbortronics DigiSnap 2000	http://www.harbortronics.com/digisnap2000_manual.pdf
Harbortronics voltage regulator	http://www.harbortronics.com/detail.php?id=45
Intuicom EB-1	http://www.intuicom.com/www/datasheets/INT_EB1_Datasheet.pdf



AVO CONTROLLER AND POWER SWITCH

AVO Power Controller as designed by Tom Murray, AVO/USGS

Appendix 2. Schematic of the Alaska Volcano Observatory (AVO) "Stamp" which allows remote power and timing control of devices.